Fundamental Investigation of Forced Wetting on Structured Surfaces

vom Fachbereich Maschinenbau
an der Technischen Universität Darmstadt zur Erlangung des Grades eines
Doktor rerum naturalium (Dr. rer. nat.)
genehmigte

Dissertation

vorgelegt von

M. Sc. Selin Manukyan

aus Istanbul, Türkei

TECHNISCHE
UNIVERSITÄT
DARMSTADT

Berichterstatter	: Prof. Dr.-Ing Cameron Tropea
Mitberichterstatter	: PD. habil. Dr.-Ing. Ilia V. Roisman
Mitberichterstatter	: Prof. Dr. Stephen Garoff
Tag der Einreichung	: 30.01.2013
Tag der mündlichen Prüfung	: 19.04.2013

Darmstadt 2013
D17

Erklärung zur Dissertation

Hiermit versichere ich, die vorliegende Dissertation ohne Hilfe Dritter nur mit den angegebenen Quellen und Hilfsmitteln angefertigt zu haben. Alle Stellen, die aus Quellen entnommen wurden, sind als solche kenntlich gemacht. Diese Arbeit hat in gleicher oder ähnlicher Form noch keiner Prüfungsbehörde vorgelegen.

Darmstadt, den 30. Januar 2013

M. Sc. Selin Manukyan

Abstract

The present work is an attempt to understand wetting on very rough surfaces for printing, coating, cooling etc. applications. Various kinds of PDMS (polydimethylsiloxane), deionized water, and glycerin-water (85%-15% vol.) mixture were used to wet the pyramidal arrays and concentric triangular circles, which have scales in millimeters. Wetting of the test substrates were done both in vertical and horizontal orientation, by dipping the substrate in a liquid bath and pumping the liquid through the center of the substrate, respectively. The apparent contact angle on each substrate was measured and a correlation between capillary number, contact angle, and feature size was sought. Existing models and contact angle evaluation methods, together with additional new approaches, have been applied and were discussed extensively.

Numerical simulations for wetting on horizontally placed substrates were performed by using a C++ based, open source CFD software package, OpenFOAM® (Open Source Field Operation and Manipulation). Kistler's dynamic wetting equation was implemented into the software. Simulation results compatible with experiments were achieved.

In conclusion, it is shown that there is not a unique boundary condition on the contact angle/line, even for one test surface, which spoils the transferability of contact angle. Moreover, roughness on these scales bears significant differences with chemical heterogeneity.

Kurzfassung

Die vorliegende Arbeit dient dazu, die Benetzung auf grob struktuierten Oberflächen für Anwendungen in der Druck-, Beschichtungs-, Kühlungstechnik etc. zu verstehen. Entionisiertes Wasser, Glycerin-Wasser (85%-15% vol.) Mischung sowie verschiedene Arten von PDMS (Polydimethylsiloxan) wurden zur Untersuchung der Benetzbarkeit von pyramidenförmigen Feldern und konzentrischen dreieckigen Kreisen, die im Größenbereich von Millimeter liegen, verwendet. In den Versuchen wurde die Benetzbarkeit der Substrate in zwei verschiedenen Ausrichtungen untersucht. In vertikaler Richtung, durch Eintauchen und Herausziehen des Substrats in/aus einen Flüssigkeitsbad; in horizontaler Richtung durch Pumpen der Flüssigkeit durch die Mitte des Substrats. Der scheinbare Kontaktwinkel auf dem jeweiligen Substrat wurde gemessen und die Korrelation zwischen Kapillarzahl, Strukturgröße und Kontaktwinkel untersucht. Die bestehenden Modelle und Auswertungsverfahren zur Bestimmung des Kontaktwinkels, sowie neue Ansätze, wurden angewendet und ausführlich diskutiert.

Numerische Simulationen der Benetzung auf horizontal angeordneten Substraten wurden unter Verwendung eines C++ basierten, CFD Software-Paket, OpenFOAM® ausgeführt. Die dynamische Benetzungsgleichung von Kistler wurde auf Basis dieser Software implementiert. Mit den experimnetellen Ergebnissen vergleichbare Resultate wurden in den Simulationen erzielt.

Abschließend wurde dargestellt, dass es weder universelle noch substratspezifische Randbedingungen für den Kontaktwinkel bzw. die Kontaktlinie gibt, die die Übertragbarkeit des Kontaktwinkels erlaubten. Somit gibt es keine Zusammenhang zwischen den Benetzungsverhalten von chemisch heterogenen Oberflächen und den verwendeten Oberflächen.

Acknowledgements

I would like to express my gratitude to my supervisors, PD. habil. Dr.-Ing. Ilia V. Roisman, Prof. Dr.-Ing Cameron Tropea, first giving me the opportunity to do my Ph.D. study at the Institute of Fluid Mechanics and Aerodynamics at the Technische Universität Darmstadt and for their guidance during my research in these 3 years.

I am cordially grateful to Prof. Stephen Garoff. Without him I would not be able to finish my Ph.D. thesis. He invested so much time on me, which I can never pay back.

I would like to specially thank to Monika Medina, who made my life bearable. Without her it would be very hard to survive. I would like to specially thank to Sebastian Fischer for teaching me patiently many things and being a supportive colleague.

I would like to thank to all of my colleagues, professors and research coordinators at SLA (Str¨mungslehre und Aerodynamik) and at CSI (Center of Smart Interfaces) for their support and scientific contribution to my research during my Ph. D. study, to Christopher Schwarz (Rapid Prototyping Center) and all SLA workshop coworkers helping me to produce and manufacture my experimental setups and test substrates.

I am thankful for having Andreas Lembach, Matthias Winter, Andreas Güttler and Christina Weickgenannt as my office colleagues. It was great to brain-storm, eat, drink and laugh with them.

I am very grateful that i had the opportunity to supervise 8 brilliant bachelor students (Marius Schneider, Jens Martin Klein, Felix Scheller, Jean Paul Beetz, Aaron Oberthr, Ali Dawi, Sebastian Mack and Amin Chowdhury), with whom I accomplished very exciting projects with excellent results.

Nomenclature

Roman Symbols

$\bar{h}$	Planck's constant
$\bar{n}$	coordinate normal to the wall
$\bar{R}$	capillary length in outer region
ΔF	difference in forces
ΔG_S^*	free energy of surface
ΔG_W^*	molar activation free energy of wetting
ℓ	mean free path
$\hat{r}$	position of the considered velocity and pressure in outer region
$\vec{k}$	volume force
$\vec{n}$	normal vector
$\vec{t}$	surface force
f	fraction of solid surface area wet by the liquid
G	Gibbs free energy
g	gravity
h	profile height
h_0	film thickness
k	Boltzmann's constant
L	characteristic length
L_δ	cut-off length for unbounded force singularity at apparent dynamic wetting line
L_c	viscous length
N	Avogadro's number
n	number of sites per unit area
P	pressure
p_c	characteristic pressure
R	contact line radius
R_1/R_2	mean radii of curvature
R_a	average roughness

r_A a variable for advancing contact angle calculation

r_R a variable for receding contact angle calculation

r_W roughness ratio/Wenzel model

R_x/R_y primary radii of curvature

r_{CB} roughness ratio of the wet surface area/Cassie-Baxter model

T temperature

t_p length of plate

v/U velocity

v_{Wall} velocity to the wall

w irreversible work done by the shear stress per unit displacement of length

W_a work of adhesion

W_c work of cohesion

w_p width of plate

x macroscopic length

x_d/y_d data points

x_t/y_t theory points

F force

F_0 surface tension force

F_v net force in advancing liquid front per length

m mass

S surface

s slip length

t time

V volume

Greek Symbols

α inclination of the substrate relative to the liquid surface

α phase variable

β slip length

δ perpendicular distance between the theoretical curve and the experimental

δ_x/δ_y small shifting parameters

ϵ_x/ϵ_y constants, minimizing the sum $D(\epsilon_x, \epsilon_y)$

η viscosity coefficient

κ curvature of the free surface

κ_S^0 frequency of molecular displacement of the surface

κ_W^0 frequency of molecular displacement in equilibrium

λ average length of an individual molecular displacement in the three phase zone

μ dynamic viscosity

Ω surface area

Φ generic ow variable

ϕ fraction of solid/liquid interface of drop contact

Φ_v total dissipation in advancing liquid front

Π surface pressure

ρ density

σ surface tension

σ_{lg} surface tension between liquid and gas

σ_{sg} surface tension between solid and gas

σ_{sl} surface tension between solid and liquid

θ^* equilibrium contact angle after imbibition

θ_0 equilibrium contact angle

θ_A advancing contact angle

θ_a apparent contact angle

θ_D dynamic contact angle

θ_m microscopic contact angle

θ_R receding contact angle

θ_S static contact angle

θ_W static apparent contact angle/Wenzel model

θ_w microscopic contact

θ_{CB} static apparent contact angle/Cassie-Baxter model

θ_{crt} critical contact angle

q_Φ flow flux

Abbreviations

Bo Bond number

Ca capillary number

CMOS complementary metaloxidesemiconductor

Fr Froude number

Oh Ohnesorge number

PDMS trimethylsiloxy terminated polydimethylsiloxane

PP physical properties number

Re Reynolds number

We Weber number

Contents

Chapter 1

Introduction

1.1 Motivation

Wetting is the ability of a liquid to maintain contact with a solid surface, resulting from intermolecular interactions when the two are brought together. Wetting is important in the bonding or adherence of two materials. The degree of wettability is determined by a force balance between adhesive and cohesive forces. In coating operations, adhesion, detergency, lubrication, and other operations in which liquids are applied directly onto the solid surfaces; wettability plays a very crucial role which cannot be ignored. Wettability affects the spontaneous imbibitions of fluids into porous media and controls the separability of particulate solids by flotation.

The fundamentals of wetting are used very often and widely in painting, coating, lubrication and printing applications. The non-perfect nature of surfaces used in industrial applications, such as metal, glass and plastic surfaces of cars and planes or paper, require more complicated dynamic models than existing static models.

In literature the significance of wettability has been recognized, but is often discussed only in terms of measured contact angles of various liquids on various substrates. In 1805 Thomas Young [16] defined a contact angle equation taking into consideration the surface energies of the existing media at the intersection point. Unfortunately it is only applicable for the static case on perfectly flat and rigid surfaces, which in real world barely exist. In 1878 Gibbs [15] tried to express the contact angle relation with thermodynamical approach, again for static case. In 1960 Zisman [99] observed that contact angle decreases directly proportional to the surface tension of the liquid. In 1975 Hoffmann [47] postulated for the first time that if the equilibrium contact angle in the static case on a flat surface is zero, then the apparent dynamic contact angle depends solely on the capillary number (Ca).

Until now there have been many publications about static wettability of Newtonian fluids on various surfaces but there is a lack of experimental and theoretical research addressing dynamic wetting combined with complex surfaces. Dynamic wetting on chemically heterogeneous and physically rough surfaces show unexpected phenomena. The special dynamical behaviors between the liquid and the solid such as low adhesion, giant hydrodynamic slip, frictionless motion, and rebounds after impacts generates the superhydrophobicity. Moreover understanding the physics of dynamic wetting between the oxidated steel sheets and the melted zinc is necessary to improve the performance of the hot dip galvanization. With modern experimental methods it is possible to comprehend the controlling mechanism of the interactions between the chemical or physical structure of a substrate and the morphology of its wetting layer to be able to manipulate the system. This allows to control the process of shape formation of the complex fluids such as colloidal solutions or biological cells. On the other side, forced dynamic wetting, which is applied for gravure printing processes, is investigated broadly to hinder the air entrainment and ribbing as the substrates speed overcomes the liquid speed. All above mentioned application areas are the proofs of the timelessness of this topic.

The present study aims to enlighten the unapparent nature of complex dynamic wetting. The complexity of contact angle variation on structured surfaces with respect to ideal surfaces are presented and the phenomenon of contact angle hysteresis and pinning on structured surfaces is discussed in detail.

1.2 Organization of the Thesis

This thesis comprises three main chapters excluding the Introduction and Conclusion chapters. The final chapter summarizes the results and concludes the work presented here.

In Chapter 2 the essentials of wetting kinetics, hydrodynamics of wetting, phenomena and theories on dynamic contact angle are introduced and a general literature survey is given.

Chapter 3 addresses vertical forced wetting (dip coating). The dip coating experiments are realized with very small capillary numbers on very rough structured substrates compared to industrial applications to understand the underlying physics behind it. Current fitting methods are examined and alternative fitting methods are suggested. The experimental results on flat and structured three-dimensional surfaces in static and dynamic cases are studied and compared with the existing models.

The second part of the thesis, chapter 4, is about horizontal forced wetting by dynamic volume change. The same structured features are placed horizontally on a surface and by pumping liquid through a hole in the middle of the substrate, the contact angle change is observed in dependence on increasing liquid volume. The results are compared to the dip coating experiments and correlations are formulated.

The final chapter summarizes the results and conclusions on forced wetting in horizontal and vertical configurations. Moreover this chapter gives an outline for possible characterization and modeling methods of dynamic wetting on structured surfaces for possible future research to improve the understanding of dynamic wetting application.

Chapter 2

Essentials of Wetting Kinetics

Wetting is the interaction of a liquid with a solid under vacuum, gas or another liquid. The intersection line of these three media is called contact-, wetting- or three phase-line. This interaction might be spreading of a liquid over a surface, penetration of a liquid into a porous medium, or displacement of one liquid by another. The contact angle expresses wettability quantitatively as a feature and helps to characterize a surface and determine the interactions between solids and liquids [1]. It is mostly measured using a sessile or resting drop. From the thermodynamic point of view, wettability is the balance between the adhesive forces, between the liquid and solid, and the cohesive forces within the liquid. The contact angle is determined by the difference of these two forces (Figure 2.1). The static equilibrium contact angle (θ_S) of the drop on the solid surface determines the wettability; a low contact angle is a sign of high wettability and a high contact angle is a sign of low wettability.

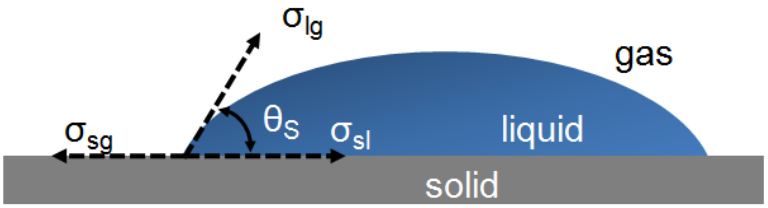

Figure 2.1: Contact angle of a liquid droplet on a rigid solid surface.

Wettability plays a major role in a wide range of industrial and biological applications such as lab-on-a-chip systems, polymer bonding for protective coatings, high speed coating/painting applications, inhibition of liquids into porous media, condensation heat transfer, food (taste) perception on the tongue and palate, eye drops (artificial tears), printing technologies, nucleation control, lubrication and friction reduction. Being able to characterize, describe and manipulate the wetting properties of a substrate for a specific liquid or a group of target liquids are at the focus of many industrial and biological applications [2].

When a liquid displaces another fluid or gas from a solid surface, this is called *dynamic wetting*. Externally imposed mechanical forces (moving substrate) or hydrodynamics (flowing liquid) cause interfacial area between the liquid and solid to drive the system away from the static equilibrium and is called *forced wetting*. In industrial coating processes it is a very common way of depositing liquid on moving substrates, where the aim is to maximize the speed and uniformity of wetting. If wetting is too slow, then the coating process cannot be fulfilled due to entrainment of air over the liquid. Forced wetting also plays an important role in enhanced oil recovery, lamination, mold filling, etc. On the other hand, the unsteadily migration of a liquid over a solid toward thermodynamic equilibrium is called *spontaneous wetting*, where an externally imposed driving force does not exist but emerges from liquid/solid interaction. Spontaneous wetting has practical relevance in biological systems, imbibition of porous media, printing applications, spreading of agricultural chemicals on leaves, spray painting large surfaces, etc. [3].

For simple liquids (Newtonian, low viscous) on inert, homogeneous solid surfaces most wetting phenomena are well understood and described in detail [4]. Moreover there are numerous studies on spontaneous, non-forced wetting at low capillary numbers on homogeneous, inert, smooth surfaces

[5; 6; 7; 8]. In such situations the dynamic contact angle often follows the well-known Hoffman-Voinov-Tanner law. Moreover, many elaborative investigations have been directed towards understanding the wetting properties of complex liquids (non Newtonian, high viscosity liquids such as polymer solutions, dispersions, emulsions) on homogeneous/heterogeneous solid and smooth surfaces. Deformable surfaces have been studied very early by Carré and Shanahan [9], where they present the importance of wetting ridges on soft solids and liquids and also are intensely being studied by Dufresne [10]. Garoff and his collaborators at Carnegie-Mellon University investigated the wetting behavior of non-Newtonian and Boger liquids (see Chapter 3). Furthermore, Homsy [11] studied viscous fingering in porous media and Shaqfeh et al. [12] investigated the viscoelastic effects on interfacial dynamics in air liquid displacement under gravity stabilization. In general, the more dynamic the wetting process, the more structured and deformable is the surface and the more complex the liquid, the greater the complexity in understanding the underlying physics.

To modify surfaces, techniques such as sputtering, vapor deposition, spin or dip coating, plasma polymerization etc. are widely used. Each application affects a given surface in its own way, possibly increasing or decreasing the surface energy. Controlling the wetting via temperature change (phase transition polymers) or applied electric potential between the liquid and solid is used as switchable substrates, which can change their wetting behavior [13; 14].

The present study focuses on forced dynamic wettability at which gas-liquid-solid (3-phase) interfaces and the associated interfacial phenomena are covered. Simple liquids are used for wetting of homogeneous smooth and heterogeneous complex structured surfaces. A detailed comparison is drawn between the existing laws and models for various wetting characteristics. The research goal was to understand how the physical factors influence a 3-phase interface, formulate and implement novel combinations of these physical factors, check the validity of existing models and if necessary develop new models for observed phenomena.

2.1 Wetting on Ideal Surfaces

An *ideal surface* is a smooth, homogeneous and non-deformable surface which has a characteristic contact angle. A drop on such a surface returns to its original shape after distortion. *Surface tension* is the reversible work of forming a unit area of surface (of solid or liquid) in equilibrium with a second medium. It is the partial derivative of the Gibbs free energy (G) of the interface to the surface area (Ω) at constant temperature (T) and pressure (P) [15].

$$\sigma = \left(\frac{\partial G}{\partial \Omega}\right)_{T,P} \tag{2.1}$$

Young in 1805 stated his famous equation on contact angle equilibrium $\sigma_{sg} = \sigma_{sl} + \sigma_{lg}\cos\theta_S$ (Figure 2.1) indicating how the surface tensions of solid-gas (σ_{sg}), solid-liquid (σ_{sl}) and liquid-gas (σ_{lg}) are in equilibrium [16]. Another way to describe the Young equation is to show the relation between work of adhesion, which is the reversible work required to separate a unit area of liquid from a solid ($W_a = \sigma_{lg}(1 + cos\theta_S)$), and the work of cohesion, which is the molecular attractive interactions between molecules ($W_c = 2\sigma_{lg}$), namely $\cos\theta_S = \frac{2W_a}{W_c} - 1$.

There are two main methods of measuring the contact angle; the sessile drop and Wilhelmy plate. In the sessile drop method, the drop is placed on a horizontal surface and observed in cross section. The average contact angle between the liquid and solid is measured by fitting an appropriate tangent at the triple point of the contact line and measuring the angle between the tangent and solid surface. This method gives a $\pm 1°$-$2°$ deviation on average. The advantage of this technique is the convenience and speed of the measurements, nevertheless the drop should be kept in a closed environment to avoid evaporation, humidity and air pressure changes and particles in the air. The volume plays a very crucial role during the measurements and, therefore, it should not be smaller or larger than the critical values, which might lead the droplet to form a liquid film or lose its axisymmetrical shape. To be able to avoid the side effects during the measurement, the method of fitting the interface shape away from the contact line for a system with a Bond number greater than one has been used more recently, where extrapolation is applied back to obtain the dynamic or static contact angle. This method is mostly used in commercial instruments.

The second method, the Wilhelmy plate technique, comprises a thin plate mounted vertically above a liquid. The plate is lowered until it touches the liquid and the force on the plate is measured as it is moved up and down with a specified rate of immersion in the liquid. The contact angle is

calculated with the following force-balance equation F=$\sigma \cos\theta$ − buoyancy, which is only a first order theory for dynamics. With this technique the measured contact angle is again the angle between the tangent and solid surface. The advancing angle is the stable angle as the plate moves down and the receding contact angle is the stable angle as the plate moves up. The advantage of this method is the prevention of the volume dependent measurement errors; moreover the measurement accuracy is quite good at 0.5°.

Not only homogeneous surfaces in the form of a sheet or rod can be measured with this method, but also this method is used for characterizing heterogeneous plates.

2.1.1 No-Slip Condition

In fluid dynamics, the no-slip condition for viscous fluids states that at a solid boundary, the horizontal component of fluid velocity parallel to the solid will be zero relative to the boundary. Particles close to a surface do not move along with a flow when adhesion is stronger than cohesion.

As with most engineering approximations, the no-slip condition does not always hold in reality. For example, at very low pressure (e.g. at high altitude), even when the continuum approximation still holds, there may be so few molecules near the surface that they "bounce along" down the surface. A common approximation for fluid slip is:

$$v - v_{Wall} = \beta \frac{\partial v}{\partial n} \tag{2.2}$$

where n is the coordinate normal to the wall and β is called the slip length. For an ideal gas, the slip length is often approximated as $\beta \approx 1.15\ell$, where ℓ is the mean free path. Some highly hydrophobic surfaces have also been observed to have a nonzero but nano-scale slip length.

While the no-slip condition is used almost universally in modeling of viscous flows, it is sometimes neglected in favor of the 'no-penetration condition' (where the fluid velocity normal to the wall is set to the wall velocity in this direction, but the fluid velocity parallel to the wall is unrestricted) in elementary analysis of inviscid flow, where the effect of boundary layers is neglected.

The no-slip condition poses a problem in viscous flow theory at contact lines, where an interface between two fluids meets a solid boundary. Here, the no-slip boundary condition implies that the position of the contact line does not move, which is not observed in reality. No-slip still allows for motion normal to the surface so if fluid elements moved down to the solid surface, and stick, the fluid body could move forward by a rolling motion. The contact line cannot move because the velocity field becomes multi-valued at the contact line, which is a consequence of the no-slip condition being applied at the contact line. Analysis of a moving contact line with the no-slip condition results in infinite stresses that cannot be integrated over. The rate of movement of the contact line is believed to be dependent on the angle the contact line makes with the solid boundary, but the mechanism behind the microscopic motion at the contact line that alleviates the singularity or at least makes is integrable, is not yet fully understood.

2.2 Static Wetting on Non-Ideal Rough Solid Surfaces

2.2.1 Wenzel's Model

According to Wenzel model [17], the liquid drop on a rough surface is imbibed by the gaps for a energetically stable case. Minimum free energy state for the system is achieved by cosθ_W at equilibrium. Wenzel's model is only valid for chemically homogeneous, physically rough surfaces.

$$\cos\theta_W = r_W \cos\theta_0 \tag{2.3}$$

where r_W is the roughness ratio ($r_W = \frac{\text{true area of the surface}}{\text{apparent area}}$), $\cos\theta_0$ is the Young's equilibrium contact angle and $\cos\theta_W$ is static apparent contact angle. The 'apparent area' in the roughness ratio is the projection of the real area onto the horizontal plane. Wenzel's model is only valid for $\theta_{crt} < \theta_W < 90°$, where the critical contact angle (θ_{crt}) is the minimum value before the droplet looses its spherical cap shape. If the contact angle is smaller than the critical contact angle, then penetration front spreads beyond the drop.

2.2.2 Cassie-Baxter Model

In case of chemically heterogeneous physically rough surfaces, Wenzel's model is not sufficient. According to Cassie-Baxter model, the liquid droplet is in equilibrium on the air cushion inbetween the structured or rough substrate.

$$\cos\theta_{CB} = r_{CB} f \cos\theta_0 + f - 1 \tag{2.4}$$

where r_{CB} is the roughness ratio of the wet surface area, f is the fraction of solid surface area wet by the liquid and $\cos\theta_{CB}$ is the static apparent contact angle [18]. The apparent contact angle is the angle between the tangent to the liquid-fluid interface and the line that represents the macroscopically seen nominal solid surface.

2.2.3 Cassie-Baxter to Wenzel Transition

The question of complete liquid penetration into roughness grooves (homogeneous wetting regime) versus entrapment of air bubbles inside the grooves underneath the liquid (heterogeneous wetting regime) is of utmost importance for understanding wetting on hydrophobic, rough surfaces. Specifically, the design of super-hydrophobic surfaces critically depends on understanding this phenomena. The transition between CassieBaxter and Wenzel models explains the pinning phenomena and the difference between lotus and rose petals. Lotus leaves have very random fine nanostructures and a very small contact angle hysteresis, which makes it superhydophobic. On the other hand rose petals have random micro- and nanostructures, which allows water to imbibe into the crude gaps but stay on air cushions between fine structures. This imbibition in rose petal allows a pinning as the balance between weight and surface tension is surpassed.

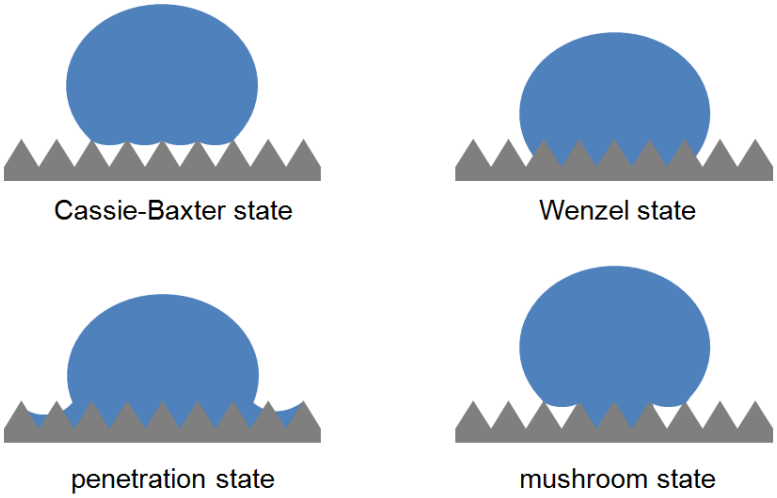

Figure 2.2: Schematic representation of Wenzel, Cassie-Baxter and transition states.

As the air pockets are no longer thermodynamically stable in the Cassie-Baxter state, the liquid begins to nucleate from the middle of the drop, creating a mushroom state (Figure 2.2). Equation 2.5 indicates the penetration condition.

$$\cos\theta_{crt} = \frac{\phi - 1}{r - \phi} \tag{2.5}$$

where $\cos\theta_{crt}$ is the critical contact angle and ϕ is the fraction of solid/liquid interface where drop is in contact with surface. The aim of the penetration is to minimize the surface energy of the droplet and arrive to Wenzel state [19]. If the apparent contact angle overcomes the critical contact angle than a liquid film is formed over the surface, through the roughnesses. This causes a transition from Wenzel state to surface film state and the equilibrium contact angle is formulated as in equation 2.6

$$\cos\theta^* = \phi \ \cos\theta_W + (1 + \phi) \tag{2.6}$$

where $\cos\theta^*$ is the equilibrium contact angle after imbibition [20].

Marmur [21] investigated theoretically the transition between the homogeneous and the heterogeneous regimes of wetting on hydrophobic, rough surfaces. With his study, he puts the Wenzel and Cassie-Baxter equations in discussion with proper mathematical thermodynamic perspective and defines the conditions for determining the transition between the homogeneous and heterogeneous wetting regimes in terms of criteria based on the detailed general solid surface topography. It turns out that the Cassie-Baxter equation can be used when a local minimum in Gibbs free energy exists, which leads to a heterogeneous wetting regime. If a border minimum in Gibbs free energy exists, then the Wenzel equation can be used, which leads to a homogeneous wetting. If the border minimum occurs at $\theta_S = \pi$ then there cannot be made any distinction between the homogeneous and heterogeneous wetting regimes.

However Gao and McCarthy claim in their studies [22; 23] that the 2D view of wetting (Wenzel and Cassie-Baxter models) is superfluous and might cause misunderstanding of the wetting of solids by liquids and demonstrate that 1D contact line perspective (three-phase contact line) is more consistent. They make a significant remark on the definition of surface tension and surface free energy, which are mostly used as interchangeably equivalent to be able to imply thermodynamic implementations about contact angle termination. However, surface tension, being a tensor and surface free energy, being a scalar non-directional property cannot be equivalent. In conclusion, the gathered data is based on different chemistries and topographies (chemical and physical heterogeneity) indicating that contact angle behavior (advancing, receding, and hysteresis) is determined by interactions of the liquid and the solid at the three-phase contact line alone and that the interfacial area within the contact perimeter is irrelevant. Wettability (advancing and receding contact angles, and thus hysteresis) is a function of the activation energies that must be overcome in order to move contact line from one metastable state to another. Contact areas play no role in this. Wenzel and Cassie-Baxter equations are valid only to the extent that the structure of the contact area reflects the ground-state energies of contact lines and the transition states between them [22].

Moreover Nosonovsky and Bhushan [24] show in their work that droplet size and surface pattern parameters affect the contact angle hysteresis and the transition from the metastable partially wetted (Cassie) state to the homogeneously wetted (Wenzel) state. They investigated experimentally and theoretically that wetting is a multiscale phenomenon, where the kinetic effects associated with the contact angle hysteresis should be studied on the microscale; and the effects of the hysteresis and the Cassie-Wenzel transition involve processes on the nanoscale.

2.3 Phenomena on Dynamic Contact Angles

In different length scale ranges such as molecular, sub-microscopic and macroscopic, the dynamic wetting (dynamic contact angle) is influenced by various forces. On ideal flat surfaces at the molecular scale, the dynamic contact angle (which is named as *microscopic contact angle* θ_w) might be caused by the significant statistical fluctuations and short range forces. In sub-microscopic scale, the dynamic contact angle might be affected by long range fluid-solid interactions such as van der Waals forces or/and electric double layer forces. In forced wetting, long range fluid-solid interaction forces are in competition with hydrodynamic forces, where both type of forces decide whether a thin film at the contact line will be formed or not. In this study, the macroscopic (intermediate) length scale of dynamic wetting is covered, where the hydrodynamic approach is applicable.

Contact angle hysteresis is caused by the existence of many thermodynamic metastable states of the contact line. At each metastable state, a new contact angle is associated. The maximum stable angle is referred to as the advancing angle (θ_A) and the minimum stable angle as the receding angle (θ_R) (Figure 2.3). Hysteresis is attributed to roughness or heterogeneity of the solid surface, which hinders free movement and causes metastable states [25]. The difference between advancing and receding angle is called as hysteresis, which makes it difficult to determine an equilibrium contact angle even for the static case. Knowledge of contact angle hysteresis is important, because it determines the pressure required to dislodge a drop in a capillary, or the limits to the capillary driving force in wicking, or the maximum substrate tilt angle before a drop slides [26].

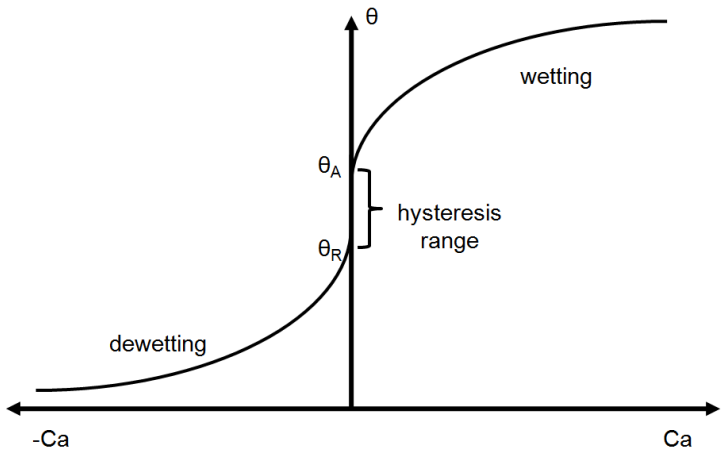

Figure 2.3: Schematic representation of velocity dependence of dynamic contact angle.

2.3.1 Molecular Kinetics at the Contact Line

The numerical studies about droplet spreading indicate that the rate of spreading depends on the relationship between slip velocity and dynamic contact angle [27; 28]. Both surface and viscous forces have a strong influence on wetting dynamics at low capillary numbers, however at high capillary numbers surface forces become relatively unimportant and the dynamic contact angle is determined only by hydrodynamics [25]. When the system is at equilibrium, the wetting line will appear to be stationary, but the three phase zone will be in thermal motion at the molecular level. This is defined as the simple absorption/desorption model of the three-phase zone in the theory of wetting kinetics. Using Eyring's model as a reference [29] (equation 2.7), Blake (equation 2.8) interpreted a formulation for kinetic contact angle in terms of material properties (ρ, σ, μ), wetting velocity (v) and equilibrium contact angle (θ_0) [30].

$$\kappa_W^0 = \left(\frac{kT}{\bar{h}}\right)\exp\left(\frac{-\Delta G_W^*}{NkT}\right) \tag{2.7}$$

where κ_W^0 is the frequency of molecular displacement in equilibrium, ΔG_W^* is the molar activation free energy of wetting, T is temperature, k Boltzmann's constant is, $\bar{h}$ is Planck's constant and N is Avogadro's number. Equation 2.7 is thermodynamically equivalent. The wetting line can only advance when the molecular displacement in the forward direction is more frequent than the reverse direction. Therefore a forward directed shear stress because of spontaneous or forced wetting, applied to the three phase zone. The greater the stress, the greater is the velocity of the wetting line. If the energy used in overcoming the molecular barrier is dissipated to the system, heat will appear, causing irreversible work. If the velocity of wetting is infinitely slow, the process can be reversible and isothermal, like all macroscopic process. The velocity of wetting is given in equation 2.8.

$$v = 2\kappa_W^0 \lambda \sinh\left(\frac{w}{2nkT}\right) \tag{2.8}$$

where v is the velocity normal to the wetting line, λ is the average length of an individual molecular displacement in the three phase zone, w is the irreversible work done by the shear stress per unit displacement of length on the wetting line, n is the number of sites per unit area.

If the force per unit wetting line, namely the shear stress required to drive the wetting line, is $F = \sigma_{lg}(\cos\theta_0 - \cos\theta)$ then the equation 2.8 simplifies to equation 2.9.

$$v = 2\kappa_W^0 \lambda \ \sinh\left[\frac{\sigma_{lg}(\cos\theta_0 - \cos\theta)}{2nkT}\right] \tag{2.9}$$

The equation 2.9 predicts that there are maximum and minimum velocity values to achieve wetting and dewetting. Any velocity greater than equation 2.10a, might cause entrainment of liquid and greater

than equation 2.10b, might fail to dewet the surface.

$$v_{180} = 2\kappa_W^0 \lambda \sinh\left[\frac{\sigma_{lg}(\cos\theta_0 + 1)}{2nkT}\right] \tag{2.10a}$$

$$-v_0 = 2\kappa_W^0 \sigma \sinh\left[\frac{\sigma_{lg}(1 - \cos\theta_0)}{2nkT}\right] \tag{2.10b}$$

In practice, limitations of wetting and dewetting velocities cause serious problems in industrial processes such as coating and petroleum recovery. Reduction of surface tension of liquid σ_{lg} with additional additives might reduce the velocity limit v_{180} unless there is a relevant increase in equilibrium contact angle θ_0. Another solution for this problem might be to increase the temperature, which causes increase both in v_{180} and $-v_0$.

The basic mathematical models mostly ignore the highly complicated nature of wetting. The above mentioned absorption/desorption model do not include the effects of surface diffusion [31], evaporation and condensation [32], molecular reorientation [33], viscoelastic deformation [34], penetration, swelling/desolution of solid, micro-roughness and micro-heterogeneity of the surface [35]. These all might cause variations in the contact angle as the contact line moves if the energy is large for Maxwell-Boltzmann statistics.

A combined theory of absorption/desorption and viscous flow models is given in equation 2.11b. Here, the molecules at the three phase zone are influenced by both interactions with solid surface and viscous interactions between fluid molecules. For this formulation free energy of surface ΔG_S^* is defined and frequency of molecular displacement of the surface κ_S^0 is interpreted. η is defined as viscosity coefficient and is equal to $\bar{h}/v$.

$$\kappa_S^0 = \left(\frac{kT}{\bar{h}}\right)\exp\left(\frac{-\Delta G_S^*}{NkT}\right) \tag{2.11a}$$

$$v = 2\kappa_S^0 \lambda\left(\frac{\bar{h}}{\eta v}\right)\sinh\left[\frac{\sigma_{lg}(\cos\theta_0 - \cos\theta)}{2nkT}\right] \tag{2.11b}$$

2.3.2 Hydrodynamics of Wetting

The classical hydrodynamic approach, applied up to the moving contact line, does not result in a physically acceptable solution for flow near a moving line due to the conflict between a moving contact line and conventional no-slip boundary condition between liquid and solid. Therefore, the force exerted by the liquid on the solid becomes infinite and the stresses at the wetting line become unbounded.

After determining mechanisms to alleviate this singularity, for the analytical description on dynamic contact angle determination the following assumptions are proposed. The inertial effects are not neglected, meaning that viscous length scale ($L_c = \mu/\rho\sigma$) is less than any other length scales relevant for contact line motion. It is assumed that the surfaces display no heterogeneity and respectively no contact angle hysteresis, where the capillary number and Reynolds number are very small (Re<<1). Moreover it is assumed that the flow profile near the wall is parabolic according to lubrication approximation and the dominant driving force is capillarity, where capillary number is very small. Moreover relaxing the no-slip condition in the vicinity of the contact line and making the exerted force on the solid finite, though leaving the stress in the liquid unbounded, the flow equations and boundary conditions are modified. Viscous bending is considered only in the mesoscale. With all these assumptions the following balance equation 2.12a between viscous and capillary forces is obtained [36].

$$\frac{3Ca}{h^2} = -\frac{d^3h(x)}{dx^3} \tag{2.12a}$$

$$h'^3(x) = \theta_m^3 + 9\text{Ca } ln(\frac{x}{L}) \tag{2.12b}$$

$$\text{for } \theta(x) < 135^\circ; \quad \theta^3(x) - \theta_m^3 = 9\text{Ca } ln(\frac{x}{L}) \text{ where } \tan(\theta(x)) = h'(x) \tag{2.12c}$$

Voinov [37] proposed an asymptotic solution (equation 2.12b) for a vanishing slope at infinity for the equation 2.12a, where h is the profile height, θ_m is the macroscopic contact angle, x is the macroscopic length and L is the characteristic (microscopic) length scales. Due to the small capillary number, far from the wetting line the liquid-solid interface takes its static shape. The macroscopic dynamic contact angle (θ_m) is determined by extrapolating the static interface to the solid surface.

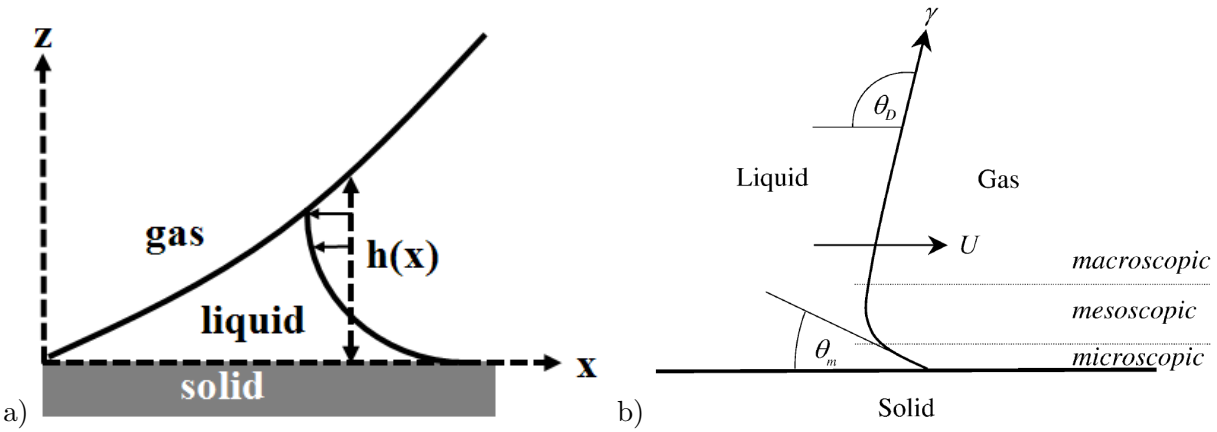

Figure 2.4: a) Parabolic flow in a wedge near an advancing contact angle. b) Viscous bending on the mesoscale for an advancing meniscus [38].

Moreover in 1986 Cox [5] extended the equation 2.12b for two liquids with viscosity ratio $M = \mu_1/\mu_2$, which is given below.

$$g(\theta(x), M) - g(\theta_m, M) = \text{Ca } ln(x/L) \tag{2.13a}$$

(2.13b)

$$\text{in the absence of } \mu_1;\ g(\theta, 0) \text{ reduces to } g(\theta) \tag{2.13c}$$

$$\text{where} \quad g(\theta) = \int_0^\theta \frac{x - \sin x\ \cos x}{2\ \sin x} dx \tag{2.13d}$$

The difference between $g(\theta)$ and $\theta^3/9$ remains smaller that 1% if the contact angle is smaller that 135°.

In summary, the wedge flow near the contact line leads directly to the ∼1/3 power, where Hoffman's empirical fit to data yields the same. In hydrodynamic scale, the strong divergence of viscous forces [39] results in an interface slope that varies logarithmically with the distance from the contact line, as confirmed experimentally by Marsh et al. [40], where body forces such as gravity or any imposed shear, will not affect the solution near the contact line [36; 41; 42].

An excellent overview of existing hydrodynamic approaches to the wetting phenomenon is given in the work of Shikhmurzaev [43]. An essential advantage of his theory is that it has all the positive features of the Navier boundary condition and eliminates its drawbacks being applied to the moving contact line problem, referring to the shear stress singularity resulting from the no-slip condition at the wall. The model holds the rolling character of the liquid motion and gives the velocity dependence of the contact angle. The boundary conditions can be easily generalized for the case of an interface between immiscible viscous fluids so that the splitting of the free inter- face at the moving contact line is described.

Moreover, Tadmor and Yadav [44] investigated experimentally and theoretically (by referencing the work of Marmur [21]) that the apparent contact angle is a unique function of the advancing contact angle, drop size and material properties such as surface tensions and densities. The apparent contact angle of a sessile drop on a horizontal surface decreases with the decreasing drop size due to the increase in hydrostatic pressure. For hysteresis, the equilibrium contact angle (θ_0) can be calculated

from θ_A and θ_R as was shown by below.

$$\theta_0 = \arccos\left(\frac{r_A\cos\theta_A + r_R\cos\theta_R}{r_A + r_R}\right) \tag{2.14a}$$

$$\text{where } r_A = \left(\frac{\sin^3\theta_A}{2 - 3\cos\theta_A + \cos^3\theta_A}\right)^{1/3} \tag{2.14b}$$

$$\text{and } r_R = \left(\frac{\sin^3\theta_R}{2 - 3\cos\theta_R + \cos^3\theta_R}\right)^{1/3} \tag{2.14c}$$

2.3.3 Empirical Models

In 1975, Hoffman proposed an empirical formulation for apparent dynamic contact angle depending on capillary number for complete wetting where the equilibrium contact angle (θ_0) assumed to be zero.

$$\theta_D = f_{Hoff}(Ca) = \arccos\left\{1 - 2\tanh\left[5.16\left(\frac{\mathrm{Ca}}{1 + 1.31\mathrm{Ca}^{0.99}}\right)^{0.706}\right]\right\} \tag{2.15}$$

The empirical function is deduced from a systematic study done with silicon oils, possessing high viscosities, displacing air in glass capillary tubes. The function is fitted so that at large capillary numbers (fast wetting line and large viscosities) it gives a suitable match. For low capillary numbers (Ca<O(0.1)), equation 2.15 reduces to

$$\theta_D = 4.54\mathrm{Ca}^{0.353} \quad (\theta_D \text{ in radians}) \tag{2.16}$$

which is nearly equivalent to Tanner's third power law ($\theta_D \sim \mathrm{Ca}^{1/3}$) [45], which is derived from hydrodynamic theory presuming a dry surface by Cox [5; 46] (see subsection 2.3.2).

Equation 2.17 is referred as *Hoffman-Voinov-Tanner* law and describes the apparent dynamic contact angles of complete wetting systems up to $\theta_D \leq 135°$.

$$\theta_D \approx \alpha\mathrm{Ca}^{1/3} \tag{2.17}$$

In his 1975 and 1983 publications, Hoffman [47; 48] also indicated that for partially wetting systems where the static contact angle is not zero, the universal behavior of the wetting curve (equation 2.15) can be modified with a shift factor of $f^{-1}_{Hoff}(\theta_0)$ where θ_0 is the nonzero static contact angle.

$$\theta_D = f_{Hoff}[\mathrm{Ca} + f^{-1}_{Hoff}(\theta_0)] \tag{2.18}$$

For $\theta_D \leq 135°$, the universal form can be simplified as $\theta_D^3 - \theta_0^3 \cong \alpha\mathrm{Ca}$. Hoffman's postulate with shift factor implies that the apparent contact angle remains close to the static contact angle at low capillary numbers and loses the affinity as soon as the capillary number exceed the shifting factor $\mathrm{Ca} > f^{-1}_{Hoff}(\theta_0)$.

Numerous empirical correlations are proposed for low and high capillary numbers, partial and complete wetting cases. Seebergh [49] introduced an empirical dynamic contact angle model for non-ideal surfaces. His empirical formulation differs for low and high capillary numbers.

$$\text{for Ca<0.001} \quad \cos\theta_s = \cos\theta_0 - 4.47\mathrm{Ca}^{0.42}(\cos\theta_0 + 1) \tag{2.19a}$$

$$\text{for Ca>0.001} \quad \cos\theta_s = \cos\theta_0 - 2.24\mathrm{Ca}^{0.54}(\cos\theta_0 + 1) \tag{2.19b}$$

Jiang [50] (equation 2.20a) and Bracke [51] (equation 2.20b) derived empirical equations for partial wetting cases by using the out-of-balance Young's force term ($\cos\theta_0 - \cos\theta_D$) which is mostly considered as a driving force for dynamic wetting.

$$\tanh(4.96Ca^{0.702}) = \frac{\cos\theta_0 - \cos\theta_D}{\cos\theta_0 + 1} \tag{2.20a}$$

$$2\sqrt{Ca} = \frac{\cos\theta_0 - \cos\theta_D}{\cos\theta_0 + 1} \tag{2.20b}$$

For all these empirical studies, the wedge-flow model of Cox theoretically gives the Hoffman's curve. Thus, his theory is proven by the data and all these empirical formulae come from arbitrary fitting of the data to power laws. Moreover, Cox also describes the minor deviations from Hoffman because of speed dependence of the inner scale parameters (see subsection 2.3.2).

2.3.4 Exclusion of Cut-off Region

To be able to treat the dynamic wetting in hydrodynamic continuum theory, the cutoff regime (L_δ) is excluded in theories. The net force (F_v) and total dissipation (Φ_v) in an advancing fluid by ignoring viscous effects at distances smaller than cutoff length are defined as following.

$$F_v = \frac{3\mu v}{\theta_a} ln \frac{1}{\epsilon_\delta} \tag{2.21a}$$

$$\Phi_v = \frac{3\mu v^2}{\theta_a} ln \frac{1}{\epsilon_\delta} \tag{2.21b}$$

where $\epsilon_\delta = L_\delta / L$ [39; 41].

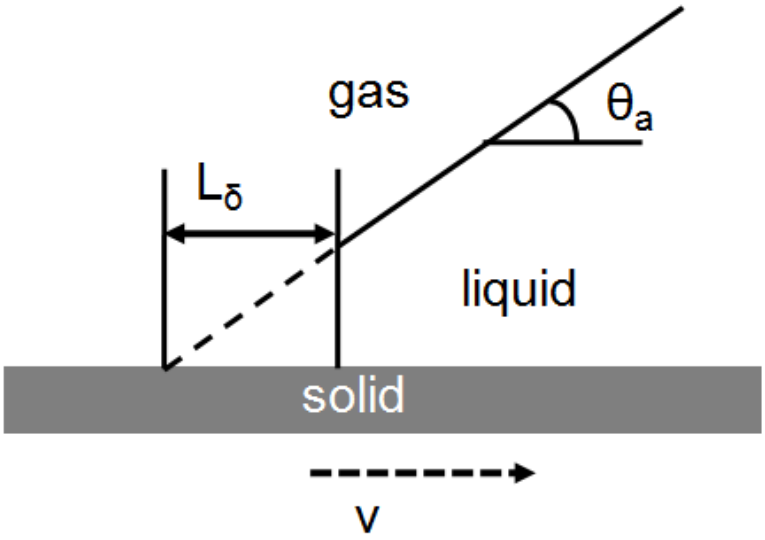

Figure 2.5: Schematic representation of cutoff regime in simple wedge flow.

According to unbounded force singularity, the Navier-Stokes equation remains valid in cut-off region but slip of the fluid over solid is applied. The most common model for slippage is

$$\mathbf{tn} : \mathbf{T} = \frac{1}{\epsilon_\beta} \mathbf{t} \cdot (\mathbf{v} - \mathbf{t}) \tag{2.22}$$

where $\mathbf{t}$ and $\mathbf{n}$ are the unit tangent and normal vectors to the solid surface, $\mathbf{T}$ is the stress tensor, $\mathbf{v}$ is the velocity of the liquid and ϵ_β is an dimensionless slip coefficient [52]. Slip boundary conditions are effective for formulating well-posed free surface problems with moving contact lines [53].

2.4 Chemical Heterogeneity

Wetting of chemically heterogeneous surfaces is widely applied to inkjet printing and biofluidic manipulation. In these applications, sessile droplets are manipulated on composite surfaces, which posses different wettability properties. A liquid droplet on such a surface is distorted by the surface energy forces to find its minimum energy configuration.

Wenzel [17] introduced an 'average' contact angle on a rough, chemically homogeneous substrate which is expressed in terms of contact angle on a planar surface. Likewise, for smooth but chemically heterogeneous surfaces, the Cassie equation [18] defines an 'average' contact angle by the weighted mean of the angles that the drop would take on a chemically homogeneous substrate. The associated

wall tension was studied both for geometrically rough [54; 55] and chemically heterogeneous surfaces [56] by many research groups.

Johnson and Dettre were able to describe qualitatively the contact angle hysteresis phenomenon on real surfaces with the help of theoretical and experimental studies [57; 58]. In the theoretical calculations the contact angle hysteresis is explained for heterogeneous surfaces, just as for rough surfaces, as a balance between vibrational energy of the drop and the heights of energy barriers between metastable wetting state of a liquid droplet resting on a solid surface. The boundary condition for the calculation is that the three-phase contact line at the microscopic range is always Young contact angle.

Extrand [59] showed with an experimental study that if the heterogeneity was completely contained with the contact area and did not intersect the contact line, then no area averaging of the contact angles occurred. These findings suggest that interactions at the contact line, not those in the interfacial contact area, control wetting of heterogeneous surfaces.

Anantharaju et al. [60] modeled a chemically heterogeneous surface by using phase field theory. Unlike other studies, where materials were characterized by a equilibrium contact angle, they allowed materials to have hysteresis and investigate the effect of heterogeneity length scale. They found that with a finite heterogeneity length scale, the advancing and receding contact angles deviate from Cassie theory.

Snoeijer et al. [61; 62] investigated in their work experimentally and theoretically the relaxation of transverse perturbations of a receding contact line by computing the evolution of interface profile (see Figure 2.6). They realized a theoretical study in the framework of lubrication theory, in which the hydrodynamics is resolved and viscous dissipation is taken account at all length scales. Their experimental study concludes that the dynamics of interface can be interpreted as a quasi-steady succession of stationary states.

Overall, contact angle hysteresis on physically rough surfaces can be formulated as a balance between the vibrational energy of a drop and the height of energy barriers between metastable states. The same can be applied for chemically heterogeneous surfaces, where the very well known 'stickslip' behavior of the contact line can be observed. On a chemically rough, physically flat surface, pinning of contact line with respect to the increasing volume of the liquid and respectively releasing from pinning by reaching the threshold value is attributed to potential barriers on the molecular scale.

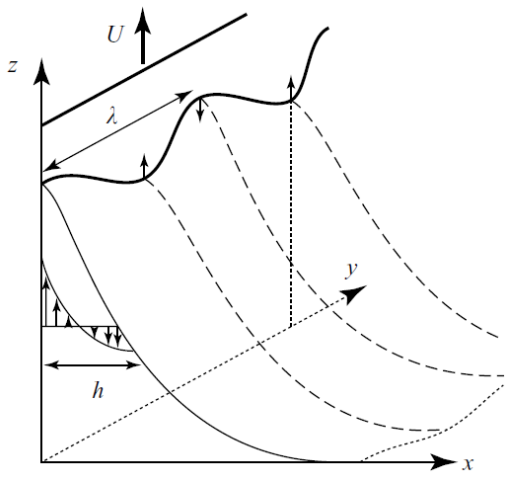

Figure 2.6: Transversely perturbed receding contact line in a dip coating experiment [61].

The energy correlations between the chemically heterogeneous surfaces and physically structured substrates enables to make an analogy for the grid construction in numerical simulations. To be able to project a 3D structure to a 2D chemically heterogeneous flat surface simplifies the numerical lattice formation and hinders the numerical errors caused by parasitic currents occurring at the edges and on the corners.

2.5 Summary

In the following chapters, forced wetting on the structured substrates will be investigated experimentally and numerically. First the dynamic forced wetting on the substrates will be observed in vertical direction in very low capillary numbers and the effect of feature size being larger or smaller that the capillary length will be discussed. In the second part, forced wetting in horizontal direction will be investigated experimentally and numerically and an analogy between horizontal and vertical wetting directions will be done.

The main deficiency to be filled with the present work is to show the major effects of feature size with respect to the capillary length on the forced dynamic wetting. Moreover the physics lying behind the observed new phenomena will be discussed.

Chapter 3

Dip Coating

Dip coating is broadly used in industry to produce thin films rapidly on very large substrates. Typical examples are paper and adhesive tapes, magnetics tapes for audio/video usage, printing and photographic (X-ray) tapes. Dip coating of the substrate starts with immersing it in the liquid at a constant speed to avoid any jitters. The liquid deposits itself as a thin film on the substrate while it is being withdrawn, with the film thickness varying based on the rate of withdrawal. If the withdrawal velocity is below the critical value, the surface comes out dry and a hydrodynamically thin film is not able to be formed on the substrate. As critical velocity is approached, the macroscopic dynamic contact angle goes to zero. For withdrawal velocities above the critical, the macroscopic contact angle remains at zero and a hydrodynamically thick film is entrained on the substrate.

An extensive literature on dip-coating on planar substrates is available [63; 64]. However, dip coating of structured surfaces with structures on the order of the capillary length is not widely investigated in the literature due to its complexity. There are very few studies on this subject, mostly on printing applications. Benkreira et al. [65] showed which parameters affect air entrainment, ribbing instabilities and the thickness of the film formed on quadrangular, trihelical and pyramidal gravure geometries by gravure coating/printing for Newtonian fluids. They conclude that an air-free and non-ribbed stable uniform coating can be obtained in very low substrate capillary numbers (Ca$\sim$0.02). Moreover they mention that the produced film thickness is mostly around 15-20% of the cell depth of the structures. Darhuber et al. [66] investigated theoretically and experimentally the selective deposition of glycerin on chemically defined hydrophobic and hydrophilic surfaces, by means of dip coating. They studied the entrained film height as a function of the withdrawal velocity. Mastranglei et al. [67] studied the capillary self-assembly process of the dip-coating on chemically and topologically patterned surfaces. They investigated the conformity of the wetting on triangular and square patterned binding sides which is critically important for lab-on-a-chip designs. Blake et al. [30] represented experimentally that the dynamic contact angle in the case of impingement of a liquid curtain onto a moving solid, is determined not only by the wetting speed but also by the entire field in the vicinity of the moving contact line. This observation on roll coating processes provides significant details about the limitations of the dynamic contact angle in predicting air entrainment.

Dip coating at low capillary numbers makes it possible to maintain an optimum laminar flow condition, which is crucial especially for multilayer applications, but as well for applications with particle loaded liquids. Low capillary dip coating is widely used for polymer film coating, solid state applications, etc. where a homogeneous, uniform coating is desired. Furthermore in polymer coating, the speed of coating causes morphological changes on the polymer configuration [68]. The change in dipping speed induces different packing shapes of the polymer chains and results in a variety of ensembles.

3.1 Previous Studies

For more than 20 years, Garoff and collaborators have made significant contributions to experimental, as well as theoretical, studies of dynamic wetting in the frame of deep coating by using various Newtonian and non-Newtonian liquids (mostly polymers). Schwartz and Garoff have studied theoretically the problem of capillary rise onto a vertical plate whose heterogeneous surface is partially coated with a low surface energy material [69]. They formulated the problem for the wettability to a doubly periodic wall. They applied several energy minimization techniques on the periodic coverage

patterns, considering the static contact angle on the patterned surfaces. Dussan, Ramé and Garoff [70] performed experiments on dynamic fluid interfaces on a cylindrical wall at very small capillary numbers and detected significant viscous deformations far from the contact line. Chen et al. [71] observed the interface shapes and flow fields, which become geometry independent near the contact line, by using particle image velocimetry and validated the data with an existing asymptotic spreading model. Marsh et al. [40] repeated the same experiments as Ramé and Garoff by tilting the cylindrical wall and for the first time showed that the Cox/Dussan method of determining a dynamic contact angle produces a geometry independent, transferable characterization of the dynamic wetting of a material system for low capillary numbers. The method explicitly considers the data away from the contact line, beyond the viscous bending region and where all viscous effects in the interface shape have become negligible. With this work they proved the validity of Cox's asymptotically matched solution for the shape of a meniscus at low capillary numbers. Moreover, they also verified that Cox's formulation gives a correct description of how the dynamic contact angle varies with capillary number for a variety of systems including those with zero and nonzero static contact angles as well as Newtonian and non-newtonian fluids. In the following years Wei et al. concluded, using the results of Ramé and Garoff, that shear thinning has a strong impact on dynamic wetting by reducing the drag of the fluid on the flat cylindrical solid near the contact line, compared to Newtonian liquids [72].

Weislogel [73] reported on experimental and analytical aspects of capillarity-controlled flow in containers of irregular geometries. In this work, capillary phenomena as relevant to small systems, such as capillary tubes and porous materials, are investigated with respect to surface tension and wetting phenomena relative to gravity. In the corner regions of the container (Figure 3.1), the interface curves in order to satisfy the contact angle condition along the perimeter of the interface. The local radius of curvature R_i of the meniscus decreases at the corner. Since the hydrostatic pressure drop across the meniscus is inversely proportional to R_i, the pressure in the liquid decreases at the tip of the meniscus at the corner.

Capillary pumping of this general sort arises in numerous contexts and is particularly prevalent in low gravity environments where system designs are heavily impacted by the presence of container irregularities such as corners. Examples of such systems include most, if not all, in-space fluids management processes ranging from the positioning, control, and transport of liquids such as fuels in storage tanks, to thermal systems such as heat pipes and capillary pumped loops, to the storage and handling of biological fluids and wastes. Furthermore, some terrestrial applications can be named, such as the wetting and spreading of fluids on irregular surface-flow processes and flows in porous media, which are commonplace in nature and industry.

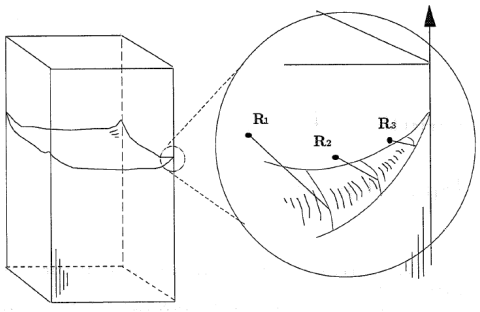

Figure 3.1: Partially filled square container [73].

Dussan et al. [74] demonstrated experimentally that the dynamic contact angle, if measured by the height of a spherical cap in a capillary tube, depends both on the speed at which the liquid spreads across the substrate, and on the size of the characteristic length scale associated with the capillary tube. Such a contact angle is not a transferable boundary condition and thus cannot be measured in one system and applied in another. Her work and that of others [40] show the correct method of measuring a dynamic contact angle that can be transferred form one geometry to another.

3.1.1 Characteristics of the Wedge Flow Near a Moving Contact Line

The Langmuir-Blodgett film coating technique is the deposition of one or more monolayers of an organic material from the surface of a liquid onto a solid by immersing (or withdrawing) the solid substrate into (or from) the liquid. The immersing (or withdrawing) is done very slowly at a rate of a few mm/min (depending on the application, the immersing/emerging velocity varies between 0.25 mm/min to 10 mm/min). A monolayer is adsorbed homogeneously with each immersion or withdrawal step, thus films with very accurate thickness can be formed. This is owing to the fact that the thickness of each monolayer is known and can therefore be added up to find the total thickness of a Langmuir-Blodgett film. The monolayers are assembled vertically and are usually composed of amphiphilic molecules with a hydrophilic head and a hydrophobic tail. (Due to this work in surface

chemistry, Langmuir was awarded the Nobel Prize in 1932.) Langmuir-Blodgett films, composed of some specific organic compounds, are extremely thin films with a high degree of structural order, which have different optical, electrical and biological properties. They are widely used in electro-optics, artificial biological systems, electronic circuits and surface acoustic wave devices [75; 76; 77]. Gaines [78] performed accurate experiments and measured the dynamic contact angle (θ_D) by means of the meniscus height method for this technique. Furthermore, he concluded that transfer ratios near 100% were possible during immersion for contact angles greater than approximately 110°, and during removal for contact angles between 30° and 50°.

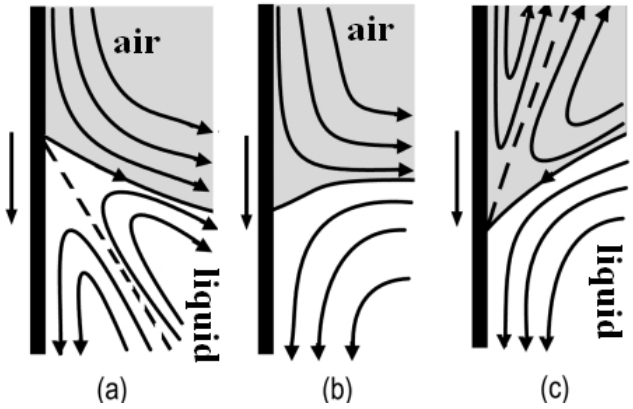

Figure 3.2: Schematic representation of flow patterns near a moving contact line during immersion of a solid substrate into a liquid bath [81].

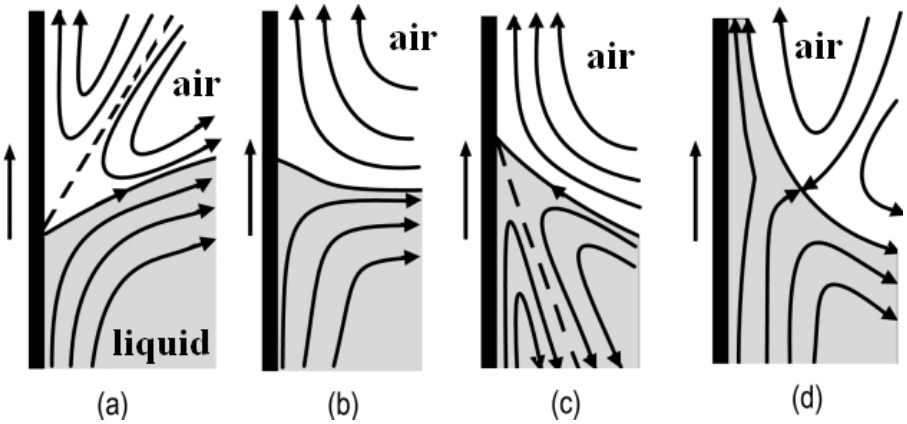

Figure 3.3: Flow patterns during removal of a solid substrate from a liquid bath [81].

During the downstroke when the solid substrate is being immersed in a liquid, regardless of the presence of a Langmuir monolayer at the air-liquid interface, there are three basic flow patterns [39; 79], shown in figure 3.2. The first flow pattern, figure 3.2a, shows a split-injection streamline in the liquid phase. Notice that the split streamline brings fresh bulk fluid towards the moving contact line and the airliquid interface moves away from the contact line. Under these conditions Langmuir-Blodgett deposition cannot take place. In addition, if a monolayer has been deposited on the solid substrate, it will be peeled away by the liquid flow. This flow pattern takes place at small dynamic contact angles, usually $\theta_D \leq 95°$. As the dynamic contact angle increases, the flow pattern changes from split-injection (Figure 3.2a) to a rolling pattern (Figure 3.2c). When there is a rolling pattern in the liquid phase, the gas phase on top shows a split-ejection pattern. Under these conditions, the interface moves towards the contact line and Langmuir-Blodgett deposition is possible. Rolling patterns in the liquid phase during downstroke take place for large dynamic contact angles, $\theta_D \geq 110°$. At intermediate contact angles, the interface remains motionless and both fluids are in a rolling motion, as shown in figure 3.2b. The angles at which the transition from split-injection to rolling takes place, may depend on the presence of surfactants at the interface. During upstrokes, when the solid substrate is being removed from the liquid pool, there are four possible flow patterns, shown in figure 3.3. The first three patterns are the mirror images of the patterns shown in figure 3.2. The last pattern, Figure 3.3d, is a dip-coating

flow pattern [80]. The first flow pattern, figure 3.3a, shows a rolling motion in the liquid phase and a split-injection streamline in the gas phase. The air-liquid interface moves away from the contact line and Langmuir-Blodgett deposition cannot take place. This flow pattern takes place for large values of the dynamic contact angle, $\theta_D \geq 90°$. The third flow pattern, Figure 3.3c shows a split-ejection streamline in the liquid phase; the air-liquid interface moves towards the contact line and Langmuir-Blodgett depositions can take place. This flow pattern takes place for values of the dynamic contact anglein the range $10° \leq \theta_D \leq 90°$. The transition angles are approximate and depend on the presence of surfactants at the interface. The second flow pattern, Figure 3.3b, is the intermediate pattern where the interface air-liquid is motionless. The last flow pattern, Figure 3.3d, shows a continuous film of liquid rising with the solid substrate. This pattern shows a split streamline with a stagnation point on the air-liquid interface, typical of dip-coating flows [80]. The air-liquid interface above the stagnation point moves up with the solid substrate but the interface below the stagnation point moves away from the solid substrate making Langmuir-Blodgett deposition impossible [81].

A simple force balance on the substrate leads to the following equation for the surface pressure:

$$\Pi(\text{surface pressure}) = -\Delta\sigma = -\left[\frac{\Delta F}{2(t_p + w_p)}\right] \approx -\frac{\Delta F}{2w_p}, \quad \text{only when } w_p \gg t_p. \tag{3.1}$$

Here w_p and t_p are the width and length of the plates cross-section, and ΔF is the difference in forces. Applying an increasing pressure at the point where the molecules are relatively close packed and have very little room to move, causes the monolayer to become unstable and destroys the monolayer.

Moreover, Huh & Scriven assumed in their 1971 study [39] that a moving contact line over a perfectly flat, solid surface disobeys the 'no-slip' boundary condition, which is obeyed by flowing liquids on solid surfaces. Using self-consistent creeping flow and lubrication approximations, a steadily moving fluid interface on a solid surface (with slip), effects of surface curvature, and the role of long-range forces, are modeled. Moreover with this model, they were able to show a corner flow geometry with a straight interface in Stokes flow (no inertia). The real surfaces being geometrically rough, chemically and electrically heterogeneous makes it very difficult to understand the forced fluid displacement. The highlight of this work is the breakdown of the hydrodynamic model, which suggests steep gradients, rheological anomalies and discontinuous processes around the contact line in reality.

3.2 Equilibrium Liquid Shape of a Liquid-Solid Interface

The Young−Laplace equation is a nonlinear partial differential equation which expresses the jump in normal stress across a static fluid/fluid boundary where the interface is supposed to have zero thickness. This equation simply states that the pressure jump across the interface is balanced by the interface curvature. In a gravitational field the equation is:

$$p_2 - p_1 = \Delta p = \rho g h - (\sigma_1 - \sigma_2)\left(\frac{1}{R_1} + \frac{1}{R_2}\right) \tag{3.2a}$$

$$\rho g h = (\sigma_1 - \sigma_2)\left(\frac{1}{R_1} + \frac{1}{R_2}\right) \tag{3.2b}$$

where R_1 and R_2 in equation 3.2b are the principle radii of curvature, σ_1 and σ_2 are the surface tensions for liquid under meniscus and on the meniscus.

The equation can be non-dimensionalized in terms of its characteristic length scale, the capillary length, and characteristic pressure by considering one of the fluids as gas, having a very low density:

$$\text{capillary length } L_c = \sqrt{\frac{\sigma}{\rho g}} \tag{3.3a}$$

$$\text{characteristic pressure } p_c = \frac{\sigma}{L_c} = \sqrt{\sigma \rho g}. \tag{3.3b}$$

The (non-dimensional) shape $z = z(x, y)$, of an axisymmetric surface can be found by substituting general expressions for curvature to give the hydrostatic Young-Laplace equations:

$$\left(\frac{1}{R_1} + \frac{1}{R_2}\right) = -\left[\frac{z''}{(1 + z'^2)^{\frac{3}{2}}} + \frac{z'}{x(1 + z'^2)^{\frac{1}{2}}}\right] \tag{3.4}$$

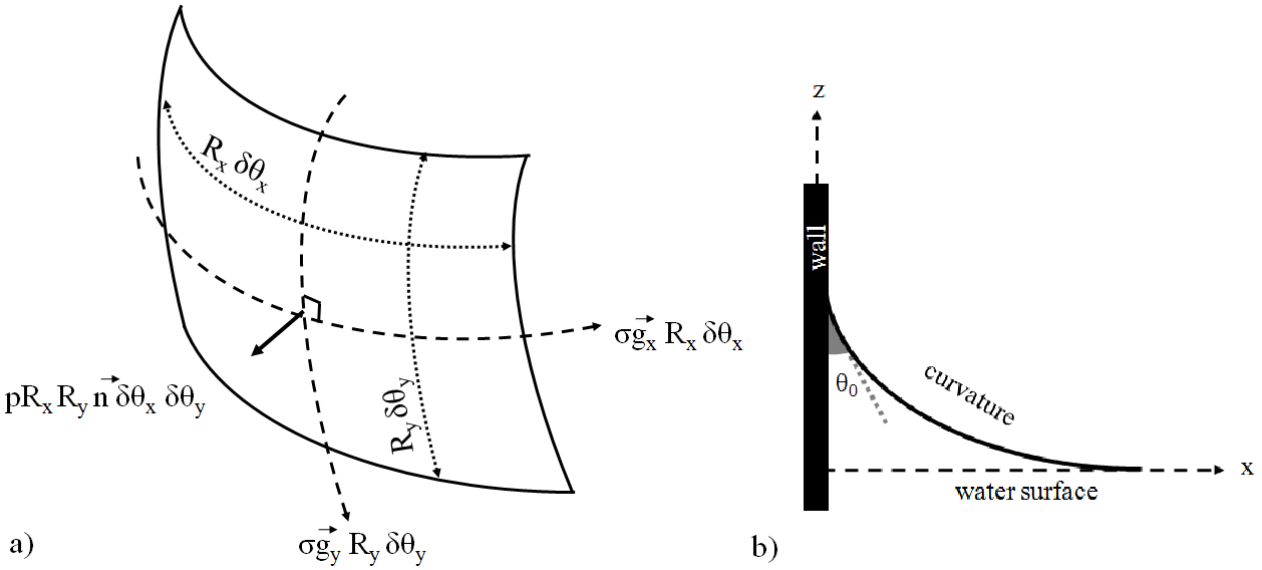

Figure 3.4: a) Surface tension forces are formulated using principal orthogonal curvilinear coordinates (R_x and R_y are the primary radii of curvatures of the surface). b) Capillary climb of water on a wall.

Here we derive an equation for the height of capillary rise in terms of x as used in figure 3.4b. The contact angle θ is measured inside the liquid where the wall and the liquid intersects. The measured contact angle defines the wettability of the system (see equations 3.5).

$$\theta = 0 \quad \text{wettable} \tag{3.5a}$$

$$0 < \theta < \frac{\pi}{2} \quad \text{partially wettable} \tag{3.5b}$$

$$\frac{\pi}{2} < \theta < \pi \quad \text{non-wettable} \tag{3.5c}$$

A simplified solution of the Young-Laplace equation is given below under the condition of one of the radii of curvature ($R_1 = R$ and $R_2 \to \infty$) goes to infinity. This exterminates the second part on the right hand side in equation 3.4.

$$\left(\frac{1}{R_1} + \frac{1}{R_2}\right) = -\frac{z''}{(1+z'^2)^{\frac{3}{2}}} \tag{3.6a}$$

$$\frac{\rho g z}{\sigma} = \frac{z''}{(1+z'^2)^{\frac{3}{2}}} \tag{3.6b}$$

$$x - x_0 = -\sqrt{4{L_c}^2 - z^2} + L_c \ln\left|\frac{-\sqrt{4L_c^2 - z^2} - 2L_c}{z}\right| \tag{3.6c}$$

When $x = 0$, $z = h$ (maximum height of the capillary rise) and $dz/dx = -\cot\theta$.

$$1 + z'^2 = \frac{1}{(1 - \frac{z^2}{2L_c^2})^2} \tag{3.7a}$$

$$\frac{1}{\sin^2\theta} = 1 + \cot^2\theta \tag{3.7b}$$

$$1 - \frac{h^2}{2L_c^2} = \sin\theta \tag{3.7c}$$

$$h = \sqrt{2}L_c\sqrt{1 - \sin\theta} \tag{3.7d}$$

$$\text{where x=0 then} \quad -x_0 = -\sqrt{4{L_c}^2 - h^2} + L_c \ \ln\left| - L_c\frac{\sqrt{4L_c^2 - h^2} - 2L_c^2}{h}\right| \tag{3.7e}$$

$$x_0 = \sqrt{2L_c^2(1 + \sin\theta)} - L_c \ \ln\left|L_c\frac{\sqrt{1 + \sin\theta} + \sqrt{2}}{L_c^2\sqrt{1 - \sin\theta}}\right| \tag{3.7f}$$

3.2.1 Inertial and Viscous Effects on Dynamic Wetting

Cox investigated analytically the inertial and viscous effects on dynamic contact angle in many of his studies [5; 46; 82]. By referencing the studies of Dussan [83] and Huh & Mason [52], Cox assumed that the slip between the liquid and the solid occurs very close to the contact line in order to remove the stress singularity at the contact line, where the Reynolds number based on the macroscopic length scale is very small. By dividing the meniscus into three regions (inner, intermediate, and outer, respectively) Cox defines inner and intermediate regions as geometry-independent, and the outer region as geometry-dominant, and obtains an asymptotic solution for each one. Moreover in the outer region, it is assumed that the viscous forces are negligible and gravity balances the surface tension, whereas in the intermediate it is the region viscous forces that balance the surface tension.

Cox defines the macroscopic contact angle in asymptotic form as $\bar{r} \to 0$ of the interface shape in the outer region.

$$\theta \ \sim (\theta_m \ + ...) + \mathrm{Ca}\{(g'(\theta_m))^{-1} \ \ln \ \bar{r} + O(\bar{r}^0)\} + ... \tag{3.8}$$

where $\bar{r} = \hat{r}/\bar{R}$, $\bar{R}$ being the macroscopic length scale (capillary length in outer region) and $\hat{r}$ the position of the considered velocity and pressure in outer region.

Cox derived a solution for determining the macroscopic contact angle (θ_m) at Re$\ll$1 for the intermediate region by assuming that the slip length is much smaller than the macroscopic length (s/$\bar{R} \ll$1). In this model, the inner scale is in general accounting for any inner mechanism, which alleviates the stress singularity. The inner scale can depend on all fluid and solid properties and on the characteristic speed of the interface. The capillary number in equation 3.8 and the generic function ($g(\theta)$) to calculate the capillary number are given in equation 3.9.

$$\mathrm{Ca} = \frac{g(\theta_m) - g(\theta_w)}{\ln(\bar{R}/s)} + O\left(\frac{1}{\ln(\bar{R}/s)}\right)^2 \tag{3.9a}$$

$$\text{where } g \text{ is give as} \quad g(\theta) = \int_0^\theta \frac{x - \sin x \ \cos x}{2 \ \sin x}dx \tag{3.9b}$$

where R is the macroscopic length scale (capillary length in the outer region), s is the slip length, θ_w is the microscopic contact angle in the close neighborhood of the contact line, and θ_m is the macroscopic contact angle.

Our range in capillary and Reynolds numbers with respect to the moving plate are given below

100cSt PDMS 0.848 mm/sec		10cSt PDMS 0.424 mm/sec
0.0125	< Re <	0.0627
0.004	> Ca >	0.0002

The very low Reynolds number proves that the parameters used for the experiments performed within this work are below any significant inertial effect.

In section 3.4.2, some validations will be given citing Cox's equation and a correlation between the experiments covered in this chapter.

3.2.2 Determining the Film Thickness by Dip Coating of Homogeneous Surfaces

The entrainment of liquid on a moving plate caused by the volumetric forces (gravity and surface tension), was quantitatively analyzed by Landau-Levich and Derjaguin [64; 84]. As the Laplace pressure is lower than the ambient pressure by an amount of $\sqrt{\sigma\rho g}$, the meniscus is curved; on the other hand this positive pressure gradient, the liquid is entrained and the capillary resistance dominates gravity. In other words, if the capillary length is larger than the characteristic length of the dynamic meniscus connecting the static meniscus to the flat film, the dynamic meniscus drags the liquid and causes a limited film thickness.

The film thickness is highly dependent on the capillary number and the inclination of the plate. The thickness of the liquid film on the substrate after dip coating and the characteristic length can be calculated as below, as indicated in Landau-Levich and Derjaguin's work:

$$h_0 = \sqrt{\frac{\sigma}{\rho g}} \frac{1}{\sqrt{1-\sin\alpha}} \left[0.9458\mathrm{Ca}^{2/3} - \frac{0.1068\cos\alpha}{1-\sin\alpha}\mathrm{Ca} \right] \tag{3.10a}$$

$$L = \sqrt{\frac{\sigma}{\rho g}} \frac{1}{\sqrt{1-\sin\alpha}} \left[0.6557\mathrm{Ca}^{1/3} - \frac{0.0740\cos\alpha}{1-\sin\alpha}\mathrm{Ca}^{2/3} \right] \tag{3.10b}$$

where h_0 is the film thickness, L is the characteristic length, α is the inclination of the substrate relative to the liquid surface, σ is the surface tension, ρ is the density, g is the gravitational constant, and finally Ca is the capillary number [85; 86]. The characteristic length becomes equal to capillary length when the inclination of the surface is zero (perpendicular to the liquid surface) and in the static state ($Ca = 0$).

3.3 Experiments

The aim of this chapter is to show experimentally how the 3D complex shapes (pyramidal arrays in various sizes, Figure 3.6) affect the dynamic wetting while it is being dipped into a liquid bath. As wetting liquid, PDMS has been chosen due to its inert character. It also allows the possibility of having a fixed surface tension and density with changing viscosities (see *Appendix B*). With respect to the capillary length for PDMS, the pyramid sizes are determined, where they are either larger, smaller or much smaller than the capillary length (Table 3.1). The pyramids are dipped into the liquid bath and withdrawn in the range of very small capillary numbers and the evolution of wetting on the pyramidal arrays along the focal axis is observed, evaluated and explained in detail.

3.3.1 Experimental Setup

For the dip coating experiments, two kinds of PDMS having viscosities of 10cSt and 100cSt are used for being able to vary the capillary number in a wider range independent of the dipping velocity, density, and surface tension. Flat and milled aluminum plates are used as wetting surfaces. Flat aluminum plates are polished to eliminate course roughness. The final roughness on the flat plates (average roughness R_a) is $0.25\pm0.02\ \mu m$. For the milled aluminum plates, a milling cutter with a 60° opening angle is used to produce pyramids with ∼0.5, ∼1 and ∼2 mm peak-to-peak widths (for exact values see Table 3.1). Unfortunately, the substrates used in experiments are not perfect structures. After careful examination of the milled substrates under the scanning electron microscope, some defects are observed, which are formed during the production. It is not possible to mill smooth edges, without causing the sharp corners to break out. The pyramids are constructed by scanning the surface by the milling cutter in both the horizontal and vertical directions. Unfortunately this process cannot guarantee that the peaks of the pyramids will be exactly in the center and slight shifts might be observed. All these defects and inhomogeneity might cause unexpected pinning of the droplets at random points or shifts in the periodicity of the contact angle. In spite of all the handicaps, the uniqueness of this milling application is its ability to produce pointy, sharp tips (of the pyramids), which is not possible to produce with conventional lithographic techniques.

For the recordings a monochrome 8-bit high-speed CMOS camera (VDS Vosskühler HCC-1000BGE) is used, which has a pixel size of 10μm×10μm and a sensor size of 10.2mm×10.2mm. A Nikon AF D 50mm f/1.4 objective lens is used with a 2×NAS Macro Teleplus MC7 teleconverter to enlarge the field of view. A 2D grid having squares 10μm×10μm is used to calibrate the vertical and horizontal magnification. To be able to focus on the middle column of pyramids on the substrate array, the focal plane is shifted by using the Scheimpflug principle (for more details, please see *Appendix C*). A syringe pump (Syringe Pump NE-1000) is used as dipping motor with which velocities between 0.4 mm/sec and 0.9 mm/sec are able to be achieved. All experiments are performed at room temperature and 45%Rh air humidity.

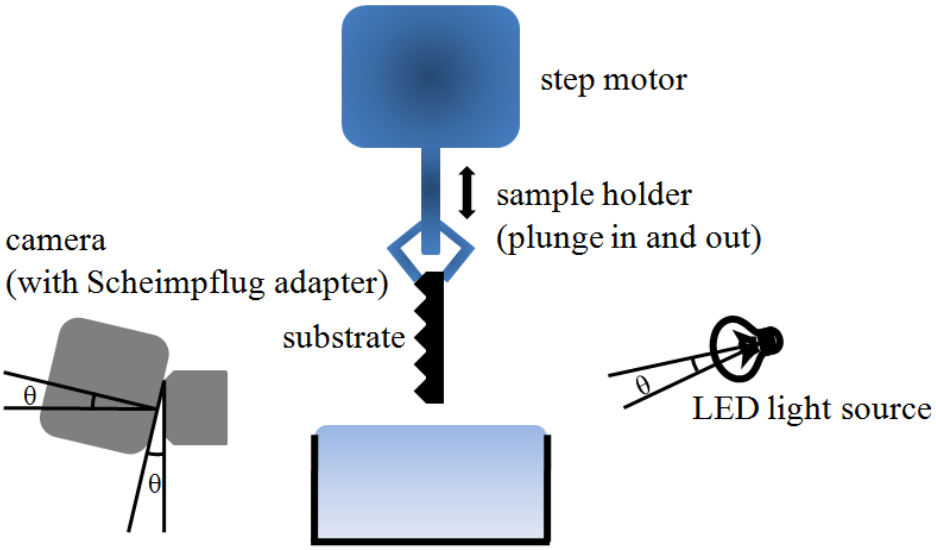

Figure 3.5: The substrates are dipped and withdrawn by using a step motor.

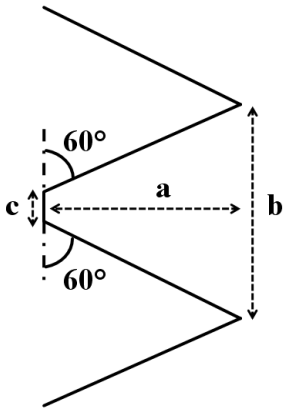

pyramid type	a [mm]	b [mm]	c [mm]
0.5 mm	0.382	0.696	0.023
1 mm	0.680	1.320	0.072
2 mm	1.604	2.448	0.240

Table 3.1: The dimensions of milled pyramidal aluminium structures.

Variables: For the experiments 3 speed variations respectively 0.424 mm/sec, 0.636 mm/sec, 0.848 mm/sec; plunging in and out[1], 2 dipping directions (advancing and receding); 2 types of PDMS varied in viscosity (10cSt and 100cSt); 3 pyramidal structures (as seen in Table 3.1) and 2 dipping orientations (0° and 45°) have been chosen.

3.3.2 Image Processing

All experimental data recorded by the high-speed camera was evaluated by MathWorks® Matlab Image Processing Toolbox. In order to reduce the uncertainty at the contact line, back scattered

[1]For clarity, plate velocities are quoted in the text with one significant figure after the decimal point. However, a mathematical rounding has not been done during the calculations.

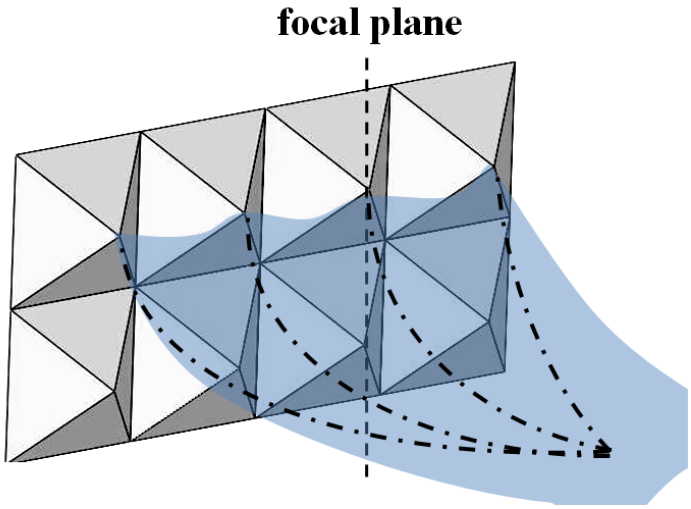

Figure 3.6: On 3D structures, the contact line of the liquid sheet possesses a curved, wavy intersection with the wall but at a certain point on the liquid surface, all curvatures merge. The focal plane is shifted to one of the columns on the apex of the pyramids.

lighting was used to be able to obtain shadowgraphic images, which allows straight-forward evaluation of contact angle on complex surfaces.

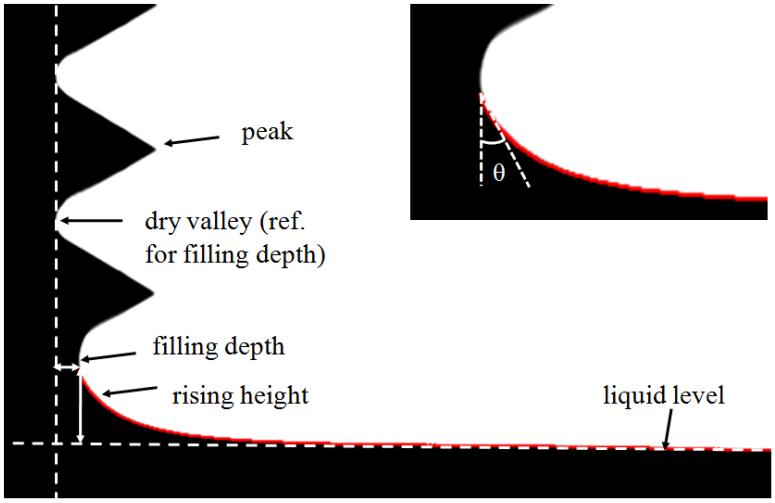

Figure 3.7: Determination of rise height, filling depth and apparent contact angle.

The image processing is restricted by the resolution of the camera, which has a huge effect on the contact angle determination. In this case, each pixel is 20μm in size and below 20μm is not detectable. According to the image processing algorithm in the MathWorks® Matlab Image Processing Toolbox, contact angle is computed by determining a contour between the liquid-gas interface using the gray value gradients and calculating the tangent between the surface and the contour. To be able to achieve an acute distinction between black (ASCII 0) and white (ASCII 1) pixels, a very sharp shadowgraphic image is needed, which reduces the gray pixels and enables more reliable results. The *graythresh* function in the MathWorks® Matlab Image Processing Toolbox, uses Otsu's method [87], which chooses the threshold to minimize the intraclass variance of the black and white pixels. By determining the gray value, and consequently the liquid-gas contour, the liquid rise height is measured. Using equation 3.7c, the contact angle can be calculated by the liquid rise height. One pixel shift at the rise height determination causes a 1° difference on the contact angle, which is a tolerable error. On the other hand, fitting a tangent on the interface to determine the contact angle causes different error factors at different positions of the contact line. If the contact angle is measured by finding the tangent on the apex of the pyramid, the error is 2°, which stems from a one-pixel shift. If the contact angle is measured by finding the apex in the valley, then the error is 7-10°, corresponding to

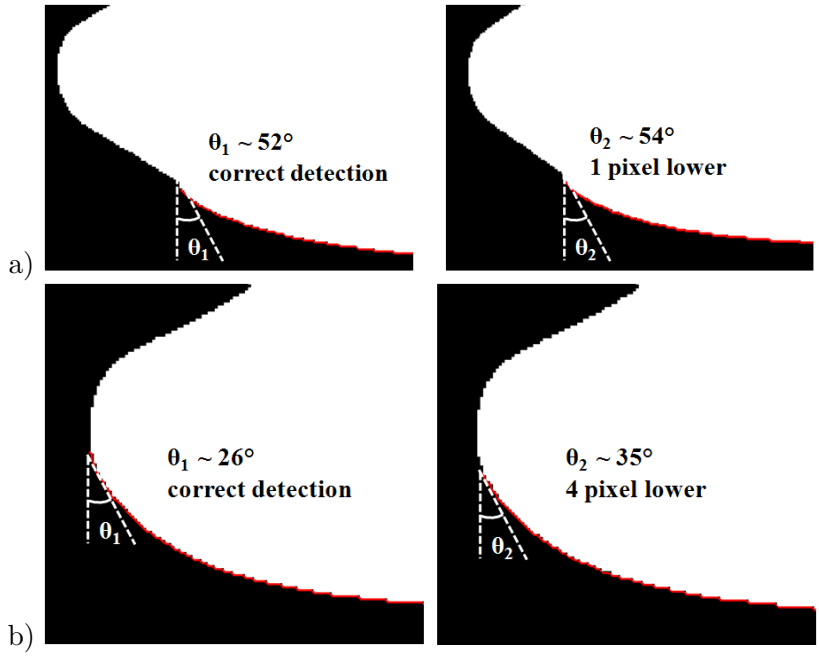

Figure 3.8: False detection of the contact line by fitting a tangent to the meniscus causes deviations in contact angle. a) In the valley, false detection errors up to 4 pixels can occur, while on the peak it is 1 pixel.

3-4 pixels, which is an intolerable range. To avoid this error, a new code is written to determine the exact contact line. Overall, the recording rate (which is in the range of 50-100 fps) and the optical resolution determine the error factor and the precision of the measured data.

3.4 Validation of Fitting on Flat surfaces

3.4.1 Fitting of the Data for the Meniscus Shape

In the literature, standard least squares analysis is the most common method for data fitting. The best fit in the least-squares sense minimizes the sum of squared residuals, each of which is the difference between an observed value and the fitted value provided by a model or theory. The standard least squares analysis faces some problems if there are substantial uncertainties in the independent variable. In our case, as x goes infinity, y is zero ($x \to \infty$, $dy/dx = 0$), which means the interface is almost horizontal, while at $x = 0$, the interface is almost vertical. This makes it impossible to minimize the horizontal and vertical deviations. Due to this problem, fitting of the data to the universal 2D Laplace curve is done in a novel manner.

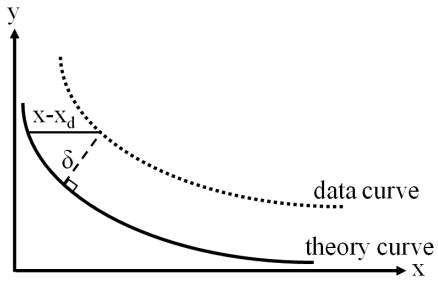

Figure 3.9: Minimization of the normal distance between data and theoretical curve.

The experimental data (x_d and y_d) is fitted to the theoretical curve (equation 3.11) by finding small shifting parameters δ_x and δ_y, which minimize the sum of squares of the normal distances between the theoretical and data curves by linearizing the data.

$$x_t = f(y_t) = -\sqrt{4L_c^2 - y_t^2} + L_c \ln \left| \frac{\sqrt{4L_c^2 - y^2} + 2L_c}{y_t} \right| \tag{3.11}$$

The unit normal vector to the theoretical curve is

$$\vec{n} = \frac{\{1; -f'(y_t)\}}{\sqrt{1 + f'^2(y_t)}} \tag{3.12}$$

Therefore, the perpendicular distance between the theoretical and experimental curves can be estimated as (Figure 3.9)

$$\delta(x) = \frac{x_d - x_t}{\sqrt{1 + [f'(y_d)]^2}}. \tag{3.13}$$

Then the data points are shifted, such that $x_{new} = x_d + \epsilon_x$, $y_{new} = y_d + \epsilon_y$, where the constants ϵ_x and ϵ_y are found by minimizing the deviation sum $D(\epsilon_x, \epsilon_y)$ of δ^2

$$D(\epsilon_x, \epsilon_y) = \Sigma\delta(y)^2 = \Sigma\frac{[x_d + \epsilon_x - f(y_d + \epsilon_y)]^2}{1 + [f'(y_d + \epsilon_y)]^2}. \tag{3.14}$$

Finding ϵ_x, ϵ_y that minimizes $D(\epsilon_x, \epsilon_y)$, is a nonlinear problem, which is solved numerically.

3.4.2 Contact Angle Measurements on Flat Smooth Surfaces

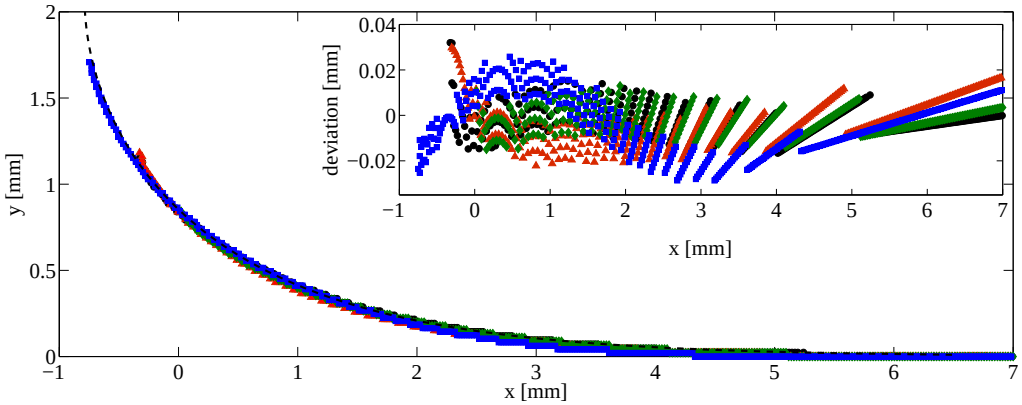

(a) Plunging into the liquid bath filled with 10cSt PDMS with a dry flat substrate at three various speeds compared with static shape and the theoretical meniscus.

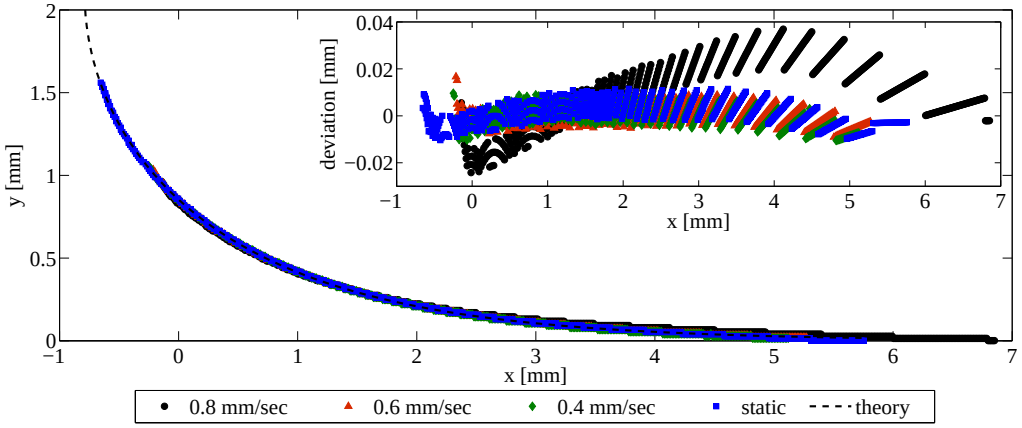

(b) Plunging into the liquid bath filled with 100cSt PDMS with a dry flat substrate at three various speeds compared with static shape and the theoretical meniscus.

Figure 3.10: The meniscus shapes are shifted relative to the theoretical curve using the minimization of normal distance.

On a smooth flat surface, the static contact angle is the classical material property needed to determine the shape of the fluid interface on the macroscopic scale. On the other hand, the classical hydrodynamic assumptions cause a singularity in the stress field at the contact line due to the motion of the contact line across the solid surface. This singularity prevents the use of the contact angle as a boundary

condition for the interface shape compared to the static case. In these experiments, the interface measurements are calibrated using a static meniscus as a reference. In the above graphs, the curve labeled *theory* is the universal 2D meniscus curve drawn using equation 3.6c. Static and dynamic meniscus curves on flat surfaces are fitted to the universal 2D meniscus curve by the fitting method explained above. As seen from figure 3.10, the interface images of static and dynamic advancing menisci on the dry flat aluminium plate compared to the static 2D Young-Laplace solution validate the optical setup. Since the theory describing static menisci is known exactly, systematic deviations between static data and the best fitted data indicate the distortions in the system. The deviation plots given as a subframe show in figure 3.10 that the greatest deflection happens on the wall, and has an amplitude of 0.04mm. Considering the recording resolution, which is 0.0225mm/pixel, the deviations on the flat aluminium surfaces are relatively small. To be able to check the sensitivity of the change in capillary length of the liquid (L_c=1.48mm for PDMS in 10 and 100 cSt), the capillary length value is varied between 1.46mm and 1.52mm with an increment of 0.001mm, and it is concluded that the deviation stays constant at changing capillary length values due to the fitting method used.

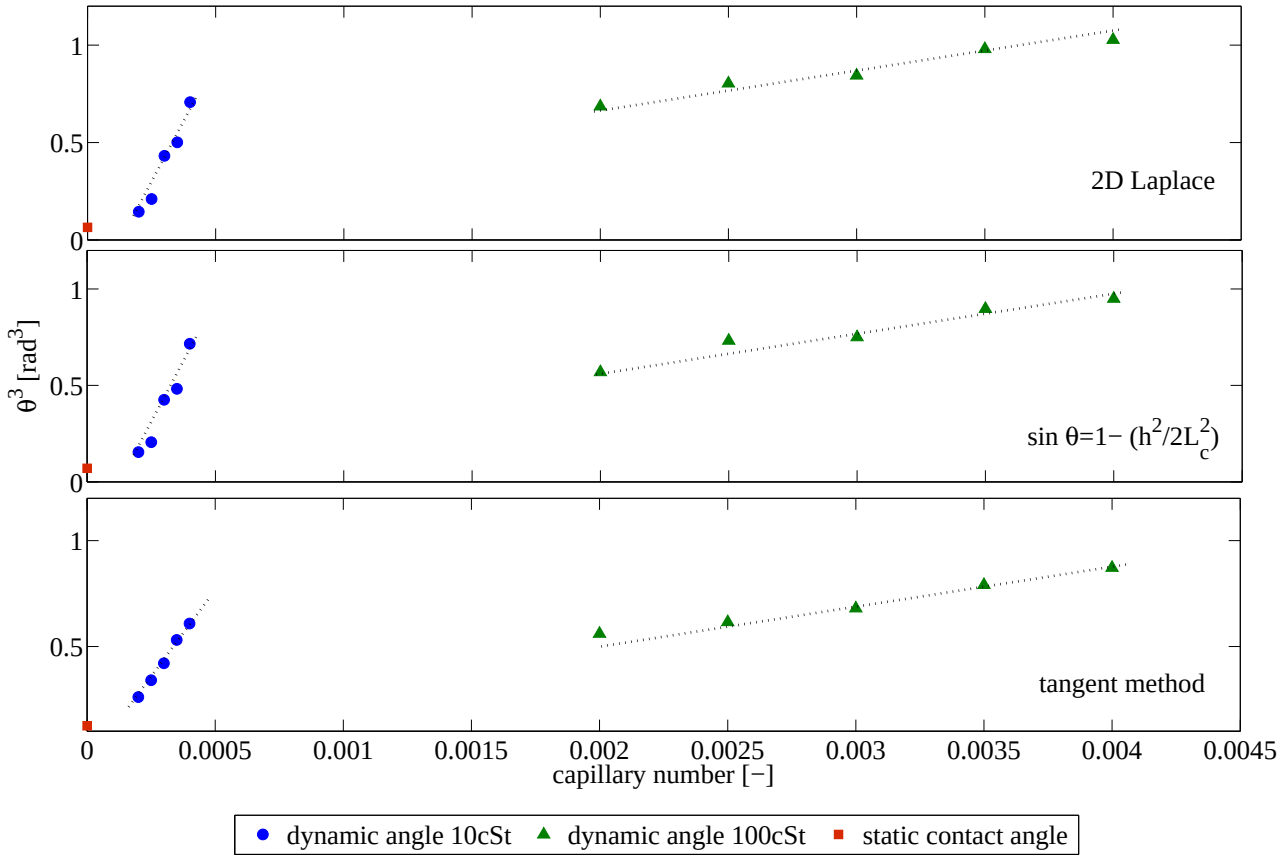

Figure 3.11: Dynamic contact angle change according to 5 respective velocity values for first advancing case for 10cSt and 100cSt.

In figure 3.11 contact angles on flat smooth surfaces are measured using 3 different methods: fitting the meniscus to the 2D Laplace curve, deriving the contact angle from the capillary rise height, and taking the tangent of the contact line, respectively. The 2D Laplace rise height derivation (equation 3.7c) is a one-point measurement and it does not yield a suitable fitting if the contact line is on the liquid. Taking the contact angle found by fitting to the 2D Laplace curve, the standard deviation is calculated for the two other methods. The deviation for the tangent method is $\sim$1.2° and for the rise height method($\sin\theta = 1 - h^2/2L_c^2$) is $\sim$0.5°. The measured dynamic contact angle data on smooth flat aluminium surface fit to Cox's 1/3 power law but with a speed varying microscopic contact angle and inner scale length, which is allowed by the theory. For a static meniscus, the correct angle is the boundary condition for the interface shape determined by the Laplace equation. For a dynamic meniscus, the inner and intermediate solutions for the physics near the contact line (which are determined by a parameter that is equivalent to a microscopic contact angle and the inner length

scale) constitute the boundary condition for the static outer solution, which then extrapolated until solid surface, represents the effective boundary condition of the dynamic contact angle. According to the measured data, it is concluded that the detection is not in the pure intermediate region but in a mixed intermediate and outer region, where a tiny amount of viscous bending and gravity effect is observed.

3.5 Results and Discussion

In this section, a detailed analysis of the experimental observations will be given, in relation with structure size, dipping velocity and liquid type, which were mentioned in previous section. All three pyramidal array structures are dipped in liquid PDMS at three plate velocities and withdrawn at the same velocities. The wetting characteristic of the systems are presented by measuring the apparent contact angle between the liquid and solid with respect to the vertical axis, by the tangent method described previously, and the maximum height of the liquid-solid interface relative to the minimum liquid level in the container (Figure 3.7). Moreover, for the advancing case (dipping into the liquid) the filling depth in the valleys are also measured in order to show what kind of an effect it has on the change in contact angle (Figure 3.7 and 3.13). The results are presented using the normalized dimensionless time (equation 3.15) for the sake of comparing the periodicity more effectively. The peak-to-peak length is the distance ***b*** referred to in Table 3.1.

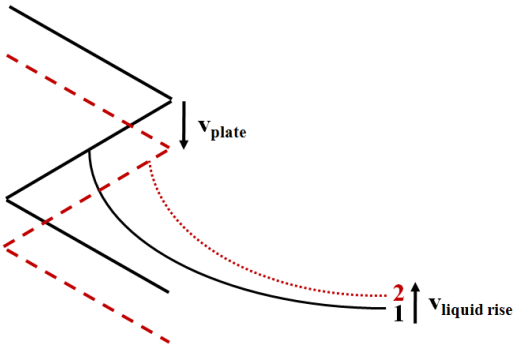

Figure 3.12: The apparent slip behavior on the lower face of the pyramid with respect to the apex and the stick behavior on the apex of the pyramid.

$$\text{normalized dimensionless time} = \frac{\text{actual time} \times (\text{plate velocity} + \text{velocity of the liquid rise})}{\text{peak-to-peak length}} \tag{3.15}$$

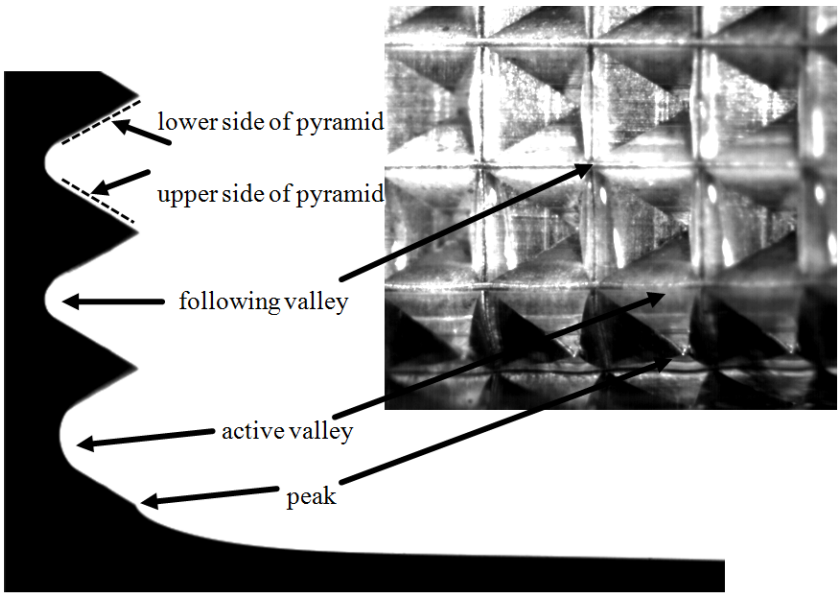

Figure 3.13: Explanatory front and side snaps of pyramidal arrays while advancing into the 10cSt PDMS.

In order to make the presented data more understandable, some definitions should be explained using images. The data plots are divided into two parts, liquid and solid, which indicates whether the detected contact line is on the solid or on the liquid film. In addition, they were organized into 4 zones, which will be explained individually in each associated subsection.

In figure 3.14 there are 4 snapshots describing the movement of the liquid front on one pyramid. In the case of a *valley*, the liquid fills the gap between two pyramids, where a very thick film is formed inside. The dynamic liquid front meets the film in the valley and overcomes it as the plate moves into the liquid. It moves until the *peak* and pins there. Being a 3D structure, the pyramid allows pinning of the liquid only on the apex where the focal plane is focused, as shown in figure 3.6. So the pinning happens locally, but not for the entire liquid front. As the contact line on the apex pins, the rest of

the liquid moves around the *peak* and starts to fill the following gap over the *peak*. As soon as the pinning is overcome, the liquid front slightly slides on the upper side of the pyramid, which is defined as *above the pyramid* in figure 3.14.

As the pyramidal structures are dipped into the liquid, the surface of the pyramids are wetted gradually. The liquid crawls through the side paths (Figure 3.15 horizontal and vertical arrows) and covers the upper part of the pyramid apex and fills the valley before the liquid front reaches the apex. Figure 3.15, the front view image, provides insight into how this gradual wetting occurs. Inside the dashed lines are dry, and outside of it, is wetted by PDMS, due to the flow (crawling) though the side paths.

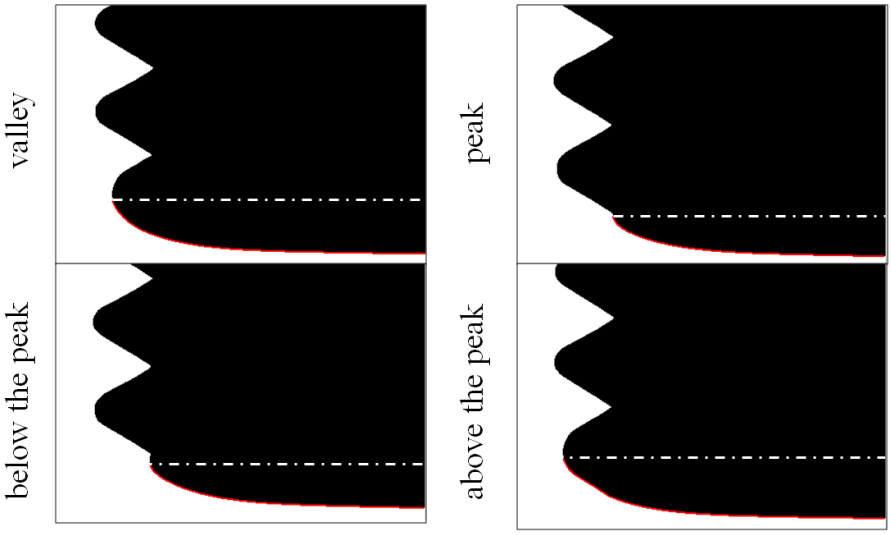

Figure 3.14: The red line shows the detected liquid meniscus shape on 4 different points on the pyramid as it is dipped into the liquid. The white dashed lines show the level, where the interface shape has its highest rise height on the solid.

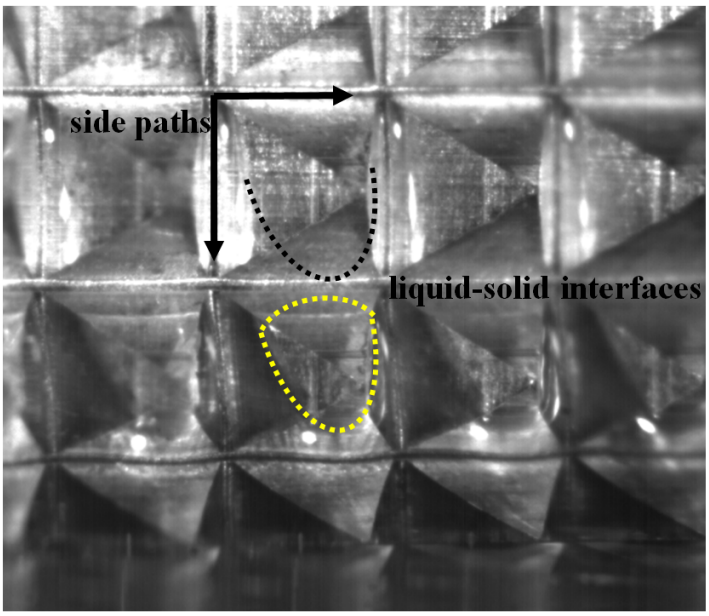

Figure 3.15: Front view of the 2mm pyramidal arrays while advancing into the 10cSt PDMS with 0.8mm/sec plate velocity. The dashed lines show the liquid-solid interface. Inside the dashed lines are dry and outside of it is wetted by PDMS. The arrows show the paths between the pyramids, each having a width '***c***' as defined in table 3.1. Between the closed dashed line and open dashed line, PDMS wets the solid by capillary crawling and covers the surface with a thin film.

3.5.1 Definition of Contact Angle on Very Rough Surfaces

In section 3.4.2, three different methods of measuring the contact angle of the meniscus shape on a flat surface are shown and explained. The extrapolation of the meniscus shape to fit the 2D Laplace solution gives us an **effective contact angle** with respect to the wall which is resolution independent. Deriving the contact angle via rise height gives us an **apparent effective contact angle** with respect to the wall which is resolution dependent but the deviation is very small. The tangent of the contact line on the liquid-solid interface gives us an **apparent contact angle** which is highly resolution dependent. In this work, due to the very rough surface features, the contact angle determination is done with the tangent method by fitting a polynomial on the meniscus shape and refining the position of the tangent very carefully with respect to the vertical axis. At the end, the results of the *tangent method* are compared with those of the *rise height method* to illuminate in which cases the choice of the chosen method is crucial.

3.5.1.1 Static and Dynamic Meniscus Shapes on Dry 3D Pyramidal Arrays

In the case of contact angle determination on smooth flat surfaces, the force balance which controls the contact angle in a static situation is referenced to the solid surface (namely to the wall); however for the experiments in this section, for the sake of defining a good transferable contact angle on the large structured surfaces, the contact angle is measured relative to the vertical axis. Figure 3.16, 3.17 and 3.18 show the static meniscus shapes and the 2D Laplace fitting at the peak and in the valley for the three different pyramidal features. In all three figures, dashed lines show the maximum capillary rise height of the liquid on the solid, to which the 2D Laplace meniscus equation is fitted. In the case of static shapes, if we focus on the contact line at the peak, we see a relatively good fitting to the theoretical meniscus curve for all feature sizes, but if we concentrate on the contact line in the valleys, we see a large deviation at the maximum capillary rise height of the meniscus shape, which decreases with decreasing feature size. Here we face a conflict in terms of how to define the measured contact angle for very rough surfaces by using the 2D Laplace equation. The roughness makes it impossible to use the 2D Laplace shape to determine the contact angle, because of the lack of a single wall or reference solid surface. On the peaks, it is possible to extrapolate the data curve and determine an **effective contact angle** but if the interface is in the valleys, it is not possible to decide if the dry valley at $x = 0$ is the reference solid surface or the peaks. If we consider the peak for data extrapolation then we lose information about what is happening in the valley, which is very interesting. If we try to extrapolate the data curve until the dry valley at $x = 0$, then the 2D Laplace equation does not reach there and it becomes impossible to determine a contact angle. In the case of dynamic meniscus shapes advancing into the liquid bath (see Figure 3.17), the deviation between the meniscus shape and theoretical curve becomes larger for 2mm and 1mm pyramids, especially in the valleys. Furthermore, in the case of dynamic meniscus shapes receding from the liquid bath (see Figure 3.18), the deviation between the meniscus shape and theoretical curve becomes smaller on the peaks and in the valleys due to the contact between the active liquid front and the liquid film on the surface. In both the static and dynamic cases, 0.5mm pyramids have the best fitting with the theoretical curve which is related to the feature depth. Due to all these conflicts the contact angle is measured by finding a tangent of the contact line at the interface with respect to the vertical and compared with the *rise height method* described later.

Static Meniscus Shapes:

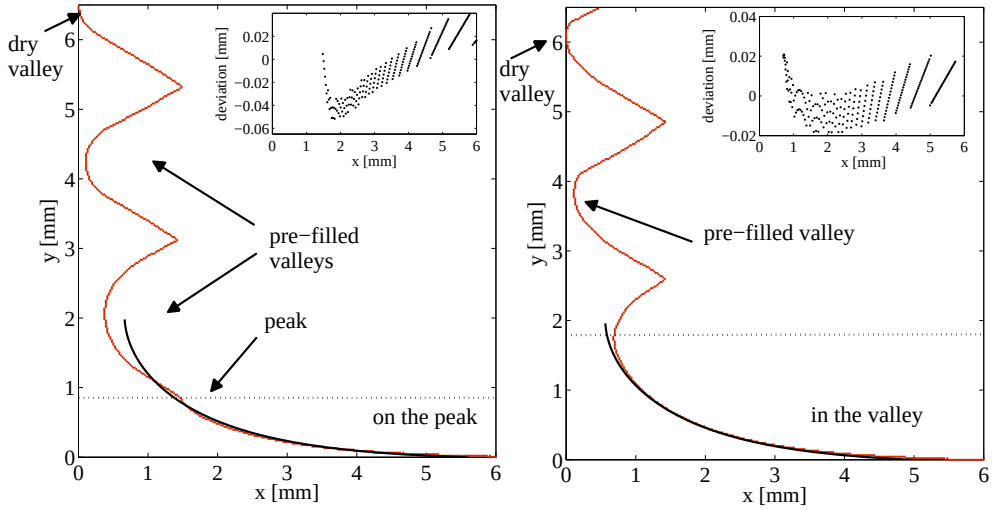

(a) Static meniscus shape on 2mm pyramidal structure dipped in 10cSt PDMS.

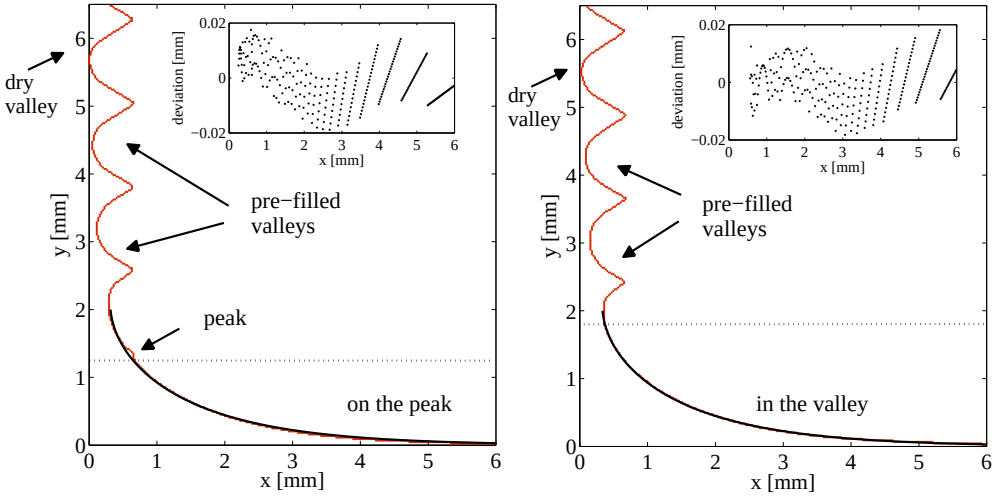

(b) Static meniscus shape on 1mm pyramidal structure dipped in 10cSt PDMS.

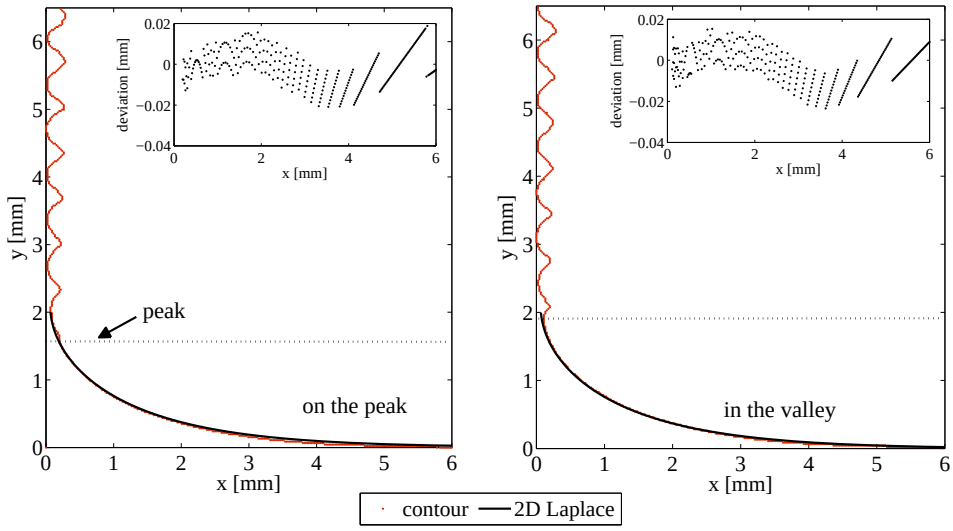

(c) Static meniscus shape on 0.5mm pyramidal structure dipped in 10cSt PDMS.

Figure 3.16: The meniscus shapes terminate at the dashed line. The $x = 0$ line represents dry wall.

Dynamic Meniscus Shapes - Advancing:

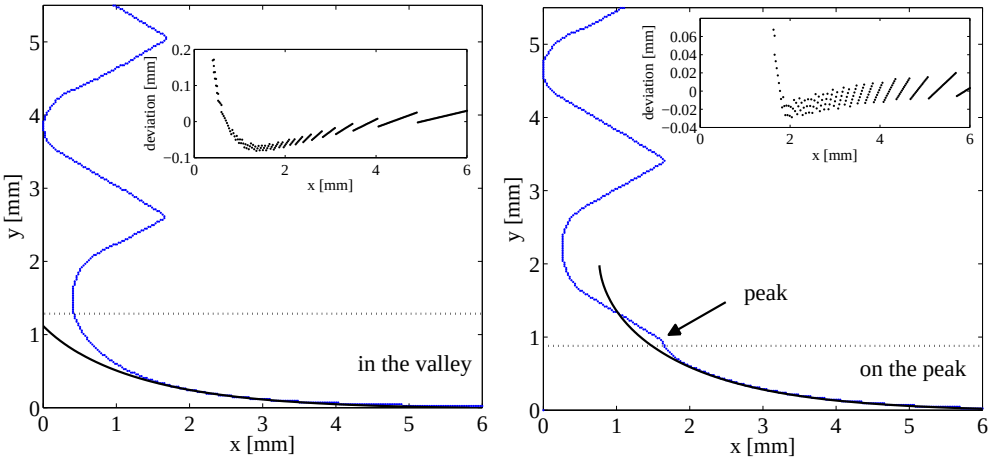

(a) Dynamic meniscus shape on 2mm pyramidal structure dipped in 10cSt PDMS.

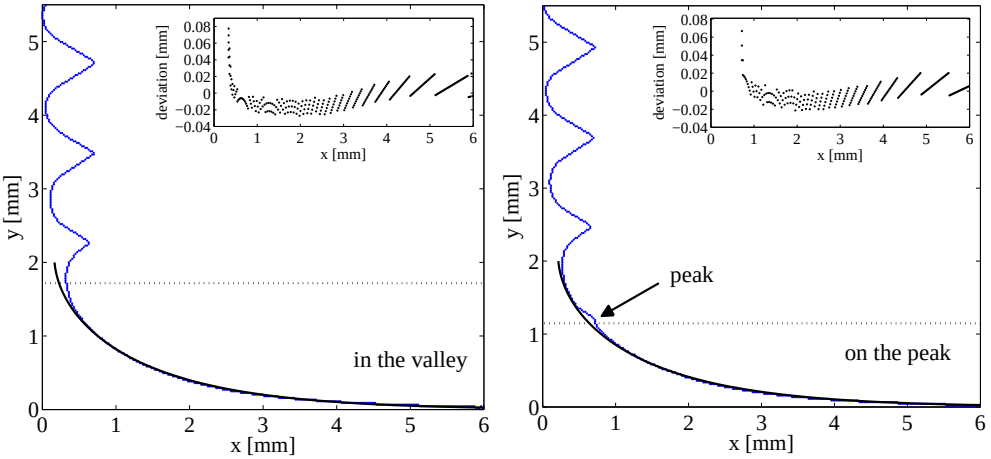

(b) Dynamic meniscus shape on 1mm pyramidal structure dipped in 10cSt PDMS.

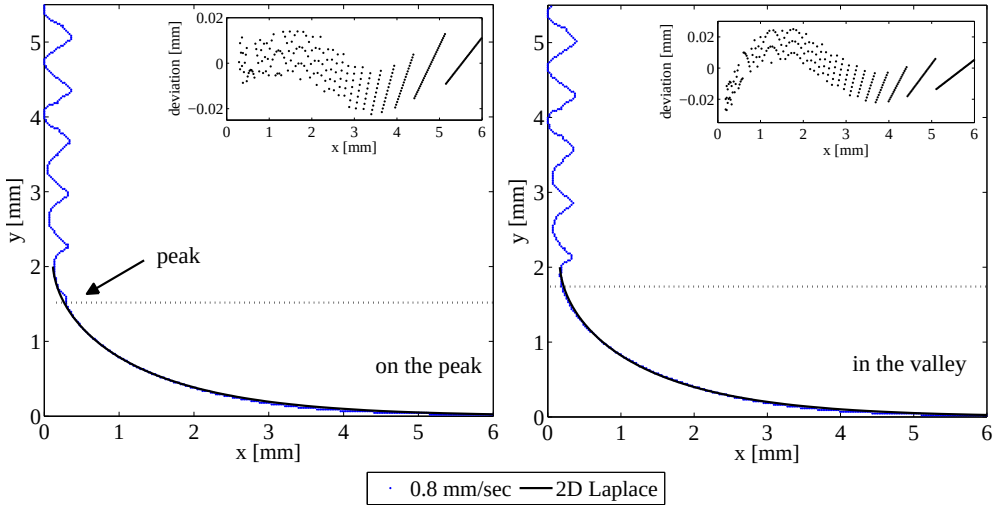

(c) Dynamic meniscus shape on 0.5mm pyramidal structure dipped in 10cSt PDMS.

Figure 3.17: The meniscus shapes terminate at the dashed line. The $x = 0$ line represents dry wall. All plates are dipped with 0.8mm/sec plate velocity.

Dynamic Meniscus Shapes - Receding:

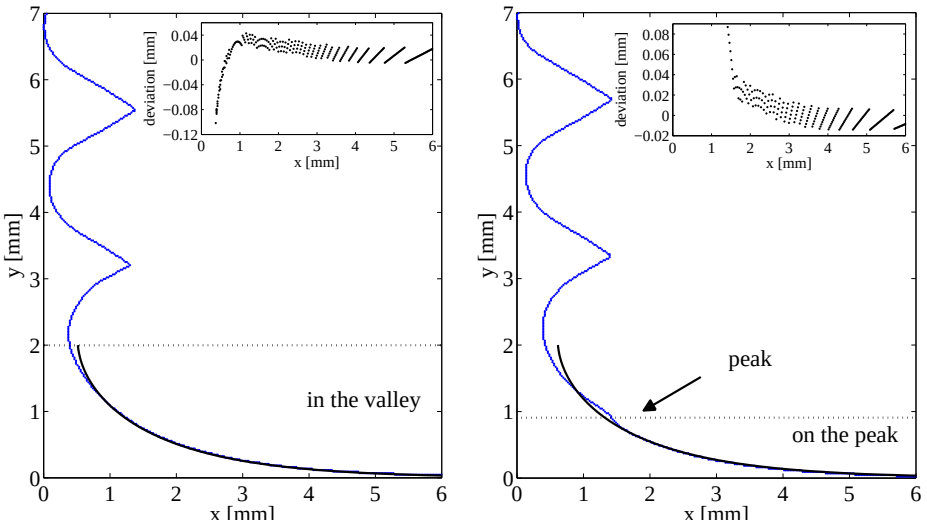

(a) Dynamic meniscus shape on 2mm pyramidal structure pulled from 10cSt PDMS.

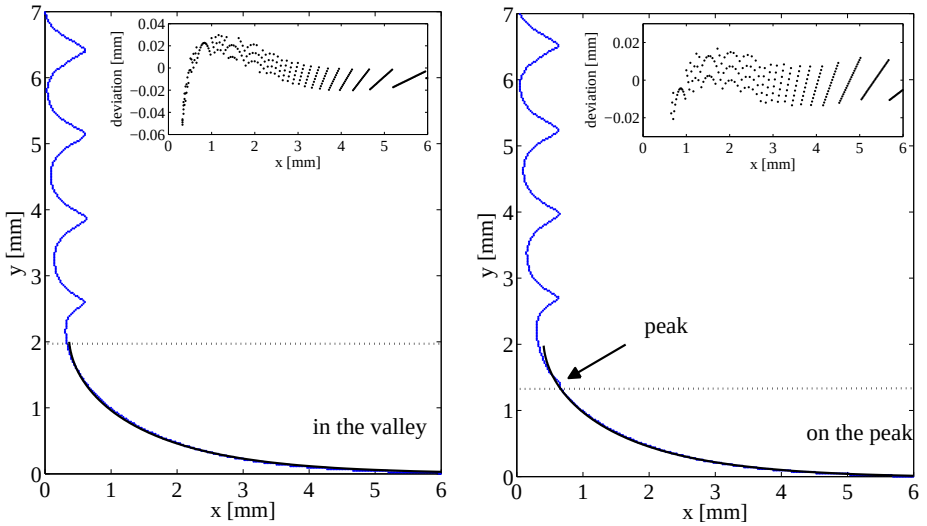

(b) Dynamic meniscus shape on 1mm pyramidal structure pulled from 10cSt PDMS.

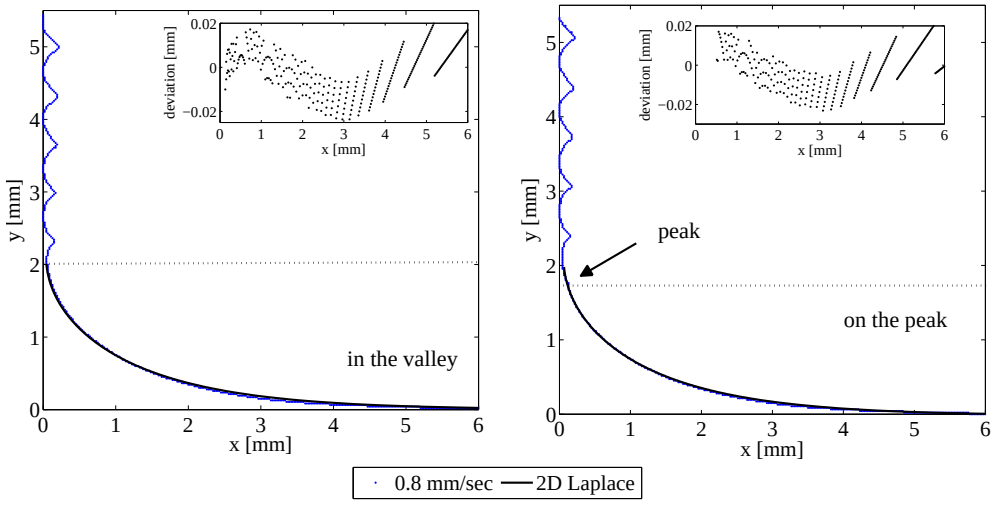

(c) Dynamic meniscus shape on 0.5mm pyramidal structure pulled from 10cSt PDMS.

Figure 3.18: The meniscus shapes terminate at the dashed line. The $x = 0$ line represents dry wall. All plates are pulled up 0.8mm/sec plate velocity.

3.5.2 Dynamic Advance On Dry 3D Pyramidal Arrays (10cSt PDMS)

In this section, the advancing case of wetting on three pyramidal arrays will be covered. The pyramidal arrays are dipped in liquid PDMS at three different speeds and the wetting evolution on them is observed. In the following sections, each pyramidal feature will be examined individually.

3.5.2.1 2mm Pyramidal Features

2mm pyramidal features have ∼1.7mm depth and ∼2.45mm peak-to-peak height, both of which are larger than the capillary length of PDMS (L_c=1.48mm for PDMS in 10cSt and 100cSt). In order to explain the evolution of wetting on the 2mm pyramidal features, the following graphical representations are divided into four zones for each periodic cycle. For each period, the contact angle change, rise height of the contact line with respect to the liquid bulk level, and the filling of the gaps between pyramids are presented. Due to the 3D shape of the pyramids (Figure 3.15), the gaps between each following pyramid (referred to as *valley* earlier) are filled partially through the side paths (the very narrow gaps between each row and column referred to as '**c**' in Table 3.1) before the dynamic liquid front reaches that point. This is an effect that cannot be observed earlier (for example in the case of horizontal rivulets dipped in a liquid bath). The complexity of 3D pyramids causes a pre-wetting of the surface, because the liquid is able to crawl though the side paths. Simply put, the contact line is curved wavy interface with a complex curvature (see Figure 3.6 and 3.15). For this reason the focal plane is shifted to one row of peaks to be able to observe the wetting effects with respect to the maximum height and depth on the surface.

In figure 3.21 the periodic data of wetting on 2mm pyramids are presented. The periodic cycle starts on the peak of the pyramid, then the liquid front slightly slides on the upper side of the pyramid into the valley, (film and builds a liquid-liquid interface) and then the dynamic liquid front reaches the lower side of the following pyramid and slides up its face until the peak. On the following plots, the liquid-liquid interface is tagged as *liquid* and 'zone 4', where the contact line overcomes the peak and fills the upper face of the pyramid (the valley between the two pyramids), which is slightly filled before the contact line arrives. The pre-filling of the valley is due to the capillary rise of the liquid through the sides of the pyramidal structure, which is a 3D effect. In Figure 3.14, this zone is denoted as *above the peak*. Here the contact angle does not change drastically, because the liquid front maintains contact with the liquid film in the valley.

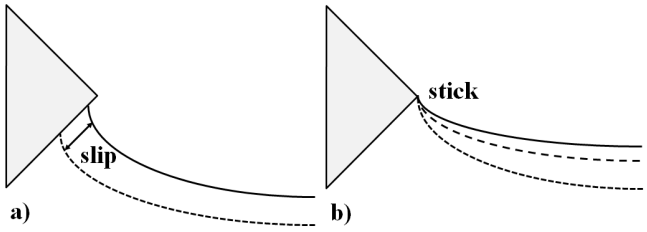

Figure 3.19: The apparent slip behavior on the lower face of the pyramid with respect to the apex and the stick behavior on the apex of the pyramid (zone 1).

As soon as the more than half of valley is filled with liquid, a change in boundary condition happens. The liquid front touches the solid (the lower face of the pyramid with respect to the apex) and makes an *apparent slip motion*. 'Zone 1' represents the this motion of the liquid on the lower face of the pyramid. Here the local contact angle of the liquid interface stays almost constant and the contact line slips over the surface and gains height without being affected by the descending substrate. The *apparent slip* velocity in 'zone 1' relative to the surface is nearly ∼0.8 mm/sec, independent of the plate velocity, although the liquid slides on the lower face of the pyramid faster than the plate velocity in the lab frame. The *apparent slip* velocity in the lab frame is 2.38 mm/sec for 0.848 mm/sec plate velocity, 1.78 mm/sec for 0.636 mm/sec plate velocity, and 1.19 mm/sec for 0.424 mm/sec plate velocity, where the lab frame velocity of *apparent slip* is overall 2.8 times larger than the plate velocity. The reason for the *apparent slip motion* is the 3D structure of the surface, where the liquid has the opportunity to follow the side paths. Figure 3.19a shows a basic sketch how the *apparent slip motion* occurs on the lower side of the pyramids with respect to the apex. Due to the large scale of the pyramids, the liquid fills the gaps between the pyramidal structures slowly from the side paths and as the liquid front meets the crawling liquid in the valley, a rapid front advances, which causes the *apparent slip motion*. After the *apparent slip motion* is over, the liquid remains contact with the solid surface, but the contact angle increases as the liquid-solid interface (rise height) decreases due to the descending plate. 'Zone 2' represents the liquid movement on the solid after the slip phase, where both the contact angle and the rise height change. In figure 3.14, 'zone 2' is labeled as *below the peak*. During the *apparent slip motion* the contact angle is ∼90° with respect to the solid and in 'zone 2' it is larger than 90° (see Figure 3.20).

After the liquid front reaches the apex, the act of contact angle changes and becomes steeper. 'Zone 3' represents the pinning of the liquid on the apex of the pyramid, where the apex pushes the liquid downwards on the contact line and at the same time increases its contact angle (see Figure 3.19b). Here, due to the plate movement, the term 'pinning' means a static case of contact line with respect to the apex of the pyramid but not with respect to the lab frame. The 'stick' velocity (the change in rise height of the intersection point) on the peak is equal to the plate velocity. 'Zone 1', 'zone 2', and 'zone 3' are all tagged as *solid*, to explicitly indicate the contact of liquid with the solid surface.

The period of the change in contact angle, rise height, and filling depth for the 2mm pyramidal array is equal to 2.41 sec, 3.24 sec, and 4.91 sec for plate velocities 0.848 mm/sec, 0.636 mm/sec, and 0.424 mm/sec, respectively. The average amplitude of the contact angle is 42.8°±1.24° while the average amplitude of rise height is 0.98±0.04mm (see also Figure 3.24a for details). This shows us that the plate velocity in this range (0.4mm/sec≤v_{plate}≤0.85mm/sec) does not affect the period and amplitude of the contact angle and rise height change. The pinning time in seconds increases gradually as the plate velocity decreases. The pinning durations are, 0.35 sec, 0.64 sec, and 0.90 sec for 0.848 mm/sec, 0.636 mm/sec and, 0.424 mm/sec plate velocities, respectively.

Now if we concentrate on the filling depth graphs plotted with respect to the contact angle and rise height change, we notice that there is a correlation between them. In figure 3.7 the filling depth is defined as the difference between the dry valley and maximum point of liquid meniscus in x-axis direction. The *active valley* is the valley, where the liquid front is moving through and the *following valley* is the one above. As the active valley is filled up to a certain value (∼0.43mm in 0.95 sec for 0.848 mm/sec plate velocity, ∼0.41mm in 1.12 sec for 0.636 mm/sec plate velocity and, ∼0.48mm in 1.37 sec for 0.424 mm/sec plate velocity) the *apparent slip motion* begins. As soon as the liquid-liquid interface is over and the liquid-solid interface begins, the slope of filling depth gets steeper until the *apparent slip motion* stops. This ends when the valley is filled up to ∼1.06mm in 0.28 sec for 0.848 mm/sec plate velocity, ∼0.92mm in 0.3 sec for 0.636 mm/sec plate velocity, and ∼0.90mm in 0.34 sec for 0.424 mm/sec plate velocity. A higher plate velocity causes a faster apparent slipping motion and faster filling of the valley. The maximum filling depth shows where the liquid touches the peak, and once the pinning on the peak begins, the next valley is filled. For 0.848 mm/sec, which is the highest plate velocity, the *following valley* never gets wetted before the active valley is completely filled (i.e., as soon as the liquid front reaches the apex). As the plate velocity decreases, the *active valley* is filled abruptly during the pinning region on the *peak* in 'zone 3' by the effect of crawling through the side paths.

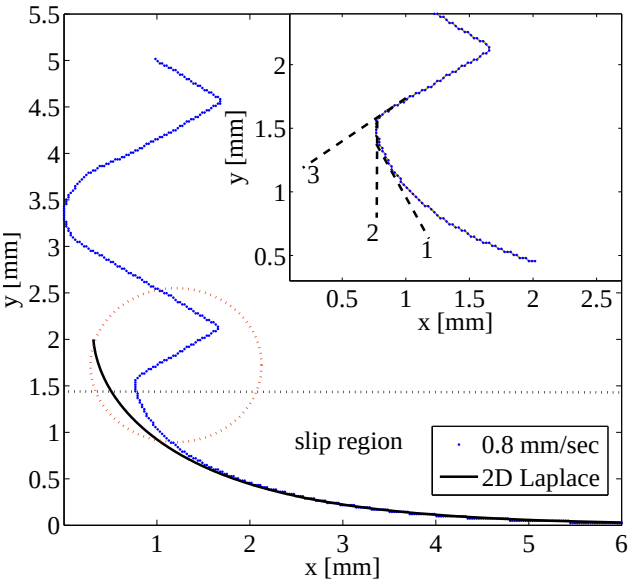

Figure 3.20: The apparent slip motion on the upper side of the pyramid. The blue dots show the contour line, the dashed line shows where the meniscus shape touches the solid surface and $x = 0$ represents the dry wall. The black line is the 2D Laplace curve fitted to the meniscus shape. The interior of the red circle is magnified on the upper right corner. The meniscus has a ∼30° contact angle with respect to the vertical (between dashed lines 1 and 2) and a ∼90° contact angle with respect to the solid surface (between dashed lines 1 and 3).

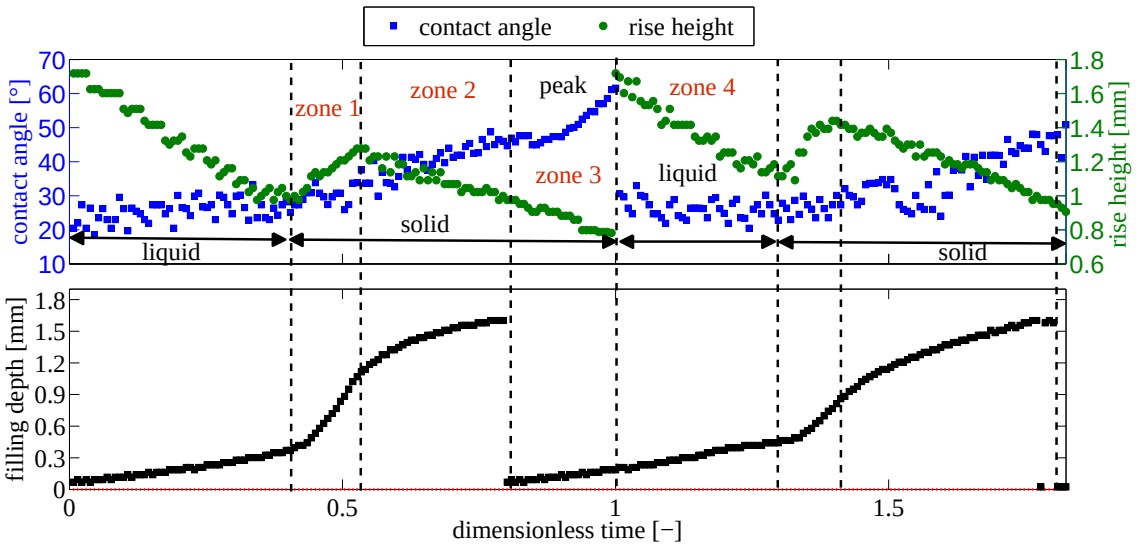

(a) 2mm pyramid, 0.8 mm/sec plate velocity, advancing.

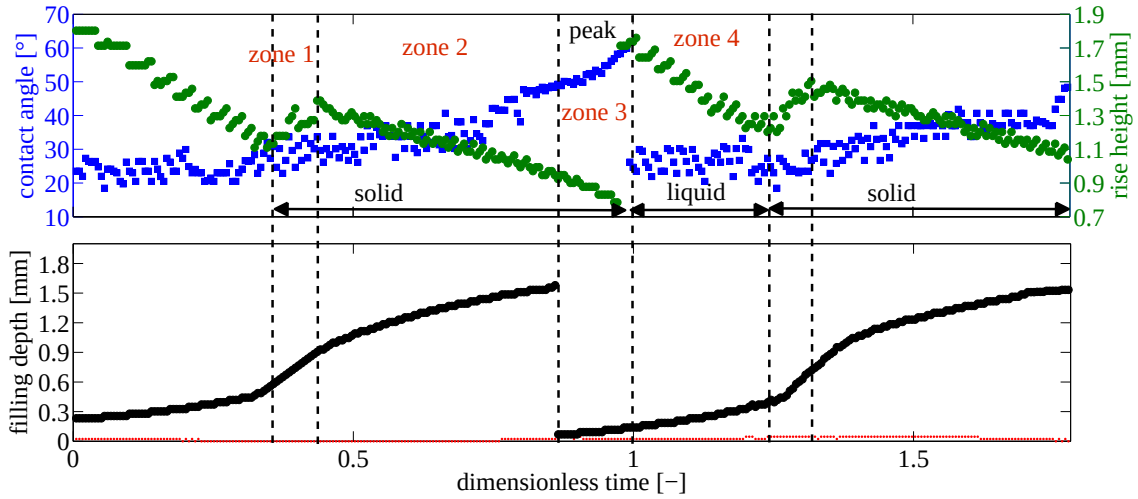

(b) 2mm pyramid, 0.6 mm/sec plate velocity, advancing.

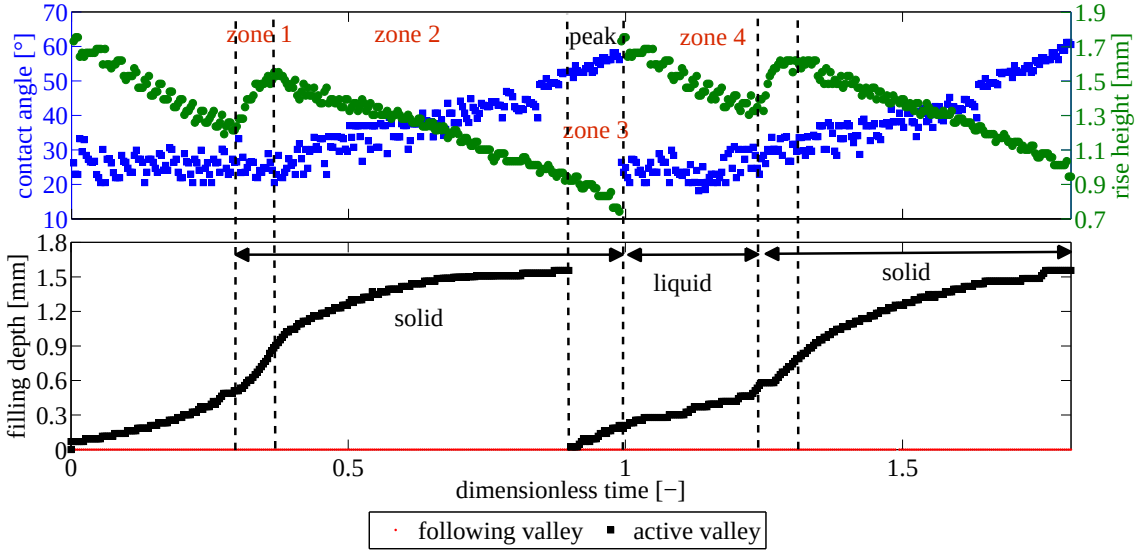

(c) 2mm pyramid, 0.4 mm/sec plate velocity, advancing.

Figure 3.21: Contact angle, rise height and filling depth of the valley versus dimensionless time for 10cSt PDMS and 2mm pyramids.

3.5.2.2 1mm Pyramidal Features

1mm pyramidal features have ∼0.7mm depth and ∼1.3mm peak-to-peak height, both of which are smaller than the capillary length of PDMS (L_c=1.48mm for PDMS in 10cSt and 100cSt). As in previous plots for 2mm pyramids, the following plots are also divided into zones and regions. In the case of 1mm pyramidal structures, due to the smaller depth and height values with respect to the capillary length, the slipping behavior ('zone 1' in Figure 3.21) does not appear. The smaller scale of the pyramidal structures and the narrower side paths between the pyramids cause a faster capillary crawl for the liquid on the surface. This affects the character of the zones, where 'zone 1' and 'zone 4' merge into 'zone 4' but the duration of 'zone 4' becomes much shorter than the sum of both zones, which means that the dynamic liquid front has a shorter contact with the liquid film in the pre-filled valley and touches the solid surface sooner as on 2mm pyramids. In 'zone 4', the contact angle and the rise height of the fluid front stay almost constant due to the liquid-liquid interface. This means that, despite the descending pyramids (and hence the liquid) downwards, the meniscus does not change its shape. At this point if we concentrate on the filling depth plots, we see that the valley between two pyramids is steadily filled. The filling of the valley causes a shift of the meniscus in the x-direction without changing the shape of it and, consequently the contact angle and meniscus height stay constant. As soon as the liquid front touches the solid surface, namely the lower side of the pyramid, both the contact angle and contact line boundary conditions change and as the contact angle increases, the contact line rise height decreases steadily until it reaches the apex of the pyramid.

Overall 'zone 2' and 'zone 3' have a liquid-solid interface, which covers the lower side of the pyramid and the peak, and as soon as the peak has been overcome a liquid-liquid interface forms rapidly. The liquid does not find an opportunity to touch the dry upper side of the pyramid and glide on it to reach the pre-filled valley. Instead, as soon as the liquid front is released pinning, it merges with the liquid film in the valley and moves forward with it (see Figure 3.22). As in the previous subsection, the slope of 'zone 3' (pinning region) is equal to the plate velocity.

The period of the change in contact angle, rise height and filling depth for the 1mm pyramidal array is 1.34 sec, 1.76 sec, and 2.65 sec for plate velocities of 0.848 mm/sec, 0.636 mm/sec, and 0.424 mm/sec, respectively. The average amplitude of the contact angle is 30.51°±3.35° and the average amplitude of rise height is 0.69±0.04mm. Here again we observe that the plate velocity does not have an effect on the amplitude and period of the contact angle and rise height. However the period of 1mm pyramids is larger that 2mm pyramids in dimensionless time and shorter in real time. The pinning time in seconds increases gradually as the plate velocity decreases. The pinning durations are 0.35 sec, 0.49 sec, and 0.55 sec for 0.848mm/sec, 0.636 mm/sec, and 0.424 mm/sec plate velocities, respectively.

As in the case of 2mm pyramids, the filling depth of the active and following valleys of 1mm pyramids provide abundant of information about the wetting process. Here as the active valley gets filled, the following valley is filled at the same time, because the liquid crawls faster through the narrow side paths where the capillary pressure is larger compared to the side paths of 2mm pyramids. This causes a continuity of the filling phase between the active and following valleys. Again the maximum filling depth shows where the liquid touched the peak and as soon as the pinning starts on the peak, the forthcoming valley gets filled by the liquid pushed through the side paths.

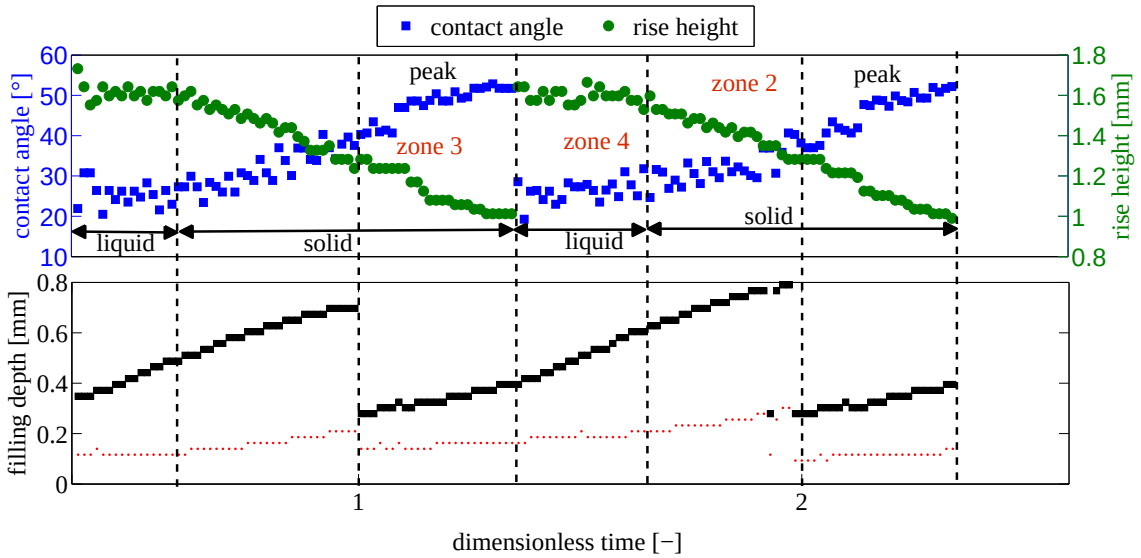

(a) 1mm pyramid, 0.8 mm/sec plate velocity, advancing.

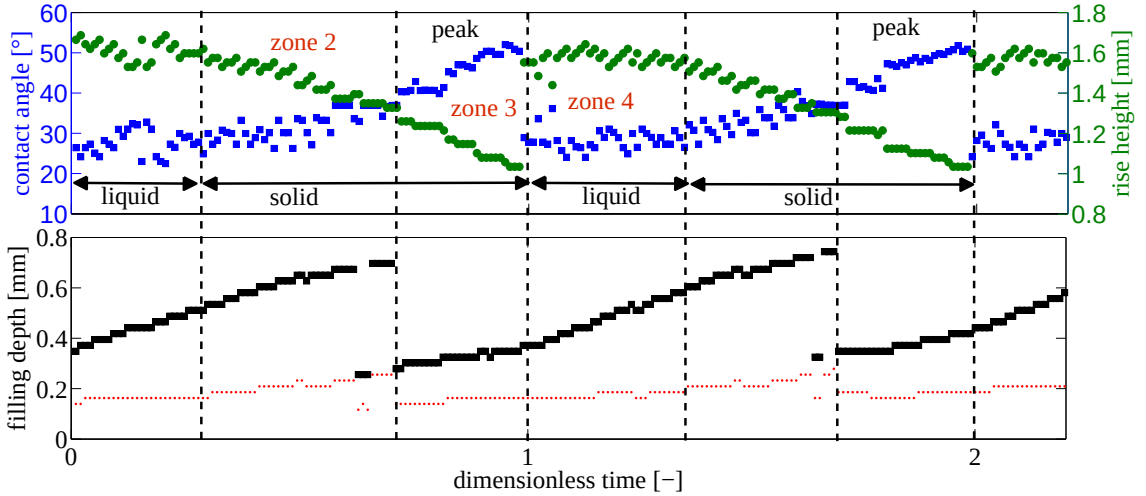

(b) 1mm pyramid, 0.6 mm/sec plate velocity, advancing.

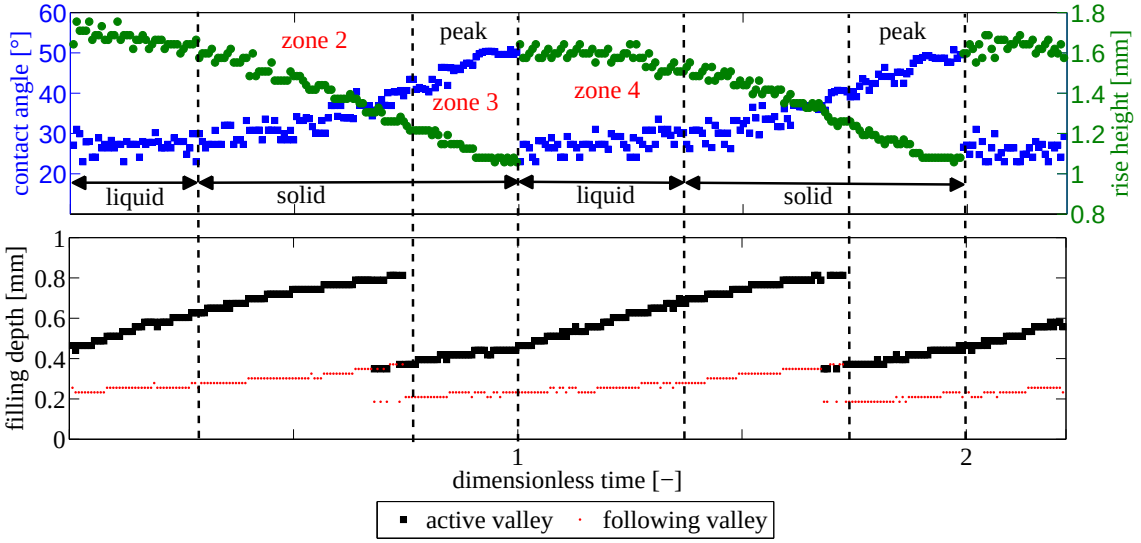

(c) 1mm pyramid, 0.4 mm/sec plate velocity, advancing.

Figure 3.22: Contact angle, rise height and filling depth of the valley versus dimensionless time for 10cSt PDMS and 1mm pyramids.

3.5.2.3 0.5mm Pyramidal Features

0.5mm pyramidal features have ∼0.4mm depth and ∼0.7mm peak-to-peak height, both of which are smaller than the capillary length of PDMS (L_c=1.48mm for PDMS in 10cSt and 100cSt). As the structure dimensions get smaller, the gradual wetting phenomenon described in the previous subsections becomes difficult to observe and, moreover, some specific features disappear, e.g. the number of wetting zones decreases. In the case of 2mm pyramid, 4 zones were observed, in the case of 1mm pyramid, one of the zones, the region of *the apparent slipping motion*, merges with the next zone, and in the case of 0.5mm pyramid, 'zone 1' and 'zone 2' disappear completely. Due to the scale size of the pyramids, *slip motion* is impossible to occur. Furthermore, 'zone 2', the region where the liquid front meets the solid surface after the liquid-liquid interface, merges with 'zone 4', because of the narrow valley width. The active valley gets filled so fast by the crawling of the liquid from side paths that the following valley gets filled before the dynamic liquid front arrives. Here again in 'zone 3', where the pinning on the peak occurs, the slope of the data is equal to the plate velocity. As a result of very small feature size, the pinning is very short. As soon as the liquid front overcomes the peak, it makes contact it with the pre-filled liquid film in the valley and preserves it.

The period of the change in contact angle, rise height and filling depth for 0.5mm pyramidal array is in seconds 0.81 sec, 1.08 sec, and 1.65 sec for plate velocities 0.848 mm/sec, 0.636 mm/sec, and 0.424 mm/sec, respectively. The average amplitude of the contact angle is 30.32°±2.61° and the average amplitude of rising height is 0.60±0.07mm. The pinning time in seconds increases gradually as the plate velocity decreases, due to the feature size. The pinning durations are, 0.12 sec, 0.14 sec, 0.22 sec for 0.848 mm/sec, 0.636 mm/sec, and 0.424 mm/sec plate velocities, respectively.

In the case of 0.5mm pyramids, as the active valley gets filled, the following valley is filled at the same time, because the liquid crawls faster through the narrow side paths where the capillary pressure is larger compared to the side paths of 2mm and 1mm pyramids. This causes a continuity of the filling phase between active and following valleys like in the case for 1mm pyramids. Here again the maximum filling depth shows where the liquid touches the peak and as soon as the pinning starts on the peak the forthcoming valley gets filled by the liquid pushed through the side paths.

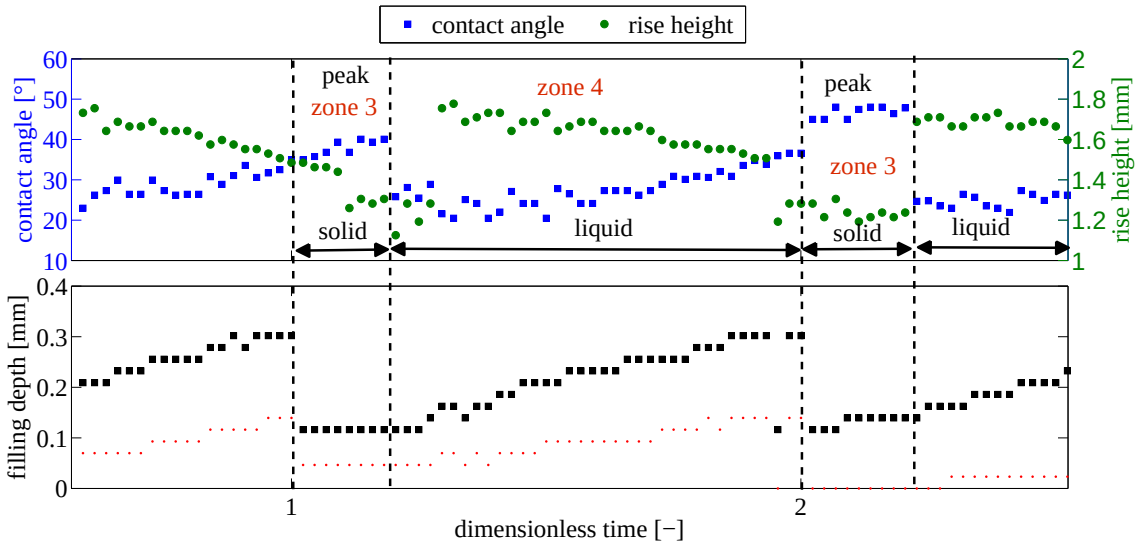

(a) 0.5mm pyramid, 0.8 mm/sec plate velocity, advancing.

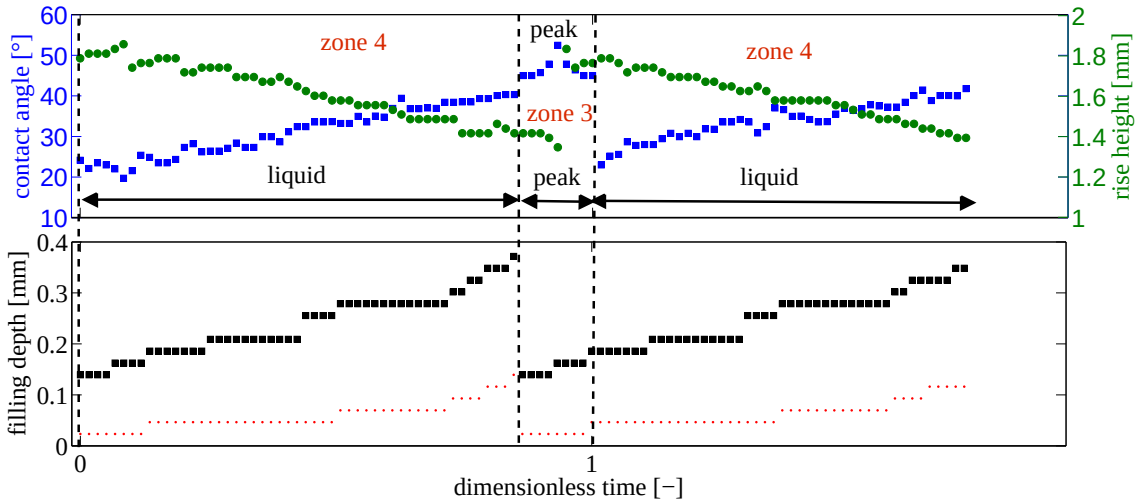

(b) 0.5mm pyramid, 0.6 mm/sec plate velocity, advancing.

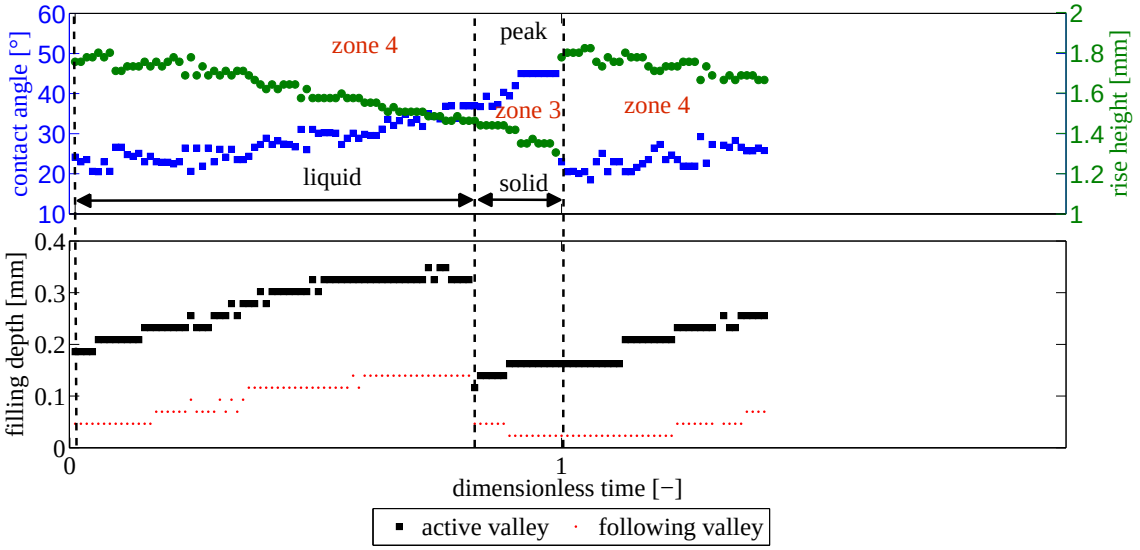

(c) 0.5mm pyramid, 0.4 mm/sec plate velocity, advancing.

Figure 3.23: Contact angle, rise height and filling depth of the valley versus dimensionless time for 10cSt PDMS and 0.5mm pyramids.

3.5.2.4 Comparison of Observations for Dynamic Advancing Contact Line

By changing the velocity and taking the feature size fixed, it is concluded that the velocity change does not drastically affect the the change in the contact angle and rise height for each structure. Figure 3.24 demonstrates that the amplitude of the rise height and contact angle for each pyramidal structure is constant, independent of the plate velocity. The maximum rise height is achieved when the dynamic liquid front touches the deepest part of the valley as it slides on the upper edge of the pyramid (in the case of 2mm pyramidal array) or pre-filled valley (in the case of 0.5mm and 1mm pyramidal arrays) just after the pinning. The minimum rise height is achieved when the dynamic front pins on the apex and is pushed downwards. Larger features can push the liquid longer downwards where the liquid cannot find the possibility to crawl up. Due to this, on larger features, the rise height is small and on smaller features, the rise height is larger. Therefore the amplitude values (difference between the maximum and minimum values) for rise height decreases as the feature size gets smaller (see Table 3.2). The change in rise height affects the contact angle change. The maximum rise height has the smallest contact angle and the minimum rise height (on the apex) has the largest contact angle. Here again, the amplitude values for contact angle decreases as the feature size gets smaller

Figure 3.24a presents the gradual formation of the *apparent slip motion* on 2mm pyramids with different plate velocities. In the case of high plate velocity, the pyramids push the liquid front lower, so the rise height becomes smaller and then the formation of *apparent slip motion* occurs. However, in the case of a slow plate velocity, the solid dwells with the capillary pressure as opposite force and cannot push the liquid as low. This difference does not affect the formation of *apparent slip motion*, but just shifts the evolution in time. The slopes and amplitude of *apparent slip motion* for all plate velocities are the same in dimensionless time, which gives us a generalization of the motion.

Advancing on a Dry Surface - Amplitudes (10cSt PDMS)

pyramid type and plate velocity	max. rise height [mm]	min. rise height [mm]	2D Laplace derivation		tangent method	
			max. contact angle [°]	min. contact angle [°]	max. contact angle [°]	min. contact angle [°]
2 mm - 0.8 mm/sec	1.72	0.78	59.44	18.94	61.1	18.47
2 mm - 0.6 mm/sec	1.76	0.78	59.44	17.03	59.9	18.47
2 mm - 0.4 mm/sec	1.75	0.74	61.04	17.51	62	18.13
average difference	Δ=0.98±0.04		Δ=42.14±1.09		Δ=42.6±1.24	
1 mm - 0.8 mm/sec	1.64	0.99	50.92	22.70	52.2	19.26
1 mm - 0.6 mm/sec	1.68	1.03	49.27	20.83	52.1	22.45
1 mm - 0.4 mm/sec	1.75	1.08	47.20	17.51	50.7	22.99
average difference	Δ=0.66±0.04		Δ=28.77±0.60		Δ=30.1±3.35	
0.5 mm - 0.8 mm/sec	1.77	1.19	42.59	16.55	47.8	20.5
0.5 mm - 0.6 mm/sec	1.83	1.34	36.16	13.62	47.8	19.7
0.5 mm - 0.4 mm/sec	1.82	1.30	37.89	14.11	45	18.4
average difference	Δ=0.50±0.07		Δ=24.12±1.27		Δ=27.3±2.61	

Table 3.2: The maximum and minimum values of rise height and contact angle for three pyramidal array in three different speeds for the advancing case.

In figure 3.25, a comparison between two contact angle determination methods is shown, which are the tangent method and the derivation of 2D Laplace. In section 3.4.2, three methods are applied on smooth flat surfaces, the tangent method, derivation of 2D Laplace and fitting to 2D Laplace. In the tangent method, the contact angle is measured by fitting a tangent at the intersection point. By derivation of 2D Laplace, the contact angle is measured by inserting the respective rise height of the liquid front with respect to the liquid bulk level into equation 3.7c. Due to the complex shape of the pyramidal features, it is preferred to use the tangent method, which minimizes data loss. Figure 3.25a proves that using the tangent method is the appropriate choice due to the changing boundary conditions during the *apparent slipping motion*. For 2mm pyramids, the contact angles measured by the tangent method does not fit the derivation of 2D Laplace method at the *apparent slipping motion* and at liquid-liquid interface regions, but show a slight similarity at the liquid-solid interface region.

In the case of 1mm and 0.5mm pyramids both methods agree. The existing theory does not fit where the liquid front is on a liquid film.

When we concentrate on the pinning time for each feature size and each plate velocity, we observe that the pinning duration increases gradually as the plate velocity decreases. Table 3.3 presents the real time periods of the liquid wetting from one peak to the next and real time pinning durations. From these values, it can be concluded that the plate velocity and the feature size affect the pinning duration. The large pyramids advancing with a low plate velocity have the longest pinning duration.

Advancing on Dry Surface - Periods (10cSt PDMS)

pyramid type and plate velocity	full period [sec]	pinning time [sec]
2 mm - 0.8 mm/sec	2.41	0.35
2 mm - 0.6 mm/sec	3.24	0.64
2 mm - 0.4 mm/sec	4.91	0.90
1 mm - 0.8 mm/sec	1.34	0.35
1 mm - 0.6 mm/sec	1.76	0.49
1 mm - 0.4 mm/sec	2.65	0.55
0.5 mm - 0.8 mm/sec	0.81	0.12
0.5 mm - 0.6 mm/sec	1.08	0.14
0.5 mm - 0.4 mm/sec	1.65	0.22

Table 3.3: The real time periods of the liquid wetting from one peak to the next and pinning time durations for all feature sizes and all plate velocities.

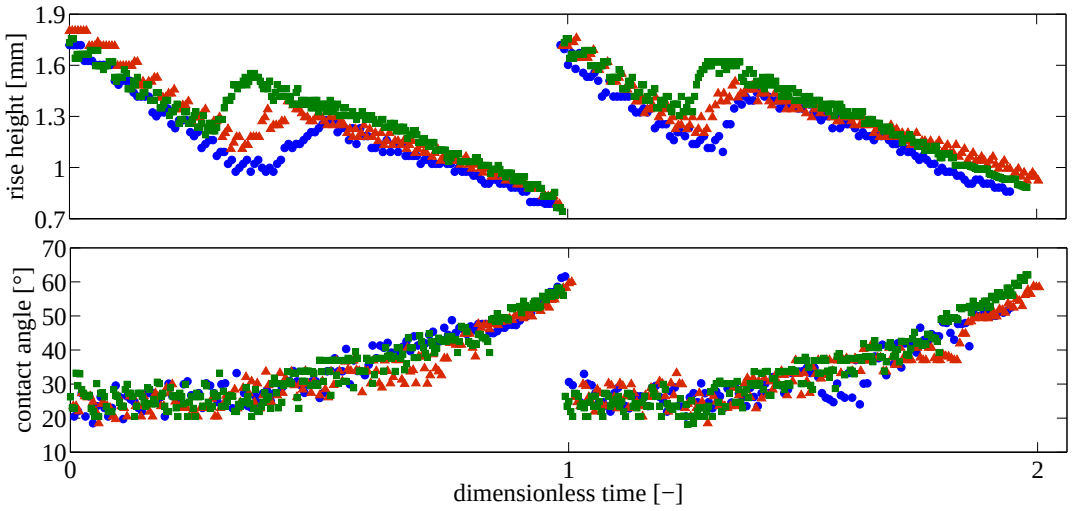

(a) 2mm pyramid, comparison of rise height and contact angle, advancing.

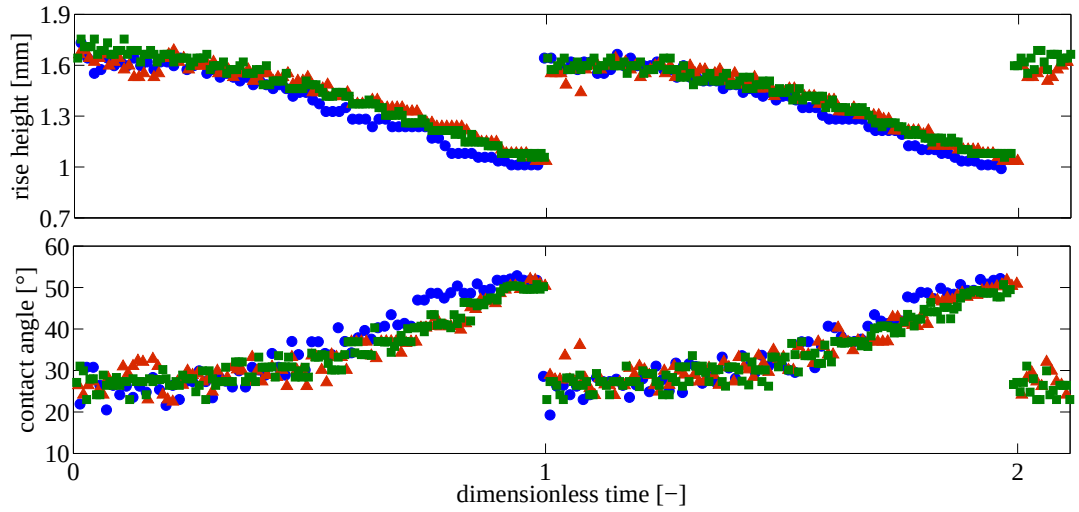

(b) 1mm pyramid, comparison of rise height and contact angle, advancing.

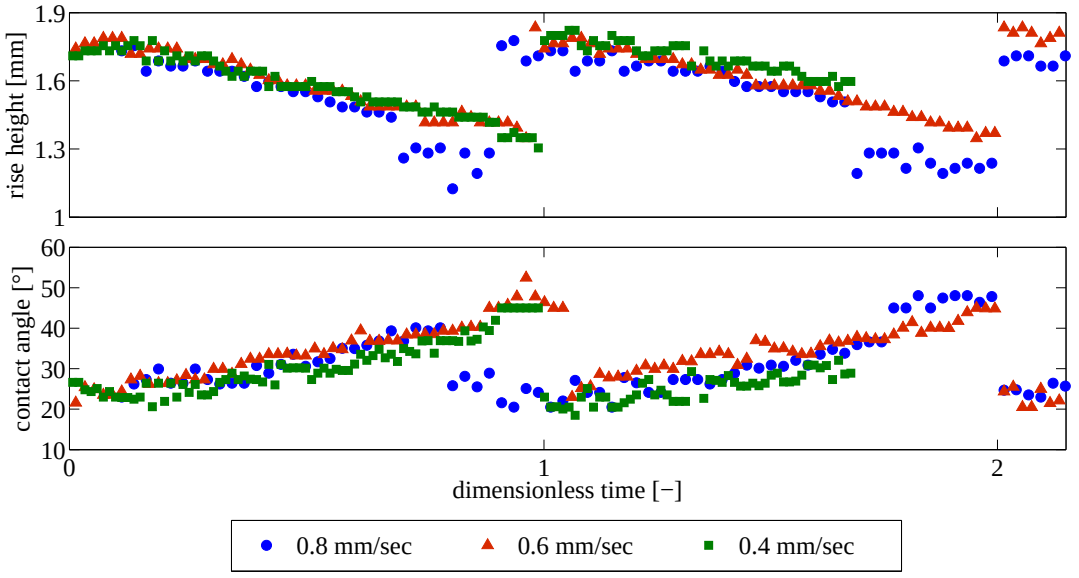

(c) 0.5mm pyramid, comparison of rise height and contact angle, advancing.

Figure 3.24: Feature size dependent comparison of contact angle and rise height versus dimensionless time for 10cSt PDMS.

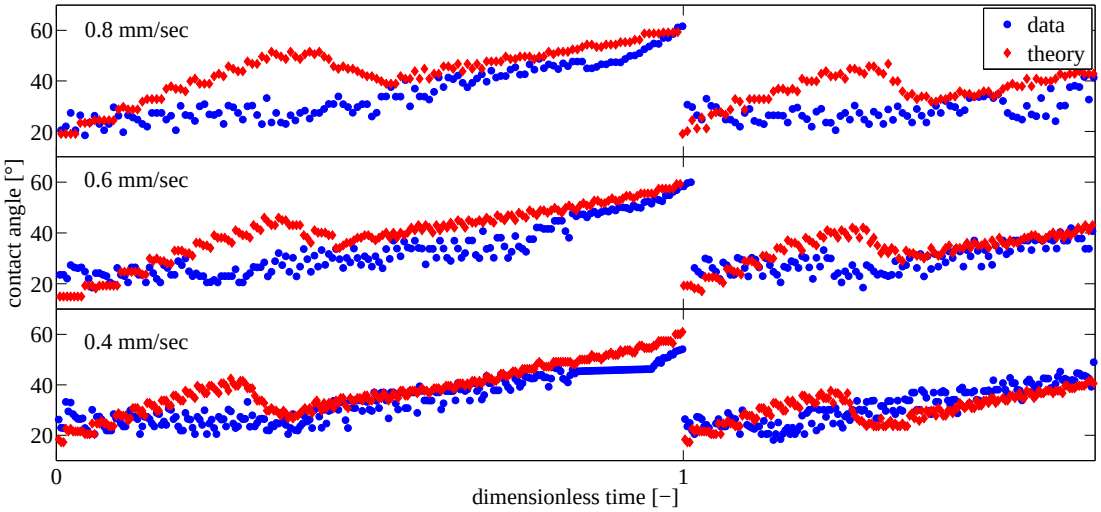

(a) 2mm pyramids, advancing.

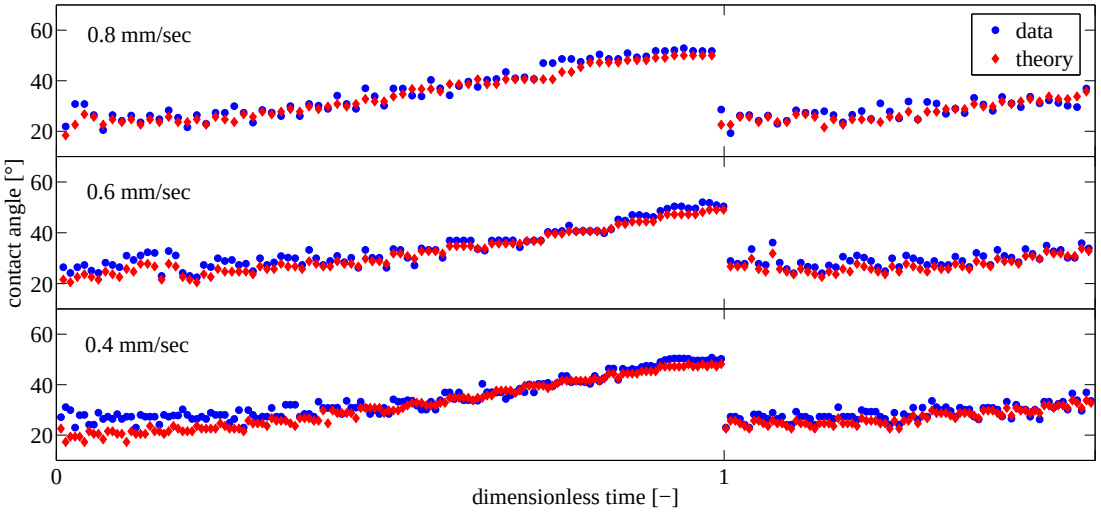

(b) 1mm pyramids, advancing.

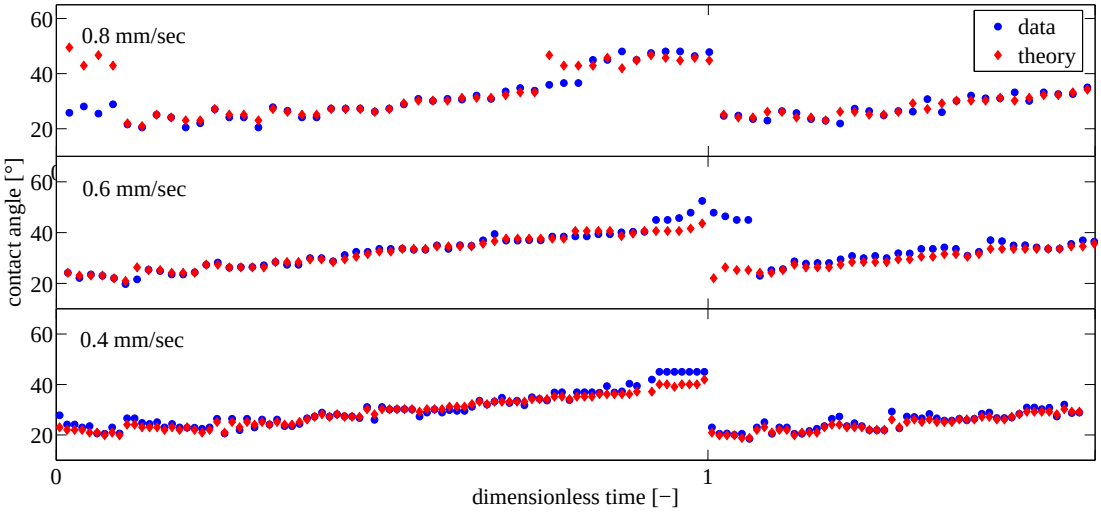

(c) 0.5mm pyramids, advancing.

Figure 3.25: Comparison of measured contact angle by tangent method (labeled as data) and 2D Laplace derivation (labeled as theory) gained from equation 3.7c.

3.5.3 Receding of Wetted 3D Pyramidal Arrays (10cSt PDMS)

In this section, the receding case of wetting on three pyramidal arrays will be covered. The pyramidal arrays are pulled up from liquid PDMS bath at three different speeds and the wetting evolution on them is observed. In the following sections, each pyramidal feature will be examined individually.

3.5.3.1 2mm Pyramidal Features

In the receding case for 2mm pyramidal structures, only two zones are observed, which are the pinning on the peaks and the liquid-liquid interface in the valleys. Aside from the liquid zone, two regions that need to be considered. In 'region 1', as the capillary rise height increases, the contact angle decreases, but as the dynamic liquid front reaches 'region 2', the contact angle stays constant as the plate is pulled up and the capillary rise height increases. The liquid front slides though the features, which are slightly coated by the same liquid (see Figure 3.26) and leaves a film as a trace on the sides of pyramid and in the valleys (see Figure 3.27). Liquid accumulation is larger in the valleys than on the sides of the pyramids, and on the peaks the film formation is very meager, due to which a pinning behavior is again observed. As soon as the liquid front reaches the apex of the pyramid, a jump occurs both in contact angle and rise height. The rise height of the liquid increases linearly as the plate is pulled upwards. The slope of the rise height in real time yields the plate velocity, as in the advancing case. When the liquid front is no longer pinned on the peak, the contact angle decreases abruptly until it reaches a minimum value in the valley where the liquid front touches the liquid tracer film and keeps its contact angle constant until it arrives at the apex of the next pyramid. Unlike the advancing case, here we do not observe the *apparent slipping motion* due to thin film formation by pulling the plate out of the liquid bath.

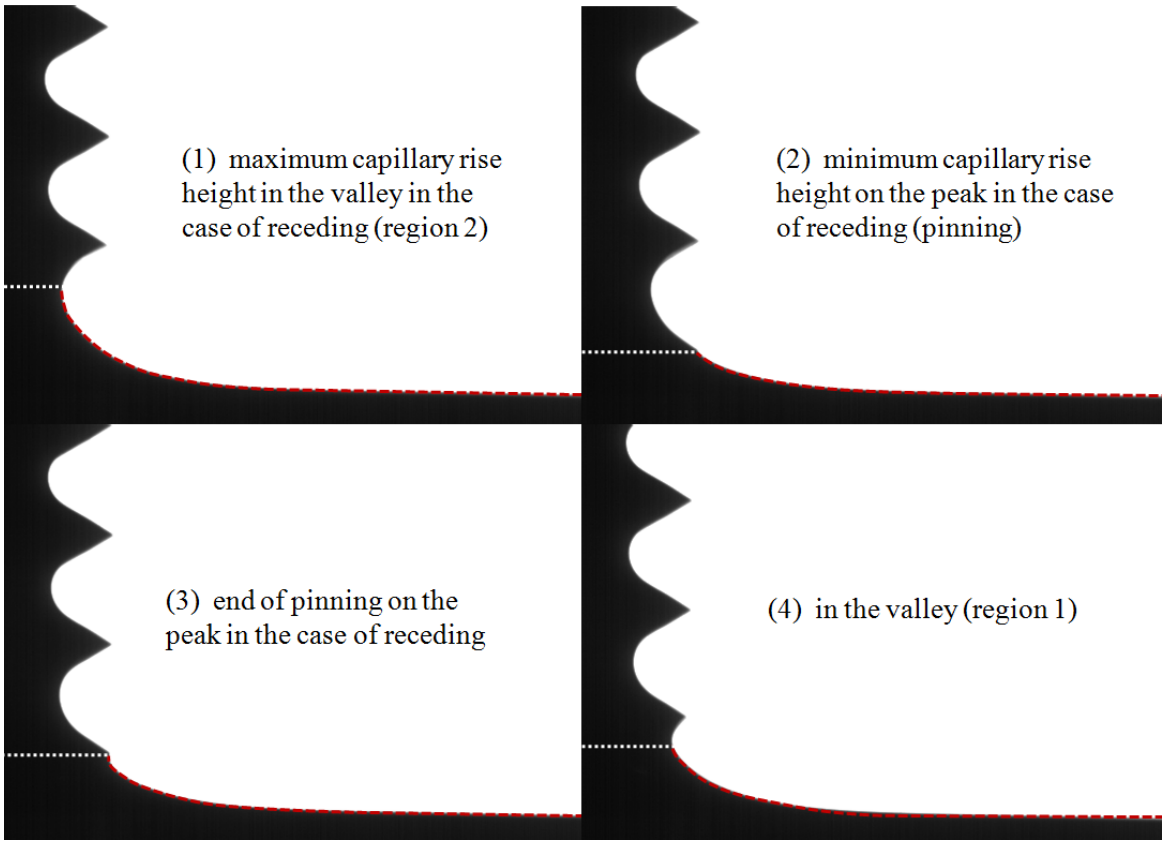

Figure 3.26: The maximum capillary rise height is measured in the center of the valley and the minimum rise height on the peak.

The period of the change in contact angle and rise height for the 2mm pyramidal array 2.39 sec, 3.18 sec, and 4.75 sec for plate velocities 0.848 mm/sec, 0.636 mm/sec, and 0.424 mm/sec, respectively. Due to the very thin film on the apex of the pyramids and faster sliding on the sides of coated pyramids, the pinning interval becomes shorter. The pinning duration increases as the plate velocity decreases.

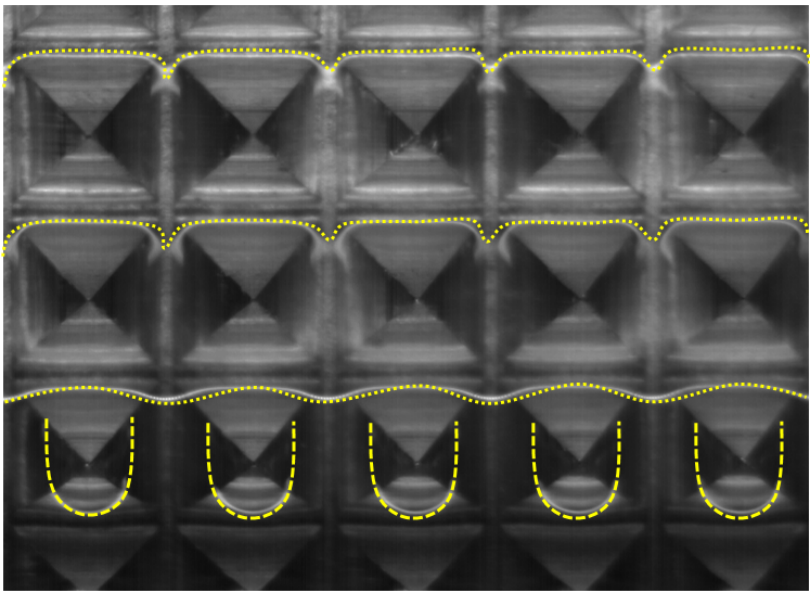

Figure 3.27: The front image of 2mm pyramidal array while receding with 0.848 mm/sec from 10cSt PDMS. The dashed curves show the dynamic liquid front. The dotted lines show the dripping liquid film, which is a gravity driven flow.

The real time pinning durations are 0.40 sec, 0.60 sec, and 0.82 sec respectively for 0.848 mm/sec, 0.636 mm/sec, and 0.424 mm/sec plate velocities. The average amplitude of the contact angle is 39.89±3.24° whereas the average amplitude of rise height is 1.15±0.02mm. The rise height amplitude is larger than in the advancing case and the contact angle amplitude is smaller. In the advancing case, the liquid uses capillary rise to crawl in the side paths but is also drawn downwards due to the gravity. In the receding case, the liquid uses capillary rise again to crawl in the side paths but is pulled upwards, against gravity.

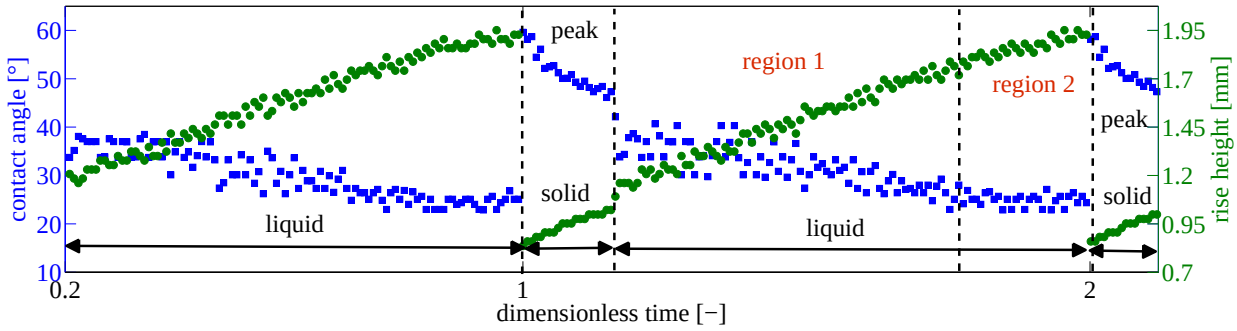

(a) 2mm pyramid, 0.8 mm/sec plate velocity, receding.

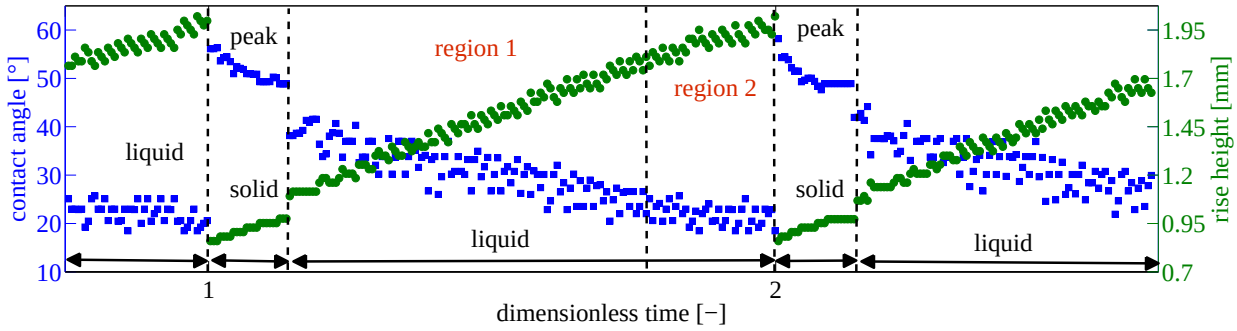

(b) 2mm pyramid, 0.6 mm/sec plate velocity, receding.

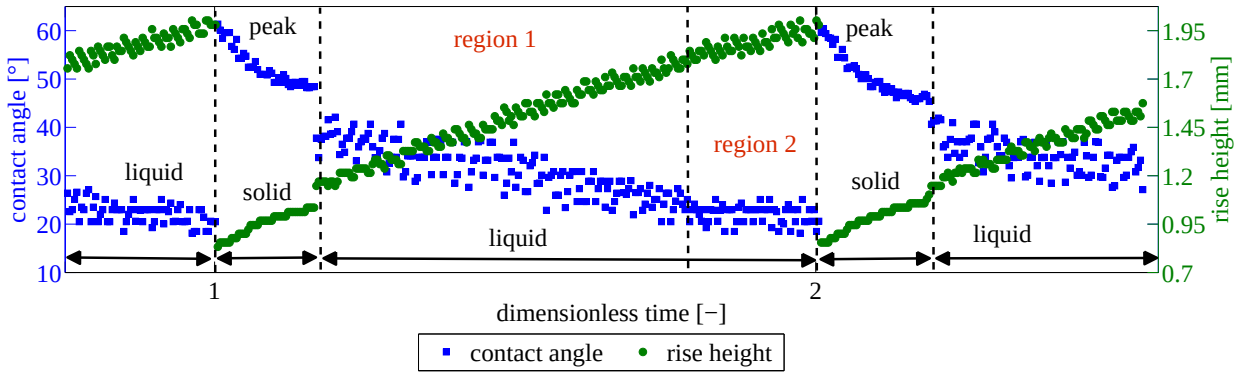

(c) 2mm pyramid, 0.4 mm/sec plate velocity, receding.

Figure 3.28: Comparison of contact angle and rise height versus dimensionless time for 10cSt PDMS for receding case and 2mm pyamids.

3.5.3.2 1mm Pyramidal Features

In the receding case for 1mm pyramidal structures, like in the case of 2mm pyramids, only two zones are observed, which are the pinning on the peaks and the liquid-liquid interface in the valleys. Aside from the liquid zone, two regions that need to be considered. In 'region 1', as the capillary rise height increases, the contact angle decreases respectively, but as the dynamic liquid front reaches 'region 2', the contact angle stays constant as the plate is pulled up and the capillary rise height increases. The liquid front slides though the features, which are slightly coated by the same liquid and leaves a film as a trace on the sides of pyramid and in the valleys. Liquid accumulation is larger in the valleys than on the sides of the pyramid, and on the peaks the film formation is very meager, a pinning behavior is again observed. As soon as the liquid front reaches the apex of the pyramid, a jump occurs both in contact angle and rise height. The rise height of the liquid increases linearly as the plate is pulled upwards. The inclination of the rise height in real time gives again the plate velocity. As the liquid front discards from pinning on the peak, the contact angle starts to decrease abruptly until it reaches

its minimum value in the valley where the liquid front touches the liquid tracer film and keeps its contact angle constant until it arrives to the apex of the pyramid.

The period of the change in contact angle and rise height for 1mm pyramidal array is in seconds 1.28 sec, 1.75 sec, 2.56 sec for plate velocities 0.848 mm/sec, 0.636 mm/sec, and 0.424 mm/sec, respectively. The real time pinning durations are 0.18 sec, 0.34 sec, 0.42 sec respectively for 0.848 mm/sec, 0.636 mm/sec, and 0.424 mm/sec plate velocities, respectively. The pinning duration increases as the plate velocity decreases but it is shorter than the 2mm pyramidal arrays. The reason for shorter periodicity is the shorter pinning interval due to the very thin film on the apex of the pyramids. The average amplitude of the contact angle is 22.54±1.27° and the average amplitude of rise height is 0.61±0.01mm.

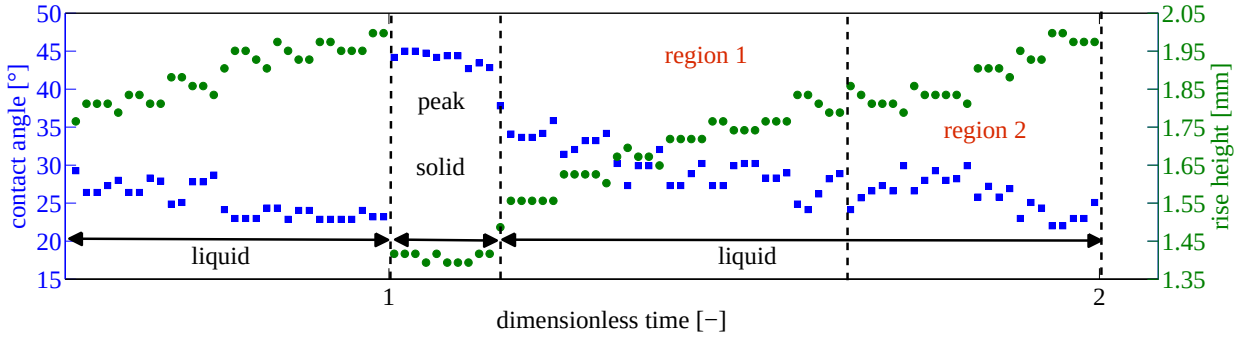

(a) 1mm pyramid, 0.8 mm/sec plate velocity, receding.

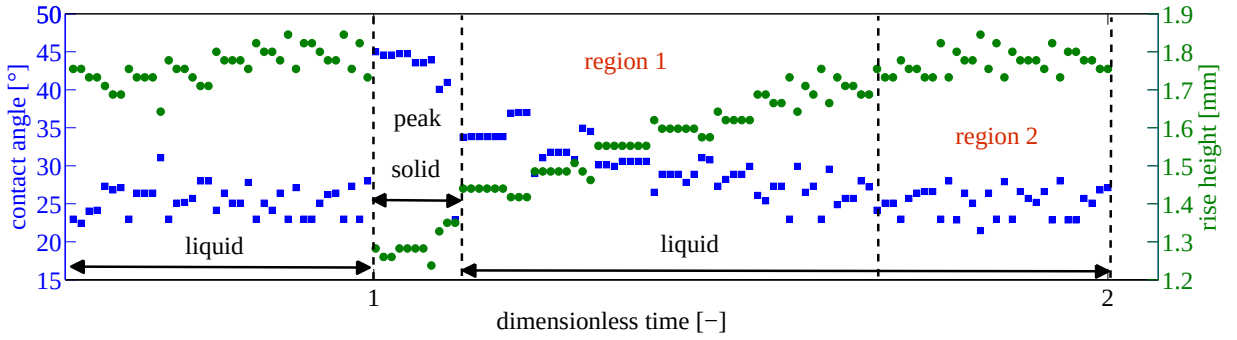

(b) 1mm pyramid, 0.6 mm/sec plate velocity, receding.

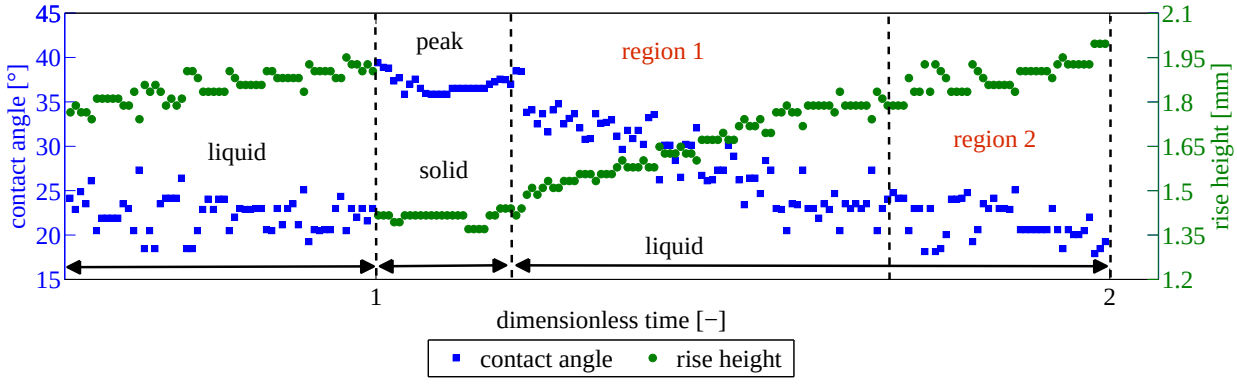

(c) 1mm pyramid, 0.4 mm/sec plate velocity, receding.

Figure 3.29: Comparison of contact angle and rise height versus dimensionless time for 10cSt PDMS for receding case and 1mm pyramids.

3.5.3.3 0.5mm Pyramidal Features

The overall behavior of contact angle and rise height change, compared to 2mm and 1mm pyramids, is the same. Here again there are two zones, solid and liquid, and moreover any different regions are not possible to observe in the liquid-liquid zone like in 2mm and 1mm pyramidal arrays. The liquid stays pinned on the apex of the pyramid only very shortly. The liquid trace in the valleys is thicker than for the 2mm and 1mm pyramids, and the liquid film build overall on the surface is thicker due to the hinderance of the liquid dripping though the rows and columns. The structured surface behaves like a film coated wall which causes a small change in the contact angle and rise height.

The period of the change in contact angle and rise height for 0.5mm pyramidal array is in seconds 0.71 sec, 0.99 sec, 1.45 sec for plate velocities 0.848 mm/sec, 0.636 mm/sec, and 0.424 mm/sec, respectively. The real time pinning durations are 0.14 sec, 0.22 sec, 0.38 sec for 0.848 mm/sec, 0.636 mm/sec, and 0.424 mm/sec plate velocities, respectively. The pinning duration increases as the plate velocity decreases. The reason for shorter periodicity is the shorter pinning interval due to the very thin film on the apex of the pyramids. The average amplitude of the contact angle is 16.03±0.99° and the average amplitude of rise height is 0.33±0.02mm.

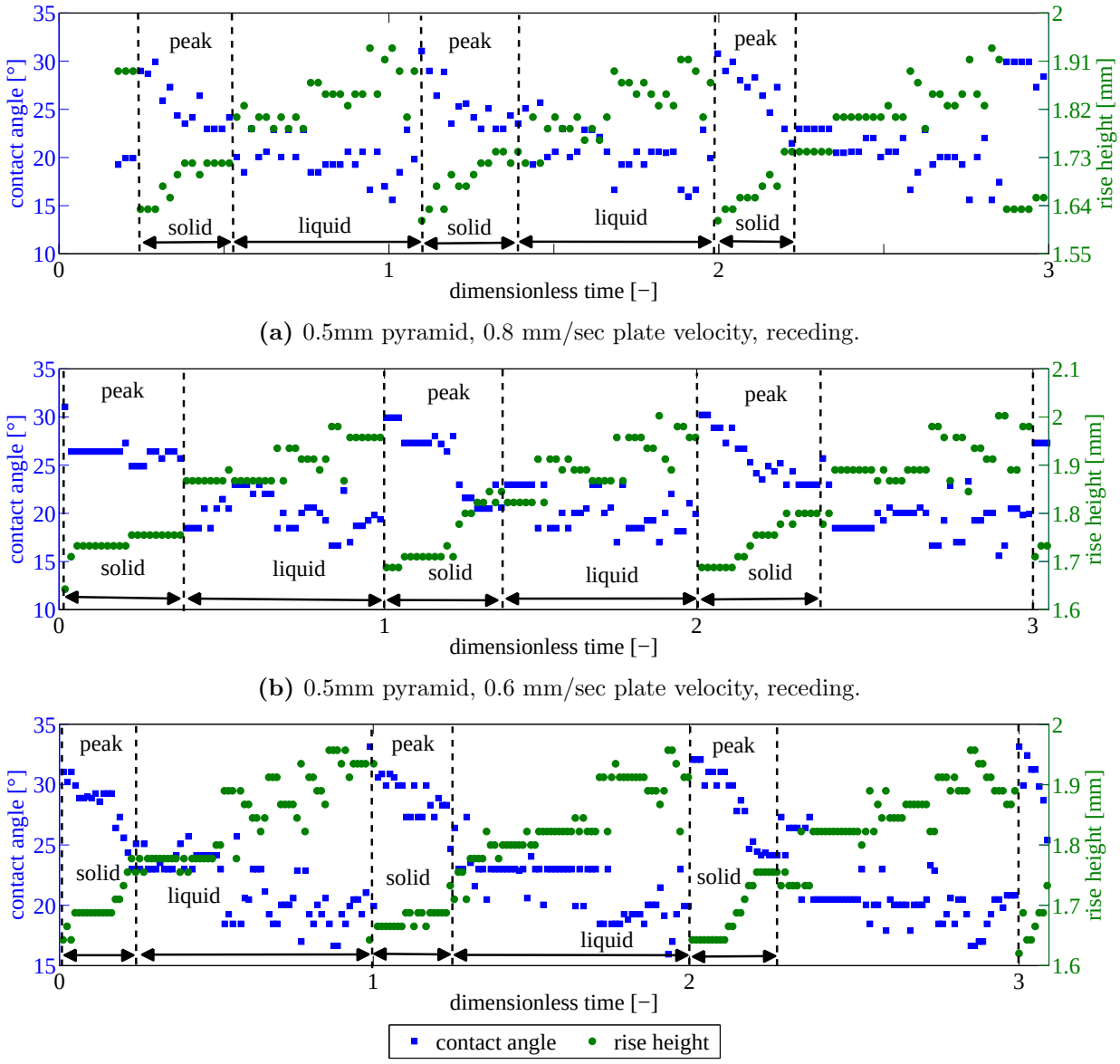

(a) 0.5mm pyramid, 0.8 mm/sec plate velocity, receding.

(b) 0.5mm pyramid, 0.6 mm/sec plate velocity, receding.

(c) 0.5mm pyramid, 0.4 mm/sec plate velocity, receding.

Figure 3.30: Comparison of contact angle and rise height versus dimensionless time for 10cSt PDMS for receding case and 0.5mm pyramids.

3.5.3.4 Comparison of Observations for Receding Contact Line

By changing the velocity and taking the feature size fixed, it is concluded that the velocity change does not drastically affect the amplitude of the contact angle and rise height for each structure. Each feature has the same period and very similar contact angle and rise height amplitudes for varying plate velocities. Figure 3.31 shows that the period for all plate velocities at fixed feature sizes have the same values. Table 3.4 comprises a comparison of the minimum and maximum values of the rise height and contact angle changes measured with the tangent method and compares the contact angle values derived from 2D Laplace fitting. In figure 3.32 the contact angle data measured by the tangent method are compared with the theoretical values provided by equation 3.7c. In contrast to the advancing case, the data originating from the tangent method and those calculated from equation 3.7c show a large deviation up to 10°, but the slopes are parallel to each other.

Receding of a Wetted Surface - Amplitudes (10cSt PDMS)

pyramid type and plate velocity	max. rise height [mm]	min. rise height [mm]	2D Laplace derivation		tangent method	
			max. contact angle [°]	min. contact angle [°]	max. contact angle [°]	min. contact angle [°]
2 mm - 0.8 mm/sec	1.95	0.83	57.43	7.58	59.6	22.87
2 mm - 0.6 mm/sec	2.02	0.85	56.62	3.93	58.2	18.47
2 mm - 0.4 mm/sec	2.00	0.83	57.43	4.98	61.35	18.13
average difference	Δ=1.15±0.02		Δ=51.66±1.21		Δ=39.89±3.24	
1 mm - 0.8 mm/sec	1.99	1.39	33.98	5.51	45	22.01
1 mm - 0.6 mm/sec	1.84	1.23	40.89	13.13	45	21.47
1 mm - 0.4 mm/sec	1.99	1.37	34.85	5.51	39	17.90
average difference	Δ=0.61±0.01		Δ=28.52±0.54		Δ=22.54±1.27	
0.5 mm - 0.8 mm/sec	1.93	1.61	24.09	8.61	31.05	15.59
0.5 mm - 0.6 mm/sec	2.00	1.64	22.70	4.98	31.05	15.59
0.5 mm - 0.4 mm/sec	1.95	1.62	23.63	7.58	33.13	15.59
average difference	Δ=0.33±0.02		Δ=16.42±0.86		Δ=16.03±0.99	

Table 3.4: The amplitudes of rise height and contact angle for 3 pyramidal arrays in three different speeds in the receding case.

Receding of a Wetted Surface - Periods (10cSt PDMS)

pyramid type and plate velocity	full period [sec]	pinning time [sec]
2 mm - 0.8 mm/sec	2.39	0.40
2 mm - 0.6 mm/sec	3.18	0.60
2 mm - 0.4 mm/sec	4.75	0.82
1 mm - 0.8 mm/sec	1.28	0.18
1 mm - 0.6 mm/sec	1.75	0.34
1 mm - 0.4 mm/sec	2.56	0.42
0.5 mm - 0.8 mm/sec	0.71	0.14
0.5 mm - 0.6 mm/sec	0.99	0.22
0.5 mm - 0.4 mm/sec	1.45	0.38

Table 3.5: The real time periods and pinning time durations for all feature sizes at all plate velocities.

All features have similar maximum capillary rise height independent of the feature size and plate velocity. The maximum capillary rise height is measured in the valley slightly above the midpoint (see Figure 3.26). On the other hand, larger features have low capillary rise height values, because as soon as the dynamic liquid front touches the peak, a jump occurs in the rise height. The maximum contact

angle is then measured at the lowest rise height value and the minimum contact angle at the highest rise height.

Table 3.4 shows the comparison between the contact angles measured by the tangent method and those derived from the 2D Laplace equation. The minimum contact angle related to the maximum capillary rise height at the liquid-liquid interface should have been zero degrees as the dynamic liquid front wets itself but none of the contact angle measurement methods show the correct value. In order to conclude a zero angle according to the 2D Laplace derivation, the capillary rise height should be $\sim$2.093mm, which is not reached here.

When we concentrate on the pinning time for each feature size and each plate velocity, we observe that the pinning duration increases gradually as the plate velocity decreases. Table 3.5 shows the values of full periods and pinning durations in seconds. From these values, it can be concluded that the plate velocity and the feature size affect the pinning duration. The large pyramids advancing with a low plate velocity have the longest pinning duration.

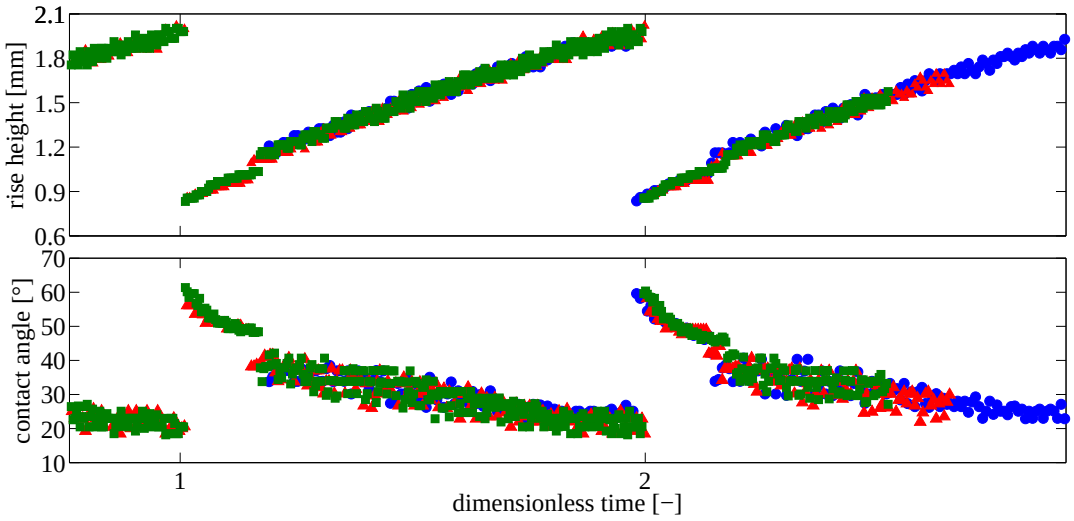

(a) 2mm pyramid, comparison of rise height and contact angle, receding.

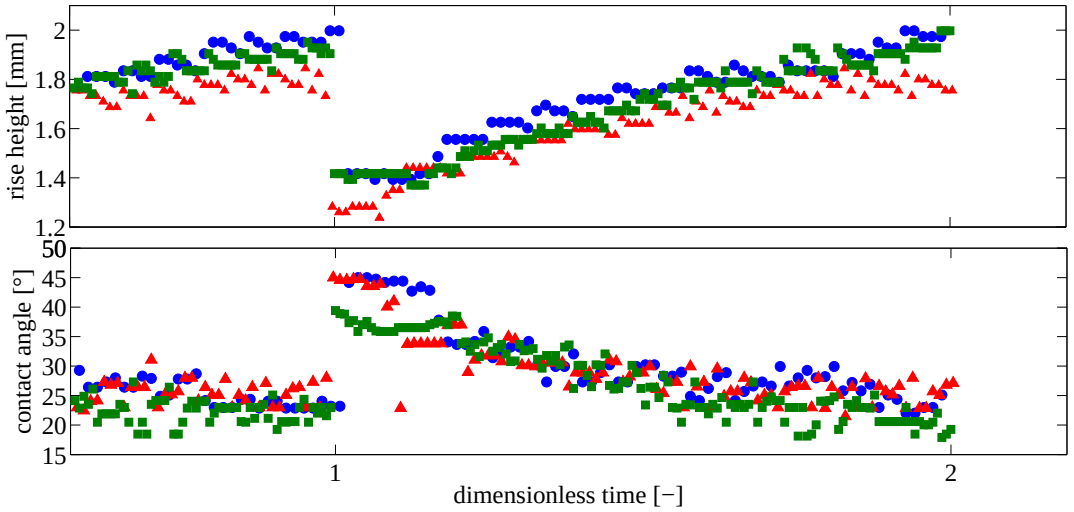

(b) 1mm pyramid, comparison of rise height and contact angle, receding.

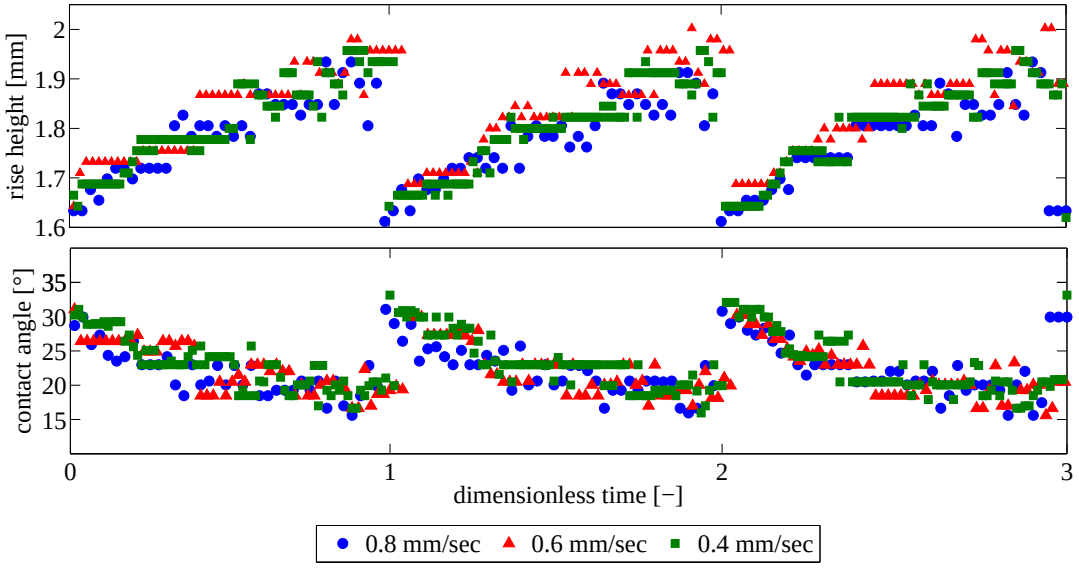

(c) 0.5mm pyramid, comparison of rise height and contact angle, receding.

Figure 3.31: Feature size dependent comparison of contact angle and rise height versus dimensionless time for 10cSt PDMS for receding case.

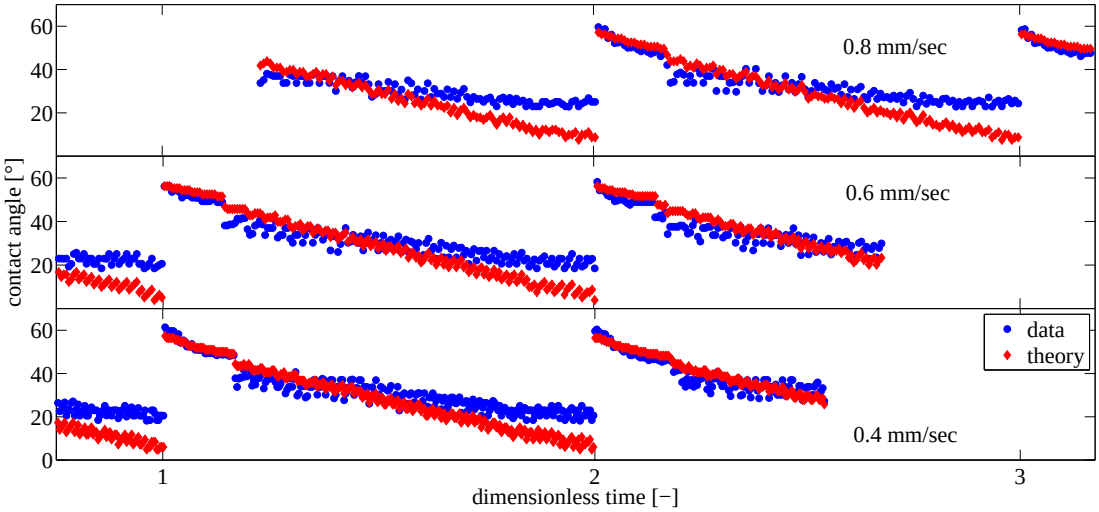

(a) 2mm pyramids, receding.

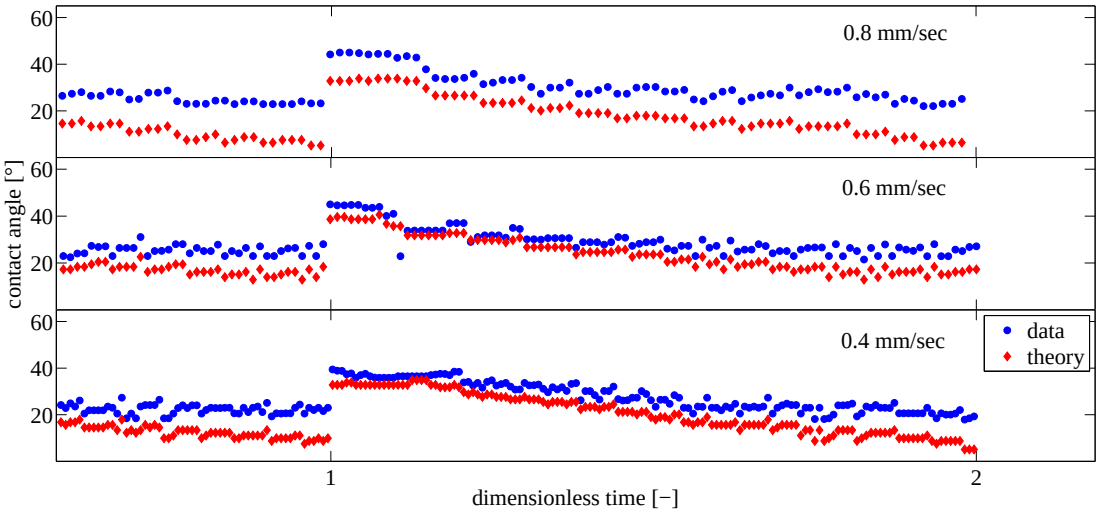

(b) 1mm pyramids, receding.

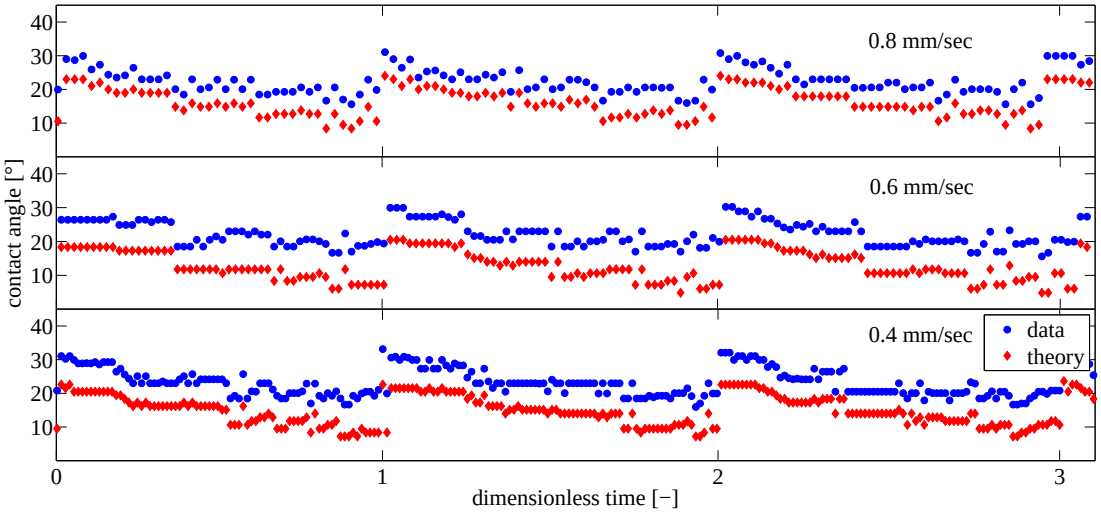

(c) 0.5mm pyramids, receding.

Figure 3.32: Comparison of measured contact angle by the tangent method (labeled as data) and 2D Laplace derivation (labeled as theory) using equation 3.7c.

3.5.4 Dynamic Advance On Dry 3D Pyramidal Arrays (100cSt PDMS)

In order to distinguish the effect of viscosity on the observed wetting formation, the experiments were repeated with a PDMS ten times more viscous than before, but with the same surface tension and density. In this subsection, the wetting evolution on three features with the previously defined maximum and minimum plates velocities will be presented.

3.5.4.1 2mm Pyramidal Features

As in the case of 10cSt PDMS wetting 2mm pyramidal arrays, here we see the four zones of wetting, including the *apparent slip motion*. In 'zone 4', as the plate is pushed downwards at 0.8 mm/sec, due to its high viscosity, the liquid wets the upper side of the pyramid very slowly and coats it with a thin film, which is why the measured contact angle in 'zone 4' is the slope of the pyramidal structure. This effect is the combined result of plate velocity and viscosity, and is not observed when the plate advances at 0.4 mm/sec into the liquid bath. There, the liquid finds enough time to wet and fill the upper side of the pyramidal structure.

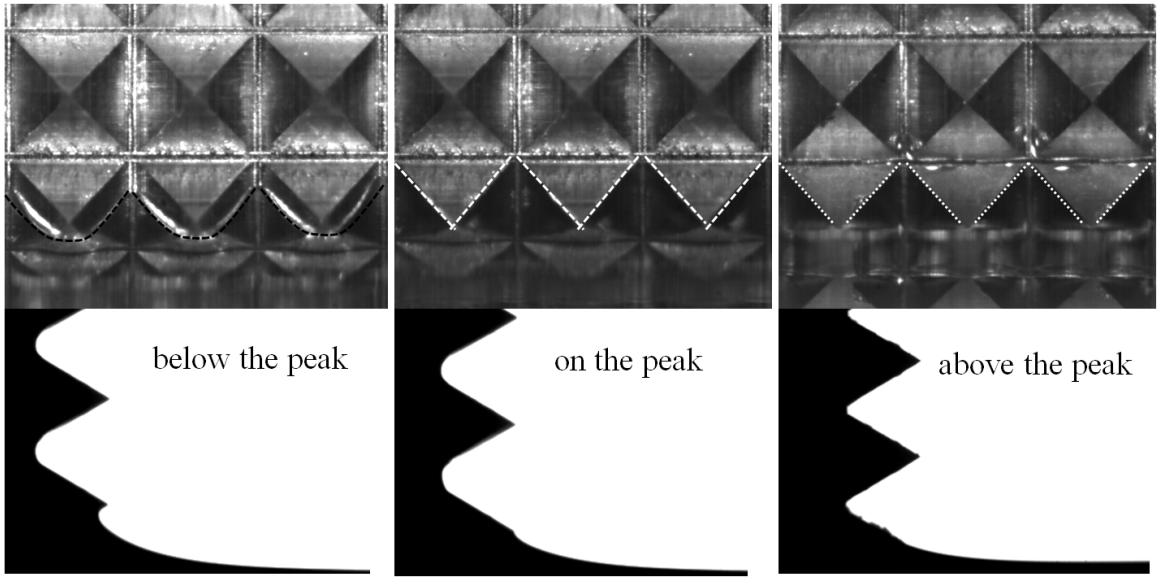

Figure 3.33: The front images of 2mm pyramids advancing into 100cSt PDMS with 0.8 mm/sec plate velocity.

If we take the *apparent slip motion* in consideration, we see something strange. Both for 0.8 mm/sec and 0.4 mm/sec plate velocities, the contact angle does not stay constant as the liquid slips on the solid, but decreases. So here the contact line boundary condition does not change into a fixed contact angle condition like in the case of 10cSt PDMS. Furthermore, the transition between 'zone 1' and 'zone 2' is not sharp like in the less viscous version. The apparent slip velocity in the lab frame is 2.87 mm/sec for 0.848 mm/sec plate velocity and, 1.92 mm/sec for 0.424 mm/sec plate velocity. The lab frame velocity of apparent slip is 3.38 times larger than the 0.848 mm/sec plate velocity, and 4.52 times larger than the 0.424 mm/sec plate velocity. In the case of 10cSt, the slip velocity has a constant proportion for all plate velocities.

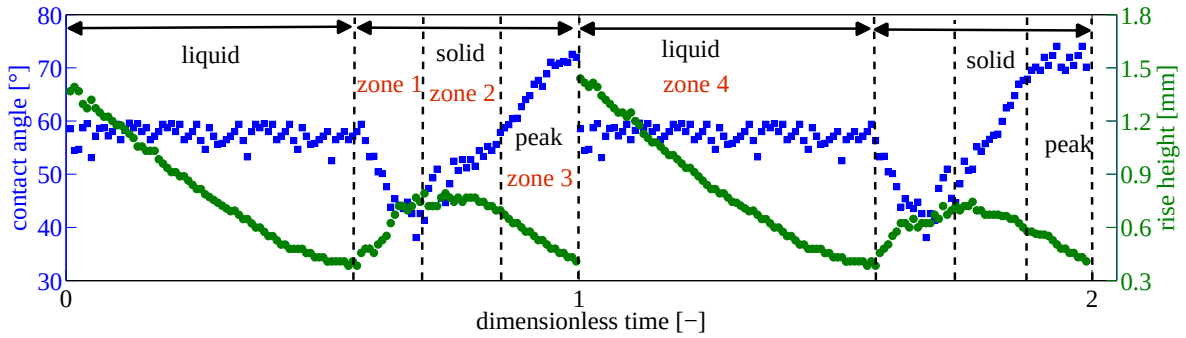

(a) 2mm pyramids, 0.8 mm/sec plate velocity, advancing.

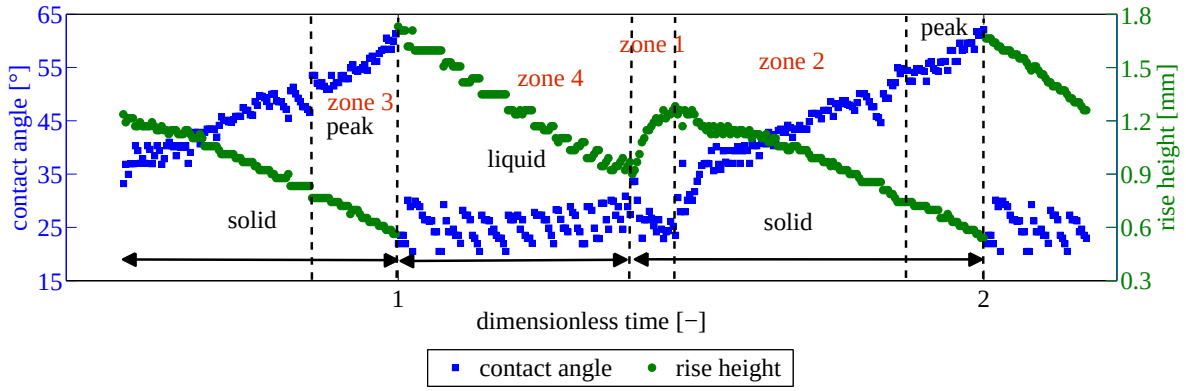

(b) 2mm pyramids, 0.4 mm/sec plate velocity, advancing.

Figure 3.34: Contact angle and rise height versus dimensionless time for 100cSt PDMS and 2mm pyramids.

The period of the change in contact angle and rise height for 2mm pyramidal array is 2.37 sec and 4.75 sec for plate velocities respectively of 0.848 mm/sec and 0.424 mm/sec. The changes in capillary height and contact angle, are 1.192mm and 33° for a 0.4 mm/sec plate velocity, respectively, while at 0.8 mm/sec they are 1.056mm and 41.5°. These values are not equal for the different plate velocities as in the case of 10cSt. This shows us that the plate velocity in this range ($0.4\text{mm/sec} \leq v_{plate} \leq 0.85\text{mm/sec}$) affects the period and amplitude of the contact angle and rise height change for high viscosity liquids. The pinning time in seconds increases gradually as the plate velocity decreases. The pinning durations are 0.19 sec and 0.79 sec for plate velocities of 0.848 mm/sec and 0.424 mm/sec, respectively.

As seen in figure 3.33, the liquid front does not just get pinned at the apex of the pyramid but also on the edges, where this does not hinder the capillary rise of the liquid through the side paths.

3.5.4.2 1mm Pyramidal Features

In the case of 1mm pyramidal structures, due to the smaller depth and height values with respect to the capillary length, the slipping behavior ('zone 1' in Figure 3.34) does not appear. The smaller scale of the pyramidal structures and the narrower side paths between the pyramids cause a faster capillary crawl for the liquid on the surface in spite of the ten times higher viscosity value. This affects the character of the zones, with 'zone 1' and 'zone 4' merging into 'zone 4', while the duration of 'zone 4' becomes much shorter than the sum of the two zones, which means that the dynamic liquid front has a shorter contact with the liquid film in the pre-filled valley compared to the 2mm pyramids, and touches the solid surface right after. In 'zone 4', the contact angle and the rise height of the fluid front stay almost constant due to the liquid-liquid interface. This means that, even though the plate pushes the pyramids (and hence the liquid) downwards, the meniscus does not change its shape. Like in the previous subsection, the slope of 'zone 3' (pinning region) gives the exact plate velocity.

The period of the change in contact angle and rise height for 1mm pyramidal array is 1.38 sec and 2.8 sec for plate velocities of 0.848 mm/sec and 0.424 mm/sec, respectively. The capillary rise height change for 0.8 mm/sec is 0.574mm and 0.4 mm/sec plate velocity is 0.332mm and the contact angle change is for 0.8 mm/sec plate velocity is 27.8° and for 0.4 mm/sec plate velocity is 18.1°. The pinning time in seconds increases gradually as the plate velocity decreases. The pinning durations are, 0.47 sec and 0.69 sec for 0.848 mm/sec and 0.424 mm/sec plate velocities, respectively.

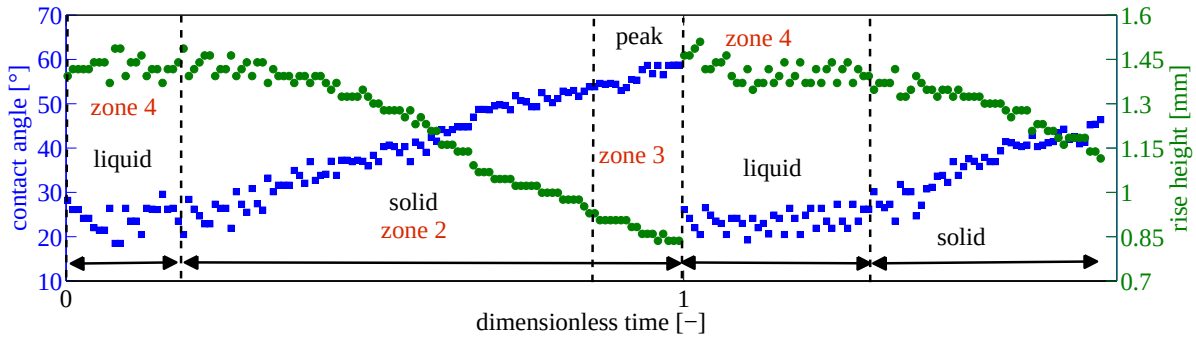

(a) 1mm pyramids, 0.8 mm/sec plate velocity, advancing.

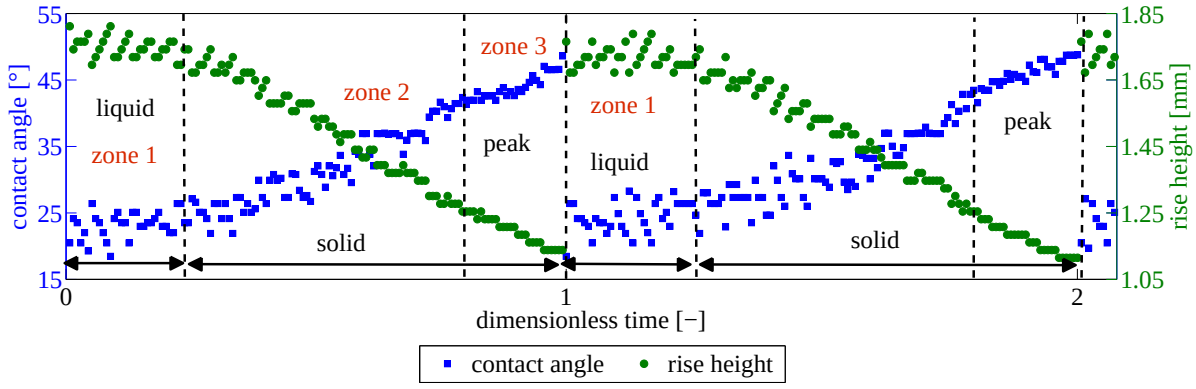

(b) 1mm pyramids, 0.4 mm/sec plate velocity, advancing.

Figure 3.35: Contact angle and rise height versus dimensionless time for 100cSt PDMS and 1mm pyramids.

3.5.4.3 0.5mm Pyramidal Features

As in the 10cSt PDMS case, as the structure dimensions get smaller, the gradual wetting phenomenon described in previous subsections becomes difficult to observe and moreover some specific formations disappear, e.g. the number of wetting zones becomes less. Here 'zone 1' and 'zone 2' disappear completely. Due to the scale size of the pyramids, the slip motion is impossible to take place. Furthermore, 'zone 2', the region where the liquid front meets the solid surface after the liquid-liquid interface, merges with 'zone 4', because of the narrow valley width.

The period of the change in contact angle and rise height for 0.5mm pyramidal array is 0.78 sec and 1.48 sec for plate velocities 0.848 mm/sec and 0.424 mm/sec, respectively. The capillary rise height change for 0.8 mm/sec and 0.4 mm/sec plate velocity is 0.627mm and the contact angle change is for 0.8 mm/sec plate velocity is 38.2° and for 0.4 mm/sec plate velocity is 30.2°. The pinning time in seconds increases gradually as the plate velocity decreases. The pinning durations are, 0.25 sec, 0.39 sec for 0.848 mm/sec and 0.424 mm/sec plate velocities, respectively.

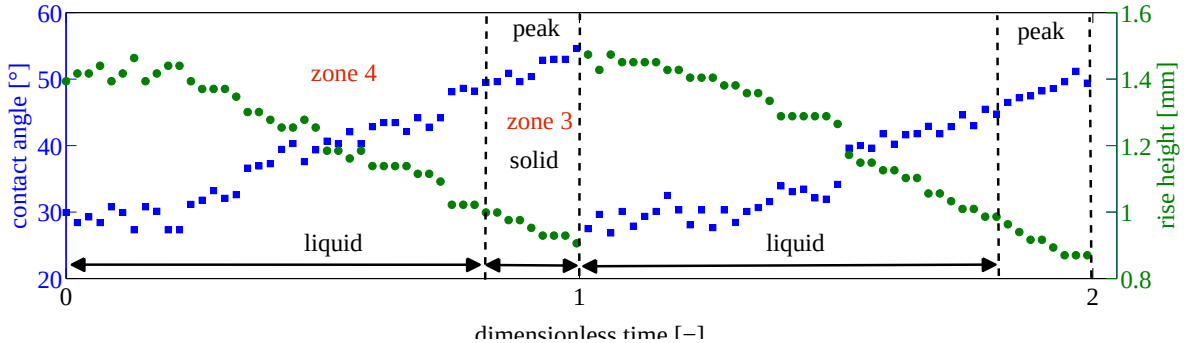

(a) 0.5mm pyramids, 0.8 mm/sec plate velocity, advancing.

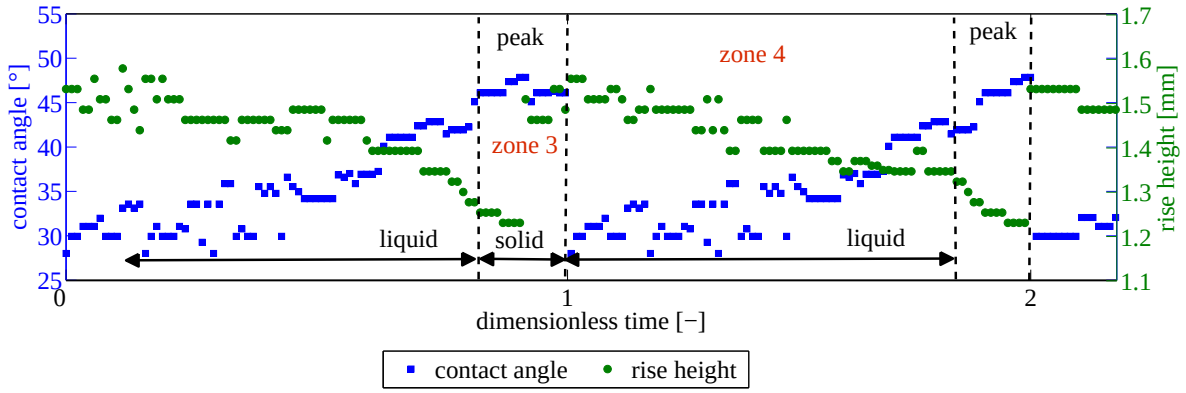

(b) 0.5mm pyramids, 0.4 mm/sec plate velocity, advancing.

Figure 3.36: Contact angle and rise height versus dimensionless time for 100cSt PDMS and 0.5mm pyramids.

3.5.4.4 Comparison All Observation for Advancing Contact line

In figure 3.37 we realize that, as in the 10cSt PDMS case, a higher plate velocity causes a lower capillary rise height and a lower *apparent slip motion* formation. Besides, the contact angle change is similar for 1mm and 0.5mm pyramidal features but due to the combined effect of viscosity and plate velocity, there is a distinguishable difference between the two plate velocities in terms of contact angle change for the 2mm pyramidal array.

Table 3.6 shows the comparison of the minimum and maximum values of rise height and contact angle change measured by the tangent method and compares the contact angle values derived from 2D Laplace fitting. In figure 3.38 the contact angle data measured by the tangent method is compared with the theoretical values provided by equation 3.7c. Like in previous cases, here again there is a disparity between the measured and interpreted contact angles at the liquid-liquid interface. Moreover in the case of 2mm pyramids, only in the pinning region where a solid-liquid interface exists, there is a good agreement between the two contact angles, but in the *apparent slip* region and 'zone 2', there is only a parallelism, not a complete agreement. Table 3.7 presents the real time periods, and real time pinning durations, which will be covered in the discussion subsection in more detail.

Advancing on a Dry Surface - Amplitudes (100cSt PDMS)

pyramid type and plate velocity	max. rise height [mm]	min. rise height [mm]	2D Laplace derivation		tangent method	
			max. contact angle [°]	min. contact angle [°]	max. contact angle [°]	min. contact angle [°]
2 mm - 0.8 mm/sec	1.44	0.38	75.2	31.7	71.9	38.1
2 mm - 0.4 mm/sec	1.73	0.54	68.9	18.5	61.3	20.5
1 mm - 0.8 mm/sec	1.46	0.83	57.4	30.9	58.7	20.5
1 mm - 0.4 mm/sec	1.76	1.13	45.1	17	48.6	18.5
0.5 mm - 0.8 mm/sec	1.47	0.90	54.6	30.4	54.6	26.8
0.5 mm - 0.4 mm/sec	1.55	1.23	40.9	26.8	46.1	28.0

Table 3.6: The comparison between maximum and minimum values of rising height and contact angle for three pyramidal arrays at three different speeds in the advancing case.

Advancing on a Dry Surface - Periods (100cSt PDMS)

pyramid type and plate velocity	full period [sec]	pinning time [sec]
2 mm - 0.8 mm/sec	2.37	0.33
2 mm - 0.4 mm/sec	4.75	0.95
1 mm - 0.8 mm/sec	1.38	0.47
1 mm - 0.4 mm/sec	2.80	0.69
0.5 mm - 0.8 mm/sec	0.78	0.25
0.5 mm - 0.4 mm/sec	1.48	0.39

Table 3.7: The real time periods and pinning time durations for all feature sizes and plate velocities.

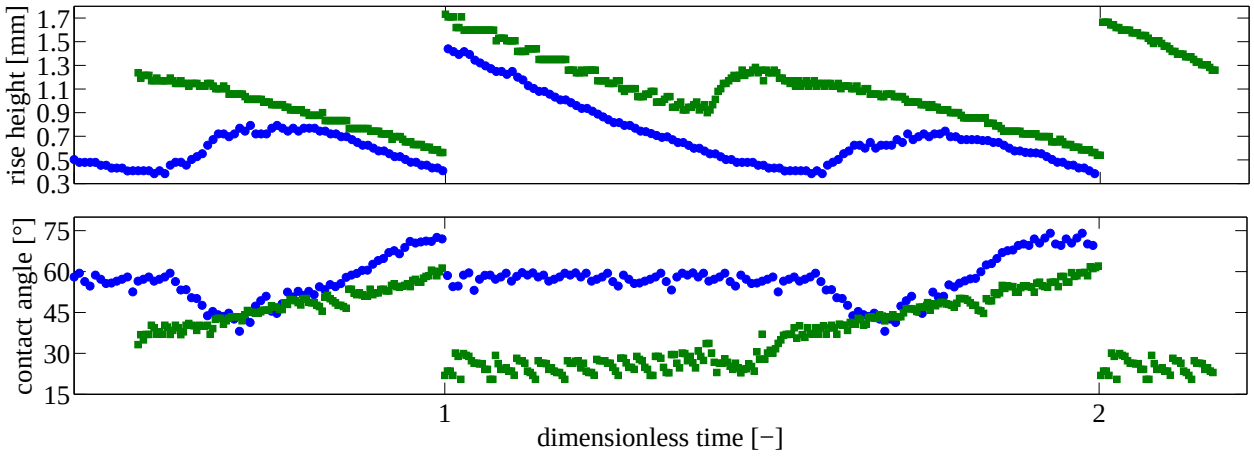

(a) 2mm pyramid, comparison of rise height and contact angle, advancing.

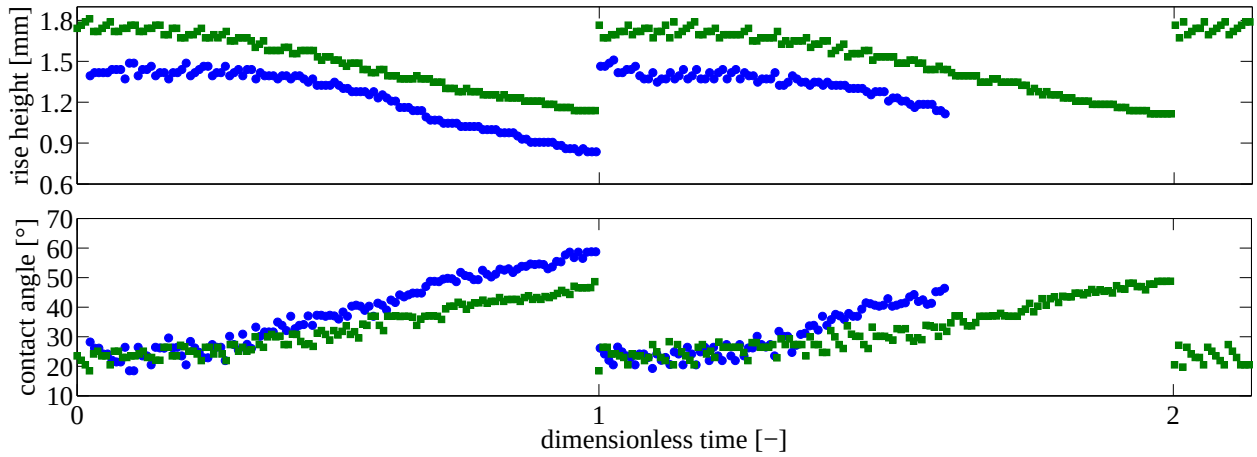

(b) 1mm pyramid, comparison of rise height and contact angle, advancing.

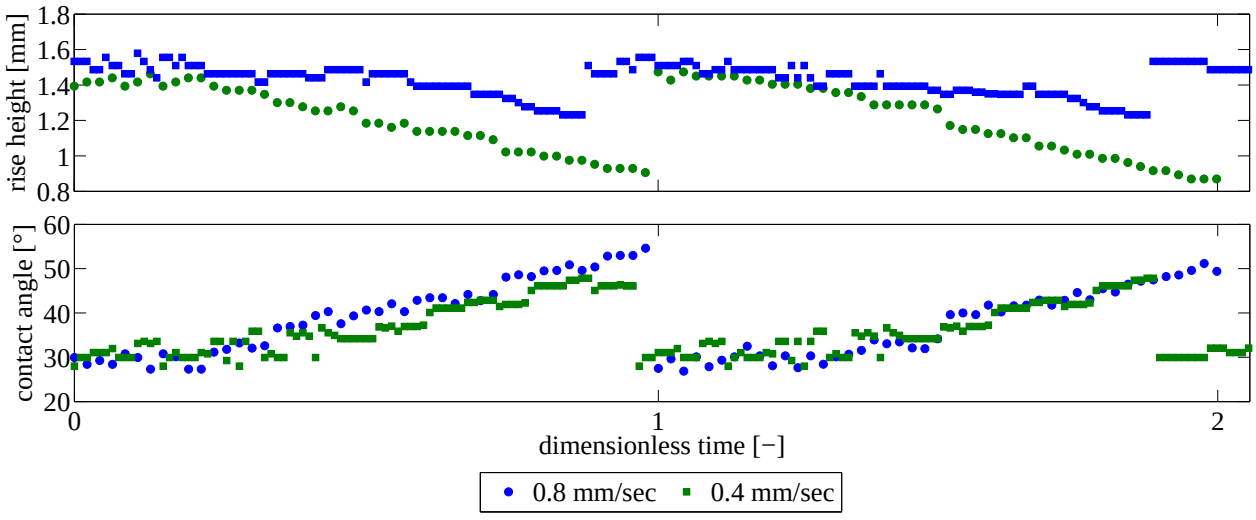

(c) 0.5mm pyramid, comparison of rise height and contact angle, advancing.

Figure 3.37: Feature size dependent comparison of contact angle and rise height versus dimensionless time for 100cSt PDMS for the advancing case.

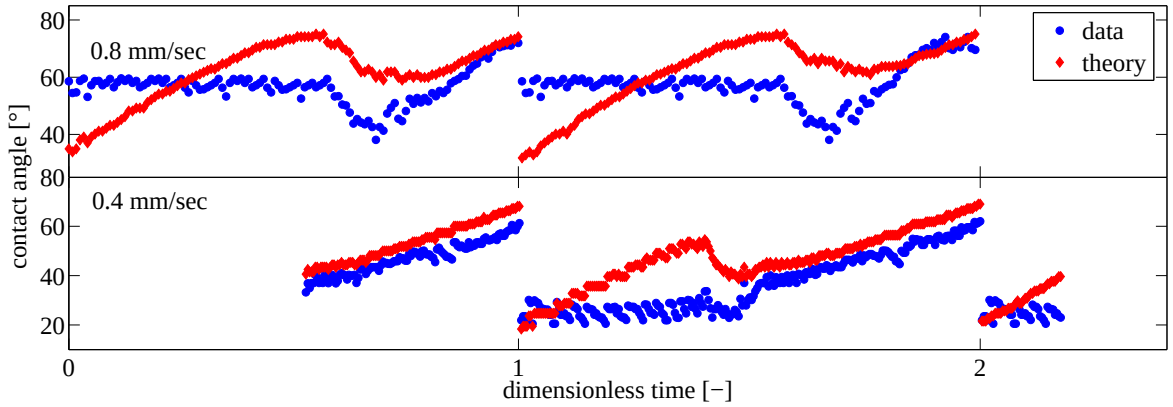

(a) 2mm pyramids, advancing.

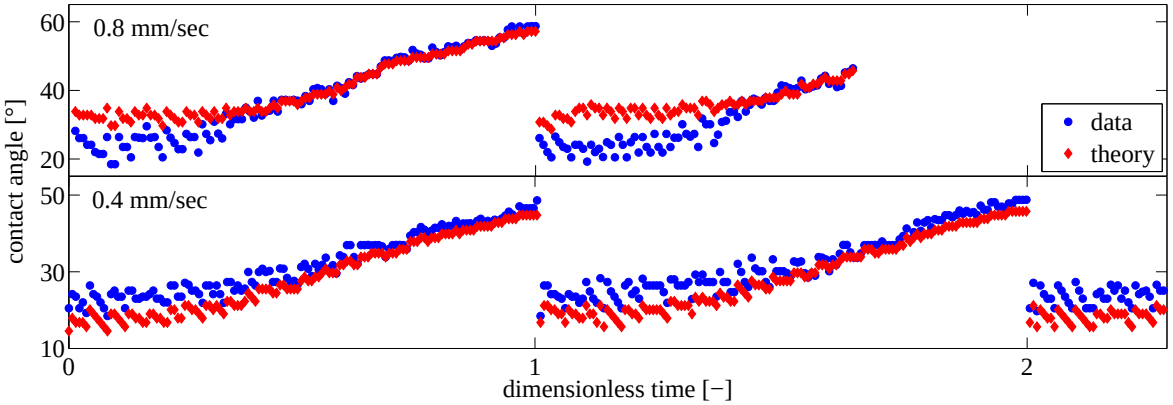

(b) 1mm pyramids, advancing.

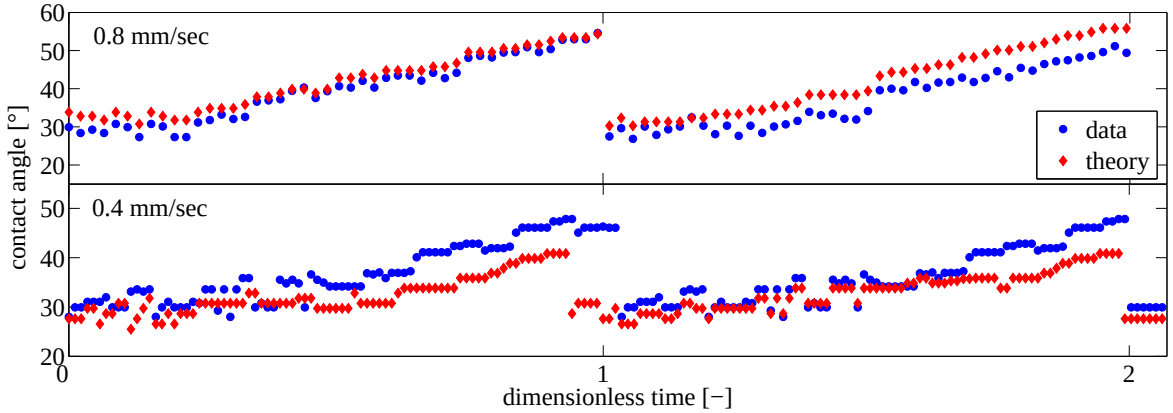

(c) 0.5mm pyramids, advancing.

Figure 3.38: Comparison of measured contact angle by the tangent method (tagged as data) and 2D Laplace derivation (tagged as theory) provided by equation 3.7c.

3.5.5 Receding of Wetted 3D Pyramidal Arrays (100cSt PDMS)

In this section, the receding case of wetting on three pyramidal arrays will be covered. The pyramidal arrays are pulled up from liquid 100cSt PDMS bath at three different speeds and the wetting evolution on them are observed. In the following plots, each pyramidal feature will be examined individually.

3.5.5.1 2mm Pyramidal Features

The dewetting formation on 2mm pyramids for 100cSt PDMS shows an exact similarity with receding from the 10cSt PDMS. Here again, only two zones are observed, which are the pinning on the peaks and the liquid-liquid interface in the valleys. Besides in the liquid zone, two additional regions need to be considered. In 'region 1', as the capillary rise height increases, the contact angle decreases respectively, but as the dynamic liquid front reaches 'region 2', the contact angle stays constant as the plate is pulled up and the capillary rise height increases. As soon as the liquid front reaches the apex of the pyramid, a jump occurs in both contact angle and rise height. The rise height of the liquid increases linearly as the plate is pulled upwards. The inclination of the rise height in real time gives again the plate velocity as it does for the advancing case. As the liquid front breaks away from pinning on the peak, the contact angle starts to decrease abruptly until it reaches its minimum value in the valley where the liquid front touches the liquid tracer film and maintains its contact angle until it arrives the apex of the pyramid. In contrast to the advancing case, here we do not observe the apparent slipping motion due to thin film formation by pulling the plate out of the liquid bath.

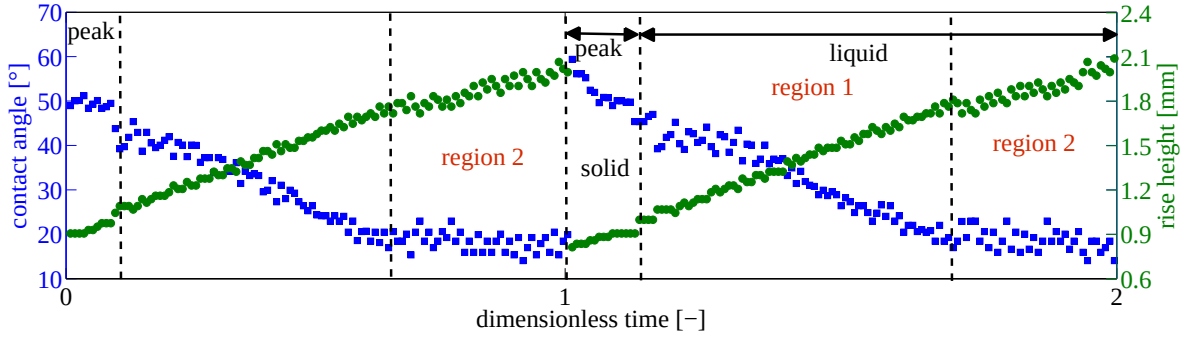

(a) 2mm pyramids, 0.8 mm/sec plate velocity, receding.

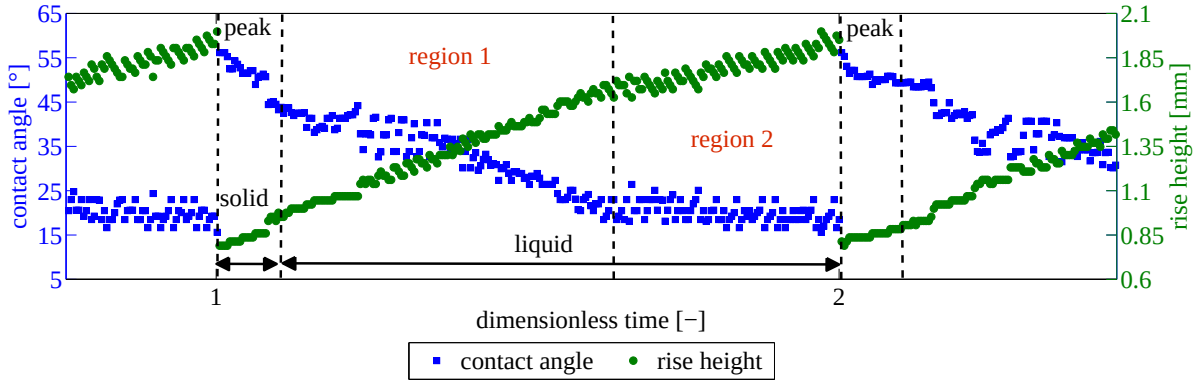

(b) 2mm pyramid, 0.4 mm/sec plate velocity, receding.

Figure 3.39: Comparison of contact angle and rise height versus dimensionless time for 100cSt PDMS for receding case and 2mm pyramids.

The period of the change in contact angle and rise height for 2mm pyramidal array is 2.37 sec and 4.77 sec for 0.848 mm/sec and 0.424 mm/sec plate velocities, respectively. The pinning duration increases as the plate velocity decreases. The real time pinning durations are 0.37 sec, 0.95 sec for 0.848 mm/sec and 0.424 mm/sec plate velocities, respectively. The contact angle change for 0.848 mm/sec plate velocity is 45.4° and for 0.424 mm/sec plate velocity is 40.5°. The capillary rise height change for 0.848 mm/sec plate velocity is 1.28mm and for 0.424 mm/sec plate velocity is 1.21mm. Table 3.8 shows that the maximum capillary rise height is the same as in the case of 10cSt PDMS.

In the advancing case, the liquid uses the capillary rise but is pushed downwards in the direction of gravity. In the receding case, liquid uses the capillary rise and moreover pulled upwards, opposite to gravity.

3.5.5.2 1mm Pyramidal Features

In the receding case for 1mm pyramidal structures, like in the case of 2mm pyramids, only two zones are observed, which are the pinning on the peaks and the liquid-liquid interface in the valleys. Besides in the liquid zone, there are two regions need to be considered. In 'region 1', as the capillary rise height increases, the contact angle decreases respectively, but as the dynamic liquid front reaches 'region 2', the contact angle stays constant as the plate is pulled up and the capillary rise height increases.

The period of the change in contact angle and rise height for 1mm pyramidal array is 1.3 sec and 2.6 sec for plate velocities 0.848 mm/sec and 0.424 mm/sec, respectively. The real time pinning durations are 0.27 sec and 0.41 sec for 0.848 mm/sec and 0.424 mm/sec plate velocities, respectively . The contact angle difference is 24.7° and 29.1°, and the capillary rise height difference is 0.35mm and 0.51mm 0.848 mm/sec and 0.424 mm/sec plate velocities, respectively.

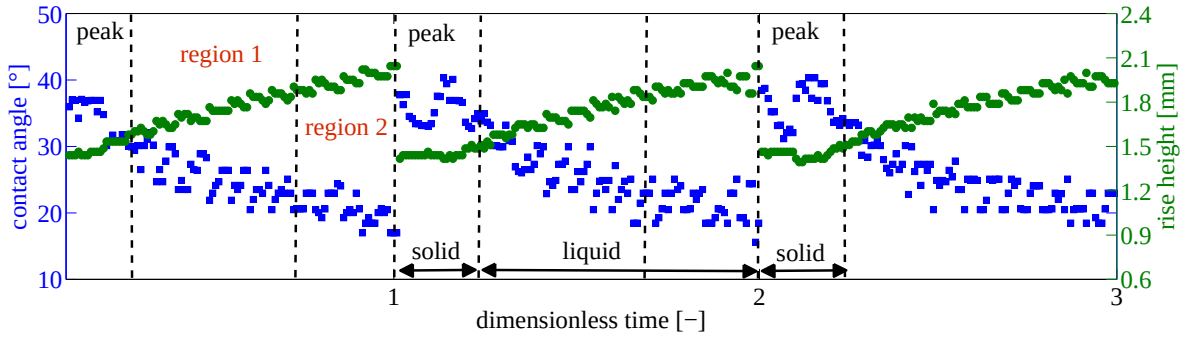

(a) 1mm pyramids, 0.8 mm/sec plate velocity, receding.

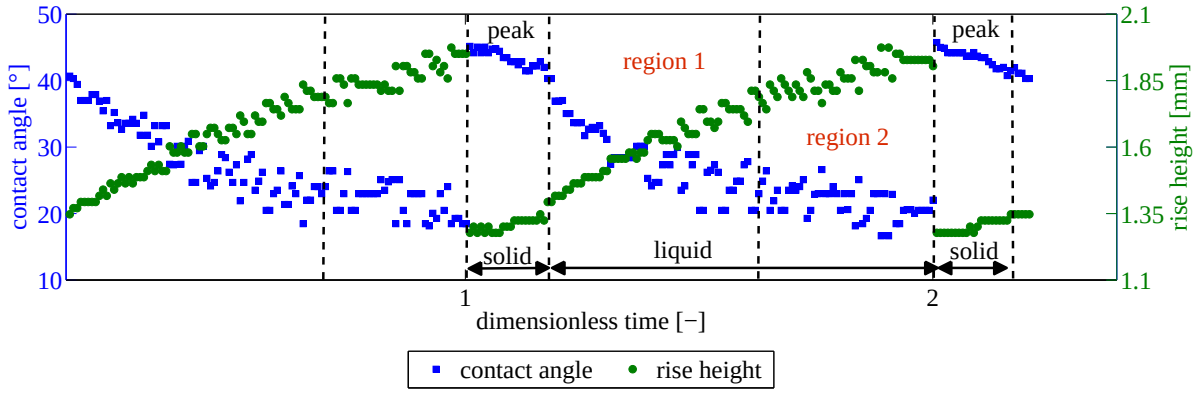

(b) 1mm pyramids, 0.4 mm/sec plate velocity, receding.

Figure 3.40: Comparison of contact angle and rise height versus dimensionless time for 100cSt PDMS for receding case and 1mm pyramids.

3.5.5.3 0.5mm Pyramidal Features

The overall behavior of contact angle and rise height change is the same for 0.5mm pyramids as 2mm and 1mm pyramids. Here again there are two zones, solid and liquid, and moreover a region difference in the liquid-liquid zone is not observed, unlike the case of 2mm and 1mm pyramidal arrays. The liquid stays pinned on the apex of the pyramid very very shortly. The liquid trace in the valleys is more than the previous features and the overall liquid film build on the surface is thicker due to the hindrance of the liquid dripping through the rows and columns. This makes the contact angle and rise height amplitudes very small.

The period of the change in contact angle and rise height for 0.5mm pyramidal array is 0.72 sec and 1.46 sec for plate velocities respectively 0.848 and 0.424 mm/sec. The real time pinning durations are 0.13 sec and 0.31 sec for 0.848 mm/sec and 0.424 mm/sec plate velocities, respectively. The contact angle change is 15.5° and 22.6° and the capillary rise height change is 0.35mm and 0.51mm for 0.848 mm/sec and 0.424 mm/sec plate velocities, respectively.

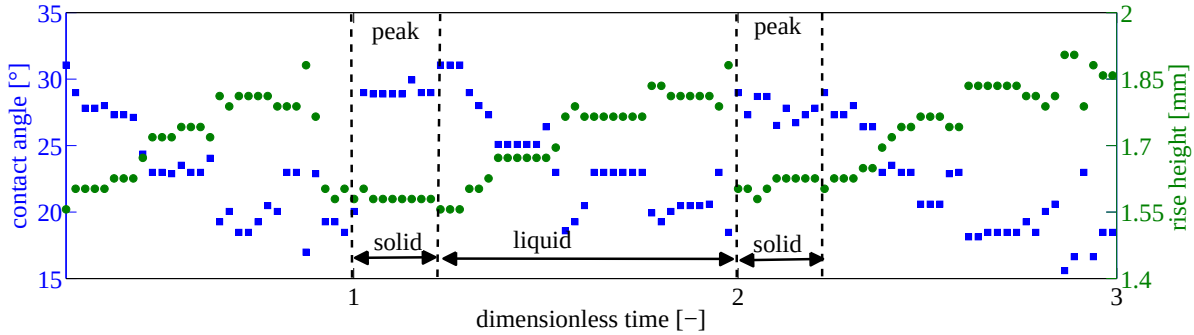

(a) 0.5mm pyramids, 0.8 mm/sec plate velocity, receding.

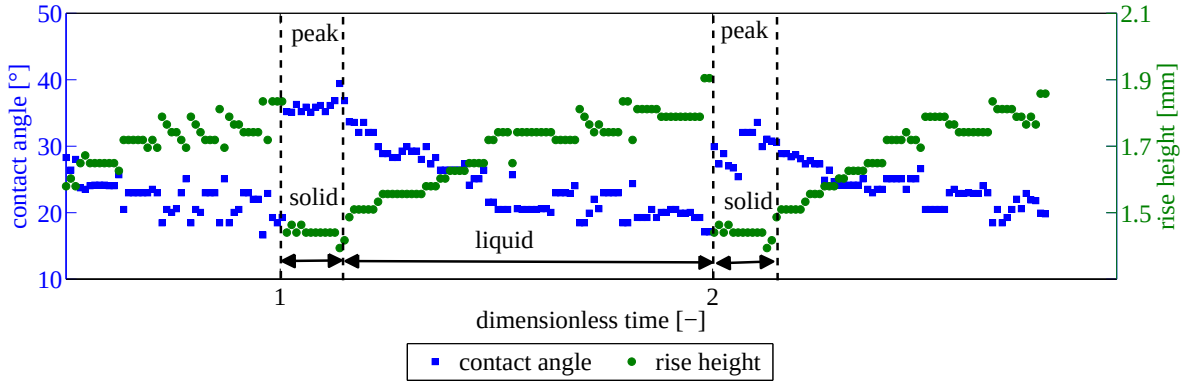

(b) 0.5mm pyramids, 0.4 mm/sec plate velocity, receding.

Figure 3.41: Comparison of contact angle and rise height versus dimensionless time for 100cSt PDMS for receding case and 0.5mm pyramids.

3.5.5.4 Comparison of Observations for Receding Contact Line

By changing the velocity and taking the feature size fixed, it is concluded that the velocity change does not drastically affect the period and amplitude of the contact angle and rise height for each structure. Figure 3.42 demonstrates that the evolution of contact angle and rise height have the same values for all plate velocities at fixed features sizes. Table 3.8 shows the comparison between the minimum and maximum values of rise height and contact angle change measured by the tangent method and compares the contact angle values derived from 2D Laplace fitting. In figure 3.43 the contact angle data measured with tangent method are compared with the theoretical values provided by equation 3.7c. The data points do not match with the derived data at the liquid-liquid interface, but display compatibility on the solid-liquid interface. All features have similar maximum capillary rise height independent of the feature size and plate velocity. On the other hand, larger features have low capillary rise height values, because as soon as the dynamic liquid front touches the peak, a jump occurs in the rise height. The maximum contact angle is then measured at the lowest rise height value and the minimum contact angle at the highest rise height.

Receding of a Wetted Surface - Amplitudes (100cSt PDMS)

pyramid type and plate velocity	max. rise height [mm]	min. rise height [mm]	2D Laplace derivation		tangent method	
			max. contact angle [°]	min. contact angle [°]	max. contact angle [°]	min. contact angle [°]
2 mm - 0.8 mm/sec	2.09	0.81	58.2	0.1	59.4	14
2 mm - 0.4 mm/sec	1.99	0.78	59.4	5.5	56.15	15.6
1 mm - 0.8 mm/sec	2.04	1.39	34	2.8	40.3	15.6
1 mm - 0.4 mm/sec	1.97	1.27	39.2	6.5	45.7	16.6
0.5 mm - 0.8 mm/sec	1.9	1.55	26.8	10.1	31.05	15.6
0.5 mm - 0.4 mm/sec	1.9	1.39	34	10.1	39	16.4

Table 3.8: The amplitudes of rise height and contact angle for three pyramidal array at three different speeds in the advancing case.

Table 3.8 shows the comparison between the contact angle measured by the tangent method and the same derived by the 2D Laplace equation. The minimum contact angle related to the maximum capillary rise height at the liquid-liquid interface is calculated as $\sim 0°$ for the 2mm pyramidal array with a plate velocity of 0.848 mm/sec, whereas the maximum contact angle on the peak at minimum capillary rise height is $\sim 60°$ for the 2mm pyramidal array with a plate velocity of 0.424 mm/sec.

Receding of a Wetted Surface - Periods (100cSt PDMS)

pyramid type and plate velocity	full period [sec]	pinning time [sec]
2 mm - 0.8 mm/sec	2.37	0.31
2 mm - 0.4 mm/sec	4.77	0.95
1 mm - 0.8 mm/sec	1.30	0.27
1 mm - 0.4 mm/sec	2.60	0.41
0.5 mm - 0.8 mm/sec	0.72	0.136
0.5 mm - 0.4 mm/sec	1.46	0.31

Table 3.9: The real time periods and pinning durations for all feature sizes and plate velocities.

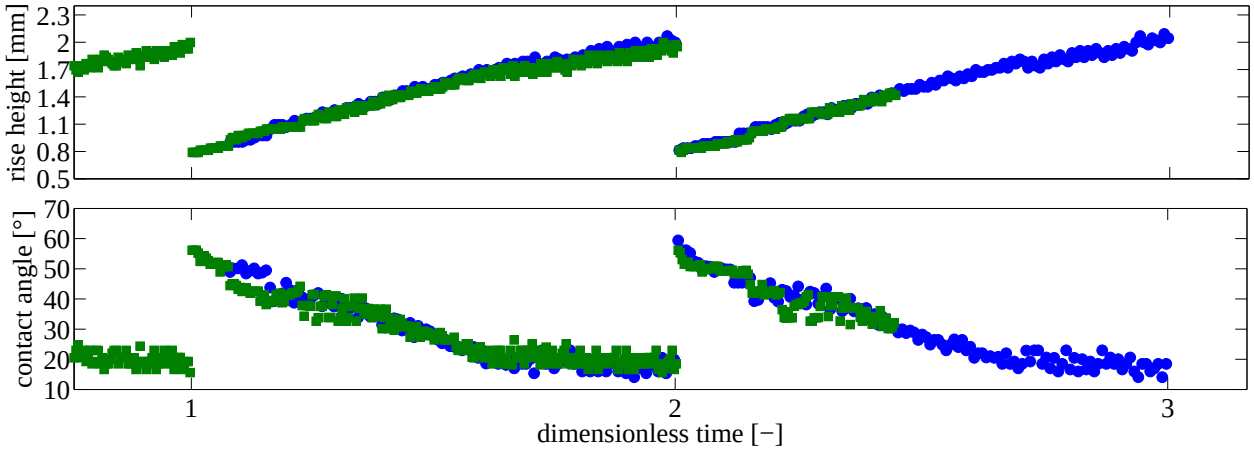

(a) 2mm pyramid, comparison of rise height and contact angle, receding.

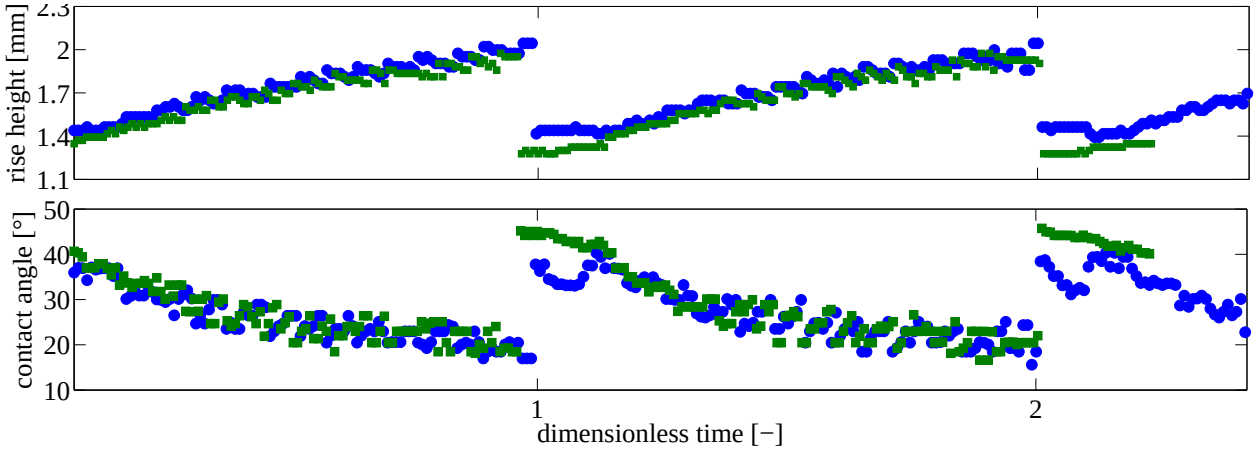

(b) 1mm pyramid, comparison of rise height and contact angle, receding.

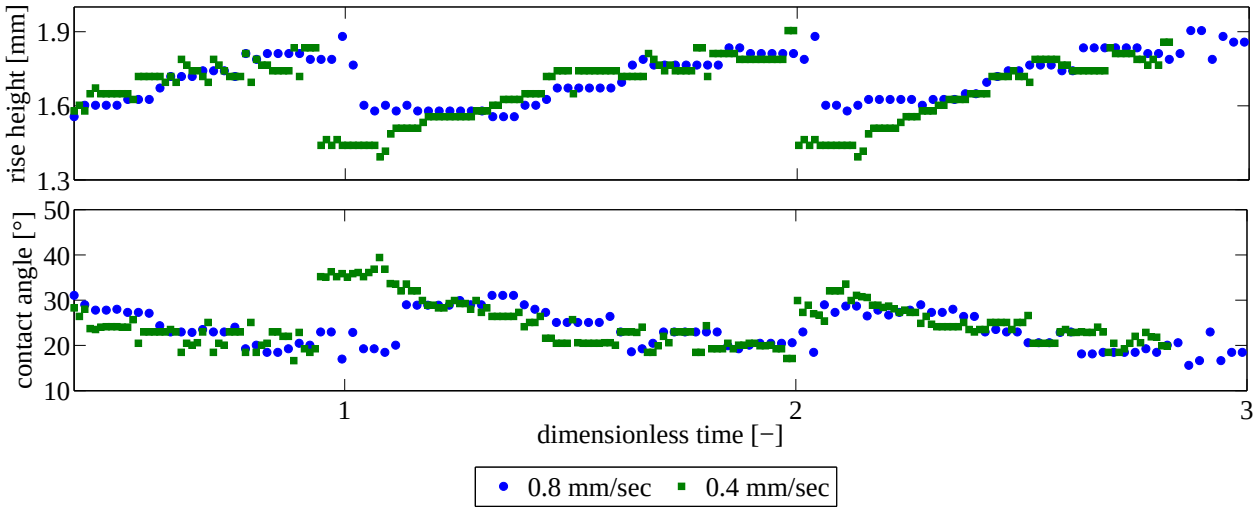

(c) 0.5mm pyramid, comparison of rise height and contact angle, receding.

Figure 3.42: Feature size dependent comparison of contact angle and rise height versus dimensionless time for 100cSt PDMS for the receding case.

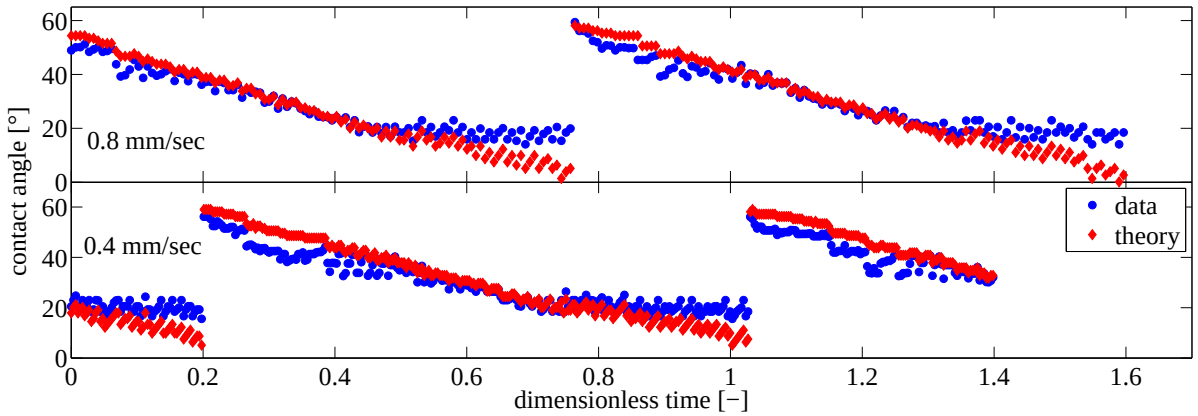

(a) 2mm pyramids, receding.

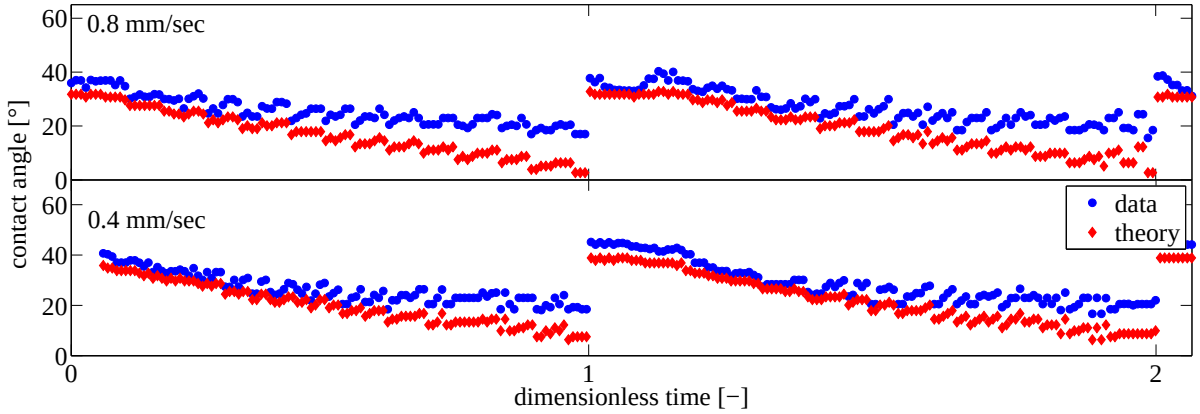

(b) 1mm pyramids, receding

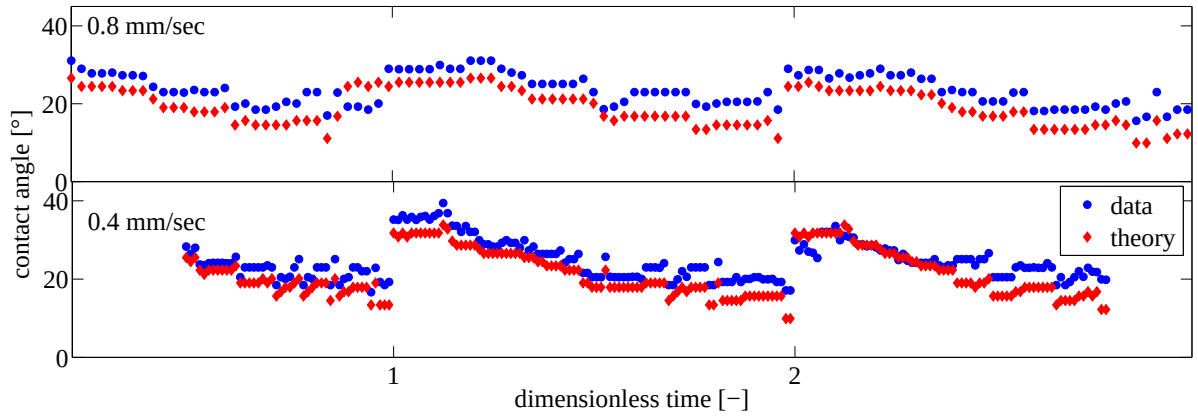

(c) 0.5mm pyramids, receding.

Figure 3.43: Comparison of measured contact angle by tangent method (tagged as data) and 2D Laplace derivation (tagged as theory) provided by equation 3.7c.

3.5.6 Comparison of Amplitudes (Capillary Rise Height) and Periods of Dynamic Advancing and Dynamic Receding

Table 3.10 summarizes the maximum/minimum capillary rise heights for all features and plate velocities in the advancing and receding cases. The gathered data show us that the maximum attainable capillary rise height for the receding case is in every situation very close and between 1.9mm and 2mm. On the other hand, the maximum attainable capillary rise height for the advancing case varies between 1.4mm and 1.8mm. If we compare the maximum capillary rise height with respect to the viscosity change, we realize that the highly viscous liquid cannot rise as much as the less viscous liquid in the valleys, where the maximum rise happens. Furthermore, the minimum capillary rise height of the meniscus for the advancing case, which is detected on the pyramid apices, is smaller than the receding case. The liquid is pushed down in the advancing case and pulled up in the receding case, where the difference in contact angles gives us the hysteresis on the apex of the pyramids. For 10cSt PDMS, the maximum accessible contact angle is 60° for advancing and the minimum accessible contact angle is 23° for receding. On the other hand, for 100cSt PDMS the maximum accessible contact angle becomes 67° and the minimum accessible contact angle 27°. These values denote that the highly viscous PDMS specimen leads to a lower capillary rise height at the pyramid apices (advancing case), which results in a larger contact angle. In figure 3.44, the dynamic contact angles derived from the rise height are given as a function of capillary numbers. The data points are consistent with $\sim Ca^{1/3}$ of Cox's model, but because the data points are very sparse, we cannot prove if Cox's equation is being followed.

The comparison of the table 3.2 and 3.6 yields us that increase in viscosity causes longer pinning duration on the apex of pyramids for 1mm and 0.5mm pyramids. However the pinning duration for 2mm pyramids stays the same. The contact line moves together with the plate, where the capillary number effects the pinning duration and hence the change on contact angle.

	pyramid type and plate velocity	rise height-advance [mm]		rise height-recede [mm]	
		max.	min.	max.	min.
10cSt -0°	**2 mm-0.8 mm/sec**	1.72	0.78	1.95	0.83
	2 mm-0.6 mm/sec	1.76	0.78	2.02	0.85
	2 mm-0.4 mm/sec	1.75	0.74	2.00	0.83
	1 mm-0.8 mm/sec	1.64	0.99	1.99	1.39
	1 mm-0.6 mm/sec	1.68	1.03	1.84	1.23
	1 mm-0.4 mm/sec	1.75	1.08	1.99	1.37
	0.5 mm-0.8 mm/sec	1.77	1.19	1.93	1.61
	0.5 mm-0.6 mm/sec	1.83	1.34	2.00	1.64
	0.5 mm-0.4 mm/sec	1.75	1.30	1.95	1.62
100cSt -0°	**2 mm-0.8 mm/sec**	1.44	0.38	2.09	0.81
	2 mm-0.4 mm/sec	1.73	0.54	1.99	0.78
	1 mm-0.8 mm/sec	1.46	0.83	2.04	1.39
	1 mm-0.4 mm/sec	1.76	1.13	1.97	1.27
	0.5 mm-0.8 mm/sec	1.47	0.90	1.90	1.55
	0.5 mm-0.4 mm/sec	1.55	1.23	1.90	1.39

Table 3.10: Comparison of the capillary rise height (maximum and minimum) for three pyramidal arrays and two liquids in the advancing and receding cases.

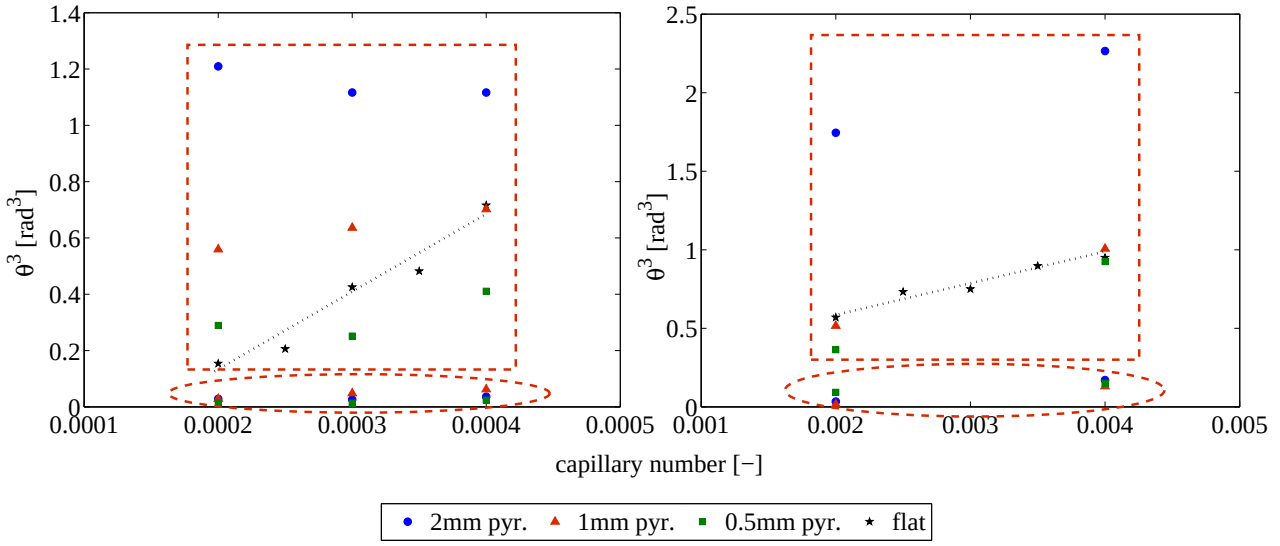

(a) Maximum (in square) and minimum (in circle) contact angles derived from capillary rise height for the advancing case. The black stars are the data points gathered from the flat surface (see Figure 3.11).

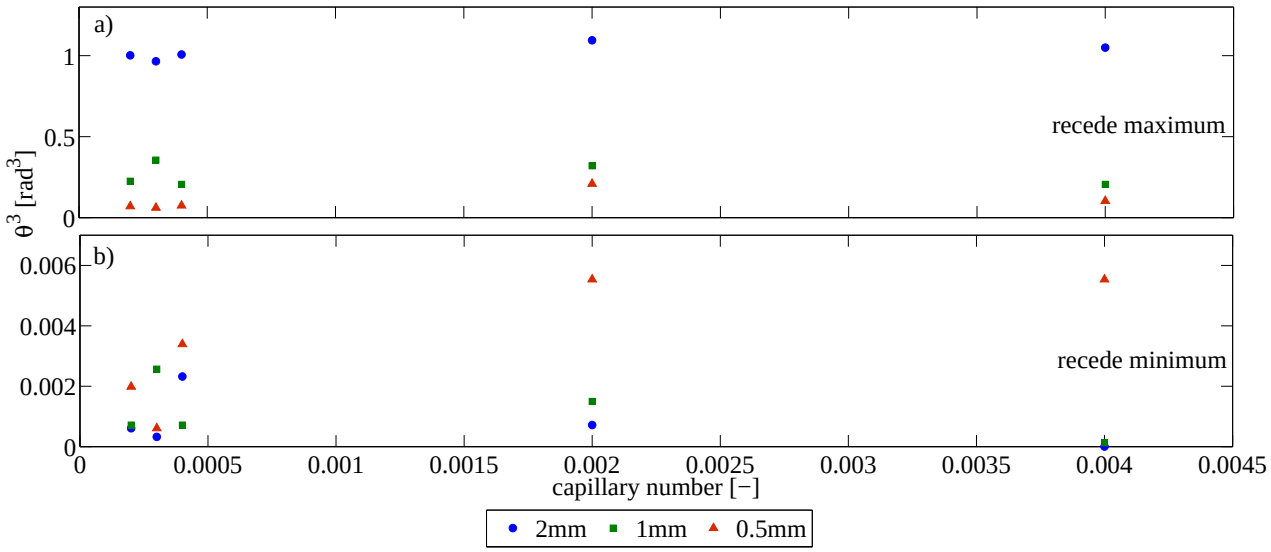

(b) Maximum and minimum contact angles derived from capillary rise height for receding case.

Figure 3.44: Macroscopic contact angle versus capillary number plotted for three different features.

3.5.7 Change in Plate Orientation

In order to check the effect of feature orientation on wetting, the substrates are rotated by 45° and dipped into 100cSt PDMS at 0.8 mm/sec and 0.4mm/sec. As depicted in figure 3.45, the gap between two respective peaks is obscured by pyramids in the previous row, which cannot be circumvented by Scheimpflug method. This shading prevents observing and measuring the capillary rise height and contact angle of a certain region (namely in the valley), where the maximum rise height is measured based on the previous observations. However a periodicity can still be evaluated and the pinning duration on the apices can be determined (see Table 3.11). The pinning time is the same for 2mm pyramidal arrays but shorter for 1mm and 0.5mm structures in both the advancing and receding processes, compared to the same experimental cycle for the non-oriented case (see Table 3.7).

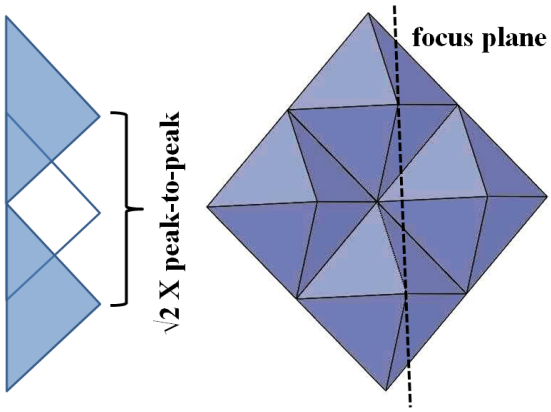

Figure 3.45: Cross section and front view of 45° rotated pyramidal array.

Periods of 45° Rotated Arrays (100cSt PDMS)

	pyramid type and plate velocity	full period [sec]	pinning time [sec]
advance	**2 mm-0.8 mm/sec-45°**	1.71	0.40
	2 mm-0.4 mm/sec-45°	3.39	0.96
	1 mm-0.8 mm/sec-45°	1.03	0.31
	1 mm-0.4 mm/sec-45°	1.88	0.62
	0.5 mm-0.8 mm/sec-45°	0.58	0.10
	0.5 mm-0.4 mm/sec-45°	1.15	0.22
recede	**2 mm-0.8 mm/sec-45°**	1.75	0.40
	2 mm-0.4 mm/sec-45°	3.35	1.15
	1 mm-0.8 mm/sec-45°	0.93	0.13
	1 mm-0.4 mm/sec-45°	1.86	0.44
	0.5 mm-0.8 mm/sec-45°	0.52	0.07
	0.5 mm-0.4 mm/sec-45°	1.13	0.17

Table 3.11: The real time periods and pinning time durations for all feature sizes and plate velocities.

Figure 3.46 shows the penetration of the liquid front as the plate is dipped into the liquid. The diagonal orientation of the side paths between the pyramids causes a more homogeneous spreading of the liquid compared to figure 3.15 and 3.33. The dimensionless period is calculated by the following equation:

$$\text{dimensionless time} = \frac{\text{actual time} \times (v_{\text{plate}} + v_{\text{liquid rise}}) \times \sqrt{2}}{\text{peak-to-peak length}}$$

for 45° rotated plate. As the feature size gets smaller and as the liquid finds suitable paths (the diagonal side paths) to flow, the surface loses its extreme physical disorder, which means for smaller feature sizes, fluid from the valleys may coat more of the peaks and the ability to pin on the peaks is diminished compared to the larger features, where pinning happens on a dry or at least drier surface. So the 0.5mm, 45° rotated plate, dipped in 100cSt behaves like a chemically heterogeneous surface. The rest of the test surfaces, due to their size, cannot show any similarity to chemically heterogeneous surfaces.

If the considered features were comparable with chemical heterogeneity, we would be able to observe any diversity in boundary conditions, where the liquid front is moving faster than the plate velocity for some combinations of variables. One of the reasons for that could be the side paths between the rows and columns of the arrays, which allow a liquid flow from the third dimension. A rotation by 45°

causes an less complicated liquid flow through the gaps between the pyramids as indicated in figure 3.46.

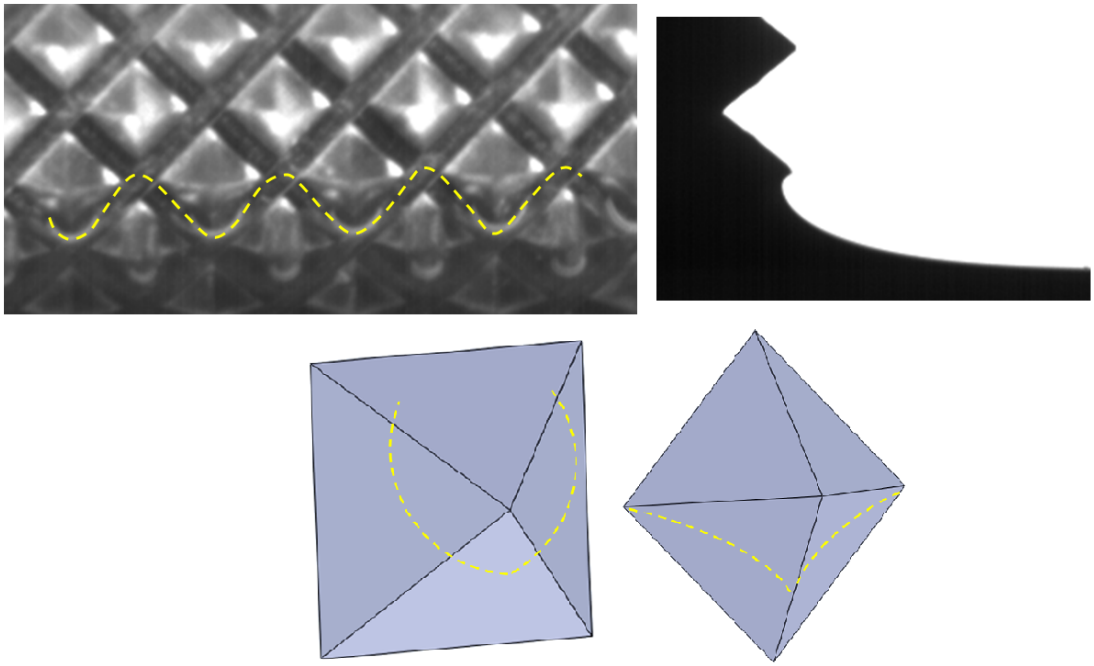

Figure 3.46: (Above) Side and front view of advancing in 100cSt PDMS with 1mm pyramids. When the features are rotated by 45°, the proceeding of the contact line becomes easier through the side paths. (Below) The propagation of liquid on the rotated and non-rotated plates are shown in dashed lines. The liquid front has an edge as hinderance on the rotated pyramid, as opposed to a wall on the 0°-rotated pyramid.

3.5.8 Transferability of Feature Size, Dipping Velocity and Feature Orientation

Transferability of a boundary condition such as a contact angle can be measured on one geometry and applied to another geometry. This is a key property application, where wetting of a system must be characterized in a more reliable controlled geometry but applied in the geometry of the application (such as a film coater). Transferable properties are distinguished from conserved properties, where the first one refers a boundary condition change and the latter one refers a property being constant in time.

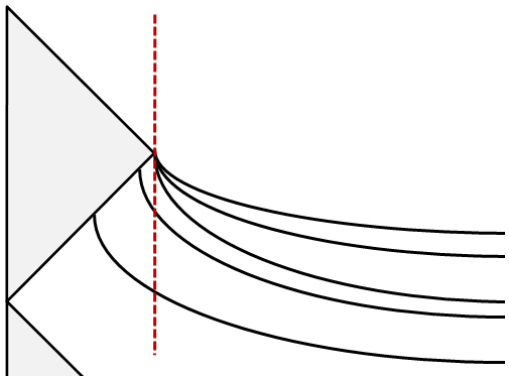

Figure 3.47: Cropped meniscus by the apex for transferability check.

In order to determine a transferable contact angle, the fluctuations on the liquid meniscus should be exterminated. 7mm away from the dry valley at $x = 0$ (see Figure 3.16) for all viscosities, plate orientations, wetting directions, and plate velocities, the fluctuation of the rise height of the meniscus shape vanishes and the meniscus shape becomes static like. However at this very far distance, an extrapolation of the meniscus shape with respect to wall is impossible and may yield a range of contact angles (see *Appendix D*).

To be able to check if there is a global contact angle for very rough surfaces on the millimeter scale, the meniscus is cropped at the apex of the pyramids (see Figure 3.47) and the rise height of the meniscus shape is measured from this reference point. Figure 3.48 and 3.49 present the capillary rise height of the meniscus shape with respect to the apex of the pyramids in dimensionless time for advancing and receding cases on 2mm and 1mm pyramids. In the case of advancing, the gathered data indicate that the maximum and minimum capillary rise heights cannot be compared due to the formation behind

the pyramid's apex inside the valleys. In the case of receding, due to the filled grooves on the surface, the maximum and minimum capillary rise are equal for all conditions individually for 1mm and 2mm pyramidal arrays. For 2mm pyramids, the macroscopic contact angle varies between 48° and 62°, and for 1mm pyramids between 33.5° and 41°, under the condition described above (change in liquid viscosity, dipping velocity and feature orientation). The results show that macroscopic contact angle is not a transferable boundary condition for very rough surfaces due to the lack of a global contact angle. Overall it can be concluded that the advancing case is not transferable in rise height (and hence in global macroscopic contact angle) but the receding case is, under the condition of cropped meniscus at the apex of the features for all variables for each feature itself individually.

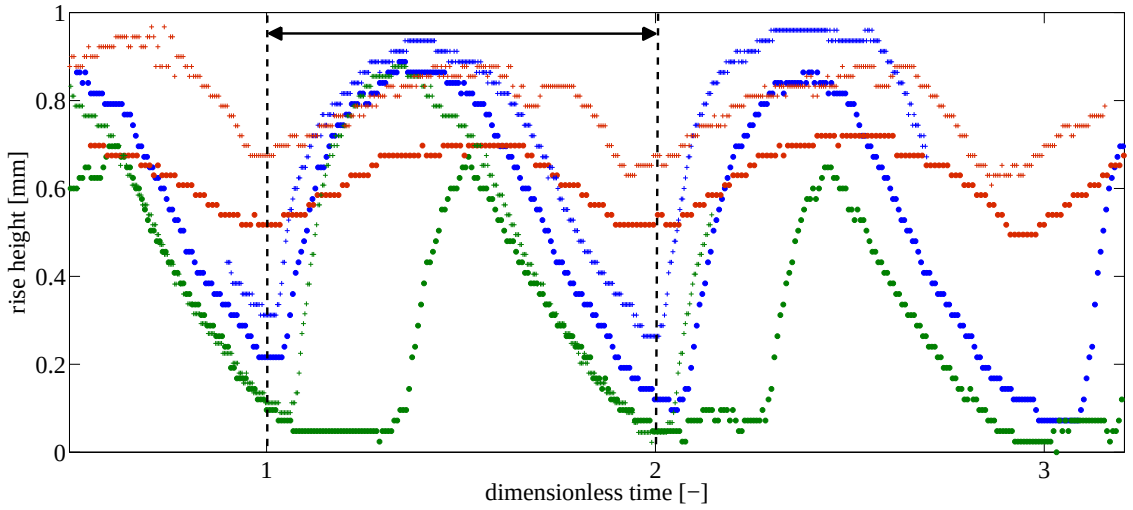

(a) 2mm pyramids, advancing.

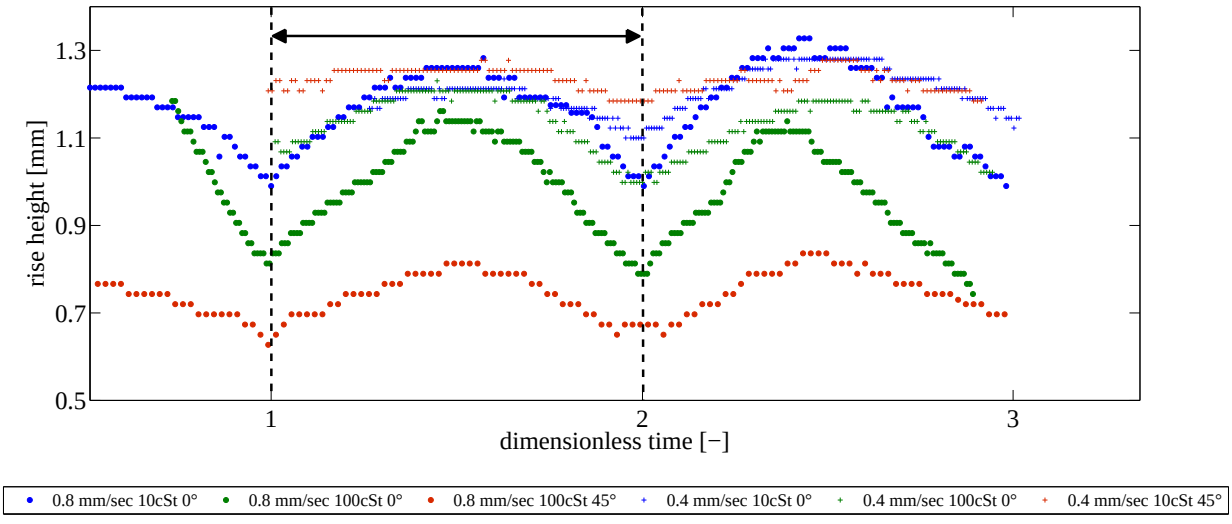

(b) 1mm pyramids, advancing.

Figure 3.48: Capillary rise height versus dimensionless time for 1mm and 2mm pyramids in the advancing case. The double arrow indicates a single period.

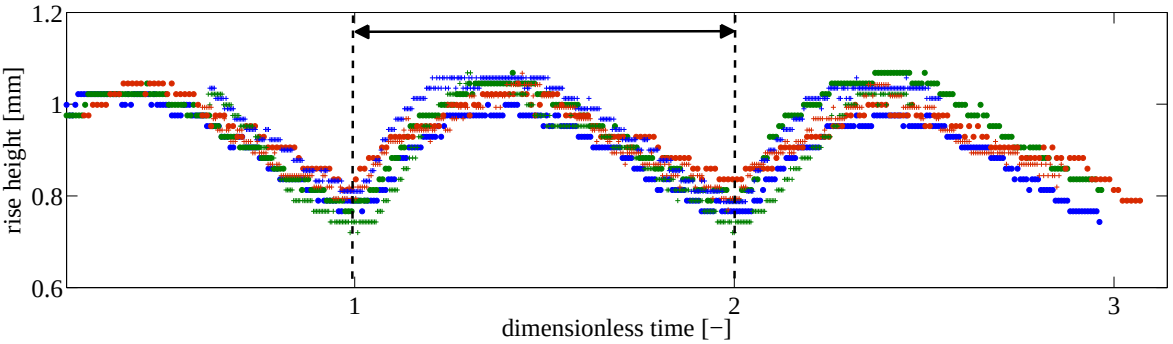

(a) 2mm pyramids, receding.

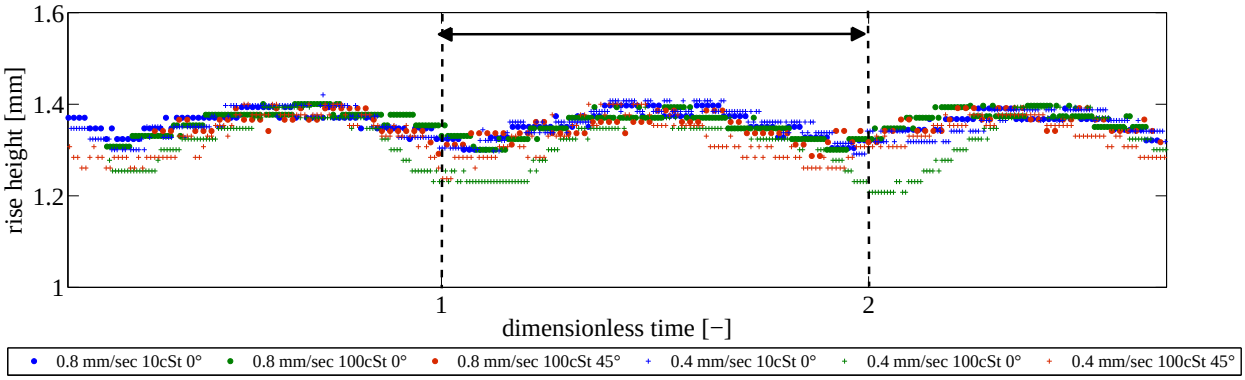

(b) 1mm pyramids, receding.

Figure 3.49: Capillary rise height versus dimensionless time for 1mm and 2mm pyramids in the receding case. The double arrow indicates a single period.

3.6 Summary and Future Work

In previous sections a detailed data analysis has been given in order to make a clear and understandable presentation of the key points regarding forced dynamic wetting on very rough surfaces. Each experiment is individually evaluated and studied to be able to hinder data loss. The gathered data are presented graphically and the essential values are shown in tables. The following key points are discussed and some explanations relevant to these key points are given in respect to the gathered and evaluated data covered in previous sections:

- Is there a correlation between chemical heterogeneity and physical roughness at this scale?
- Is there a transferability between different feature sizes and plate orientations and is contact angle a transferable boundary condition for very rough 3D surfaces?
- Is there a global contact angle?

We can conclude that there is a compliance in the periodicity of wetting between the very large features coupled with different advancing/receding velocities and plate orientations, if the meniscus is handled far from the contact line with a given boundary condition. This proves that contact angle is not a transferable boundary condition for very rough 3D surfaces, due to the fluctuations on the surface caused by large features. These fluctuations on the surface cause a range of contact angles and a global contact angle cannot be determined. Only in the case of receding, a particular contact angle range for each feature size for all orientations and liquids can be given, but in the advancing case the contact angle range varies for each individual combination of feature size, plate speed and plate orientation. There can be no correlation between chemical heterogeneity and physical roughness at these large scales.

In the case of 2mm advancing pyramidal array, an *apparent slip motion* is observed, where the system boundary condition changes from a contact line boundary condition to a fixed contact angle condition. The contact angle stays constant (at $\sim 30^\circ$ with respect to vertical) as the contact line is pushed downwards faster than the plate velocity. In the case of *sticking* on the apex of the pyramid, the system changes from a constant contact angle condition to a fixed contact line condition. The contact line pins and is pushed downwards by the plate velocity, where the contact angle increases. The *apparent slip motion* is only observed on 2mm pyramidal arrays, whose depth and width scales are larger than the capillary length of the test fluids. To be able to measure the change in boundary conditions on different positions on the surface, the contact angle is measured by taking the tangent of the meniscus at the contact line triple point and compared with orthodox methods. When the dynamic liquid front meets the pre−filled valleys and wets itself, the contact angle relative to the surface becomes zero degrees, but the tangent method is not adequate to measure this properly. The contact line motion stays in quasi-steady state for essentially all the time, except the jumps after pinning, where the visco-capillary relaxation time is on the order of milliseconds. In conclusion, the gathered data prove that hydrodynamic behavior is dominant for the performed experiments.

It is often assumed that there is some mapping between chemically heterogeneous surfaces and rough surfaces. On very rough surfaces (on the order of millimeters), this cannot be true because of the flow within the roughness features. Fluid rivulets in the valleys of the roughness features are formed either by capillary pressure developed between the roughness features or by break-off of the liquid left behind as local portions of the contact line jump after being pinned by a defect. The velocity scale for these rivulets is an added velocity scale to the moving contact line problem. For example, for 10cSt PDMS, the liquid film in the grooves grows ahead of the dynamic liquid front (contact line) at a different speed than the contact line is forced to move. The pre-filling of the valleys might have an effect on preventing the formation of *apparent slip movement* on the 1mm and 0.5mm pyramids.

In Summary

- There is no single contact angle boundary condition even for one test surface if the contact angle on the surface is taken into consideration.
- There is no transferability for contact angle in the case of advancing into the liquid. A varying range of contact angles for each individual structured surface should be considered for the coating process.
- There is transferability of the contact angle in the case of receding from the liquid. A particular range of contact angles can be defined for each individual structured surface.

For a more fundamental analysis of the effect of viscosity on contact angle, experiments are required at the same capillary number with the same fluid in different viscosities while staying in the hydrodynamic range. Moreover, a wider range of viscosities for the same fluid should be tested at the same capillary number.

Chapter 4

Wetting on Structured Surfaces with Dynamic Volume Change

Wetting on structured surfaces has been investigated by many research groups by considering the Cassie-Baxter and Wenzel states for static sessile droplets. Chemically or physically patterned surfaces differ in three interrelated features, the electrostatic surface potential, the shape of the liquid-gas interface and fluid flow, all of which affect the phase change process [88]. The size and scale of the structured surfaces determine which solid-liquid-gas interactions are dominant. Macro-sized structures increase the contact area between the heat transfer fluid and underlying solid. Moreover micro-sized structures increase nucleation sites, enhancing condensation or boiling. Submicron-sized structures an increase in the surface potential and lead to increase the interfacial area. Lately, the research group of Wang [89] demonstrated that the design of asymmetric nanostructured surfaces achieve a uni-directional liquid spreading, where the liquid propagates in a single direction and pins in all others.

Priest et al. observed that the wettability of structured surfaces for liquids residing in the Cassie-Baxter state is strongly dependent on both the solid fraction and the continuity of the solid component [90; 91]. They showed experimentally that being a high or low energy defect, the chemical heterogeneity affects the wetting significantly. On high energy defects, the advancing measurements departed from equilibrium theory; and on low energy defects, the receding data deviate from the theory. Liu et al. managed to change thermodynamically the state of a water droplet on a hydrophobic surface from Wenzel to Cassie [92]. They applied heat either to the micro-patterned hydrophobic substrate (by heating the object) or to the droplet (by heating with a pulsed laser), which ensued a Leidenfrost regime that shifted the droplet from a more stable Wenzel state to a less stable Cassie state. Duncan et al. [93] investigated drop size dependent contact angle measurements on flat surfaces by pumping liquid from a hole on the substrate, in an attempt to link line tension values to the surface properties of solids and liquids . Brandon et al. [94] simulated three dimensional drops on partially wetting chemically heterogeneous smooth solid surfaces in equilibrium by using the software package Surface Evolver [95]. They concluded that in the case of volume increase and decrease, the drop advances via the slip-stick mechanism similar to that observed in experiments. Moreover, the calculated drop shapes were in agreement with the Young and Young-Laplace equations. Johnson and Dettre [57] performed a theoretical and computational study on concentric circular bands having alternating surface energies, which provides an infinitely sharp transition between regions of different surface tensions. It is concluded that the advancing contact angles remain relatively constant over a wide coverage of the concentric band while receding angles drop rapidly with decreasing coverage.

In this chapter, wetting on structured surfaces is investigated in correlation with dynamic volume change. Liquids are pumped though a hole through the center of the substrate with increasing volume and a dynamic contact angle is measured with respect to time, volume change and change in contact line radius. A correlation between dynamic viscosity, structure size, and advancing contact angle is concluded from the experimental results. Numerical simulations parallel to the experiments were performed for water and water-glycerin mixture, and a good agreement between experiments and numerical simulations has been obtained.

4.1 Dynamic Contact Angle Measurement on Advancing Liquid Volume

4.1.1 Experimental Setup

For the experiments, four variations of silicon oil (5/10/20/50cSt), deionized water, and glycerin-water mixture (85%-15% vol.) are used. Silicon oil enables us to obtain a fixed density and surface tension, and just vary the dynamic viscosity. Flat and milled aluminum plates are used as wetting surfaces. Flat aluminum plates are polished to remove the crude roughness (R_a=0.25±0.02 μm). For the milled aluminum plates a milling cutter with a 60° opening angle is used to produce pyramidal arrays and concentric triangular circles. The concentric triangular circles, which provide a 2D axisymmetric environment, have 0.2mm, 0.5mm, and 0.75mm peak-to-peak width respectively, while the pyramids (see Table 4.1), which provide a 3D array environment, have 0.5mm, 1mm, and 2mm peak-to-peak width, which were also used for the experiments covered in Chapter 3 (Table 3.1). Each substrate has a 0.8 mm (⌀ diameter) hole at the bottom in the center of the features for liquid injection. For the recordings a 8-bit monochrome high speed CMOS camera (VDS Vosskühler HCC-1000BGE) is used, which has a pixel size of 10μm×10μm and a sensor size of 10.2mm×10.2mm. A Nikon AF D 50mm f/1.4 objective lens is used with a 2×NAS Macro Teleplus MC7 teleconverter to enlarge the field of view. A 2D grid having squares of 10μm×10μm is used to calibrate the vertical and horizontal magnification. For pumping the liquid, a syringe pump (Syringe Pump NE-1000) is used. All liquids are pumped at the same mechanical pumping rate, but due to the various viscosities of the test liquids, the outlet flow rate differs for each fluid, which results in disparate volume changes per unit time. All experiments are performed at room temperature and 45%Rh. To be able to focus on the contact line at the structured surfaces, the Scheimpflug principle is applied as the recording is taken. The Scheimpflug principle is outlined in *Appendix C*.

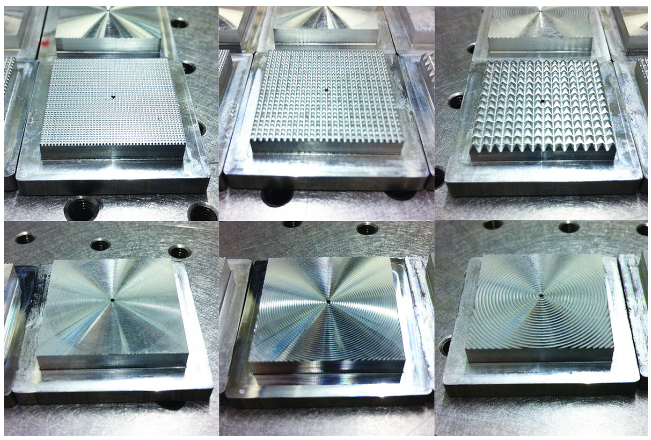

Figure 4.1: (Above) The milled pyramids in sizes of 0.5mm, 1mm, and 2mm. (Below) The milled concentric circles in sizes of 0.2mm, 0.5mm, and 0.75mm.

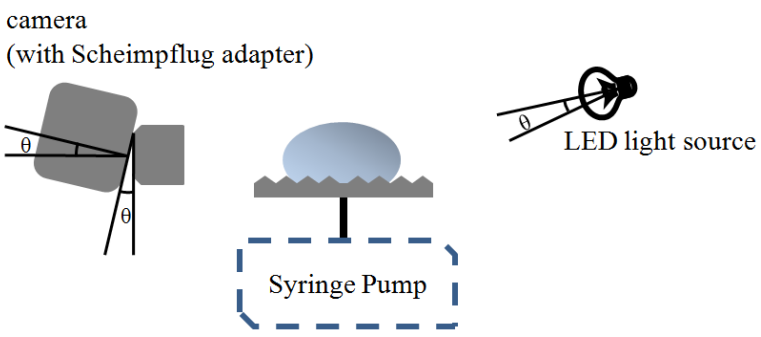

Figure 4.2: The test liquids are pumped through the hole at the center of the substrate.

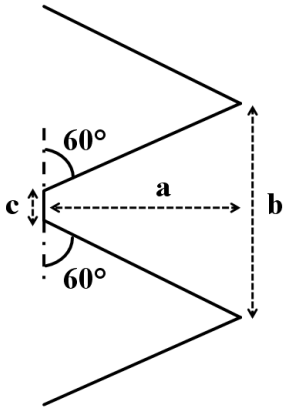

conc. circles	a [mm]	b [mm]	c [mm]
0.2 mm	0.185	0.293	0.011
0.5 mm	0.382	0.696	0.023
0.75 mm	0.579	1.050	0.034

Table 4.1: The dimensions of milled concentric triangular aluminium structures.

4.1.2 Image Processing

All experimental data recorded by the high-speed camera is evaluated by MathWorks® Matlab Image Processing Toolbox. To be able to reduce the uncertainty at the contact line, a background image without any droplet on it, is subtracted from each dynamic image. With this method, evaluation of contact angle on complex surfaces becomes very straightforward.

Figure 4.3: Background picture is subtracted from the main recording and converted to binary.

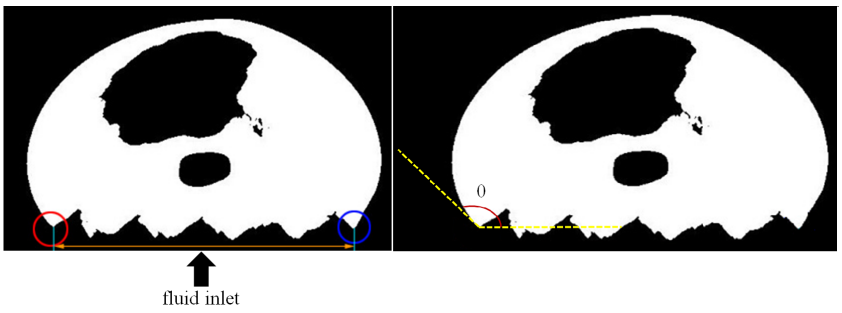

Figure 4.4: (Left) The contact line diameter is measured as shown by the dark yellow double arrow by taking the horizontal distance between the detected contact points. (Right) The contact angle is measured between the tangent on the drop contour and the horizontal line at the contact point.

The image processing is restricted by the resolution of the camera, which has a significant effect on the contact angle determination. According to the image processing algorithm in the MathWorks® Matlab Image Processing Toolbox, the contact angle is computed by determining a contour between the liquid-gas interface using the gray value gradients and calculating the tangent between the horizontal solid surface and the liquid contour. To be able to achieve an acute distinction between black (ASCII 0) and white (ASCII 1) pixels, a very sharp shadowgraphic image is needed, which reduces the gray pixels and allows more reliable results. The *graythresh* function in the MathWorks® Matlab Image Processing Toolbox uses Otsu's method [87], which chooses the threshold that minimizes the intra-class variance of the black and white pixels. Determination of the gray value, and consequently the liquid-gas contour, plus fitting the suitable tangent cause an error of 3-5% depending on the contact angle value. The error is larger if the contact angle is between 85° and 105°, and smaller for other values except contact angles smaller than 7°. Contact angles smaller than 7° cannot be determined

correctly with this method. All measured contact angles are **apparent contact angles**, which is defined in section 3.5.1.

Figure 4.5: Enlarged view of the contact point. The tangent drawn to the air-liquid interface is related to the gray threshold, which affects the determination of the contact angle considerably.

4.1.3 Features of Surface Wetting

4.1.3.1 Surface Coating

Aluminium[1] is a high-energy surface due to the strong metallic bonds. Most molecular liquids (in this case silicon oil) achieve complete wetting with high-energy surfaces. On a bare flat aluminium surface, silicon oil completely wets the surface, whereas on structured surfaces silicon oil penetrates through the grooves and covers even the peaks by crawling up from the bottom line. Due to the very low surface tension of silicon oil, all aluminum surfaces are coated with a commercial nano-particle spray (KIWI®), in order to increase the static contact angle of silicon oil on aluminium. The coating increases the static contact angle of silicon oil variations approximately three times compared to the contact angle on a non-coated aluminium surface. The coating also increases the static contact angle of deionized water and glycerin-water (85%-15% vol.) mixture. In order to check if the coating is soluble in any of the test liquids, a flat, polished aluminium sample was coated with the aforementioned spray coating and sessile droplets of all test liquids were placed on it, covered with a quartz cuvette to stabilize the vapor pressure and hinder external effects. After a one-minute wait, no changes in contact angle or contact line diameter is observed. In addition, the coating enables easier removal of the liquid remains. After each experiment, samples are rinsed with acetone and isopropanol to solve the organic and inorganic residue, as the coating facilitates the peeling of greasy liquids such as glycerin and silicon oil on milled rough surfaces.

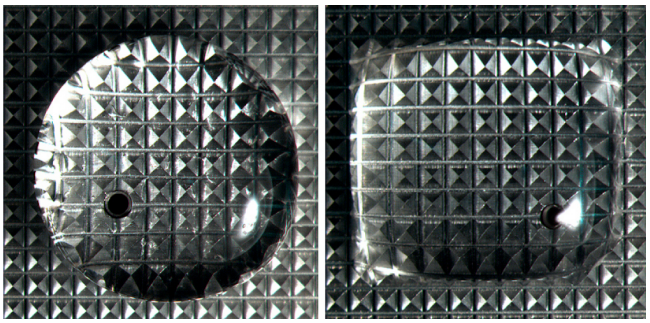

Figure 4.6: A drop of water on coated 1mm pyramidal surface (left) and on non-coated 1mm pyramidal surface (right).

[1] Aluminium has a native oxide layer on it, so the liquid actually wets the aluminium-oxide.

liquids	static contact angle	advancing contact angle	receding contact angle	equilibrium contact angle
water	102°	125.3°±2.6°	15.2°±1.7°	53.38°±2.1°
glycerin 85%	97°	104.7°±1.3°	29.6°±1.2°	60.69°±1.4°
silicon oil 5cSt	63°	64.3°±0.3°	39.5°±0.4°	51.68°±0.3°
silicon oil 10cSt	63°	65.2°±3.7°	39.5°±0.5°	52.14°±2.7°
silicon oil 20cSt	63°	66.7°±2.4°	39.5°±0.4°	52.60°±1.3°
silicon oil 50cSt	63°	67.1°±1.8°	39.5°±0.6°	53.06°±2.0°

Table 4.2: Advancing, receding and equilibrium contact angles of test liquids on coated flat aluminium surface (see Figure 4.7). The equilibrium contact angle is measured by using the equation 2.20a.

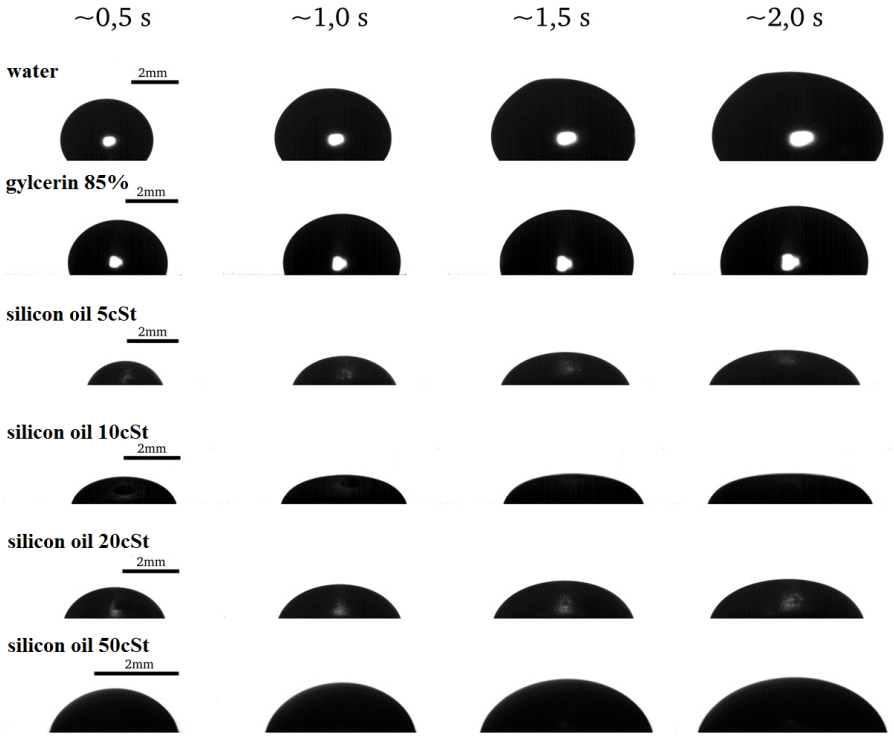

Figure 4.7: Image sequence of 6 liquids on a coated flat aluminium surfaces.

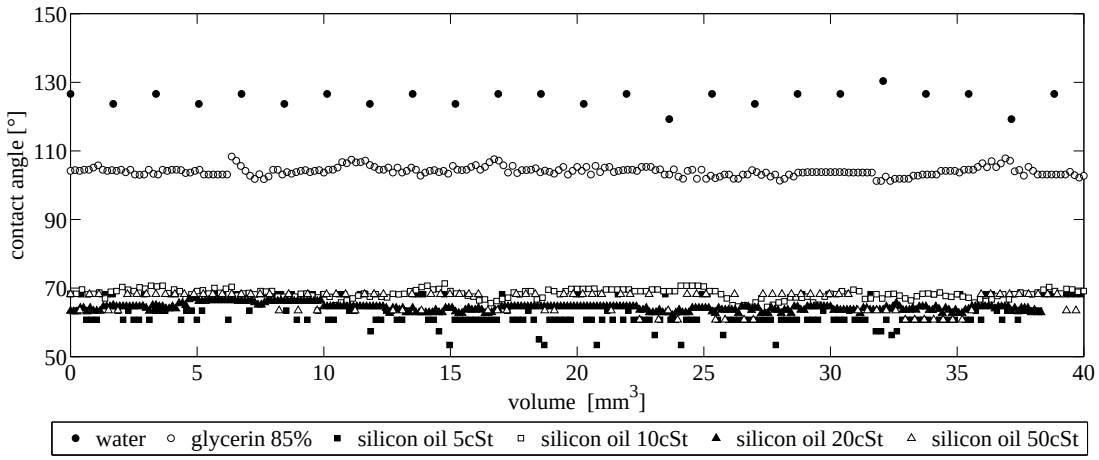

Figure 4.8: Advancing contact angle versus volume rate of 6 liquids on coated flat aluminium surfaces.

4.1.3.2 Features of Test Liquids and Structured Substrates

For the experiments, two different 3D structures, axisymmetric concentric triangular circles and pyramidal arrays, have been chosen. The axisymmetric concentric triangular circles enable a 3D structure with a 2D projection, which does not affect the observation direction due to the axisymmetry of the features but inhibits the detection of the contact angle behavior in the gaps between features. On the other hand, 3D pyramidal arrays complicate the contact angle detection due to the observation direction. Diagonal and horizontal observation directions figure 4.9 give completely different results for the change in contact angle and contact line, where in diagonal direction the liquid front overcomes the edges of the pyramid and in horizontal direction the sides of the pyramids. If the horizontal direction is chosen, the liquid movement in the rows can be observed by using the Scheimpflug method. The peak-to-peak distance for all concentric triangular circles are smaller that the capillary length of all test liquids, on the other hand, the peak-to-peak distance for only two of the pyramidal arrays are smaller than the capillary length of all the test liquids. In the previous chapter, the significance of feature size being larger that the capillary length of the test liquid was explained. In this study, the first aim is to compare the dip coating results with horizontal wetting results and establish a connection/disconnection between them, and secondly to compare the dynamic contact angle change on assorted features.

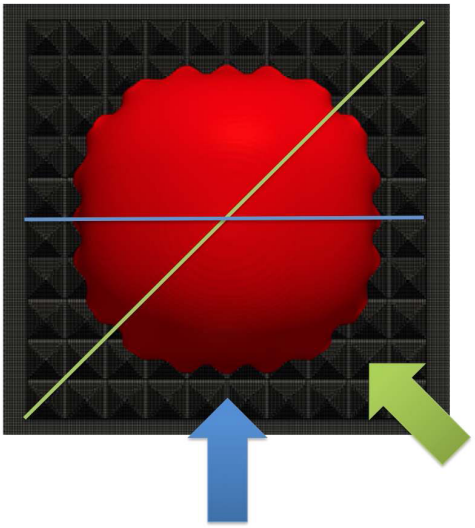

Figure 4.9: Possible diagonal and horizonal observation points for contact angle measurements for 3D pyramidal structured surfaces.

4.1.4 Experimental Results

4.1.4.1 Water

The surface tension of water is one of the highest after that of quicksilver and some metal alloys. According to Young, the surface tensions at the contact line are necessary and sufficient to determine the static contact angle. For the dynamic contact angle however, the dynamic viscosity also plays a crucial role in determining the contact angle, beside surface tension. In this subsection, the effect of surface structure on the advancing contact angle for water will be presented.

Due to the axisymmetry of concentric triangular circles, the periodicity of the contact angle change during the evolution of droplet growth is more obvious compared to the complex 3D shape of the pyramidal arrays. In the 3D pyramidal structures, the liquid has the chance to penetrate through the grooves between structures and looses the periodicity as the drop's volume increases. However due to the volume change, the period of the contact angle as a function of volume is not constant but increasing.

The data given above is interpreted in terms of the relation between volume increase and dynamic contact angle. The contact angle of the water droplet on a flat surface varies between 123° and 127° (Figure 4.8), which includes the uncertainty of the image precessing technique mentioned previously. In the case of concentric triangular circles, the contact angle of the water droplet fluctuates in the range 150°-143° for 0.2mm peak-to-peak, 145°-120° for 0.5mm peak-to-peak and 148°-110° for 0.75mm peak-to-peak separation. As the distance between peaks expands, the difference between the minimum and maximum dynamic contact angle grows, because of the larger contact area on the substrate. Here we observe that the larger features have the lowest contact angle, due to liquid accumulation in the grooves. On the other hand, water reaches almost the same maximum contact angle, where the contact line is pinned on the apex of the ridge, on each feature size.

In the case of pyramidal arrays, the contact angle of water droplet varies in the range 132°-111° for 0.5mm peak-to-peak, 124°-98° for 1mm peak-to-peak, and 121°-77° for 2mm peak-to-peak separations. As the size of the pyramids increase, water, having a very low viscosity, penetrates through the channel-shaped grooves between the pyramids and respectively, the liquid is not supported by the sharp points. Thus steady-state of contact line is lost much earlier than on the pyramidal concentric circles, in which case the contact line is surrounded by a circular symmetrical structure. Subsequently, the contact line crosses the next row of structure and then builds itself up again. In figure 4.10 the upper and lower

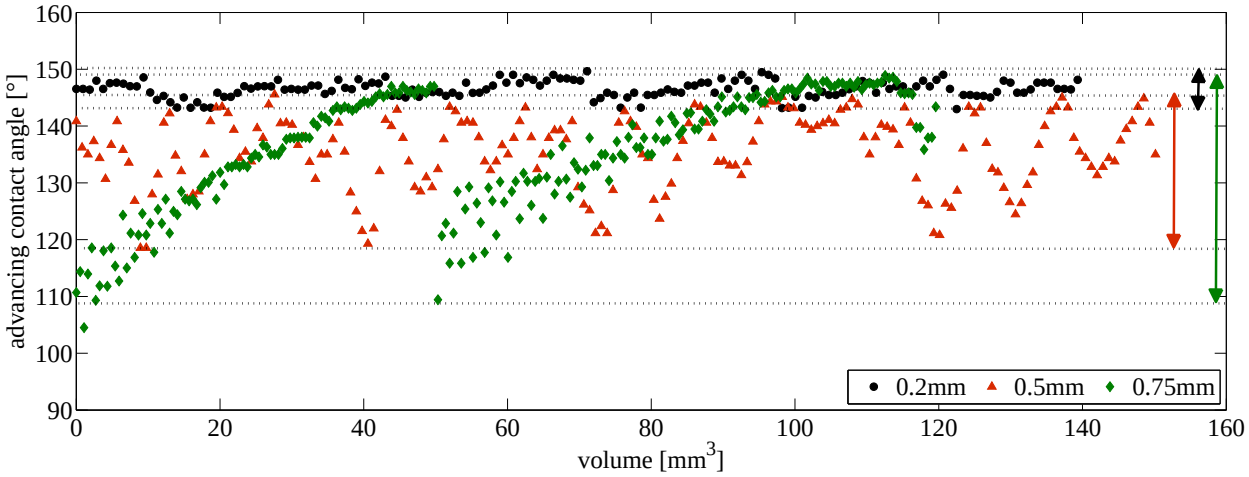

(a) Water droplet growing on three different concentric triangular circles.

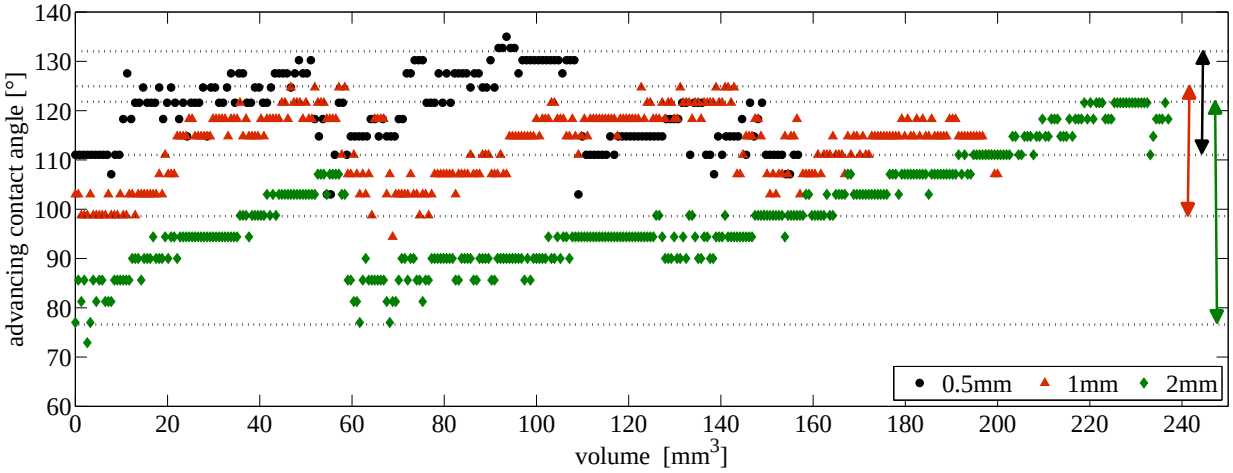

(b) Water droplet growing on three different pyramidal arrays.

Figure 4.10: The dynamic contact angle of the growing water droplet is evidently larger on concentric triangular circles than pyramidal arrays. The double arrows show the difference between maximum and minimum contact angles.

limits of contact angle change are marked by dashed lines, and double arrows, the amplitude. An important distinction here is that the entire contact line is pinned on the apex of the ridge in the concentric case but in the pyramidal array case, the contact line is partially pinned where it meets the pyramid apices, and advances where the contact line is between two pyramidal structures. If the observation direction relative to the pyramidal rows is picked in diagonal orientation (see Figure 4.9), then the $\sqrt{2}\times$peak-to-peak distance is the relevant gap for contact angle change. Here the challenging question that we need to pose is whether it is feasible and logical to try to determine a contact angle on 3D structured surfaces, and if yes, how to define it independent of the different feature types and sizes to be able to generalize it.

Figure 4.11 presents the change in contact line radius of the growing water droplet on concentric triangular circles and pyramidal arrays. The periodicity measured from the contact line radius is stable for the small features and increases for the large features. On 0.2mm concentric triangular circles, the contact line pinning duration is 0.21 sec, whereas for 0.5mm pyramids it is 0.6 sec. On the other hand, for a concentric circular pattern made of 0.75mm pyramids the pinning durations ascend at 1 sec, 1.26 sec, and 1.87 sec as the volume increases. On the pyramidal arrays, the pinning duration is 0.27 sec for 0.5mm pyramids, which is half of the value for the 0.5mm concentric triangular circles. The first pinning lasts 0.51 sec and the second 0.81 sec for 1mm pyramids and for 2mm pyramids the pinning durations are 0.71 sec, 0.84 sec and 2.31 sec as the volume increases.

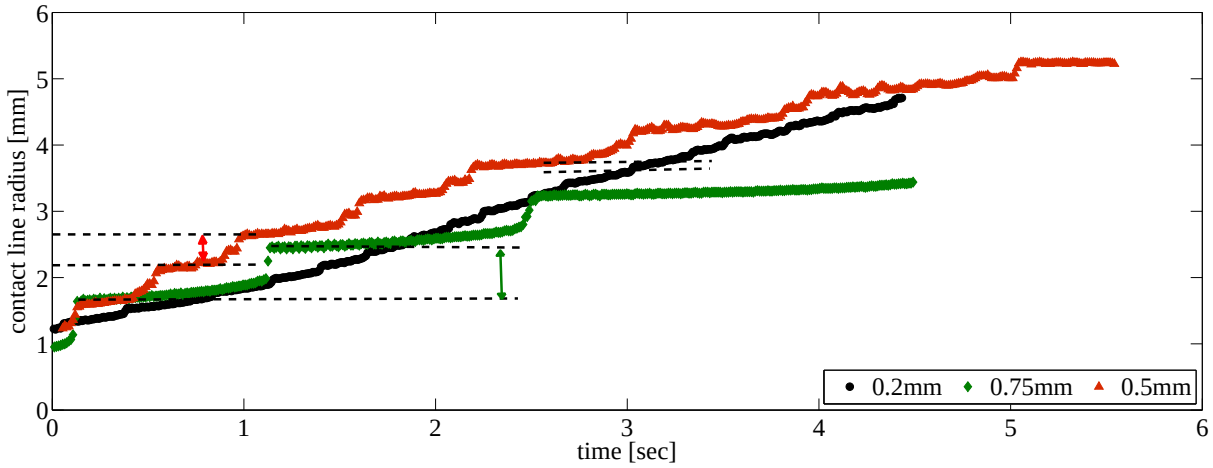

(a) The change of contact line radius of water droplet on three concentric triangular circles.

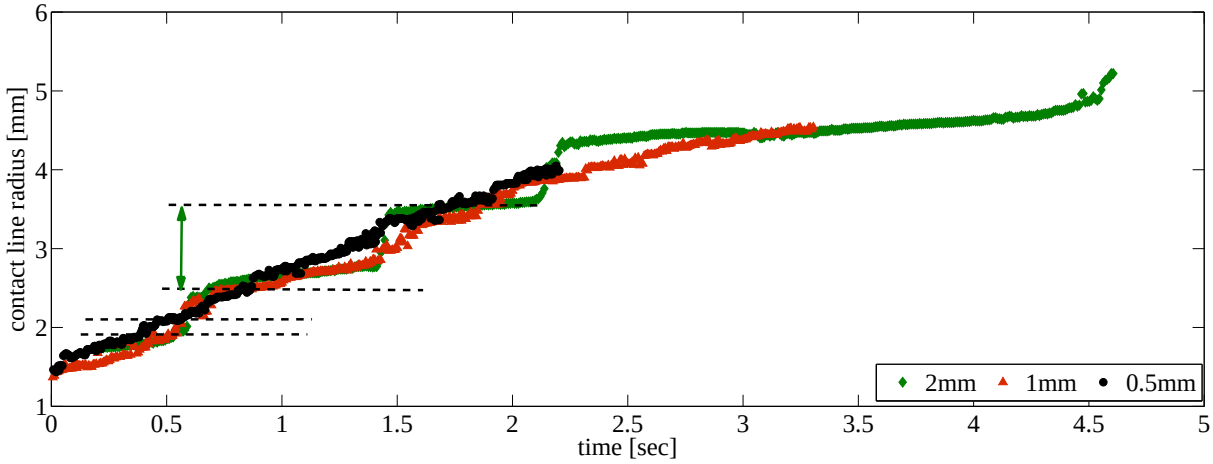

(b) The change of contact line radius of water droplet on three pyramidal arrays.

Figure 4.11: The dashed lines present the jumps of contact line between pyramidal features. The stepwise jumps exhibit a more evident periodicity on concentric triangular circles than on pyramidal arrays.

4.1.4.2 Glycerin-Water Mixture (85%-15% vol.)

Being a polyol, pure glycerin wets most high energy surfaces. A suspension with water decreases the viscosity, and slightly the density, but does not affect the surface tension greatly. A suspension of glycerin with water has a significant measurable contact angle compared to pure glycerin in the static case. [1]

The same experiment described previously for water has been repeated for glycerin. The dynamic contact angle is measured as the volume increases. Here the dynamic contact angle difference between the larger pyramidal structures and small concentric triangular circles is more noticeable than in the case of water. The dynamic contact angle is $\backsim$40% larger on concentric triangular circles than on the flat surface and the fluctuations are, as expected, greater on 0.75mm pyramidal concentric circles than on 0.2mm concentric triangular circles.

In the case of concentric triangular circles (see Figure 4.12a), the contact angle varies between 139°-132° for 0.2mm peak-to-peak, 141°-113° for 0.5mm peak-to-peak and, 142°-106° for 0.75mm peak-to-peak concentric circles. The amplitude is getting larger as the feature size gets bigger, which means that the liquid fills the grooves between the concentric features. For all features sizes, the liquid reaches almost the same maximum contact angle by pinning on the apex of the ridges. In the case of pyramidal arrays (see Figure 4.12b), the contact angle varies between 130°-98° for 0.5mm

[1] This information raises some question marks because it contradicts with Young's equation.

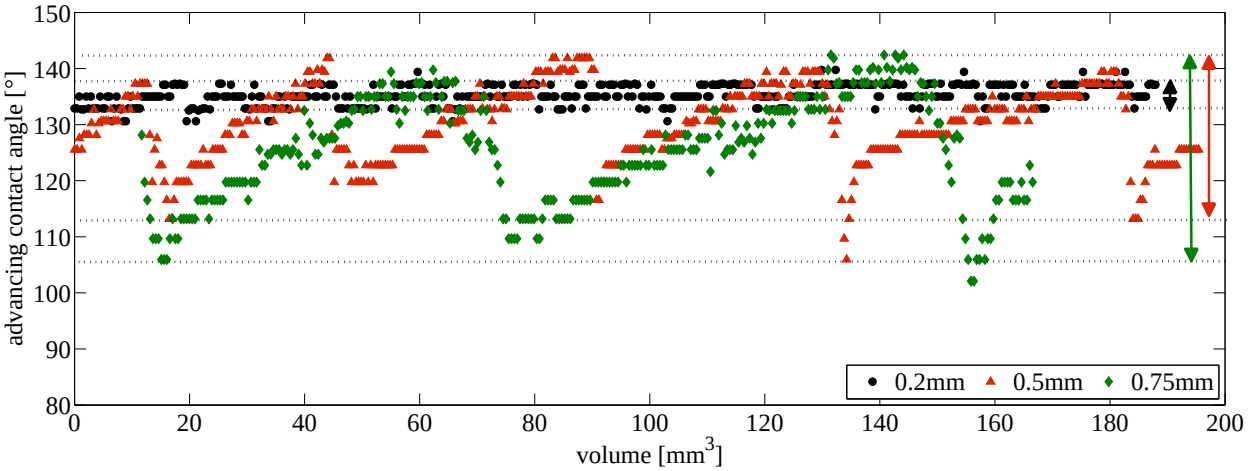

(a) Glycerin 85% droplet growing on three different concentric triangular circles.

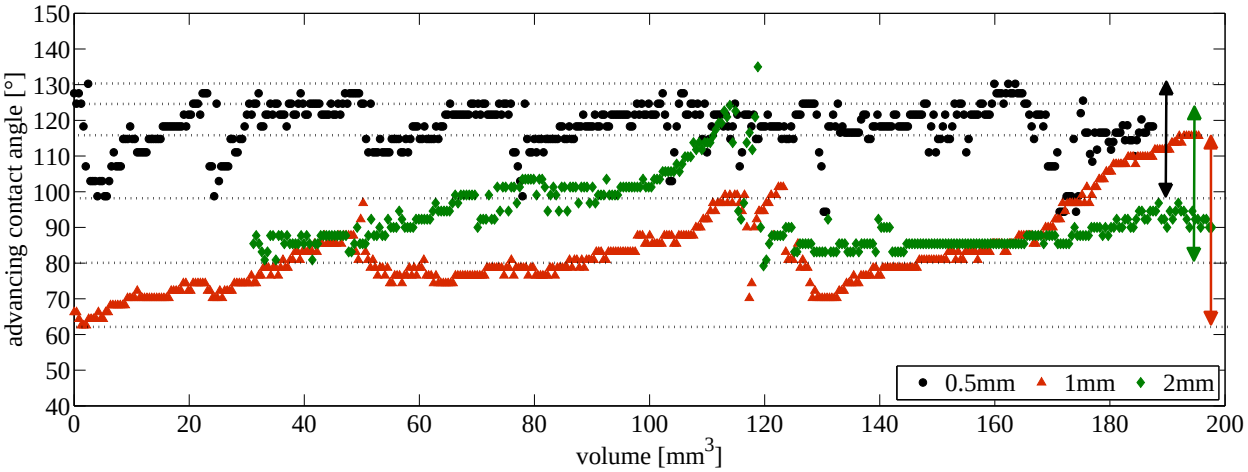

(b) Glycerin 85% droplet growing on 3 different pyramidal arrays.

Figure 4.12: The dynamic contact angle of the growing droplet of glycerin-water suspension is evidently larger on concentric triangular circles surfaces than pyramidal arrays. The double arrows show the difference between maximum and minimum contact angles.

peak-to-peak, 115°-62° for 1mm peak-to-peak and, 124°-79° for 2mm peak-to-peak pyramids. In this case, we do not observe any relation between the amplitudes and maximum/minimum contact angle. If we consider the question we posed in the previous subsection about the determination of contact angle on 3D array, we see that even for a very viscous fluid (∼100× more than water), contact angle determination becomes very unreliable due to the chaotic penetration of liquid and the non-systematic shape of the contact line.

Figure 4.13 presents the change in contact line radius of a growing water droplet on concentric triangular circles and pyramidal arrays. On 0.2mm concentric triangular circles, contact line pinning duration is 0.45 sec, whereas on 0.5mm pyramidal circles it is increasing in a stepwise fashion to 0.81 sec, 1.09 sec, 1.11 sec, 1.26 sec and on 0.75mm pyramidal circles it is 1.54 sec and 2.10 sec. On the pyramidal arrays, pinning duration is 0.71 sec for 0.5mm pyramids. In the case of 1mm and 2mm pyramids, the pinning time ascends gradually. The first pinning lasts 0.51 sec and the second 0.81 sec for 1mm pyramids, while for 2mm pyramids it is 2.16 sec and 2.3 sec.

4.1.4.3 Silicon Oil Variations (5/10/20/50 cSt)

Silicon oil is a good lubricant which is widely used in industrial applications. Being able to produce silicon oil of various viscosities enables us to fix the density and surface tension, and just examine the effects of viscosity. For the experiments, four different silicon oils are used whose viscosities are

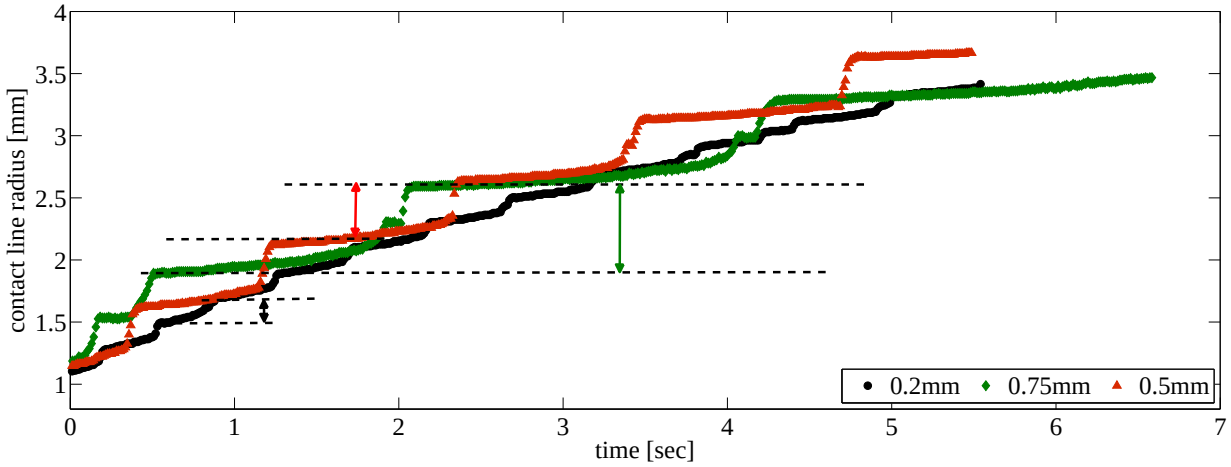

(a) The change of contact line radius of glycerin droplet on 3 concentric triangular circles.

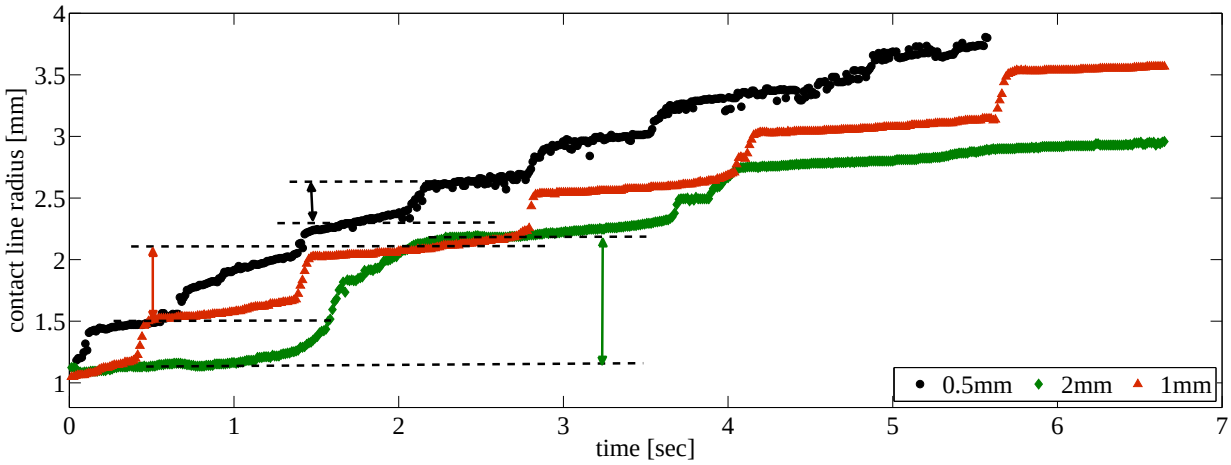

(b) The change of contact line radius of water droplet on 3 pyramidal arrays.

Figure 4.13: The dashed lines present the jumps of contact line between pyramidal features. The stepwise jumps are more periodic on concentric triangular circles than on pyramidal arrays.

respectively 5, 10, 20 and 50 times that of water, while they all have the same surface tension, equal to 1/3 that of water.

First of all the contact angle behavior of each silicon oil have been investigated separately for concentric triangular circles (see Figure 4.14) and 3D pyramidal structures (see *Appendix D*). Then the contact angle behavior for specific structures in terms of this dependence on viscosity is investigated. In the case of concentric triangular circles, each successive contact angle change starts with the sliding of the contact line in the groove, through the ridge until the apex, where the contact line pins shortly. For all silicon oils, a force driven oscillatory behavior in contact angle change is observed, which is caused by the increasing volume of the droplet. In table 4.4 it is shown that all silicon oil types have a stepwise increase in the maximum contact angle as the viscosity increases on concentric triangular circles. Moreover the difference between the maximum and minimum contact angles increases as the feature size increases. This is also indicated in figure 4.14 by the double arrows. In the case of large features and wide gaps between each peak, the liquid finds the chance to penetrate through the grooves and attains a larger contact angle change. These observations show us that, for the same type of liquid the feature size do not make a significant difference in the maximum advancing contact angle but larger features lower the minimum advancing contact angle and thus widens the amplitude of the contact angle change. On the other hand, the measured data on pyramidal arrays do not give any related or similar results to concentric circles due to problems with contact line detection. The grooves in the case of pyramidal arrays act like capillary channels, which is why the spreading of silicon oil

is controlled by the viscosity in the grooves. The data plots of silicon oil propagation on pyramidal arrays are given in *Appendix D*. In that case, the maximum contact angles change without any relation between viscosities and feature sizes. The measured values look very random and do not support any general conclusion.

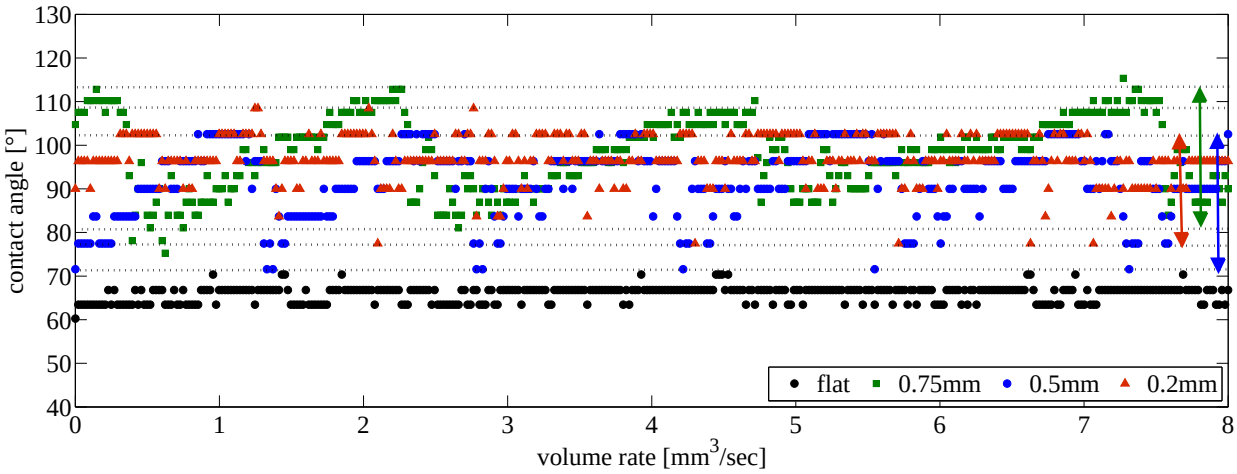

(a) Silicon oil 5cSt droplet growing on flat surface and on three different concentric triangular circles.

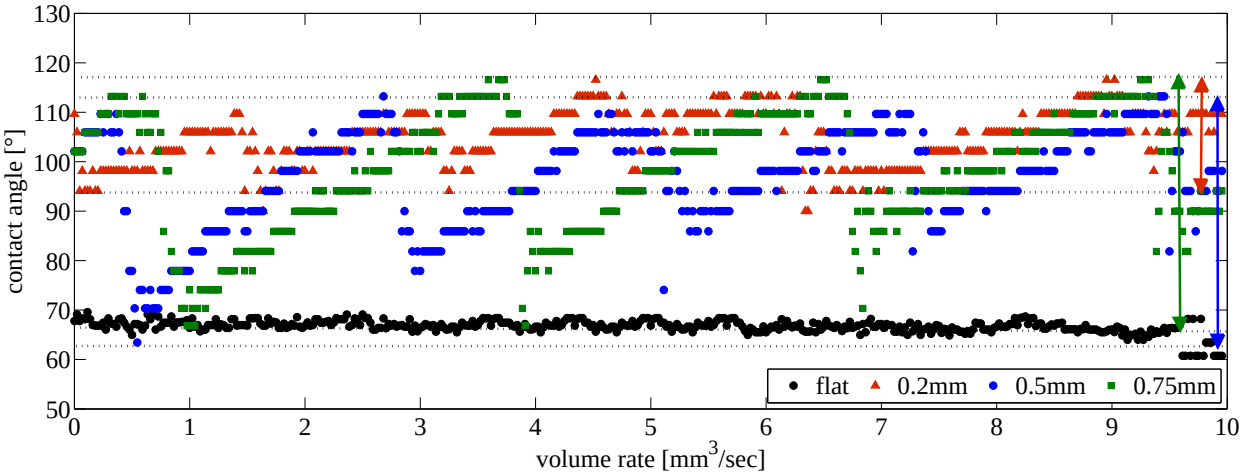

(b) Silicon oil 10cSt droplet growing on flat surface and on three different concentric triangular circles.

In figure 4.15 we see the stepwise oscillation of the contact line radius of the growing silicon oil droplets on concentric triangular circles. The periodicity ascends (force driven oscillation, where amplitude remains same but periodicity increases) as the feature size gets larger, and as the viscosity increases. Table 4.3 shows the ascending pinning durations for each silicon oil type on each concentric triangular circle.

feature type	silicon oil 5cSt	silicon oil 10cSt	silicon oil 20cSt	silicon oil 50cSt
0.2mm con.circ.	0.21 sec	0.32 sec	0.49sec	0.55 sec
0.5mm con.circ.	0.49 sec	1.16 sec	1.93 sec	0.75 sec
0.75mm con.circ.	0.55/0.75/0.92 sec	1.65sec	2.43 sec	1.45/1.92 sec

Table 4.3: Periodicity values of four silicon oil types on three concentric triangular circles.

Figure 4.16 and 4.18 show how the wetting liquid propagates though the grooves and acquires a polygonal shape and loses its spherical form. On small features, the less viscous silicon oil (5cSt) droplet adopts straight edges as the volume increases; however the more viscous silicon oil (50cSt) partially preserves its spherical features. The propagation direction is not homogeneous for all silicon

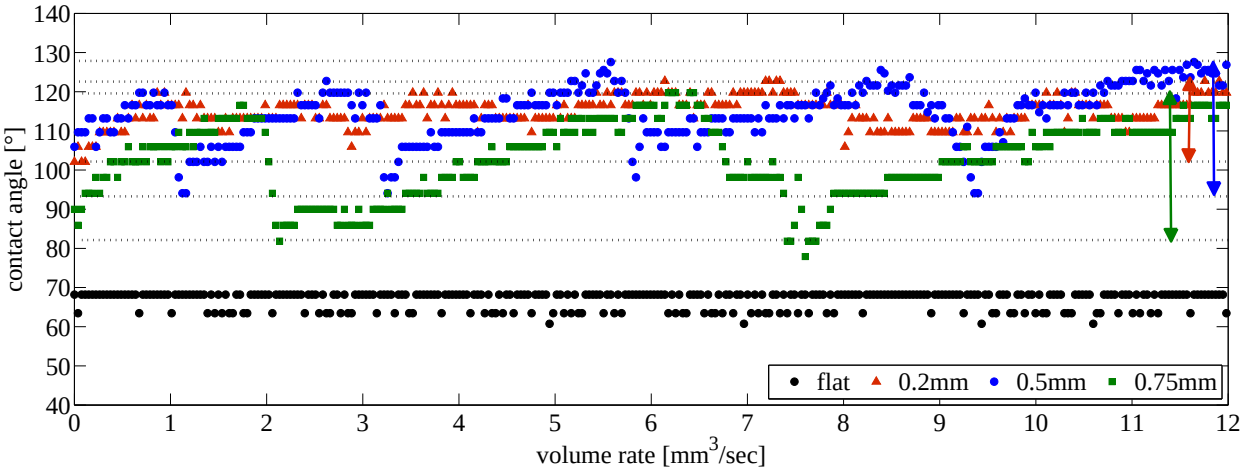

(c) Silicon oil 50cSt droplet growing on flat surface and on three different concentric triangular circles.

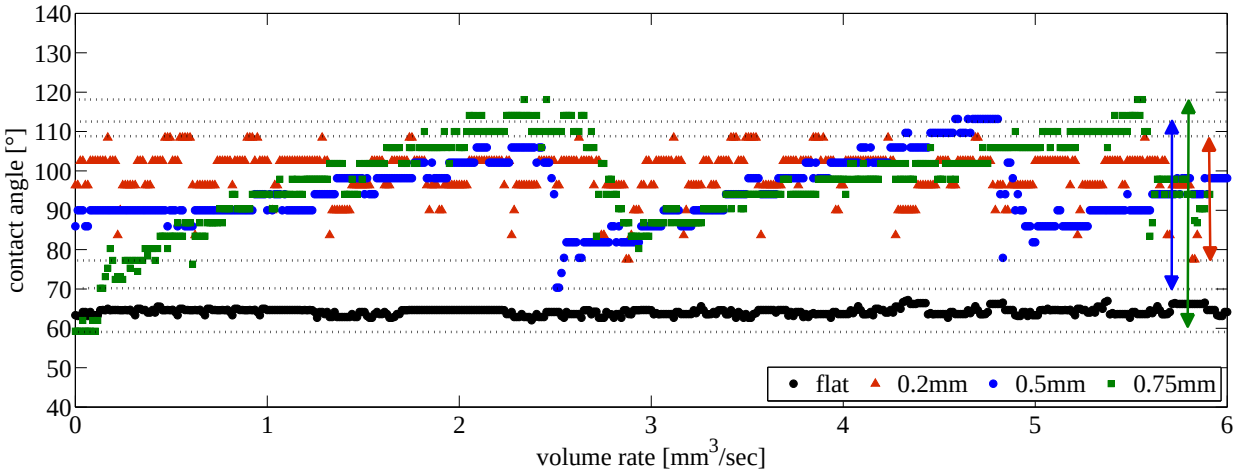

(d) Silicon oil 20cSt droplet growing on flat surface and on three different concentric triangular circles.

Figure 4.14: a) The growing droplet of silicon oil 5cSt displays very similar max. and min. contact angles. b) The minimum contact angle of the growing droplet of silicon oil 10cSt decreases as the feature size increases but the maximum contact angle measured on each substrate stays nearly the same, which is also valid for c) and d).

oil types. The liquid front designates a random propagation direction as seen in figure 4.18 (red arrows) and spreads out.

In figure 4.17, a comparison of contact angle change between the different fluids on each concentric circular pattern is drawn. Here we see that silicon oil 50cSt, having the highest viscosity, maintains the highest dynamic contact angle, and silicon oil 5cSt the lowest dynamic contact angle on all three concentric triangular surfaces. The dashed lines indicate the maximum contact angle. Overall, the dynamic contact angle with respect to volume change and feature size has a larger value than the average dynamic contact angle on the flat surface.

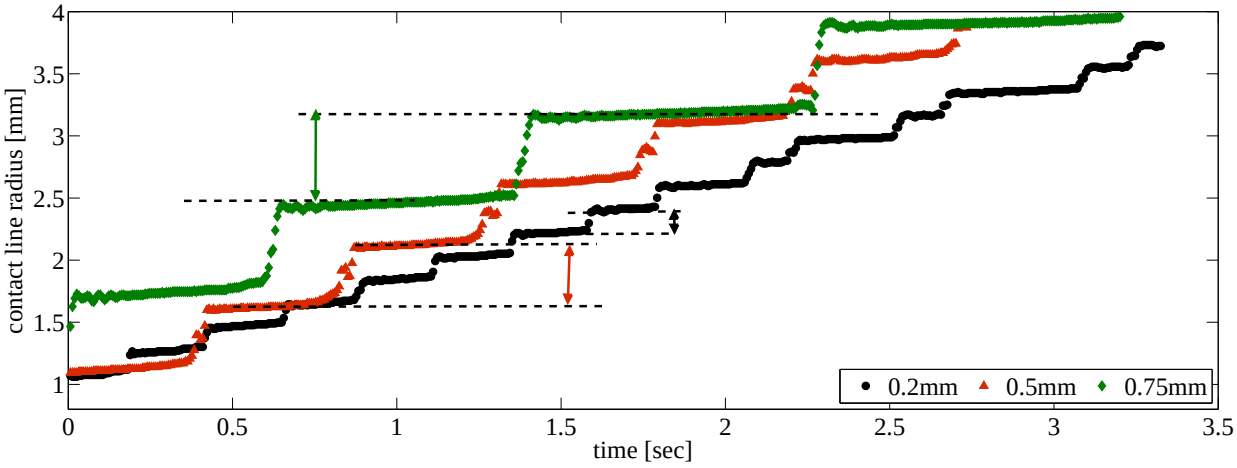

(a) The change of contact line radius of silicon oil 5cSt droplet on 3 concentric triangular circles.

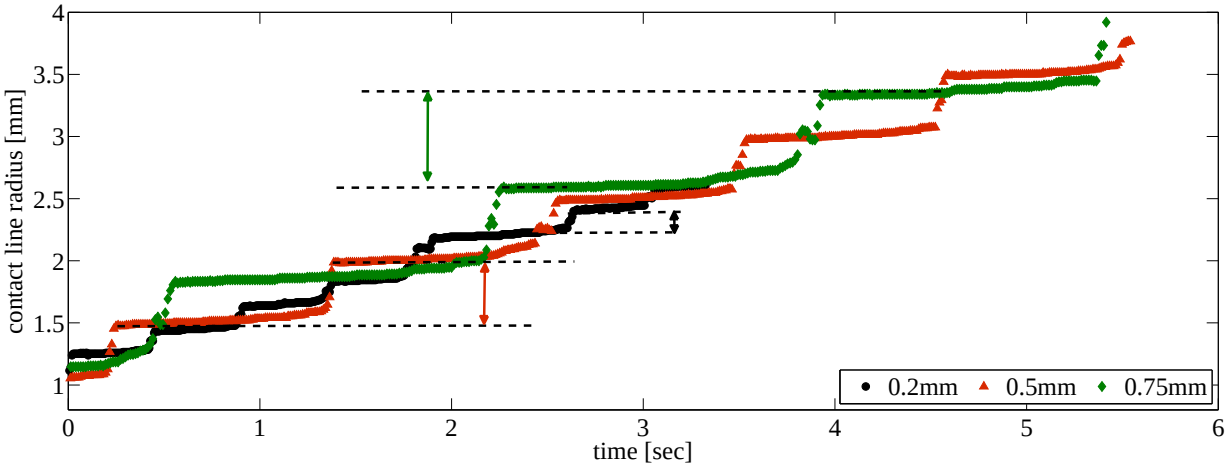

(b) The change of contact line radius of silicon oil 10cSt droplet on 3 concentric triangular circles.

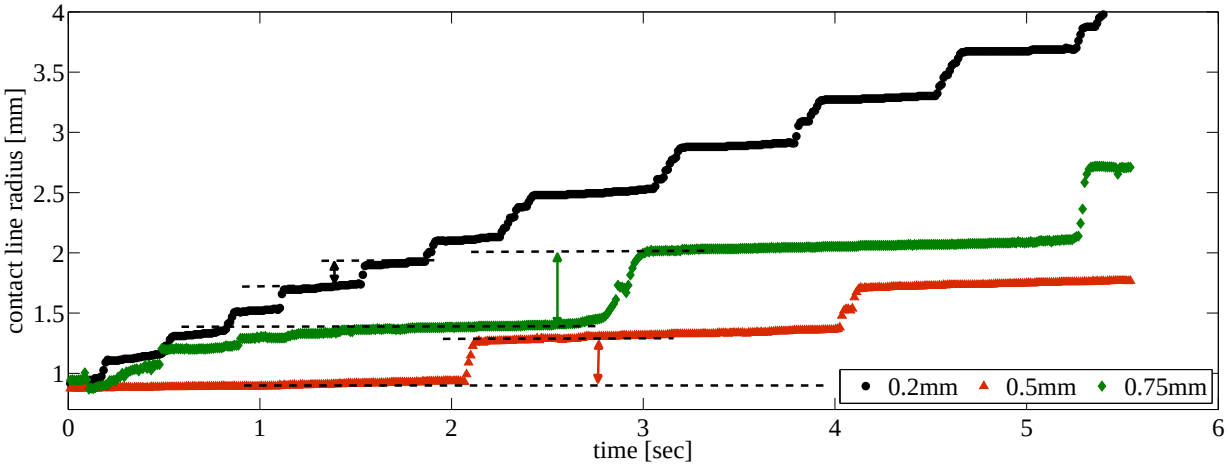

(c) The change of contact line radius of silicon oil 20cSt droplet on 3 concentric triangular circles.

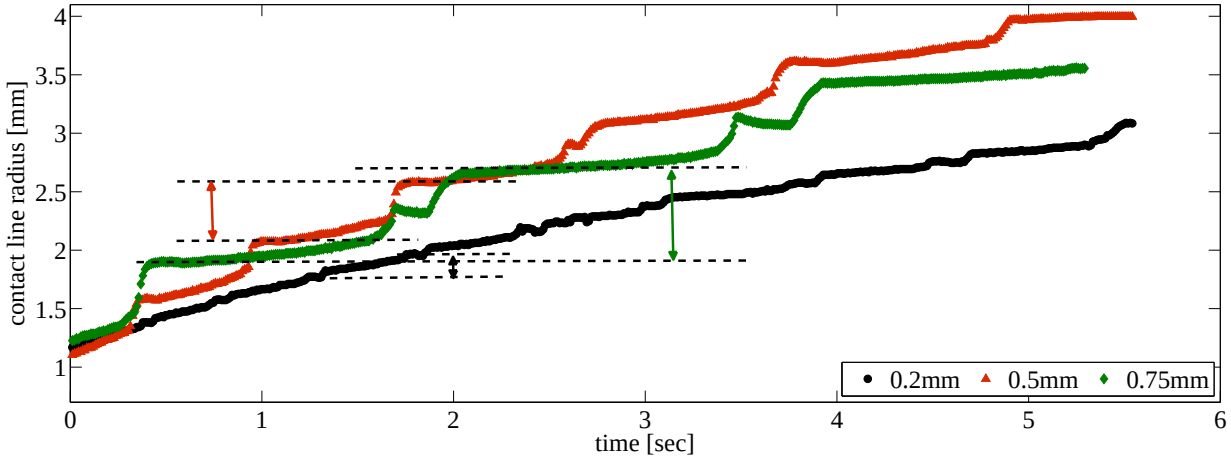

(d) The change of contact line radius of silicon oil 50cSt droplet on 3 concentric triangular circles.

Figure 4.15: The dashed lines present the periodic stepwise jumps of contact line between concentric triangular features.

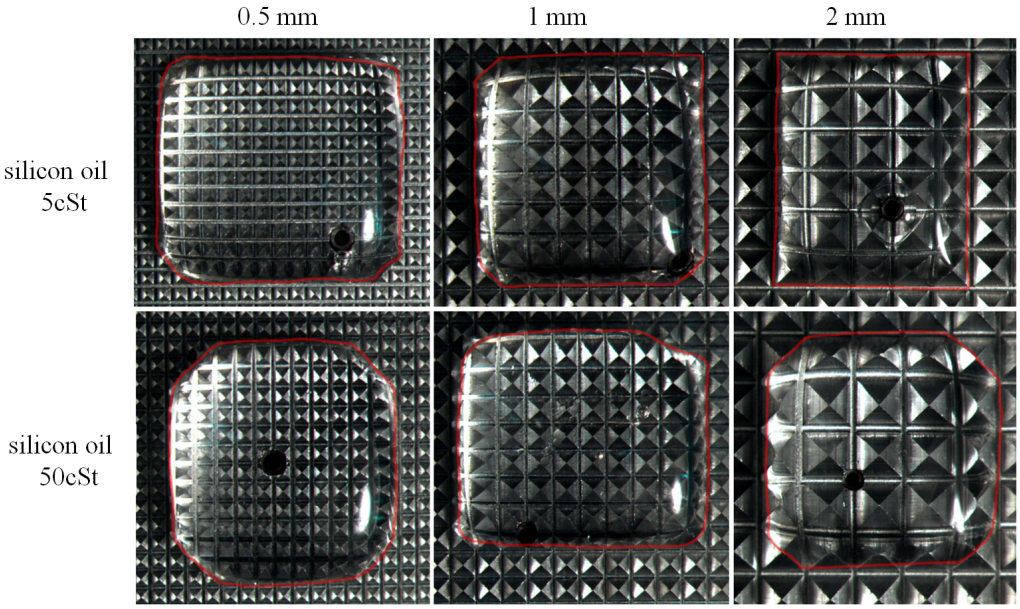

Figure 4.16: Comparison of the propagation of silicon oils in very low and high viscosities on pyramidal arrays of three different feature sizes. On small pyramids the polygonal contact line shape is less detectable. The red lines frame along the contact line.

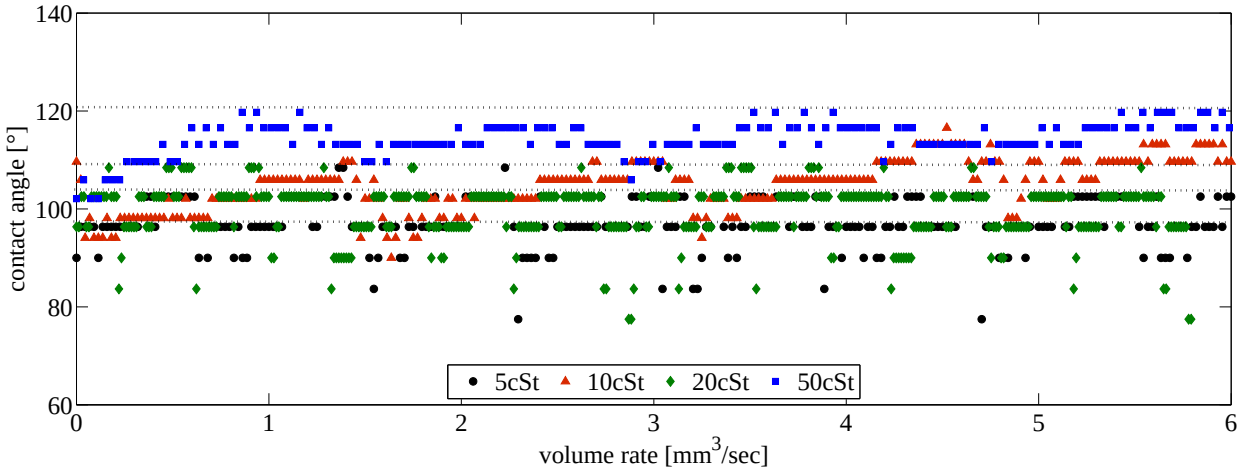

(a) Contact angle variation versus volume rate for all silicon oil types on 0.2mm concentric triangular circles.

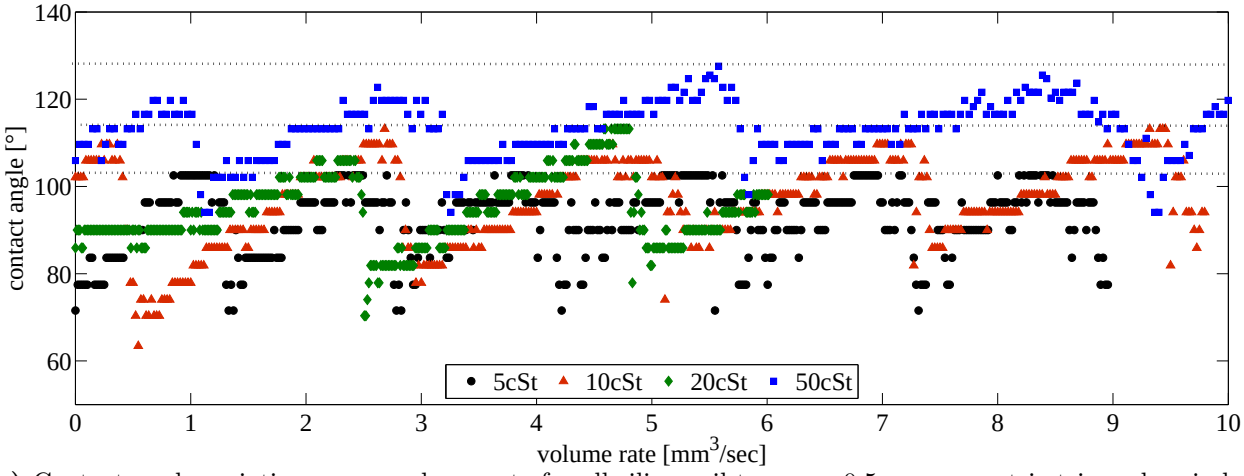

(b) Contact angle variation versus volume rate for all silicon oil types on 0.5mm concentric triangular circles.

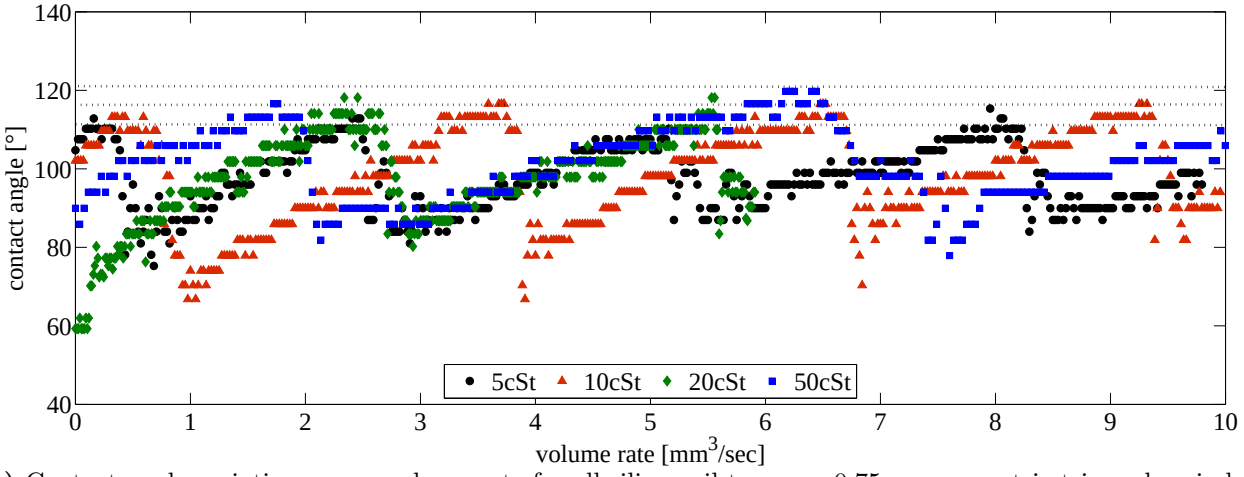

(c) Contact angle variation versus volume rate for all silicon oil types on 0.75mm concentric triangular circles.

Figure 4.17: Comparison of silicon oil variations on three different surfaces with concentric triangular circular features.

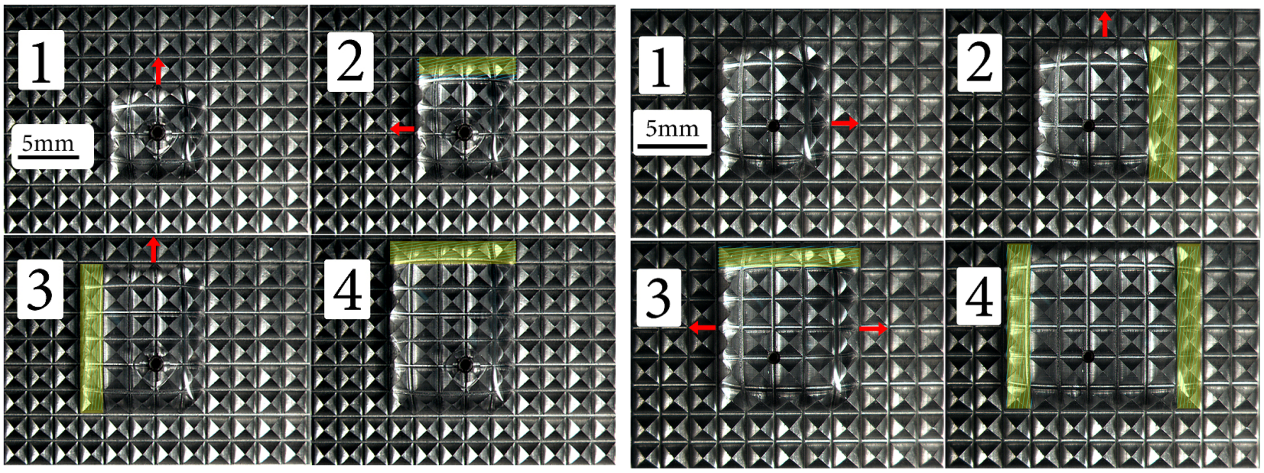

Figure 4.18: Overhead view recordings make it clear that silicon oil does not propagate in spherical form on the pyramidal arrays in a rectangular fashion, which causes a viscosity driven flow in the grooves. (Left) Silicon oil 5cSt is growing on 2mm pyramidal array. (Right) Silicon oil 50cSt is growing on 2mm pyramidal array. The propagation direction is indicated by a red arrow in each case. The propagated liquid is highlighted in yellow.

4.1.5 Discussion

The most important difference between concentric triangular circles and pyramidal arrays is the axisymmetrical arrangement, which hinders the penetration of the liquid from the source through the gaps in many directions inhomogeneously. In the case of concentric triangular circles, the entire contact line pins on the apex at once, then it is released from the apex by volume change, slides on the side of the triangle until it touches the next triangle (see Figure 4.19). After the jump to the next triangle, a local equilibrium state is reached, where the growing sessile droplet partially fills the grooves between each circle. The air in the grooves cannot escape due to the concentric form of the substrate and is trapped under the fluid at local equilibrium.

Comparison of Maximum and Minimum Contact Angles on Structured Features

features	water		gly.-water		sil. 5cSt		sil. 10cSt		sil. 20cSt		sil. 50cSt	
	max.	min.	max.	min.	max.	min.	max.	min.	max.	min.	max.	min.
concentric 0.2mm	150°	143°	139°	132°	108°	77°	116°	94°	108°	77°	122°	102°
	Δ=7°		Δ=7°		Δ=31°		Δ=22°		Δ=31°		Δ=20°	
concentric 0.5mm	145°	120°	141°	113°	102°	71°	113°	63°	113°	70°	127°	97°
	Δ=25°		Δ=28°		Δ=31°		Δ=50°		Δ=43°		Δ=30°	
concentric 0.75mm	148°	110°	142°	113°	112°	75°	116°	66°	118°	60°	120°	81°
	Δ=38°		Δ=29°		Δ=37°		Δ=50°		Δ=58°		Δ=39°	
pyramid 0.5mm	132°	111°	130°	98°	108°	46°	102°	81°	78°	51°	114°	52°
	Δ=21°		Δ=32°		Δ=62°		Δ=21°		Δ=27°		Δ=62°	
pyramid 1mm	124°	98°	115°	62°	90°	40°	85°	47°	99°	64°	87°	55°
	Δ=24°		Δ=53°		Δ=50°		Δ=38°		Δ=35°		Δ=32°	
pyramid 2mm	121°	77°	124°	79°	90°	22°	114°	24°	79°	51°	107°	24°
	Δ=44°		Δ=45°		Δ=68°		Δ=90°		Δ=28°		Δ=83°	
flat	∼125°		∼104°		∼64°		∼65°		∼66°		∼67°	

Table 4.4: Comparison of the maximum and minimum contact angles measured for advancing contact angle on three concentric pyramids and three pyramidal arrays. The standard deviation is between ±1°-4°.

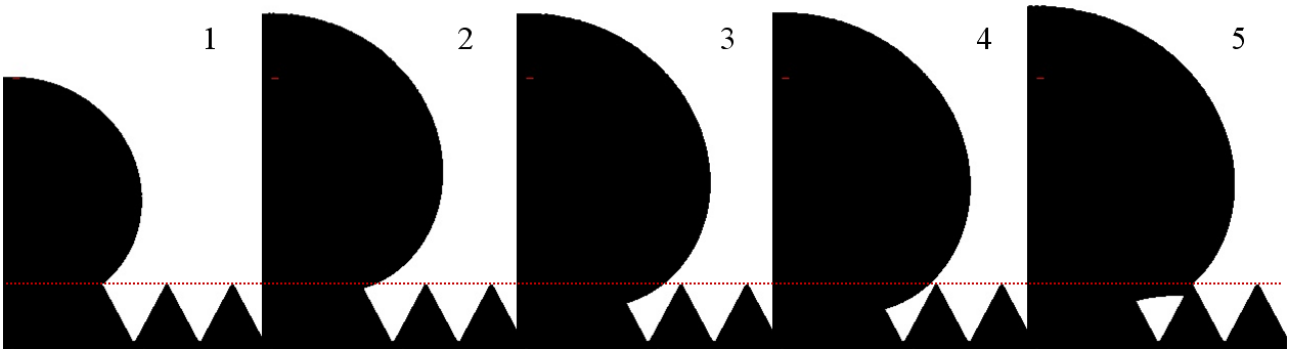

Figure 4.19: Formation of pinning. The dashed line shows the level of apices. At 1, the contact line is pinned. At 2, the volume increases as the contact line stays pinned. At 3 and 4, the contact line slides on the side of the triangle and at 5 the contact line jumps to the next triangle by covering an amount of air under the droplet.

In the pyramidal array case, the liquid has the ability to penetrate through the pyramids, attempting to minimize the surface energy. This prevents the air in gaps be trapped under the droplet. A point pinning occurs on the contact line on various pyramids and leads to additional flows through the grooves between the pyramids in many directions. These new flows couple with contact angle and reduce the difference between the maximum and minimum values. This formation is not periodic but systematic and very complex compared to concentric triangular circles. A point pinning (on pyramids) or an complete pinning (on concentric circles) of the contact line makes a big difference in the pinning strength of the surface. In table 4.4, the accessible average maximum and minimum advancing contact angles and the differences are given. In figure 4.20, these results are shown schematically. It is observed that for all liquids, the concentric circles increase the maximum accessible contact angle as the volume of the droplet increases. On the pyramidal arrays, maximum accessible contact angle for all test fluids remains between the contact angle values on the flat surface and on the concentric triangular circles. By using three different fluids (water, glycerin mixture and silicon oil) having three different surface tensions, it is observed that a higher surface tension causes a higher the maximum accessible dynamic contact angle. Moreover, it can be deduced that an increase in feature size for concentric triangular circles leads to an increase in the difference between the maximum and minimum contact angle values. The same cannot be claimed for the pyramidal arrays, where a non-homogeneous liquid propagation is formed. With these experiments, it can be assumed that the increment in surface tension causes a contact angle rise for the dynamic case (considering the values of water, glycerin mixture and silicon oil). Moreover for purely static cases, Cassie-Baxter and Wenzel suggested some models for rough surfaces, but considering our experiments, where the liquid is in quasi-steady state and cannot relax to the lowest energy state, these methods are not applicable.

According to hydrodynamic theory, the dynamic contact angle is a function of the capillary number, which contains the viscosity, surface tension and contact line velocity. The combination of viscosity, surface tension, and substrate feature size yield the maximum reachable contact angle in the hysteresis range for zero contact line velocity. In our case, to be able to check the isolated effect of viscosity on the maximum achievable contact angle on structured surfaces, four types of silicon oils (having the same surface tension and density but different viscosities) are used. It is observed that viscosity (at fixed surface tension and density) does not affect the contact angle on smooth flat surfaces but makes a slight difference on structured features. According to the observations, as the viscosity of the silicon oil increases, the maximum reachable contact angle on the structured surface increases. Moreover it is observed that the dynamic volume change (by pumping liquid and increasing the volume) does not affect the dynamic contact angle of the liquid on the flat surface, whereas on rough surfaces the dynamic volume change causes a contact angle rise depending on the surface feature characteristics. The red circle on figure 4.20 shows how the increase in viscosity causes a maximum accessible contact angle shift on the same concentric circled patter. The assumption is that a higher viscosity causes a higher contact angle as the volume increase. The high viscous liquid tends to pin longer on the apex as the volume of the droplet increases, where a larger pinning causes a larger contact angle. In our case, the maximum accessible contact angle is detected not on the peak but around the peak, at the end of slip on the triangle (on Figure 4.21 the dashed line labeled as 4). However the contact line is here slipping much slower as the drop size increases, which means that viscous force is dominant at this point.

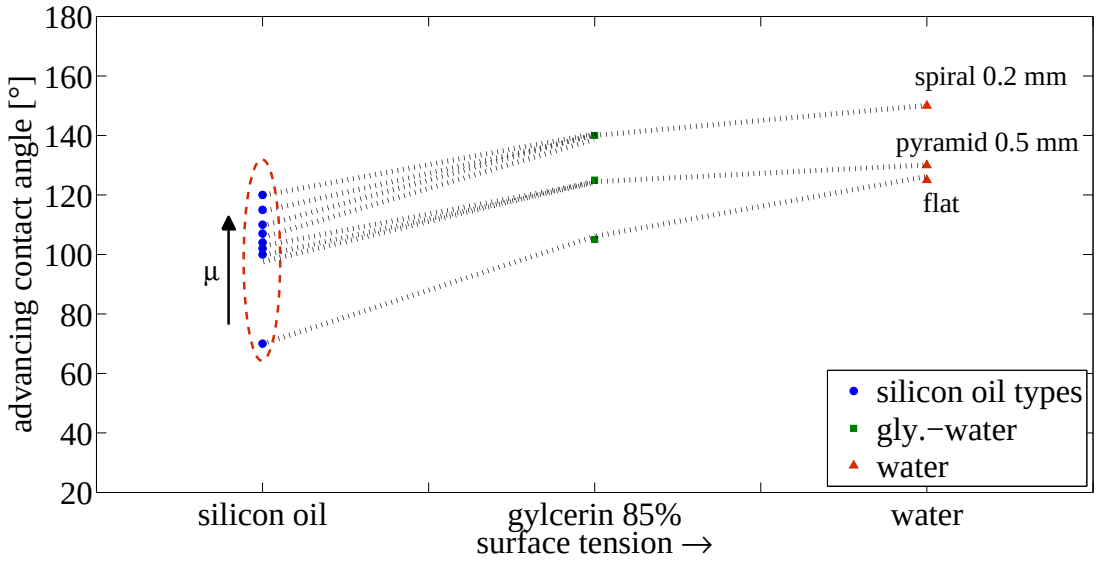

Figure 4.20: The maximum dynamic accessible contact angle depending on viscosity and substrate structure type.

Figures 4.21 and 4.19 present how the contact line develops during one period. The contact line pins on the apex for a long time, then slides very shortly until 1/4 of the peak-to-peak distance. Afterwards, the liquid front comes into contact with the apex of the next pyramid, followed by an associated abrupt jump in the contact line. The pinning duration on the apex of the feature gets larger as the viscosity of the liquid increases. The jumping duration is ∼8% of the whole period and the jumping velocity decreases from ∼10 mm/sec to ∼1.5 mm/sec as the viscosity of the fluid increases and the feature size decreases. Figure 4.22 and 4.23 show a single period consisting of pinning, sliding and jumping. Figure 4.23 presents that there are three velocity components in one period, pinning+sliding velocity, where viscous effects are dominant, a jumping velocity, where fluid is relaxing, and a forcing velocity, which is the forcing velocity from one peak to the other, respectively.

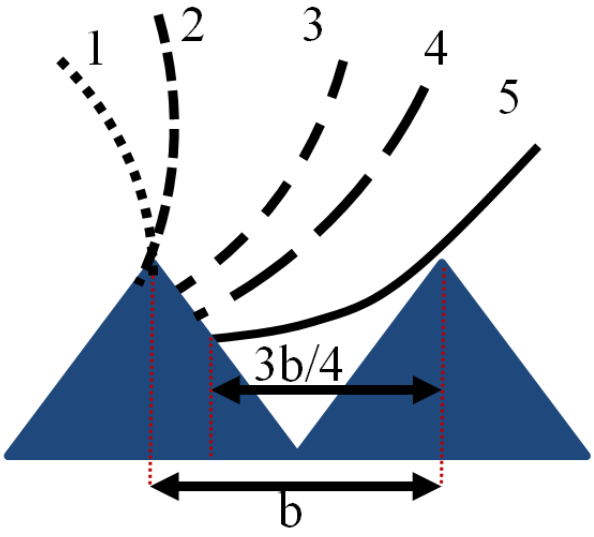

Figure 4.21: Formation of pinning. Between 1 and 3, the contact line is pinned on the apex. The contact line slips until 1/4 of the peak-to-peak distance (between 3 and 4) and jumps to the next apex (5).

The visco-capillary relaxation time is the time needed for the liquid to turn from an unstable state to a steady state and is equal to $t_{relax} = \frac{\mu \Delta l}{\sigma}$. Δl is the distance, where the liquid jumps from one triangle to the other (see Figure 4.22). The visco-capillary relaxation time for four types of silicon oil is in the order of milliseconds, which is very short compared to the rate of volume change. Forcing time is calculated as the ratio of feature size to contact line velocity at the jump ($t_{force} = \frac{peak-to-peakdistance}{v_{jumping}}$) and is 0.3 sec for the high viscous fluids (50cSt silicon oil and glycerin mixture). The Reynolds number during jump is in the order of 10^{-5} and the capillary number is in the range of 3.7×10^{-5} <Ca<0.006. Bond number based on feature size is in the range of 0.03<$Bo_{feature}$<0.3 and Bond number based on droplet size is in the range of 0.13<Bo_{drop}<4, which means that the droplet flattens by gravity by time.

In conclusion, by examining the gathered data it can be asserted that viscosity increases the advancing contact angle if the proper feature shapes are present. Just considering the four silicon oil types, it is observed that the most viscous oil reaches the highest dynamic contact angle and the less

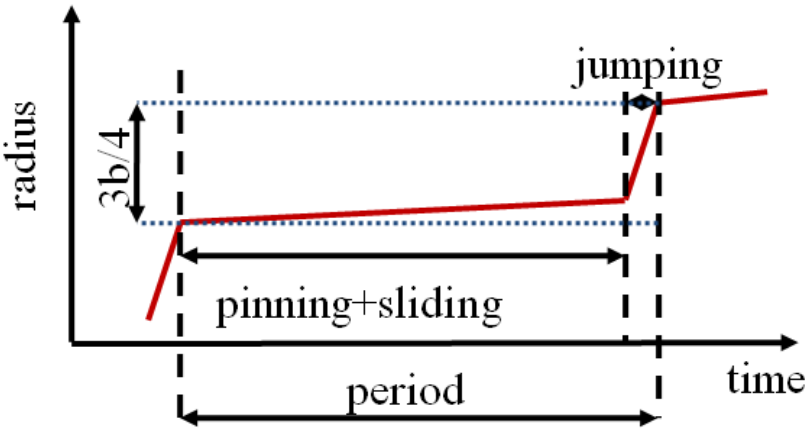

Figure 4.22: Duration of a full period consisting of pinning, sliding and jumping. Between two pinning points, the distance is 3/4 of the peak-to-peak distance.

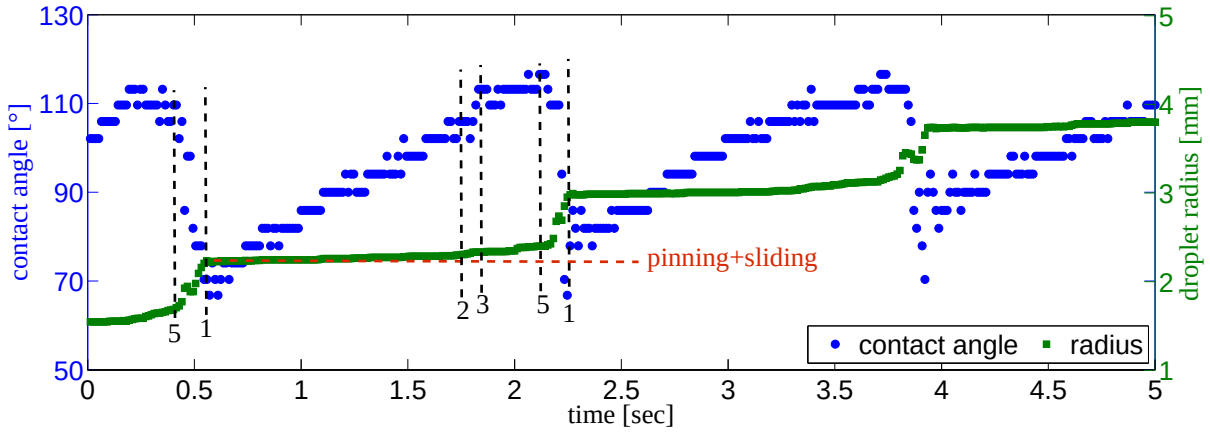

Figure 4.23: The contact angle and droplet radius change of a growing 10cSt silicon oil droplet on 0.75m concentric circle. The red line is the duration of pinning and sliding. Between the dashed lines, The numbers are relevant to the figure 4.21.

viscous oil reaches the lowest dynamic contact angle on the same axisymmetrically patterned substrate. A high viscosity value of the liquid causes a longer pinning duration, which enables a larger contact angle (in the case of fixed surface tension and density). The difference between the maximum dynamic contact angle of various silicon oils is larger on concentric triangular circle compared to the pyramidal ones due to the penetration of liquid through the gaps between the pyramids and the stronger pinning of the contact line on the concentric circles where the entire contact line is pinned at the same time. The jumping velocity from one peak to the next, decreases as the feature size gets smaller and the viscosity gets higher. The less viscous silicon oil (5cSt) on 0.75mm concentric circles has the highest jumping velocity, and the high viscous silicon oil (50cSt) on 0.2mm concentric circles has the lowest jumping velocity. Moreover by examining the contact angle measurement on 3D pyramidal arrays, we can conclude that the gathered data is not useful to analyze due to the complex, curved shape of the contact line and the contact line detection. Overall, the dynamic contact angle, affected by the change in volume and surface features, has a larger value than the average dynamic contact angle on the flat surface for all liquids, including water and glycerin-water mixture.

4.2 Numerical Simulations

In this study the fluid flow is governed by the conservation of mass and momentum as expressed by the continuity equation and the Navier-Stokes equation. The continuity equation, its integral form is

$$\frac{\mathrm{D}m}{\mathrm{D}t} = \frac{\mathrm{D}}{\mathrm{D}t} \iiint\limits_{(V(t))} \rho \,\mathrm{d}V = \iiint\limits_{(V)} \frac{\partial \rho}{\partial t} \,\mathrm{d}V + \iint\limits_{(S)} \rho v_i n_i \,\mathrm{d}S = 0. \tag{4.1}$$

This equation states that the rate of change of the mass inside a control volume is equal to the net flux of mass through its boundary.

Obviously, the conservation of momentum for the control volume V is given as

$$\vec{F} = \frac{\mathrm{d}}{\mathrm{d}t}(m\vec{v}) = \frac{\mathrm{D}}{\mathrm{D}t} \iiint\limits_{(V(t))} \rho\vec{v} \,\mathrm{d}V = \iiint\limits_{(V)} \frac{\partial(\rho\vec{v})}{\partial t} \,\mathrm{d}V + \iint\limits_{(S)} \rho\vec{v}(\vec{v}\cdot\vec{n}) \,\mathrm{d}S. \tag{4.2}$$

On the other hand, the force $\vec{F}$ can be written as the sum of two terms as

$$\vec{F} = \iiint\limits_{(V)} \rho\vec{k} \,\mathrm{d}V + \iint\limits_{(S)} \vec{t} \,\mathrm{d}S \tag{4.3}$$

where $\vec{k}$ and $\vec{t}$ denote the volume force and the surface force, respectively. Then, we can finally arrive at the Navier-Stokes equation for impulse conservation

$$\iiint\limits_{(V)} \frac{\partial(\rho\vec{v})}{\partial t} \,\mathrm{d}V + \iint\limits_{(S)} \rho\vec{v}(\vec{u}\cdot\vec{n}) \,\mathrm{d}S = \iiint\limits_{(V)} \rho\vec{k} \,\mathrm{d}V + \iint\limits_{(S)} \vec{t} \,\mathrm{d}S. \tag{4.4}$$

These equations, together with the respective boundary conditions, can be solved numerically.

4.2.1 Fundamentals of Numerical Simulations with OpenFOAM®

OpenFOAM® (Open Source Field Operation and Manipulation) is a C++ based, open source software, which uses predefined solvers to solve the numerical problem. OpenFOAM® utilizes the finite-element-method and the finite-volume-method for discretization. For the following simulations the predefined solver *interfoam* is applied. The solver uses a combination of the SIMPLE (Semi-Implicit Method for Pressure Linked Equations) algorithm for stationary problems and the PISO (Pressure Implicit with Splitting of Operations) algorithm for instationary problems. These algorithms are iterative processes to solve the Navier-Stokes equations for the velocity and pressure. The post-processing of the simulations is done with *ParaView*, which provides a graphical representation of the results, including vector fields or contours of the transition surfaces.

The solution region is divided by the numerical grid into cells. These cells represent the control volume, where the conservation equations are applied. In the middle of each cell exists a (nodal) point, for which the solutions for the various discrete field sizes are computed. The finite-volume-method uses the conservation equations in integral form for the cell walls of the control volumes. Due to the flux suspension over all cell walls in the computational domain, the method is globally conservative and therefore very popular for fluid mechanics problems.

The following equation shows the integral form of the conservation equation for a generic flow variable Φ:

$$\underbrace{\frac{\mathrm{d}}{\mathrm{d}t} \iiint\limits_{(V)} \rho\Phi \,\mathrm{d}V}_{\text{instationary term}} + \underbrace{\iint\limits_{(S)} \rho\Phi(\vec{v}\cdot\vec{n}) \,\mathrm{d}S}_{\text{convective term}} = \underbrace{\iint\limits_{(S)} \Gamma(\nabla\Phi\cdot\vec{n}) \,\mathrm{d}S}_{\text{diffusive term}} + \underbrace{\iiint\limits_{(V)} q_\Phi \,\mathrm{d}V}_{\text{source term}}. \tag{4.5}$$

In equation 4.5, the instationary term is solved with the help of the implicit Euler method. The convective term describes the flux from all sides of the control volume as a result of convection. The fluxes at each side of the cell are approximated by the central difference or updraft method. The

diffusive term (also called Laplace term) can also defined as in convective term by interpolation. In this study, the surface tension force, implemented as source term, is the impulse balance.

$$F_0 = \iiint_{(V)} \sigma\kappa\nabla\alpha \,\mathrm{d}V. \tag{4.6}$$

The curvature κ of the free surface is the divergence of the normal vectors $\vec{n}$ of the surface. Since this vector points in the same direction as $\nabla\alpha$, the curvature may be described as follows:

$$\kappa = -\nabla \cdot \vec{n} = -\nabla \cdot \left(\frac{\nabla\alpha}{|\nabla\alpha|} \right). \tag{4.7}$$

The discretization of time, space, and velocity is described by the Courant number, given as $C_0 = \frac{v\Delta t}{\Delta x}$. Since the space steps correspond to local cell size, the Courant number states how many cells are moving in a time step. For explicit methods a Courant number less than unity is used in order to prevent to skip of individual cells and keep the process stable.

In computational fluid dynamics, the volume-of-fluid (VOF) method, which is not a standard flow-solving algorithm, is a numerical technique for tracking and locating the fluid-fluid interface. The Navier-Stokes equations describing the motion of the flow have to be solved separately. The VOF method assigns for each cell a phase fraction α, which denotes the cell as empty (α=0) or full (α=1) with the predefined second fluid except surrounding phase. The transport equation (equation 4.8) is inserted in the solver to be able to calculate the phase distribution in forthcoming time steps. The changes added to convective term at each position change.

$$\text{transport equation } \frac{\mathrm{D}\alpha}{\mathrm{D}t} = \frac{\partial\alpha}{\partial t} + \vec{v} \cdot \nabla\alpha = 0 \tag{4.8}$$

Among the advantages of VOF is its frugality in terms of computing resources over the *marker-and-cell* method, which has relatively high memory and computational requirements. The reason is that while the marker-and-cell method has to calculate the motion of the particles in addition to the solving the equations of the flow field, only a single additional equation needs to be solved in VOF. Another important point is that the conservation of mass is guaranteed, which is a great expense for *level-set method*. Moreover changes in the surface topology can be readily handled by VOF and the rupture or the connection of surfaces can be calculated. In addition, the VOF method is easily extensible to additional phase fractions α, so as to be used for flows with more than two phases.

Among the disadvantages of the VOF method is the fact that the interface must be reconstructed and the exact course of the phase boundary is not known immediately after the solution of the transport equation. Furthermore, in the numerical approximation of the interface, the free surface of low-order methods are smeared and there may be an artificial mixture of the two phases. Higher order methods often lead to instabilities. So a compromise must be made and sudden changes of the phase distribution from $\alpha = 0$ to $\alpha = 1$ cannot be obtained.

4.2.2 Numerical Parameters Used in Computation

In order to simulate the experiments mentioned in the beginning of the chapter, the same volume change in time is implemented in simulation. The temperature of the liquid(s) and the surrounding are fixed at 25°C to avoid thermodynamic effects. The ambient pressure is fixed at 1 atm. Structured surfaces similar to those used in the experiments are created with the ICEM CFD software from CAD sketches and a structured grid out of hexahedrons is produced to be able to realize a 3D simulation environment. The hexahedronal grid enables a the maximum possible number of neighboring cells, where the orthogonality between the cells is maximum. This hinders the non-physical behavior of the flow at the contact line. As contact angle model, an implementation of Kistler's model (Hoffman's law) is used. For the implementation of Kistler's model (Hoffman's law) the same procedure as in the dissertation of Berberovic [96] and Jasak [97] is used. To be able to determine the iterative roots of Hoffman's empirical equation (equation 4.9), Ridders' numerical method [98] is used, which is a variation of the false position method.

$$x^{0.706} - \frac{1}{5.16}\left[1 + 1.31x^{0.99}\right]^{0.706} \tanh^{-1}\left[\frac{1-\cos\,\theta_e}{2}\right] = 0, \quad \text{where} \quad x = f_{Hoff}^{-1}(\theta_e), \tag{4.9}$$

This numerical variation of Ridders finds the center of the two points, which have opposite algebraic signs, where in between the possible root should exist. Then by using this new central point (x_3), another point is calculated (x_4) by equation 4.10b, which is closer to the root of the equation. This process continues as well, until $f(x_n)$ drop below the tolerance limit around zero.

$$x_3 = \frac{x_1 + x_2}{2} \tag{4.10a}$$

$$x_4 = x_3 + (x_3 - x_1)\frac{\text{sign}[f(x_1) - f(x_2)]f(x_3)}{\sqrt{f(x_3)^2 - f(x_1)f(x_2)}} \tag{4.10b}$$

4.2.3 Numerical Results and Comparisons with Experiments

Due to the significant difference in liquid properties, water and glycerin-water mixture (85%-15% vol.) are chosen as the simulation liquids. The glycerin mixture has a viscosity 100 times larger than that of water, which makes the simulation shorter compared to water for the same time interval. Surface tension affects the magnitude of the pressure jump across the interface. The fluid velocity near the interface in this case is solely due to the oscillation of the interface, which is also known as parasitic current. The restricted computational time is mainly due to the low parasitic flows at the interface, which is provided by the dominant surface tension over parasitic flow on the surface. It is also related to the mesh construction in the simulation. The magnitude of the parasitic current increases with the mesh resolution. For a proper discretization of the VOF function, the magnitude of these currents has to be decreased as the mesh size increases. This is why a detailed but not very fine mesh is used in these simulations. The mesh resolution is 125μm$\times125\mu$m for a single cell.

The simulation results for water and glycerin (85%) droplets on flat surfaces indicate an exponential growth, which is less obvious in experiments (see Figures 4.24a and 4.24b). In the case of water droplet experiments, the growth of contact angle is nearly linear, although for the glycerin (85%) droplet it is slightly exponential. In the case of contact line diameter change on pyramidal arrays, the simulation results show qualitatively the same characteristic zig-zag evolution observed in experiments. Both in experiments and simulations it is observed that there is an oscillatory behavior both on the vertical and horizontal axes, respectively in time and contact line diameter. Due to the 3D array structure, the oscillation is neither simple harmonic nor damped. The chaotic fluctuations of the change in data makes it difficult to compare the simulation and experimental results, but it cannot be claimed that the simulations are completely irrelevant to the experimental data. The intervals on the x-axis (time) are large in the beginning because the contact line stays pinned for longer on the apices as the volume is small. As soon as the volume gets larger, the energy needed to escape from pinning becomes smaller and the jumps become more frequent. The jumps on the y-axis (contact line diameter) in both water and glycerin (85%) droplet simulations give exactly the peak-to-peak distance of the features, which evidences the pinning on the apices. In experiments, the jumps on the y-axis (contact line diameter) for water and glycerin (85%) droplets yields the same peak-to-peak values on both 0.5mm and 1mm pyamidal arrays.

Moreover, figures 4.24a and 4.24b show us that the penetration on structured surfaces is restricted by the pyramids. Due to this, both water and glycerin mixture are able to propagate faster on flat surfaces than on structured surfaces with hindrances. Glycerin possesses a smaller surface tension than water by 18% and a 100$\times$ larger viscosity, which makes the penetration in the simulations slower compared to water. At the end of 1 second, water's simulated contact line diameter reaches $\backsim$5mm while glycerin's contact line diameter reaches $\backsim$4.5mm, on a flat surface. One of the reasons for that is the equilibrium contact angle on a flat surface, which affects the height and contact line diameter of the drop.

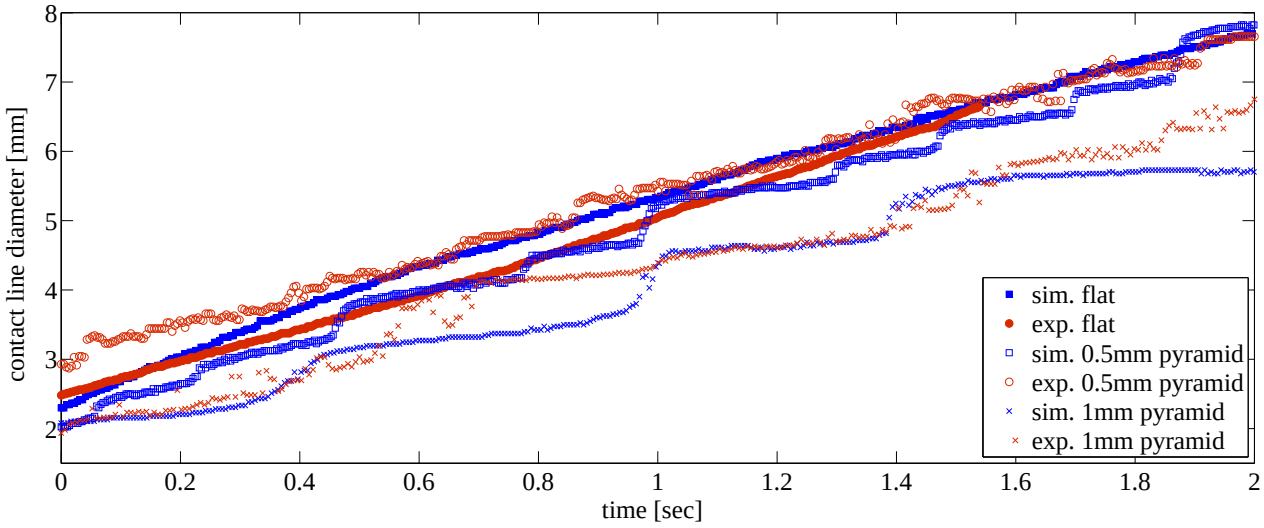

(a) Simulation and experimental results for contact line diameter versus time for water droplet on flat surface and two different pyramidal structures.

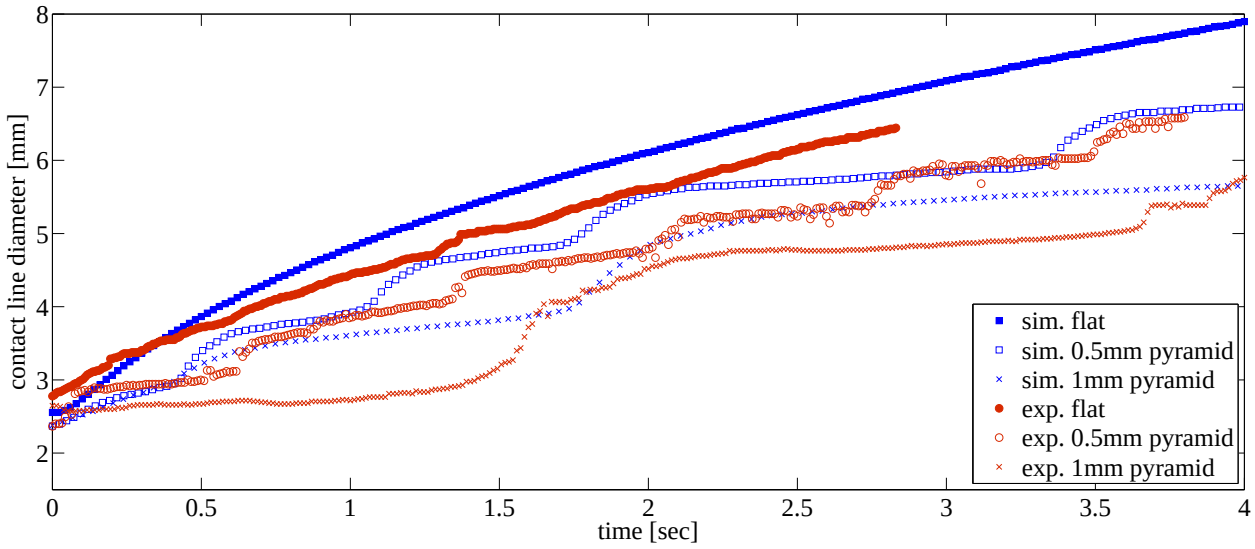

(b) Simulation and experimental results for contact line diameter versus time for glycerin (85%) droplet on flat surface and two different pyramidal structures.

Figure 4.24: Comparison of the contact line diameter evolution for water and glycerin mixture droplets.

For the two cases of simulations with water and glycerin-mixture, the equilibrium contact angle on a flat surface is taken to be 127° and 103°, respectively, as an initial boundary condition. However according to the numerical simulation results, the dynamic contact angle of the water droplet on a flat surface starts from 115° and increases until 132°, which is in contrast with the experimental result, where the contact angle fluctuates between 123°-126° from the beginning of the drop evolution. On the other hand, the contact angle of the glycerin (85%) droplet oscillates between 101°-106° in simulations and between 102°-108° in experiments. Figures 4.25b/c and 4.26b/c show the comparison of experimental results for contact angle change versus time for water and glycerin (85%) droplets on 0.5mm and 1mm pyramidal arrays. We see that the applied Kistler's model exhibits a pretty good matching of the simulation data to the experiments. Here it can be seen that the simulation results for the contact angle for water and glycerin (85%) droplets on 0.5mm pyramidal arrays deviate up to 10° from the experimental results.

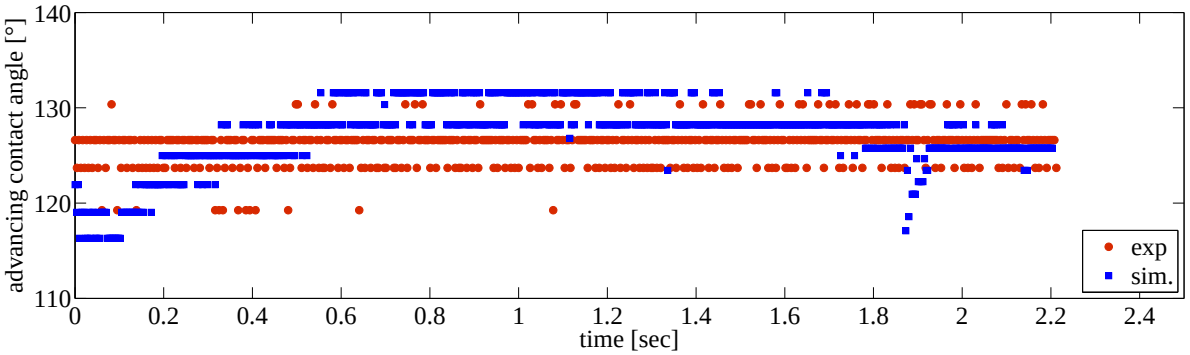

(a) Simulation and experimental results for dynamic contact angle on flat surface.

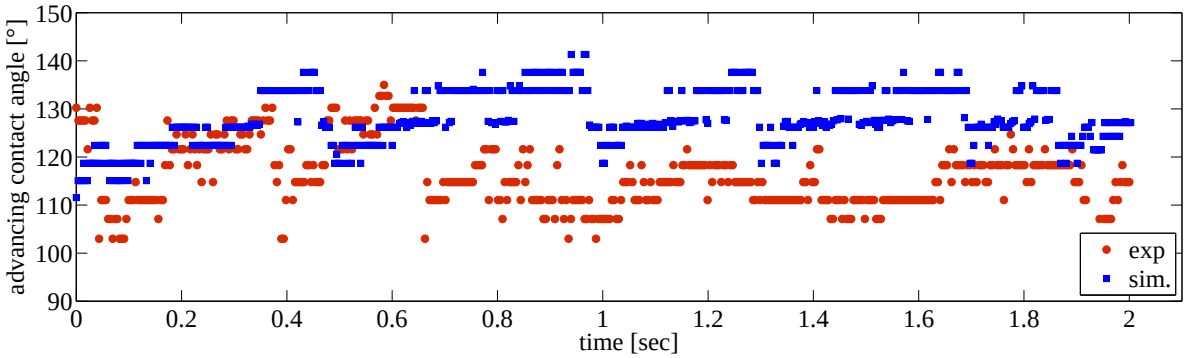

(b) Simulation and experimental results for dynamic contact angle on 0.5 mm pyramidal array.

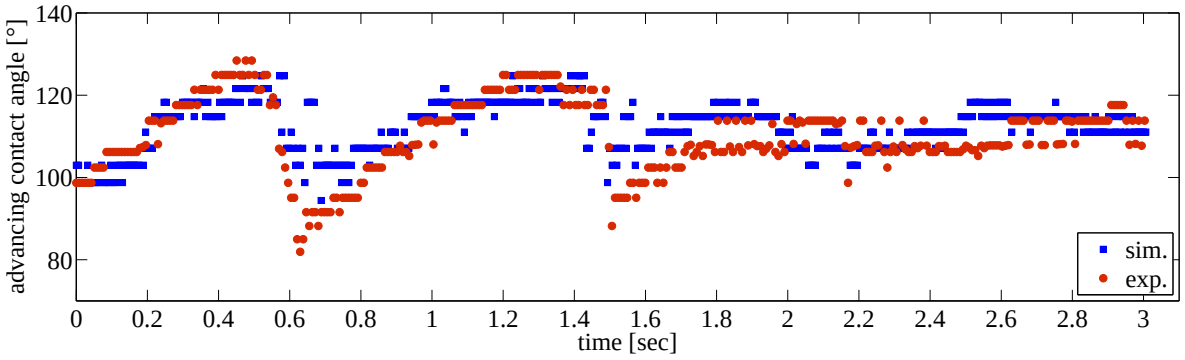

(c) Simulation and experimental results for dynamic contact angle on 1 mm pyramidal array.

Figure 4.25: Comparison of numerical simulations and experimental results for water.

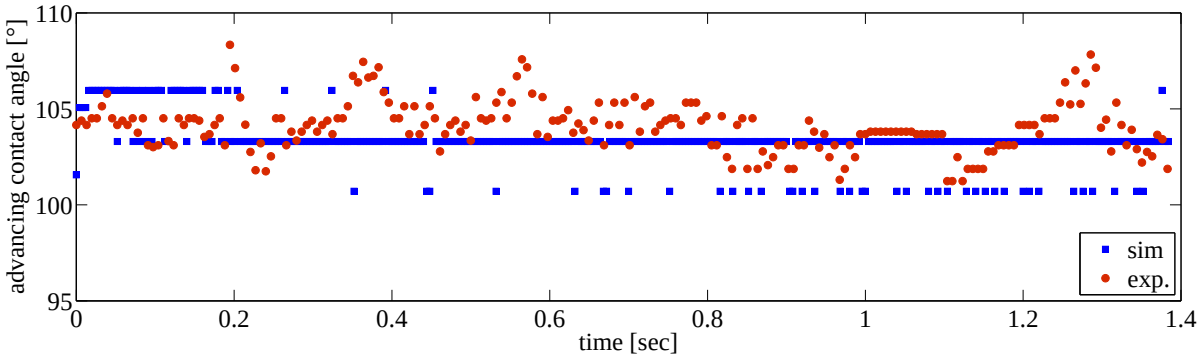

(a) Simulation and experimental results for dynamic contact angle on flat surface.

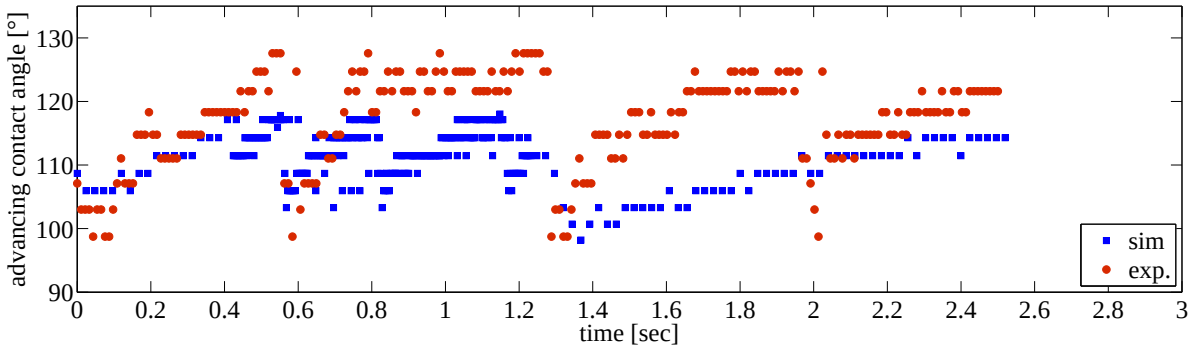

(b) Simulation and experimental results for dynamic contact angle on 0.5 mm pyramidal array.

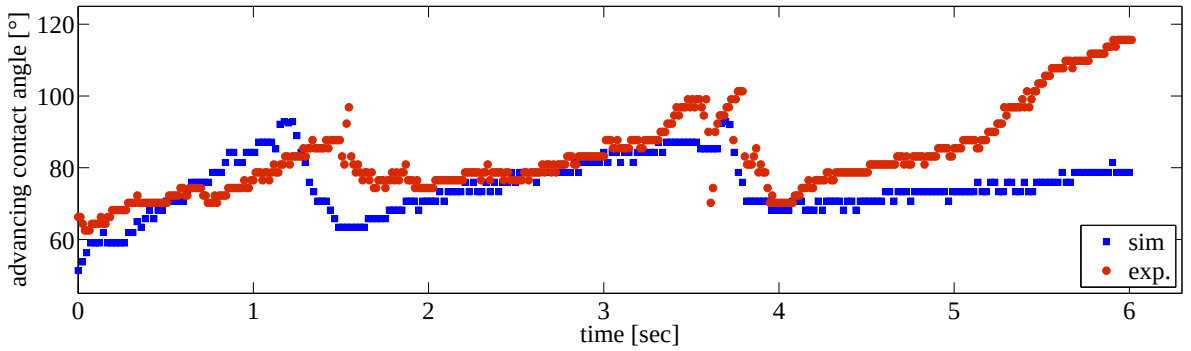

(c) Simulation and experimental results for dynamic contact angle on 1 mm pyramidal array.

Figure 4.26: Comparison of numerical simulations and experimental results for glycerin-water mixture (85%-15% vol.).

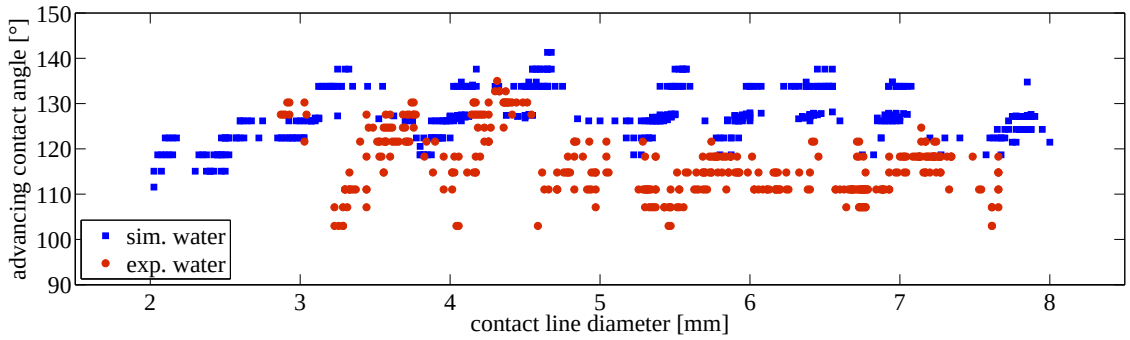

(a) Simulation and experimental results for dynamic contact angle on 0.5 mm pyramidal array for water as a function of contact line diameter.

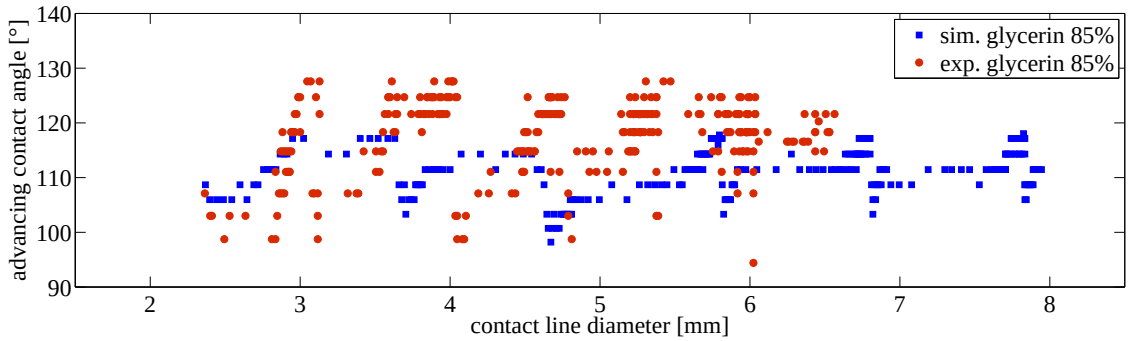

(b) Simulation and experimental results for dynamic contact angle on 0.5 mm pyramidal array for glycerin mixture as a function of contact line diameter.

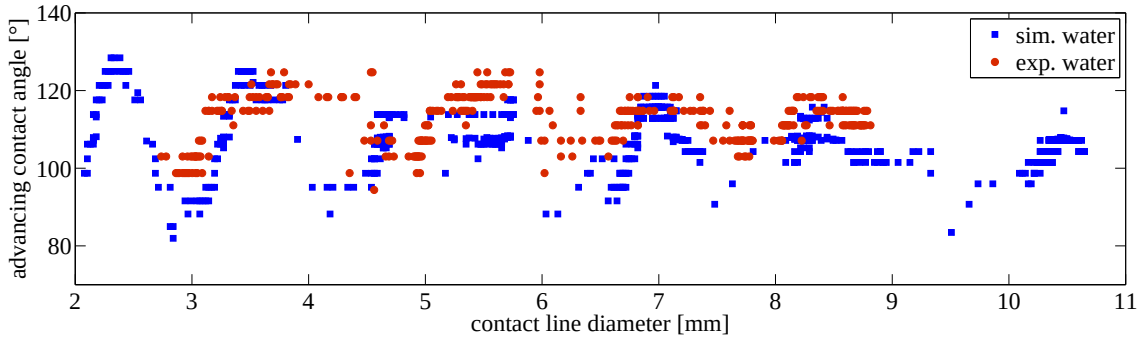

(c) Simulation and experimental results for dynamic contact angle on 1 mm pyramidal array for water as a function of contact line diameter.

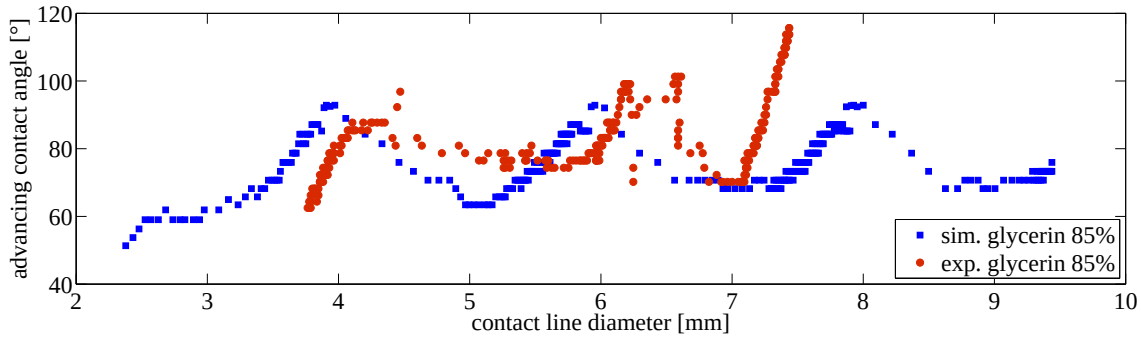

(d) Simulation and experimental results for dynamic contact angle on 1 mm pyramidal array for glycerin mixture as a function of contact line diameter.

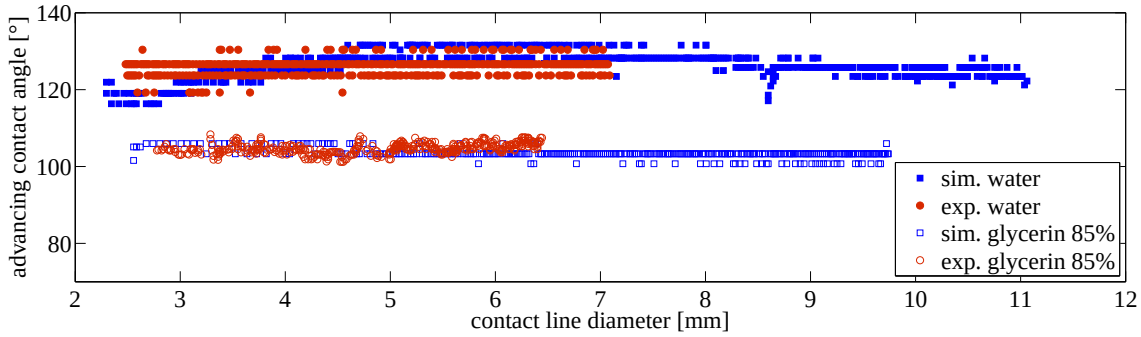

(e) Simulation and experimental results for dynamic contact angle on flat surface for water and glycerin mixture as a function of contact line diameter.

Figure 4.27: Comparison of water and glycerin-water mixture in terms of the relation between contact angle and contact line diameter..

4.2.4 Discussion

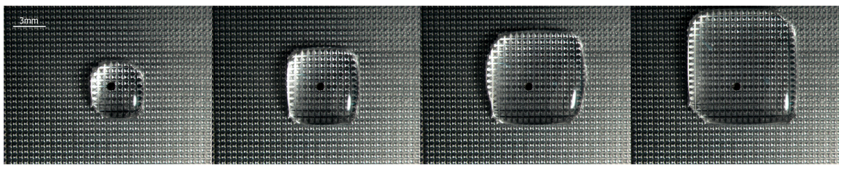

(a) Top snapshots from experiments of glycerin mixture on 1mm pyramidal array with a time step of 0.6 seconds.

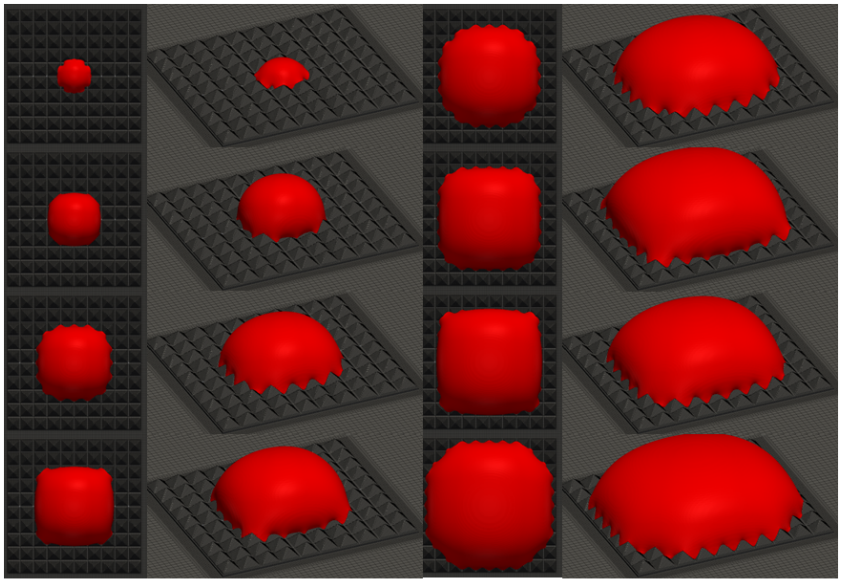

(b) Top and side snapshots from numerical simulations of glycerin mixture on 1mm coated pyramidal array with a time step of 0.2 seconds.

Figure 4.28: Simulation and experimental results for growing glycerin mixture droplet on 1mm pyramidal array.

By assigning the equilibrium contact angle, obtained from experiments, to Kistler's equation, compatible numeric results for growing liquid droplets on pyramidal arrays are achieved. Being a low viscosity liquid, water shows discrepancies in simulations on small pyramids, where the inertial forces

are dominant. On the other hand, water simulations on large pyramids show more consistent results with experiments. As for the highly viscous glycerin mixture, the agreement between simulations and experiments are poor in the case of small features, where viscous forces are dominant, but on large pyramids the simulation results are very compatible.

Figure 4.28a shows top view snapshots of a growing glycerin (85%) droplet on a coated 1mm pyramidal array. The polygonal growth of the droplet due to the coating on the surface was able to be simulated by using Kistler's dynamic wetting model. Figure 4.28b shows the top and side views of the simulated droplet under the above mentioned experimental conditions. The complex curved contact line is very clear to observe on simulation images compared to the experiment images because of the optical refractions and reflections caused by the transparent liquid and shiny surface in experiments.

Overall, both qualitative and quantitative data demonstrate that the applied Kistler model is an appropriate choice for dynamic wetting simulations on very rough surfaces. However some additional corrections and shift factors might be needed for a better agreement between simulations and experiments. The applied Kistler equation is applicable only for contact angles smaller than or equal to 135◦. For contact angles smaller than 135◦, a shift factor of $f^{-1}_{Hoff}(\theta_0)$ is added to the capillary number, where θ_0 is the nonzero static contact angle. This shift factor can be modified for a more general application. Moreover, the contact angle might not be the only initial boundary condition. Beside contact angle, topological boundary, interfacial slip, and low hydrodynamic drag should also be considered as boundary condition.

4.3 Summary and Future Work

Dynamic wetting of water, glycerin, and silicon oil droplets on concentric triangular circles and pyramidal arrays have been investigated with respect to drop volume change. Emphasis has been placed upon understanding the effect of viscosity on dynamic wetting on structured surfaces. A force driven oscillation in contact line radius was observed, where the amplitude (the jumping distance) remained the same and the period increased systematically. By fixing the density and surface tension and varying the viscosity of silicon oil, it is observed that high viscosity of the same liquid causes on the same structured surface a longer pinning duration, which enables a larger advancing dynamic contact angle. A similar observation was also made in chapter 3 in the case of dip coating experiments. To be able to demonstrate and prove the isolated effect of viscosity and the influence of viscosity on contact line pinning duration, the number of test liquids should be increased and all test should be done at a fixed capillary number in low hydrodynamic range.

Numerical simulations are performed for wetting on 3D pyramidal arrays with water and glycerin-water mixture by implementing Kistler's dynamic wetting equation. Compatible results to experiments are found for flat surfaces and 1mm pyramidal arrays, where viscous forces dominate, whereas on 0.5mm pyramidal arrays, the results are not very compatible. In order to achieve more compatible simulation results, further variables mention above (topological boundary, interfacial slip, and low hydrodynamic drag) should be set as boundary conditions.

Chapter 5

Conclusion

In the present study, the forced wetting of very rough surfaces has been investigated in the vertical and horizontal alignment, by dipping the substrate into a liquid bath and pumping liquid through the center of the substrate, respectively. Various kinds of PDMS (polydimethylsiloxane), deionized water, and glycerin-water (85%-15% vol.) mixture were used to wet pyramidal arrays and concentric triangular circles, whose features are on the scale of millimeters. The whole system was in quasi-steady state and in a low Reynolds and capillary number range. The apparent contact angle on each substrate was measured and a correlation between capillary number, contact angle, and feature size was sought. Existing models and contact angle evaluation methods, together with additional new approaches, have been applied and were discussed extensively. Numerical simulations for wetting on horizontally placed substrates were performed by using a C++ based, open source CFD software package, OpenFOAM®. Kistler's dynamic wetting equation was implemented into the software and simulation results compatible with experiments were achieved.

With the experiments accomplished in this study, it is concluded that contact angle is not a transferable boundary condition, due to the fluctuations on the surface caused by very rough 3D features. These fluctuations on the surface result in a range of contact angles and a global contact angle cannot be determined. Moreover, in the case of dip coating experiments, the effect of the liquid flow though the side grooves on the velocity of the main liquid front is observed. The additional velocity component exerts a push on the liquid front, which is only observed for the pyramid, which has a feature size larger than the capillary length of the test liquid. In conclusion, it is shown that there is not a unique boundary condition on the contact angle/line, even for one test surface, which spoils the transferability of contact angle. Moreover, it was found that roughness on these scales bears significant differences with chemical heterogeneity.

Suggestions for future work:

The following key points are recommended for future research efforts:

- The influence of viscosity on wetting on very rough surfaces isolated from the velocity at fixed capillary numbers should be investigated systematically.
  - In order to accomplish this task in the case of dip coating, PDSM with varying viscosities can be used, with which the effects of density and surface tension can be eliminated. The plate velocity should be coupled with the present viscosity of the test liquid to be able to fix the capillary number by staying in low Reynolds number hydrodynamics.
  - In the case of wetting on horizontally aligned structured surfaces by increasing the droplet volume, how the effect of pinning on contact angle changes with respect to the viscosity should be investigated in detail by using 2D structures, where the droplet elongation along the groves is restricted and only the fluid spreading normal to the grooves is allowed.
- The numerical simulations can be improved by using further boundary conditions on topology, interfacial slip, and low hydrodynamic drag.
- The imaging can be done at a higher resolution to minimize the errors caused by the present pixel size and the image processing can be optimized with respect to the improved resolution.

Finally, it is hoped that the present study is a helpful contribution to understand the wetting behavior on surfaces with very large scale roughness features.

Appendix A

Physical Meaning of Dimensionless Numbers

Buckingham π theorem is a formalization of Rayleigh's method of dimensional analysis. An equation involving n number of physical variables expressed in terms of k independent fundamental physical quantities yields an equation involving a set of $p = n-k$ dimensionless parameters constructed from the original variables. Here six parameters are used to describe the wetting process, which are relevant to the dynamics of flow. These parameters are, velocity (v), density (ρ), contact line radius (R), surface tension (σ), dynamic viscosity (μ) and gravity (g) , respectively. Due to Buckingham π theorem, with 6 parameters and 3 dimensions (mass, length and time) the number of independent dimensionless groups is 3.

- **Reynolds number** is the fraction of total momentum transfer (inertia pressure ρv^2) to molecular momentum transfer (viscous pressure $\mu v/R$). Reynolds number is used in the absence of free surface.

$$Re = \frac{\rho v R}{\mu} \tag{A.1}$$

- **Weber number** is defined as the ratio of the momentum in the vapor layer (inertial forces) divided by the surface tension force restraining the liquid. Weber number is used in the presence of free surface.

$$We = \frac{\rho v^2 R}{\sigma} \tag{A.2}$$

- **Bond number** is the ratio of body force to surface tension. A high Bond number indicates that the system is relatively unaffected by surface tension effects; a low number (typically less than one is the requirement) indicates that surface tension dominates. The Bond number is the most common comparison of gravity and surface tension effects.

$$Bo = \frac{\rho g R^2}{\sigma} \tag{A.3}$$

  Using the 3 dimensionless numbers described above, more dimensionless numbers can be interpreted according to demand.

- **Froude number** shows the ratio of a body's inertia to gravitational forces. It is used to determine the resistance of an object moving through water.

$$Fr = \frac{We}{Bo} \tag{A.4}$$

- **Capillary number** is the relative effect of viscous forces versus surface tension acting across an interface between a liquid and a porous media.

$$Ca = \frac{We}{Re} = \frac{\mu v}{\sigma} \tag{A.5}$$

- **Ohnesorge number** shows the relation between the viscous forces to inertial and surface tension forces. This is often used to relate to free surface fluid dynamics such as dispersion of liquids in gases and in spray technology. **Oh** does not contain the velocity of the contact line.

$$Oh = \frac{\sqrt{We}}{Re} = \frac{\mu}{\sqrt{\rho\sigma D}} \tag{A.6}$$

- **Physical properties number** shows only the relation between physical properties of liquids and is independent of droplet diameter, contact line velocity or droplet size.

$$PP = \frac{Re^{4/3}Fr^{1/3}}{We} = \sigma(\frac{\rho}{\mu^4 g})^{1/3} \tag{A.7}$$

Appendix B

Properties of Test Liquids

As test liquids deionized water, glycerin-water mixture (85%-15% vol.) and PDMS (trimethylsiloxy terminated polydimethylsiloxane) with two different viscosities (10cSt and 100cSt) are used. Deionized water is mainly used as a reference liquid to compare the effect of viscosity, surface tension and density of two complex test fluids. Glycerin ($C_3H_8O_3$) is a simple polyol compound, which is a colorless, odorless, viscous liquid that is widely used in pharmaceutical applications mainly as a means of improving smoothness, providing lubrication; moreover glycerin used as an anti-freeze for automotive applications before being replaced by ethylene glycol, which has a lower freezing point. Glycerin has three hydroxyl groups that are responsible for its solubility in water. In industrial food preparations, glycerol serves as a humectant, solvent, and sweetener, and may help preserve food. Silicon oils are widely used as lubricants or hydraulic fluids. They are excellent electrical insulators and non-flammable. They have excellent temperature-stability and heat-transfer characteristics, which make them good cooling liquids and anti-foamer. PDMS $(C_2H_6SiO)_n$) is a common variant of silicon oil, an optically clear, inert, non-toxic, non-flammable liquid, which is widely used as lubricant, heat resistant, antifoaming agent, etc.. It is a viscoelastic fluid, which acts like a viscous liquid under high temperature and long flow times and acts like a solid under low temperatures and short flow times. The advantage of using PDMS in experiments is being able to keep the density and surface tension more or less same for various viscosities as seen in the Table B.1.

liquids @20°	ρ (kg/m^3)	σ (kg/s^2)	μ (kg/ms)	L_c
water	1000	72.8×10^{-3}	1×10^{-3}	2.72
glycerin 85%	1250	63.4×10^{-3}	109×10^{-3}	2.27
PDMS 10cSt	935	20.1×10^{-3}	9.35×10^{-3}	1.48
PDMS 100cST	970	20.9×10^{-3}	97×10^{-3}	1.48
Silicon oil 5cSt	925	19.7×10^{-3}	4.625×10^{-3}	1.47
Silicon oil 10cSt	935	20.1×10^{-3}	9.35×10^{-3}	1.48
Silicon oil 20cSt	945	20.6×10^{-3}	18.9×10^{-3}	1.49
Silicon oil 50cSt	965	20.7×10^{-3}	48.25×10^{-3}	1.47

Table B.1: Properties of test liquids. L_c is the capillary length.

Appendix C

Scheimpflug Principle

The Scheimpflug principle is a optogeometric rule, which distorts the plane of focus in an imaging system. By shifting or tilting the camera of the lens separately from each other, it is possible to move (tilt or shift) the plane of focus in the horizontal or vertical axis relative to lens axis. Austrian army Captain Theodor Scheimpflug developed and applied this method to correct perspective distortion in aerial photographs (patented in Great Britain in 1904 under GB119/1904). In the present study, the Scheimpflug arrangement allows an off-axis camera placement, while keeping the entire contact line in focus.

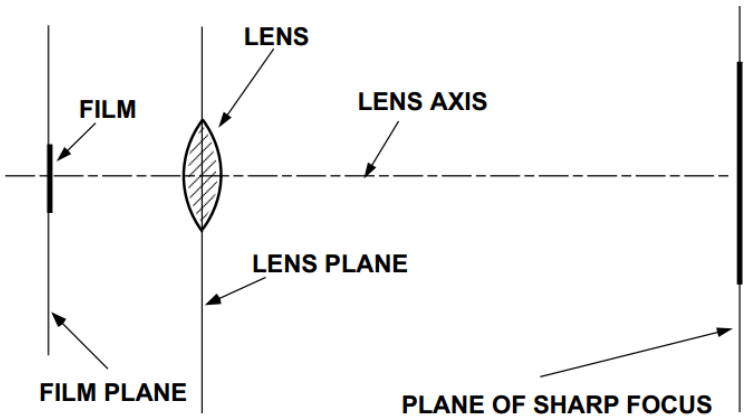

Figure C.1: Schematic representation of the basic optical geometry of an imaging system. Film, lens and focus planes are parallel to each other and perpendicular to the lens axis [100].

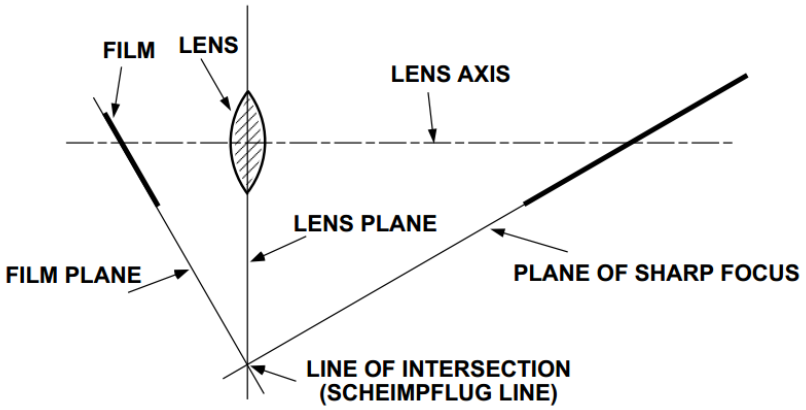

Figure C.2: Schematic representation of the basic optical geometry of a Scheimpflug imaging system. The lens plane and the film plane are no longer parallel to one another. As a consequence, the sharp focus plane is also tilted [100].

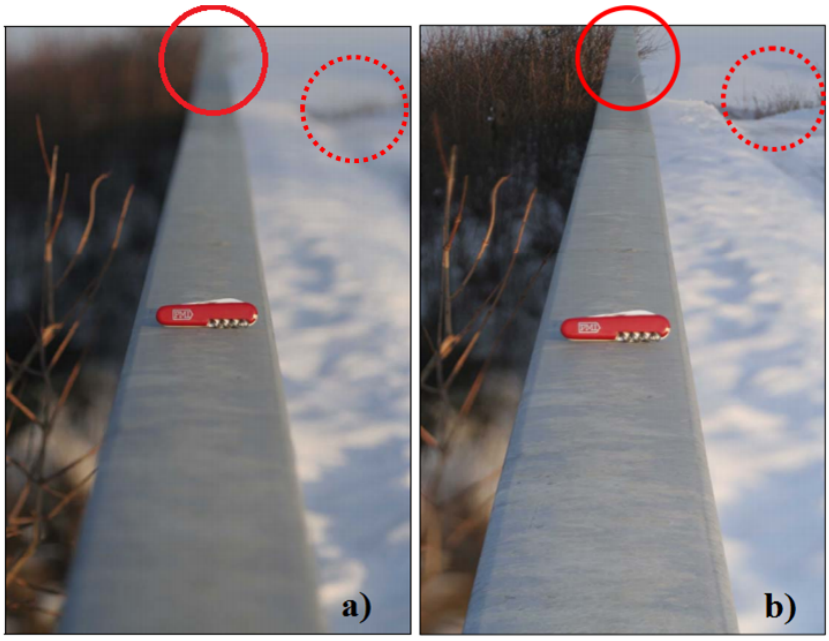

Figure C.3: With the help of a Scheimpflug adapter, the focal plane can be tilted. This enables the photographer to be able to focus on a horizontal plane. In the first image, the focus plane is parallel to the camera, therefore only one single line in the middle is in focus. In the second image, plane of focus is tilted, so a line from bottom to top is now taken in focus [101].

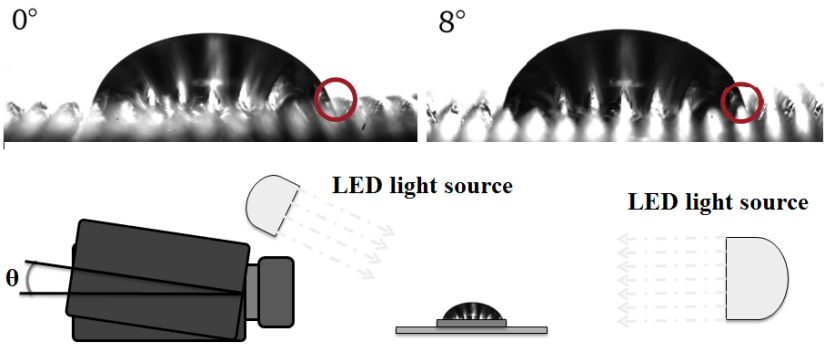

Figure C.4: The recordings for this work are done using two light sources to adjust the tilted setup. Swinging the camera in 8° helps us to detect the contact line more accurately by shifting the plane of focus.

Figure C.5: A black accordion covers the gap between objective and camera, as the camera tilted or shifted unattached to the objective.

Appendix D

Complimentary Data Plots

D.1 Fluctuation Decay Graphs (related to Chapter 3)

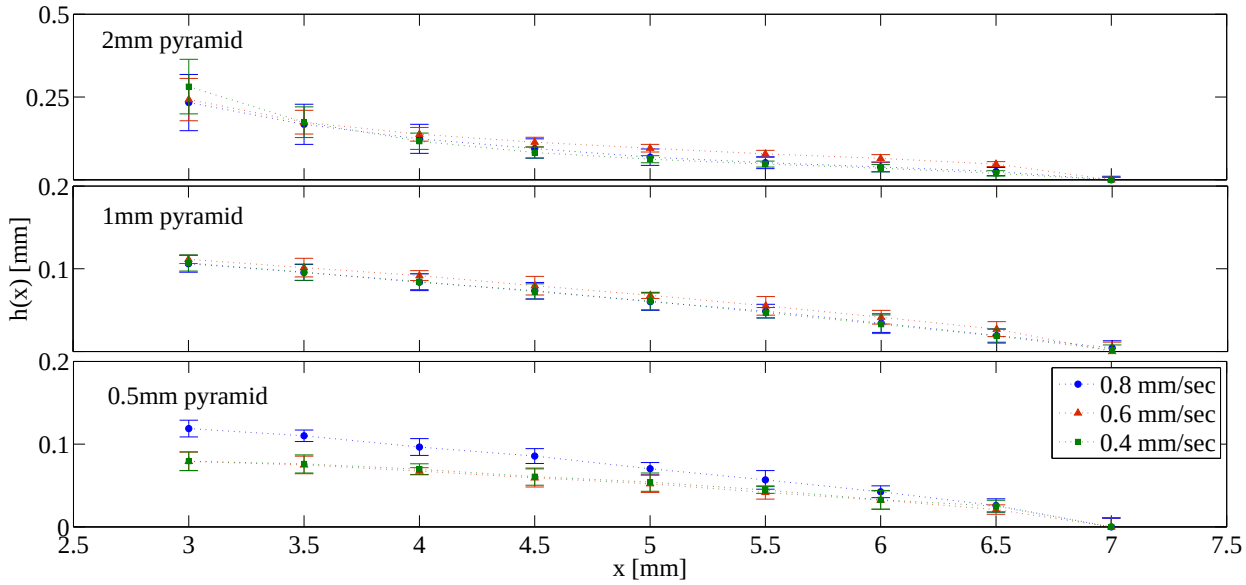

Figure D.1: 10cSt PDMS, advancing case.

Figure D.1 shows the averaged height of meniscus at specific positions far away from the wall (minimum point of the features) of the substrates. Here we see that the fluctuations on the meniscus shape caused by the 3D feature decay at x=7mm for all feature sizes. An extrapolation of meniscus shape from this far cannot be done correctly.

D.2 Contact Angle and Radius Measurements on Pyramidal Arrays (related to Chapter 4)

Figures D.2 and D.3 show the systematic, but non-periodic evolution of the growing droplet on the pyramidal arrays. The black dots are the contact angle measurements on flat surface. The contact angle on pyramidal arrays are fluctuation around the black dots.

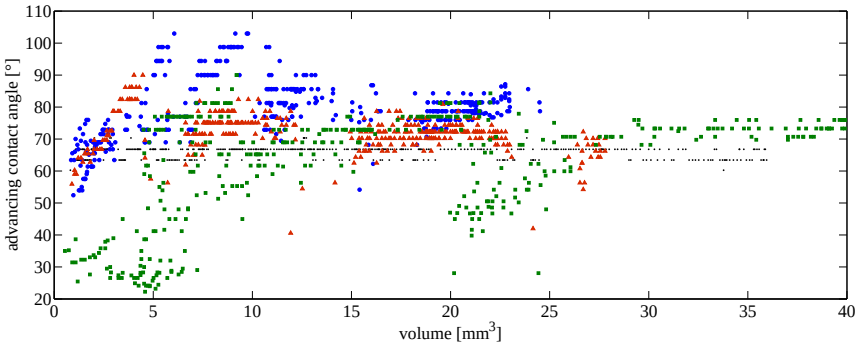

(a) Silicon oil 5cSt droplet growing on 3 different pyramidal structures.

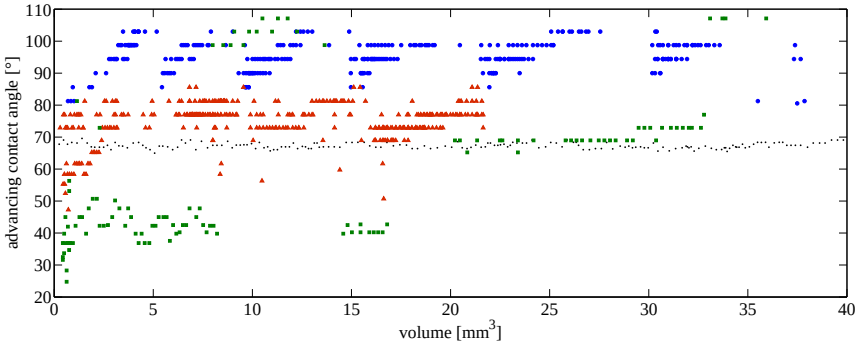

(b) Silicon oil 10cSt droplet growing on 3 different pyramidal structures.

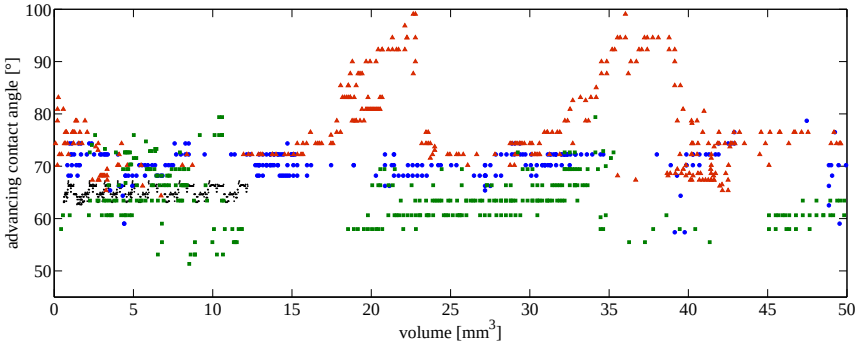

(c) Silicon oil 20cSt droplet growing on 3 different pyramidal structures.

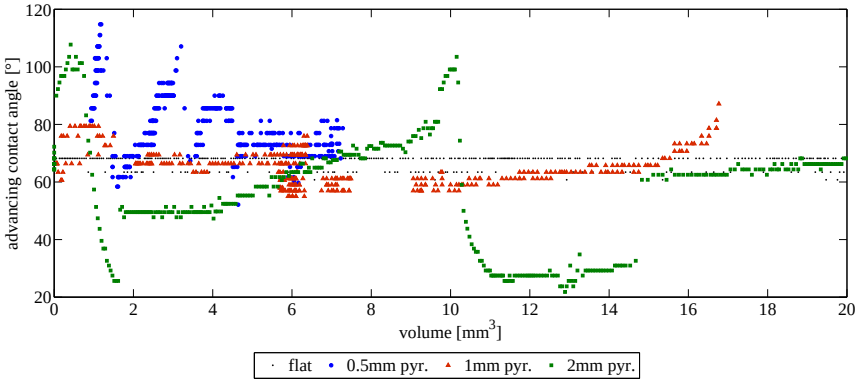

(d) Silicon oil 50cSt droplet growing on 3 different pyramidal structures.

Figure D.2: The dynamic contact angle of the growing silicon oil droplets in various viscosities is presented in relation with the volume increment on pyramidal arrays.

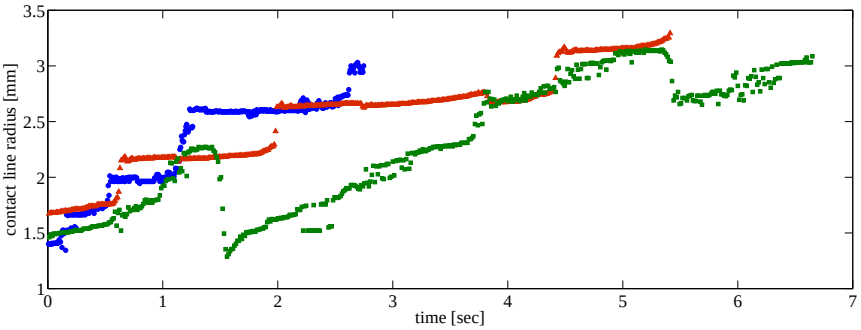

(a) The change of contact line radius of silicon oil 5cSt droplet on 3 pyramidal arrays.

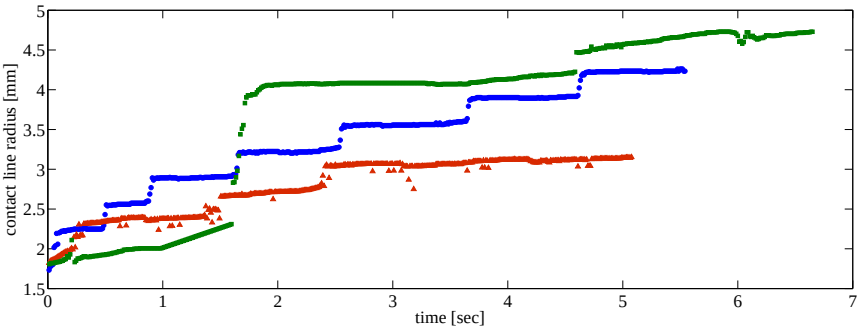

(b) The change of contact line radius of silicon oil 10cSt droplet on 3 pyramidal arrays.

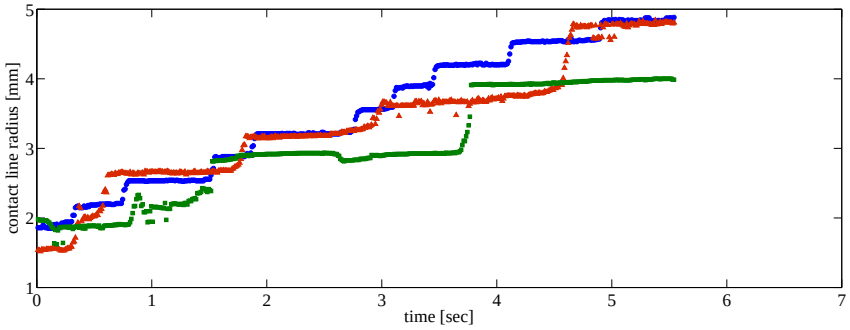

(c) The change of contact line radius of silicon oil 20cSt droplet on 3 pyramidal arrays.

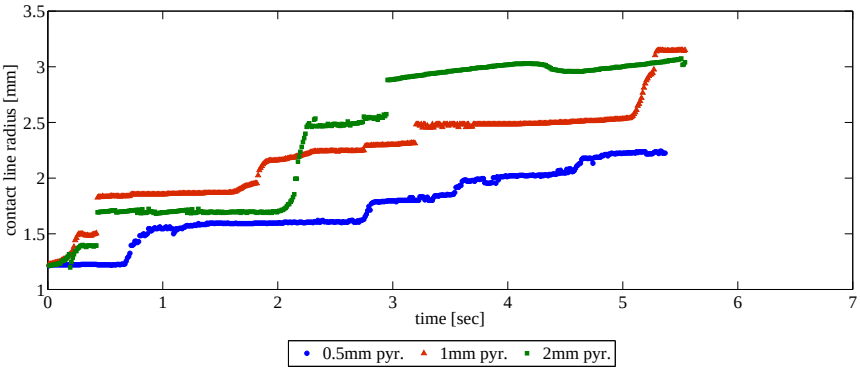

(d) The change of contact line radius of silicon oil 50cSt droplet on 3 pyramidal arrays.

Figure D.3: The stepwise change in radius with respect to time for 4 silicon oil types.

Bibliography

[1] Berg J.C., 'Wettability', Chapter 1, Pergamon, New York, 1993. 3

[2] Proposal for the Establishment of a Cluster of Excellence, Smart Interfaces, Techische Universität Darmstadt, April 2007. 3

[3] Berg J.C., 'Wettability', Chapter 6, Pergamon, New York, 1993. 3

[4] Adamson A.D., 'Physical Chemisty of Surfaces', John Wiley & Sons, 1990. 3

[5] Cox R.G., J. Fluid Mech., 131 , 1-26, 1983. 4, 10, 11, 20

[6] De Coninck J., de Ruijter M.J., Voué M., Current Opinion in Colloid Interface Science, 6:49, 2001. 4

[7] Shikhmurzaev Y.D., J. Phys.: Condense Matter, 14:319, 2002. 4

[8] Blake T.D., Journal of Colloid and Interface Science, 2991, 2006. 4

[9] Carré A., Gastel J., Shanahan M.N.R., Nature, 379, 1996. 4

[10] Style R.W., Dufresne E.R., Soft Matter, 8, 7177, 2012. 4

[11] Homsy G.M., Annu. Rev. Fluid Mech. 19, 271311, 1987. 4

[12] Lee A.G., Shaqfeh E.G., Khomami B., J. Fluid Mech., 531, 5983, 2005. 4

[13] Seyrat E., Hayes R.A., J. App. Phys. 90:3, 2001. 4

[14] Butt T.D., Graf K., Kappl M., 'Physical Chemistry Interfaces', Wiley-VCH, Berlin 2003. 4

[15] Gibbs J.W. 'The Collected Works of J.W. Gibbs, Vol. 1, Thermodynamics', Yale Univ. Press, New Haven, 1992. 1, 4

[16] Young T., Phil. Trans., 95:65, 85, 1805. 1, 4

[17] Wenzel R.N., Ind. Eng. Chem. 28:8, 988994, 1936. 5, 12

[18] Cassie A.B.D., Baxter S., Trans. Faraday Soc. 40, 546551, 1944. 6, 12

[19] Thiele U., D. Quéré, Colloids and Surfaces, 206, 13, 4146, 2008. 6

[20] Ishino C., Okumura K., European Physical Journal 25:4, 415424, 2008. 6

[21] Marmur A., Langmuir 19:20, 83438348, 2003. 7, 10

[22] Gao L., McCarthy T.J., Langmuir, 23, 3762, 2007. 7

[23] Gao L., McCarthy T.J., Langmuir, 2524, 14105-14115, 2009. 7

[24] Nosonovsky M., Bhushan B., Langmuir, 24, 1525-1533, 2008. 7

[25] Berg J.C., 'Wettability', Chapter 5, Pergamon, New York, 1993. 7, 8

[26] Berg J.C., 'Wettability', Chapter 3, Pergamon, New York, 1993. 7

[27] Haley P.J., Miskis M.J., J. Fluid Mech., 223:57, 1991. 8

[28] Ruckenstein E., Dunn C.S., Journal of Colloid and Interface Science, 59:135, 1977. 8

[29] Powell R.E, Roseveare W.E., Eyring H., Ind. Eng. Chem., 33:430, 1941. 8

[30] Blake T.D., Ruschak K.J., Nature, 282:489, 1979. 8, 15

[31] Cazabat A.M., Fraysse N., Heslot F., Colloids and Surfaces, 52:1, 1991. 9

[32] Wayner P.C.Jr., Colloids and Surfaces, 52:71, 1991. 9

[33] van Damme H.S., Hogt A.H., Feijen J., J. Coll. Inter. Sci., 114:167, 1986. 9

[34] Shanahan M.E.R., J. Phys. D: Appl. Phys., 21:981, 1988. 9

[35] Brochard F., de Gennes P.G., Langmuir, 7:3216, 1991. 9

[36] Bonn D., Eggers J., Indekeu J., Meunier J., Rolley E., Reviews of Modern Physics, 812, 739, 2009. 9, 10

[37] Voinov O.V., J. Appl. Mech. Tech. Phys. 18, 216, 1977. 10

[38] Blake T.D., Bracke M., Shikhmuzaev, Physics of Fluids 11:8 1999. 10

[39] Huh C., Scriven L.E., J. Coll. Inter. Sci. 35:85 1971. 10, 12, 17, 18

[40] Marsh J.A., Garoff S., Dussan E.B.V., Phys. Rev. Let. 70-18:2778, 1993. 10, 16

[41] de Gennes P.G., Reviews of Modern Physics 57:827 1985. 10, 12

[42] Eggers J., Stone H.A., J. Fluid Mech., 505, 309321 2004. 10

[43] Shikhmurzaev Y.D., J. Fluid Mech. 334, 211 1997. 10

[44] Tadmor R., Langmuir 20 18:765964, 2004. 10

[45] Tanner L.H., J. Phys. D: Appl. Phys. 12:1473, 1979. 11

[46] Cox R.G., J. Fluid Mech., 357249 1998. 11, 20

[47] Hoffman R. L., J. Coll. Inter. Sci. 50:2, 228 1974. 1, 11

[48] Hoffman R. L., J. Coll. Inter. Sci. 94:2, 470 1983. 11

[49] Seebergh J.E., Berg J.C., Chem. Eng. Sci. 47:4455, 1992. 11

[50] Jiang T.S., Oh S.G., J.C. Slattery, J. Col. Inter. Sci. 69:74 1979. 11

[51] Bracke M., de Voeght F., Joos P., Prog. Coll. Polym. Sci. 79:142 1989. 11

[52] Huh C., Mason S.G., J. Fluid Mech., 81:401 1977. 12, 20

[53] Kröner D., Z. Angew. Math. Mech., 67:T303 1973. 12

[54] Borgs C., de Coninck J., Kotecký R., Zinque M., Phys. Rev. Lett. 74, 2292 1995. 13

[55] Swain P.S., Lipowsky R., Langmuir, 14 23, 67726780 1998. 13

[56] D. Urban, K. Topolski and J. de Coninck, Phys. Rev. Lett. 76, 4388 1996. 13

[57] Johnson R.E., Dettre R.H., Journal of Physical Chemistry, 68-7, 1744, 1964. 13, 75

[58] Johnson R.E., Dettre R.H., Journal of Physical Chemistry, 69-5, 1507, 1965. 13

[59] Extrand C.W., Langmuir 19, 3793-3796 2003. 13

[60] Anantharaju N., Panchagnula M.V., Vedantam S., Langmuir, 25:13, 74107415 2009. 13

[61] Snoeijer J.H., Andreotti B., Delon G., Fermiger M., J. Fluid Mech., 579, 6383 2007. 13

[62] Delon G., Snoeijer J.H., Fermiger M., Andreotti B., J. Fluid Mech., 604, 55-75 2008. 13

[63] Deryagin B.M., Levi S.M., 'Film Coating Theory', New Yok Focal Press 1964. 15

[64] Landau L., Levich B., Acta Pysicochim URSS, 17, 42-54, 1942. 15, 21

[65] Benkreira H., Cohu O., Chemical Engineering Science, 536, 1223-1231, 1998. 15

[66] Darhuber A.A., Troian S.M., Davis J.M., Miller S.M., Journal of Applied Physics, 886, 5119-5121, 2000. 15

[67] Mastrangeli M., Ruythooren W., van Hoof C., Celis J.P., J. Micromech. Microeng., 19, 045015, 2009. 15

[68] Roland S., Gaspard D., Prudhomme R.E., Bazuin C.G., Macromolecules, 45 13, 54635476 2012. 15

[69] Schwartz L.W., Garoff S., Langmuir, 1 219-230 1985. 15

[70] Ramé E., Garoff S., Journal of Colloid and Interface Science, 177:234-244 1996. 16

[71] Chen Q., Ramé E., Garoff S., J. Fluid Mech. 337, 49-66, 1997. 16

[72] Wei Y., Rame E., Schwartz L.W., Garoff S., J. Phys.: Condens. Matter 21:464126 2009. 16

[73] Weislogel M., NASA Technical Memorandum 107364, 1996. 16

[74] Ngan C.G., Dussan E.B.V., J. Fluid Mech. 118, 27-40, 1982. 16

[75] Roberts G., 'LangmuirBlodgett Films', Plenum Press, New York, p. 317, 1990. 17

[76] Binks B.P., Adv. Colloid Interface Sci. 34:343 1991. 17

[77] Bikerman J.J. , Proc. R. Soc. Lond. Ser. A Mater. Phys. Sci. 170:130 1939. 17

[78] Gaines G.L. Jr., 'Insoluble Monolayers at LiquidGas Interface', Interscience publishers, New York, 1966. 17

[79] Savelski M.J., Shetty S.A., Kolb W.B., Cerro R.L., J. Colloid Interface Sci. 176:117 1995. 17

[80] Groenveld P., Chem. Eng. Sci. 25:1259 1970. 18

[81] Elena Diaz M., Cerro R.L., Thin Solid Films 460:274278, 2004. 17, 18

[82] Cox R.G., J. Fluid Mech., 168, 169:194, 1986. 20

[83] Dussan E.B.V, J. Fluid Mech., 77:665, 1979. 20

[84] Derjaguin B., Comptes endus Doklady de l'Akademie des Science de l'URSS, 39, 13-16 1943. 21

[85] Wilson S.D.R., J. Eng. Math., 16:209-221, 1982. 21

[86] Maleki M., Reyssat M., Restagno F., Quéré D., Clanet C., Jounal of Colloid and Interface Science, 354:359-363, 2011. 21

[87] Otsu, N., IEEE Transactions on Systems, Man, and Cybernetics, Vol. 9, No. 1, pp. 62-66, 1979. 23, 77

[88] Plawsky J.L., Ojha M., Chatterjee A., Wayner P.C., Chem. Eng. Comm. 196, 658-696, 2008. 75

[89] Chu K., Xiao R., Wang E.N., Nature Mateials 9:413, 2010. 75

[90] Priest C., Albrecht T.W.J., Sedev R., Ralston J., Langmuir, 35:10 5655-5660, 2009. 75

[91] Forsberg P.S.H., Priest C., Brinkmann M., Sedev R., Ralston J., Langmuir, 26:2 860-865, 2010. 75

[92] Liu G., Fu L., Rode A.V., Craig V.S.J., Langmuir 27:2595-2600, 2011. 75

[93] Duncan D., Li D., Gaydos J., Neumann A.W., Journal of Colloid and Interface Science 169:256-261 1995. 75

[94] Brandon S., Wachs A., Marmur A., Journal of Colloid and Interface Science, 191:110-116, 1997. 75

[95] http://www.susqu.edu/brakke/evolver/evolver.html 75

[96] Berberovic E., 'Investigation of Free-surface Flow Associated with Drop Impact: Numerical Simulations and Theoretical Modeling', PhD thesis, TU Darmstadt, Darmstatd, 2010. 95

[97] Jasak, H., 'Error analysis and estimation for the finite volume method with applications to Fluid Flows', PhD thesis, Imperial College of Science, Technology and Medicine, London, 1996. 95

[98] Ridders C. , IEEE Transactions on Circuits and Systems 26: 979980 1979. 95

[99] Sharfrin E., Zisman W.A., The Journal of Physical Chemistry 645, 519524 1960. 1

[100] Merklinger H.M., 'Shutterbug', November 1992. 109

[101] Anwendngsbeispiele mit dem Universalbalgengert Novoflex Balpro TS, V 28.07.2006. 110